STUDY ON THE APPLICATIONS OF THE
FINITE DIFFERENCE – TIME DOMAIN METHOD
FOR SOLUTION OF ELECTROMAGNETIC PROBLEMS

by

Walid Afif Chamma

A Thesis submitted to the Faculty of Graduate Studies
of the University of Manitoba in partial fulfillment
of the requirements for the degree of
Doctor of Philosophy
in
Electrical Engineering

Winnipeg, Manitoba,
January 1993
© Walid Chamma

Canada

Name _____

Dissertation Abstracts International is arranged by broad, general subject categories. Please select the one subject which most nearly describes the content of your dissertation. Enter the corresponding four-digit code in the spaces provided.

Electronics and Electrical
SUBJECT TERM

| 0 | 5 | 4 | 4 |

SUBJECT CODE

U·M·I

Subject Categories

THE HUMANITIES AND SOCIAL SCIENCES

COMMUNICATIONS AND THE ARTS
Architecture 0729
Art History 0377
Cinema 0900
Dance 0378
Fine Arts 0357
Information Science 0723
Journalism 0391
Library Science 0399
Mass Communications 0708
Music 0413
Speech Communication 0459
Theater 0465

EDUCATION
General 0515
Administration 0514
Adult and Continuing 0516
Agricultural 0517
Art 0273
Bilingual and Multicultural 0282
Business 0688
Community College 0275
Curriculum and Instruction 0727
Early Childhood 0518
Elementary 0524
Finance 0277
Guidance and Counseling 0519
Health 0680
Higher 0745
History of 0520
Home Economics 0278
Industrial 0521
Language and Literature 0279
Mathematics 0280
Music 0522
Philosophy of 0998
Physical 0523

Psychology 0525
Reading 0535
Religious 0527
Sciences 0714
Secondary 0533
Social Sciences 0534
Sociology of 0340
Special 0529
Teacher Training 0530
Technology 0710
Tests and Measurements 0288
Vocational 0747

LANGUAGE, LITERATURE AND LINGUISTICS
Language
  General 0679
  Ancient 0289
  Linguistics 0290
  Modern 0291
Literature
  General 0401
  Classical 0294
  Comparative 0295
  Medieval 0297
  Modern 0298
  African 0316
  American 0591
  Asian 0305
  Canadian (English) 0352
  Canadian (French) 0355
  English 0593
  Germanic 0311
  Latin American 0312
  Middle Eastern 0315
  Romance 0313
  Slavic and East European 0314

PHILOSOPHY, RELIGION AND THEOLOGY
Philosophy 0422
Religion
  General 0318
  Biblical Studies 0321
  Clergy 0319
  History of 0320
  Philosophy of 0322
Theology 0469

SOCIAL SCIENCES
American Studies 0323
Anthropology
  Archaeology 0324
  Cultural 0326
  Physical 0327
Business Administration
  General 0310
  Accounting 0272
  Banking 0770
  Management 0454
  Marketing 0338
Canadian Studies 0385
Economics
  General 0501
  Agricultural 0503
  Commerce-Business 0505
  Finance 0508
  History 0509
  Labor 0510
  Theory 0511
Folklore 0358
Geography 0366
Gerontology 0351
History
  General 0578

Ancient 0579
Medieval 0581
Modern 0582
Black 0328
African 0331
Asia, Australia and Oceania 0332
Canadian 0334
European 0335
Latin American 0336
Middle Eastern 0333
United States 0337
History of Science 0585
Law 0398
Political Science
  General 0615
  International Law and
    Relations 0616
  Public Administration 0617
Recreation 0814
Social Work 0452
Sociology
  General 0626
  Criminology and Penology ... 0627
  Demography 0938
  Ethnic and Racial Studies 0631
  Individual and Family
    Studies 0628
  Industrial and Labor
    Relations 0629
  Public and Social Welfare 0630
  Social Structure and
    Development 0700
  Theory and Methods 0344
Transportation 0709
Urban and Regional Planning 0999
Women's Studies 0453

THE SCIENCES AND ENGINEERING

BIOLOGICAL SCIENCES
Agriculture
  General 0473
  Agronomy 0285
  Animal Culture and
    Nutrition 0475
  Animal Pathology 0476
  Food Science and
    Technology 0359
  Forestry and Wildlife 0478
  Plant Culture 0479
  Plant Pathology 0480
  Plant Physiology 0817
  Range Management 0777
  Wood Technology 0746
Biology
  General 0306
  Anatomy 0287
  Biostatistics 0308
  Botany 0309
  Cell 0379
  Ecology 0329
  Entomology 0353
  Genetics 0369
  Limnology 0793
  Microbiology 0410
  Molecular 0307
  Neuroscience 0317
  Oceanography 0416
  Physiology 0433
  Radiation 0821
  Veterinary Science 0778
  Zoology 0472
Biophysics
  General 0786
  Medical 0760

EARTH SCIENCES
Biogeochemistry 0425
Geochemistry 0996

Geodesy 0370
Geology 0372
Geophysics 0373
Hydrology 0388
Mineralogy 0411
Paleobotany 0345
Paleoecology 0426
Paleontology 0418
Paleozoology 0985
Palynology 0427
Physical Geography 0368
Physical Oceanography 0415

HEALTH AND ENVIRONMENTAL SCIENCES
Environmental Sciences 0768
Health Sciences
  General 0566
  Audiology 0300
  Chemotherapy 0992
  Dentistry 0567
  Education 0350
  Hospital Management 0769
  Human Development 0758
  Immunology 0982
  Medicine and Surgery 0564
  Mental Health 0347
  Nursing 0569
  Nutrition 0570
  Obstetrics and Gynecology .. 0380
  Occupational Health and
    Therapy 0354
  Ophthalmology 0381
  Pathology 0571
  Pharmacology 0419
  Pharmacy 0572
  Physical Therapy 0382
  Public Health 0573
  Radiology 0574
  Recreation 0575

Speech Pathology 0460
Toxicology 0383
Home Economics 0386

PHYSICAL SCIENCES
Pure Sciences
Chemistry
  General 0485
  Agricultural 0749
  Analytical 0486
  Biochemistry 0487
  Inorganic 0488
  Nuclear 0738
  Organic 0490
  Pharmaceutical 0491
  Physical 0494
  Polymer 0495
  Radiation 0754
Mathematics 0405
Physics
  General 0605
  Acoustics 0986
  Astronomy and
    Astrophysics 0606
  Atmospheric Science 0608
  Atomic 0748
  Electronics and Electricity 0607
  Elementary Particles and
    High Energy 0798
  Fluid and Plasma 0759
  Molecular 0609
  Nuclear 0610
  Optics 0752
  Radiation 0756
  Solid State 0611
Statistics 0463

Applied Sciences
Applied Mechanics 0346
Computer Science 0984

Engineering
  General 0537
  Aerospace 0538
  Agricultural 0539
  Automotive 0540
  Biomedical 0541
  Chemical 0542
  Civil 0543
  Electronics and Electrical 0544
  Heat and Thermodynamics ... 0348
  Hydraulic 0545
  Industrial 0546
  Marine 0547
  Materials Science 0794
  Mechanical 0548
  Metallurgy 0743
  Mining 0551
  Nuclear 0552
  Packaging 0549
  Petroleum 0765
  Sanitary and Municipal 0554
  System Science 0790
Geotechnology 0428
Operations Research 0796
Plastics Technology 0795
Textile Technology 0994

PSYCHOLOGY
General 0621
Behavioral 0384
Clinical 0622
Developmental 0620
Experimental 0623
Industrial 0624
Personality 0625
Physiological 0989
Psychobiology 0349
Psychometrics 0632
Social 0451

Nom _____

Dissertation Abstracts International est organisé en catégories de sujets. Veuillez s.v.p. choisir le sujet qui décrit le mieux votre thèse et inscrivez le code numérique approprié dans l'espace réservé ci-dessous.

SUJET

☐☐☐☐ U·M·I

CODE DE SUJET

Catégories par sujets

HUMANITÉS ET SCIENCES SOCIALES

COMMUNICATIONS ET LES ARTS
Architecture 0729
Beaux-arts 0357
Bibliothéconomie 0399
Cinéma 0900
Communication verbale 0459
Communications 0708
Danse 0378
Histoire de l'art 0377
Journalisme 0391
Musique 0413
Sciences de l'information 0723
Théâtre 0465

ÉDUCATION
Généralités 515
Administration 0514
Art 0273
Collèges communautaires 0275
Commerce 0688
Économie domestique 0278
Éducation permanente 0516
Éducation préscolaire 0518
Éducation sanitaire 0680
Enseignement agricole 0517
Enseignement bilingue et
   multiculturel 0282
Enseignement industriel 0521
Enseignement primaire 0524
Enseignement professionnel 0747
Enseignement religieux 0527
Enseignement secondaire 0533
Enseignement spécial 0529
Enseignement supérieur 0745
Évaluation 0288
Finances 0277
Formation des enseignants 0530
Histoire de l'éducation 0520
Langues et littérature 0279

Lecture 0535
Mathématiques 0280
Musique 0522
Orientation et consultation 0519
Philosophie de l'éducation 0998
Physique 0523
Programmes d'études et
   enseignement 0727
Psychologie 0525
Sciences 0714
Sciences sociales 0534
Sociologie de l'éducation 0340
Technologie 0710

LANGUE, LITTÉRATURE ET LINGUISTIQUE
Langues
   Généralités 0679
   Anciennes 0289
   Linguistique 0290
   Modernes 0291
Littérature
   Généralités 0401
   Anciennes 0294
   Comparée 0295
   Mediévale 0297
   Moderne 0298
   Africaine 0316
   Américaine 0591
   Anglaise 0593
   Asiatique 0305
   Canadienne (Anglaise) 0352
   Canadienne (Française) 0355
   Germanique 0311
   Latino-américaine 0312
   Moyen-orientale 0315
   Romane 0313
   Slave et est-européenne 0314

PHILOSOPHIE, RELIGION ET THÉOLOGIE
Philosophie 0422
Religion
   Généralités 0318
   Clergé 0319
   Études bibliques 0321
   Histoire des religions 0320
   Philosophie de la religion 0322
Théologie 0469

SCIENCES SOCIALES
Anthropologie
   Archéologie 0324
   Culturelle 0326
   Physique 0327
Droit 0398
Économie
   Généralités 0501
   Commerce-Affaires 0505
   Économie agricole 0503
   Economie du travail 0510
   Finances 0508
   Histoire 0509
   Théorie 0511
Études américaines 0323
Études canadiennes 0385
Études féministes 0453
Folklore 0358
Géographie 0366
Gérontologie 0351
Gestion des affaires
   Généralités 0310
   Administration 0454
   Banques 0770
   Comptabilité 0272
   Marketing 0338
Histoire
   Histoire générale 0578

Ancienne 0579
Médiévale 0581
Moderne 0582
Histoire des noirs 0328
Africaine 0331
Canadienne 0334
États-Unis 0337
Européenne 0335
Moyen-orientale 0333
Latino-américaine 0336
Asie, Australie et Océanie 0332
Histoire des sciences 0585
Loisirs 0814
Planification urbaine et
   régionale 0999
Science politique
   Généralités 0615
   Administration publique 0617
   Droit et relations
      internationales 0616
Sociologie
   Généralités 0626
   Aide et bien-àtre social 0630
   Criminologie et
      établissements
      pénitentiaires 0627
   Démographie 0938
   Études de l' individu et
      de la famille 0628
   Études des relations
      interethniques et
      des relations raciales 0631
   Structure et développement
      social 0700
   Théorie et méthodes. 0344
   Travail et relations
      industrielles 0629
Transports 0709
Travail social 0452

SCIENCES ET INGÉNIERIE

SCIENCES BIOLOGIQUES
Agriculture
   Généralités 0473
   Agronomie. 0285
   Alimentation et technologie
      alimentaire 0359
   Culture 0479
   Élevage et alimentation 0475
   Exploitation des péturages ... 0777
   Pathologie animale 0476
   Pathologie végétale 0480
   Physiologie végétale 0817
   Sylviculture et faune 0478
   Technologie du bois 0746
Biologie
   Généralités 0306
   Anatomie 0287
   Biologie (Statistiques) 0308
   Biologie moléculaire 0307
   Botanique 0309
   Cellule 0379
   Écologie 0329
   Entomologie 0353
   Génétique 0369
   Limnologie 0793
   Microbiologie 0410
   Neurologie 0317
   Océanographie 0416
   Physiologie 0433
   Radiation 0821
   Science vétérinaire 0778
   Zoologie 0472
Biophysique
   Généralités 0786
   Medicale 0760

SCIENCES DE LA TERRE
Biogéochimie 0425
Géochimie 0996
Géodésie 0370
Géographie physique 0368

Géologie 0372
Géophysique 0373
Hydrologie 0388
Minéralogie 0411
Océanographie physique 0415
Paléobotanique 0345
Paléoécologie 0426
Paléontologie 0418
Paléozoologie 0985
Palynologie 0427

SCIENCES DE LA SANTÉ ET DE L'ENVIRONNEMENT
Économie domestique 0386
Sciences de l'environnement 0768
Sciences de la santé
   Généralités 0566
   Administration des hipitaux .. 0769
   Alimentation et nutrition 0570
   Audiologie 0300
   Chimiothérapie 0992
   Dentisterie 0567
   Développement humain 0758
   Enseignement 0350
   Immunologie 0982
   Loisirs 0575
   Médecine du travail et
      thérapie 0354
   Médecine et chirurgie 0564
   Obstétrique et gynécologie ... 0380
   Ophtalmologie 0381
   Orthophonie 0460
   Pathologie 0571
   Pharmacie 0572
   Pharmacologie 0419
   Physiothérapie 0382
   Radiologie 0574
   Santé mentale 0347
   Santé publique 0573
   Soins infirmiers 0569
   Toxicologie 0383

SCIENCES PHYSIQUES
Sciences Pures
Chimie
   Genéralités 0485
   Biochimie 487
   Chimie agricole 0749
   Chimie analytique 0486
   Chimie minérale 0488
   Chimie nucléaire 0738
   Chimie organique 0490
   Chimie pharmaceutique 0491
   Physique 0494
   PolymCres 0495
   Radiation 0754
Mathématiques 0405
Physique
   Généralités 0605
   Acoustique 0986
   Astronomie et
      astrophysique 0606
   Electronique et électricité 0607
   Fluides et plasma 0759
   Météorologie 0608
   Optique 0752
   Particules (Physique
      nucléaire) 0798
   Physique atomique 0748
   Physique de l'état solide 0611
   Physique moléculaire 0609
   Physique nucléaire 0610
   Radiation 0756
Statistiques 0463

Sciences Appliqués Et Technologie
Informatique 0984
Ingénierie
   Généralités 0537
   Agricole 0539
   Automobile 0540

Biomédicale 0541
Chaleur et ther
   modynamique 0348
Conditionnement
   (Emballage) 0549
Génie aérospatial 0538
Génie chimique 0542
Génie civil 0543
Génie électronique et
   électrique 0544
Génie industriel 0546
Génie mécanique 0548
Génie nucléaire 0552
Ingénierie des systèmes 0790
Mécanique navale 0547
Métallurgie 0743
Science des matériaux 0794
Technique du pétrole 0765
Technique minière 0551
Techniques sanitaires et
   municipales 0554
Technologie hydraulique 0545
Mécanique appliquée 0346
Géotechnologie 0428
Matières plastiques
   (Technologie) 0795
Recherche opérationnelle 0796
Textiles et tissus (Technologie) ... 0794

PSYCHOLOGIE
Généralités 0621
Personnalité 0625
Psychobiologie 0349
Psychologie clinique 0622
Psychologie du comportement ... 0384
Psychologie du développement .. 0620
Psychologie expérimentale 0623
Psychologie industrielle 0624
Psychologie physiologique 0989
Psychologie sociale 0451
Psychométrie 0632

✪

STUDY ON THE APPLICATIONS OF THE FINITE DIFFERENCE-TIME

DOMAIN METHOD FOR SOLUTION OF ELECTROMAGNETIC PROBLEMS

BY

WALID AFIF CHAMMA

A Thesis submitted to the Faculty of Graduate Studies of the University of Manitoba in partial fulfillment of the requirements of the degree of

DOCTOR OF PHILOSOPHY

(c) 1993

ABSTRACT

A study of the Finite Difference–Time Domain (FDTD) numerical technique, which is based on the finite–difference solution of the time–dependent Maxwell's curl equations and its application to scattering and antenna problems, is done together with a development of a general purpose FDTD code. A stability study of the FDTD method is conducted which involved the effect of the spatial step size of the FDTD lattice, the pulse width of the excitation plane wave, the distance between the modeled target and the lattice walls, and the use of different Absorbing Boundary Conditions (ABC) on the FDTD solutions. This study is also extended to investigate the accuracy and limitations of using non–uniform gridding inside a FDTD mesh. The FDTD code was then applied to scattering problems of both conducting and dielectric structures, and also included a comparative analysis of three different FDTD thin wire modeling procedures. Also, using FDTD, a study on the EMP field penetration into a cavity is done through the computation of the transient response and frequency content of fields inside a cavity for different aperture and lossy wall configurations. For antenna applications, design curves relating the cross–polarization radiation field levels to the feed location are obtained for a transmission line–fed rectangular microstrip patch antennas modelled using the FDTD.

In the application of the FDTD method to scattering problems, the transient response of conducting and dielectric circular cylinders due to a step plane wave is computed and the correspondence between the transient response and the rise time of the excitation wave is investigated. The transient response of conducting and dielectric spheres illuminated by a Gaussian plane wave is also computed using the FDTD method and compared with those obtained from analytic solution.

Also the field penetration inside a conducting box with an open top illuminated by an EMP plane wave is computed. The effect of changing the aperture geometry and loading the box with lossy material on the field magnitude and frequency content inside the box is analyzed. It is observed that the aperture edges geometry having the smaller edge size perpendicular to the polarization of the incident plane wave resulted in a significant reduction of the transient field magnitude at the early time in addition to a resonance phenomena. Adding the absorbing material on the aperture wall reduced the transient field magnitude penetrating inside the box cavity, while adding the absorber at the inner walls caused the field resonance to attenuate at a faster rate.

The performance of different thin wire modeling procedures in the FDTD technique is investigated, where the current magnitude and phase distribution along thin dipoles are

computed using three modeling procedures. The computed results are compared with those obtained from the Method of Moments (MoM).

In the applications to antennas, the FDTD method is used to analyze the input and radiation characteristics of a line fed rectangular microstrip patch antenna and the effect of the transmission line location along the patch length on the co–polar and cross–polar radiation field levels is investigated for three patch sizes.

ACKNOWLEDGMENTS

TABLE OF CONTENTS

LIST OF PRINCIPLE SYMBOLS

Unless otherwise stated, the symbols most commonly used in this thesis have the following meaning:

E	Electric field intensity.
H	Magnetic field intensity.
μ	Permeability of a medium.
μ_r	Relative Permeability of a medium.
ϵ	Permitivity of a medium.
ϵ_r	Relative Permitivity of a medium.
σ	Conductivity of a medium.
∇	Gradient operator.
x, y, z	point location in a Cartesian coordinate system.
$\hat{a}_x, \hat{a}_y, \hat{a}_z$	unit vectors of a Cartesian coordinate system.
E_x, E_y, E_z	x, y, z–component of the electric field intensity.
H_x, H_y, H_z	x, y, z–component of the magnetic field intensity.
i, j, k	location index of a point in a FDTD lattice.
n	FDTD time step index.
$i\Delta, j\Delta, k\Delta$	point location in the space of a FDTD lattice.
$\Delta x, \Delta y, \Delta z$	FDTD lattice space increment.
δt	FDTD time step increment.
$F^n(i, j, k)$	field expression F inside a FDTD lattice at location (i, j, k) and time step index n.

$\left.\begin{array}{l} E_x^n\ (i,\ j,\ k) \\ E_y^n\ (i,\ j,\ k) \\ E_z^n\ (i,\ j,\ k) \end{array}\right\}$ x, y, z–component of the electric field intensity inside a FDTD lattice at

location (i, j, k) and time step n.

$\left.\begin{array}{l} H_x^n\ (i,\ j,\ k) \\ H_y^n\ (i,\ j,\ k) \\ H_z^n\ (i,\ j,\ k) \end{array}\right\}$ x, y, z–component of the magnetic field intensity inside a FDTD lattice at

location (i, j, k) and time step n.

$\epsilon\ (i,\ j,\ k)$ Permitivity of a medium at location (i, j, k) in a FDTD lattice.

$\mu\ (i,\ j,\ k)$ Permeability of a medium at location (i, j, k) in a FDTD lattice.

$\sigma\ (i,\ j,\ k)$ Conductivity of a medium at location (i, j, k) in a FDTD lattice.

ABC Absorbing Boundary Conditions.

EMP Electromagnetic pulse.

FT Fourier transform operator.

DFT Discrete Fourier transformation.

RCS Radar Cross–Section.

L wave operator.

$L^+,\ L^-$ factors of the wave operator L.

D_q^p p–th partial derivative with respect to q.

U wave function.

U_{qq} second partial derivative of wave function U with respect to q ($D_q^2 U$).

λ wavelength of a sinusoidal waveform.

c speed of light.

l ratio between adjacent spatial steps in a non–uniform FDTD lattice (Chapter III).

$r,\ \theta,\ \phi$ field point location in a spherical coordinate system.

$Tan\delta$ loss tangent.

LIST OF FIGURES

Figure   **Page**

Figure   **Page**

Figure   **Page**

Figure   **Page**

Figure   Page

Figure   **Page**

CHAPTER I

INTRODUCTION

Generally, geometries with complex shapes and material composition constitute a broad class of important practical problems in electromagnetic engineering. To solve them one requires the determination of the scattering or antenna parameters obtained from the solution of the respective boundary value problems. Obtaining such parameters, using either analytic or numerical techniques, will provide an efficient and inexpensive way to analyze specific electromagnetic problems or to arrive at a final antenna design to be examined experimentally. In electromagnetic applications, the knowledge of the current distribution on the body is sufficient to determine other electrical quantities that are important in the analysis of such applications.

In recent years, the effect of impulsively excited electromagnetic bursts, resulting from lightning or nuclear bursts, on electronic equipment, devices and installations have raised the interest in electromagnetic transient field penetration and coupling into structures that are complex both in shape and physical parameters. Also, the development of the technology necessary to obtain the transient solution to electromagnetic scattering problems directly in the time–domain has coincided with a growing interest in wide–band radar design for high resolution and target–classification cases. The transient response of a specified object when illuminated by an incident pulse will provide [1] first, all the information about the electromagnetic scattering properties of the target over the frequency band defined by the incident smoothed impulse. Second, the radar cross–section can be obtained from the impulse response by a Fourier transform. Third, the response of the target due to any wave form can be obtained from the impulse response by a simple convolution procedure. Finally, the impulse response can provide a better understanding of electromagnetic scattering phenomena.

The analysis of the electromagnetic interaction with such complex structures will be difficult to achieve analytically since, generally, the geometry of such structures will not

match with the known orthogonal coordinate systems. In this case the problems will be limited to structures whose surface coincide with the coordinate surfaces of a separable coordinate system.

Approximate techniques such as the geometrical optics, physical optics, and the Rayleigh approximation, which treat scattering and diffraction as local phenomena, are applied to obtain estimates of the scattered response.

With the advent of digital computer capabilities that can keep track of the geometrical details of a body in addition to any associated numerical computations, developed numerical techniques capable of solving electromagnetic interaction problems are only limited by the characteristics of the formulation and the storage capability and speed of the computer.

Two different numerical methods can be used to handle such problems. In traditional methods, the scattering problems are commonly solved in the frequency–domain. In these methods, the computation of the frequency response of the structure is followed by the Fourier transformation of the response. This means, the frequency–domain data must be generated at an adequate number of frequencies to enable the Fourier transform computation. The alternate approach is to solve the problem in the time–domain, so that the required time–domain responses can be generated directly.

Frequency–domain methods provide the response of an object for all angles of incidence at a single frequency, while time–domain methods provide solutions for many frequencies from a single transient calculation resulting from an incident wave arriving from a particular direction.

Because the frequency–domain techniques have been the traditional way of solving electromagnetic problems, a large number of general or dedicated numerical codes are already available. This facilitates the use of frequency–domain codes. However, the radar scattering problems normally deal with objects in free space. Consequently, all numerically efficient codes deal with integral equation formulations that reduce the problem to one that deals with the unknown field quantities on the object's surface. Unfortunately, the use of the integral equation formulations requires the Green's functions of unbounded regions. This requirement restricts the formulation to conducting or homogeneous objects. Inhomogeneous objects can also be handled, but will require a volume integral equation, which normally re-

quires an excessive computation time. In addition, because integral equations are valid over the entire surface or volume distribution of the sources, their solution, using a linearization process, i.e. an application of the moment methods, reduces to a solution of a matrix equation. The resulting matrix is dense and its size increases with the object size. Consequently, the method is useful only for small objects, especially when non–conducting or coated conducting objects are to be investigated. This limitation of small object size, with respect to the wavelength, restricts the accurate computation of the frequency–domain data to low and intermediate frequencies, and in generating the time–domain data limits their accuracy. Nevertheless, excellent solution techniques and codes are developed that can handle varieties of object configurations and complexities.

The use of integral equation formulations in the time–domain overcomes the difficulty of generating numerous frequency–domain data for a Fourier transform. However, they again use the Green's function of the unbounded regions, and consequently the most efficient codes that use surface integral equations are restricted to conducting or homogeneous objects. For inhomogeneous objects the volume integral equation must be used which increases computation time.

Another method which is used in the time–domain analysis is the Singularity Expansion Method (SEM) [2]. In SEM the method of moments is employed where the zeroes of the determinant of the system matrix define the locations of the natural resonances of the structure in terms of exponentially damped sinusoids, hence using frequency–domain formulations. SEM pole singularities can be also derived directly from its time–domain response [3]. This approach can be employed to substantially reduce the computation time, achieved by extrapolating the time–domain response that has been computed only for earlier time steps.

Time–domain analysis is also obtained by different techniques that are based on solving Maxwell's equations directly in time–domain by the use of finite–difference techniques. The time–domain Maxwell's equations represent a more general form than the frequency–domain Helmholtz equations, which are usually restricted to solving scattering problems having time harmonic fields, whereas time–domain approach can handle continuous waves as well as a single–pulse transient response.

One technique which have been used recently utilizes the Computational Fluid Dynamics (CFD) techniques to solve Maxwell's equations [4]. This technique, which is referred to as the time–domain finite–volume (TDFV) , is based on the Riemann integration method [5]. This technique has been used to solve a range of problems involving electrically large scatterers, inhomogeneous and layered dielectrics, cavities, frequency dependent materials, and some canonical radiation problems [6].

A second technique solves Maxwell's equations in the differential form using the point–matched finite–element formulation [7]. This formulation allows the use of conforming mesh generation which is adopted in the finite–element technique.

Another scheme is the Transmission Line Method (TLM) [8,9]. This method although a transmission line simulation of Maxwell's equations, is in essence an explicit time–domain technique that solves Maxwell's equations in the differential form.

One last scheme, which is the one adopted in this thesis, solves the differential form of the time dependent Maxwell's equations is the Finite Difference–Time Domain (FDTD) method. This method applies a simple second–order accurate central–difference approximations [10] for the space and time derivatives of the electric and magnetic fields directly to the respective differential operators of the curl equations. This technique is fully explicit and there is no need to setup or solve a system of linear simultaneous equations.

In Chapter II, the theory and formulation of the FDTD method is presented,as well as, the mechanism of how the technique operates. A literature survey that summarizes the advances and the areas of research fields to which the FDTD method has been applied to, is also included.

In Chapter III, a stability study involving the FDTD method is done.It included the use of Absorbing Boundary Conditions (ABC) in truncating the FDTD lattice, and the effect of the spatial and time step sizes of the lattice on the FDTD solution in both uniform and non–uniform meshes.

In Chapter IV, the application of the FDTD method to scattering problems is implemented. The transient response of a circular cylinder and a sphere geometry illuminated by transient pulses is computed for both conducting and dielectric cases, and compared with

analytical solution in the sphere case. Also in this chapter, the field penetration inside a conducting box with an open top illuminated by an EMP plane wave is computed and the effect of changing the aperture geometry and loading the box with lossy material on the field magnitude and frequency content inside the conducting box is analyzed. This chapter also investigates the capability of the FDTD method to model thin conducting wires where different thin wire modeling procedures are used to compute their corresponding current magnitude and phase distribution along their lengths.

The application of the FDTD method to antenna analysis is discussed in Chapter V, where the FDTD technique is used to model and analyze the input and radiation characteristics of a line fed rectangular microstrip patch antenna. The effect of the transmission line location along the patch length on the co–polar and cross–polar radiation field pattern levels is studied, and curves relating cross–polarization levels to feed location are obtained.

Chapter VI includes the conclusions of the work presented and some recommendations for future work.

CHAPTER II

THEORY AND REVIEW OF THE FINITE DIFFERENCE–TIME DOMAIN (FDTD) METHOD

2.1. Theory and Formulation

The Finite Difference–Time Domain (FDTD) method is a direct solution of the time–dependent Maxwell's curl equations in time–domain by use of finite–difference technique. It is analogous to existing finite–difference solutions of fluid flow problems encountered in computational aerodynamics where the numerical model is based on a direct solution of the corresponding partial differential equation. In FDTD the propagation of an electromagnetic wave into a volume of space containing a dielectric or a conducting structure or their combination is being modeled. By time stepping, the incident wave is tracked as it first propagates to the structure and then interacts with it through current excitation, diffusion, penetration and diffraction.

2.1.1. FDTD Algorithm Details

The FDTD numerical technique treats the irradiation of the scatterer as an initial value problem. At $t=0$, a plane wave excitation is assumed to be turned on. The propagation of waves from this source is simulated by solving a finite–difference analog of the time–dependent Maxwell's equations on a lattice of points including the scatterer. In a region of space which is source–free constituting of electrical parameters that are independent of time, Maxwell's time–dependent curl equations are given by,

$$\frac{\partial H}{\partial t} = -\frac{1}{\mu} \nabla \times E$$

$$\frac{\partial E}{\partial t} = \frac{1}{\epsilon} \nabla \times H - \frac{\sigma}{\epsilon} E$$

(2.1)

where **E** is the electric field in *volts/ meter* ; **H** is the magnetic field in *amperes/ meter* ; ϵ is the electrical permitivity in *farads/ meter* ; μ is the magnetic permeability in *henrys/ meter*; σ is the electrical conductivity in *mohs/ meter*. Assuming isotropic physical parameters, Maxwell's equations can be written in the rectangular coordinates *(x, y, z)* as,

$$\frac{\partial H_x}{\partial t} = \frac{1}{\mu}\left[\frac{\partial E_y}{\partial z} - \frac{\partial E_z}{\partial y}\right] \tag{2.2a}$$

$$\frac{\partial H_y}{\partial t} = \frac{1}{\mu}\left[\frac{\partial E_z}{\partial x} - \frac{\partial E_x}{\partial z}\right] \tag{2.2b}$$

$$\frac{\partial H_z}{\partial t} = \frac{1}{\mu}\left[\frac{\partial E_x}{\partial y} - \frac{\partial E_y}{\partial x}\right] \tag{2.2c}$$

$$\frac{\partial E_x}{\partial t} = \frac{1}{\epsilon}\left[\frac{\partial H_z}{\partial y} - \frac{\partial H_y}{\partial z} - \sigma E_x\right] \tag{2.3a}$$

$$\frac{\partial E_y}{\partial t} = \frac{1}{\epsilon}\left[\frac{\partial H_x}{\partial z} - \frac{\partial H_z}{\partial x} - \sigma E_y\right] \tag{2.3b}$$

$$\frac{\partial E_z}{\partial t} = \frac{1}{\epsilon}\left[\frac{\partial H_y}{\partial x} - \frac{\partial H_y}{\partial y} - \sigma E_z\right] \tag{2.3c}$$

Equations (2.2) and (2.3) are a system of six coupled differential equations which forms the basis of the FDTD algorithm for electromagnetic wave interactions with general three–dimensional objects. Following Yee's [10] notation of applying a set of finite–difference equations for the system of (2.2) and (2.3) a space lattice point is denoted as

$$(i,j,k) = (i\Delta ,j\Delta ,k\Delta) \tag{2.4}$$

and any function of space and time as

$$F^n (i, j, k) = F (i\Delta, j\Delta, k\Delta, n\delta t) \qquad (2.5)$$

where $\Delta = \Delta x = \Delta y = \Delta z$ is the lattice space increment, δt is the time increment, (i, j, k) are integers denoting the location inside the FDTD lattice, and n is an integer denoting the time stepping index.

Yee uses the central–difference expressions for the space and time derivatives that are both second order accurate in Δ and δt, respectively,

$$\frac{\partial F^n (i,j,k)}{\partial x} = \frac{F^n(i + \frac{1}{2}, j, k) - F^n (i - \frac{1}{2}, j, k)}{\Delta} + O(\Delta^2) \qquad (2.6)$$

$$\frac{\partial F^n (i,j,k)}{\partial t} = \frac{F^{n+1/2}(i, j, k) - F^{n-1/2}(i, j, k)}{\delta t} + O(\delta t^2) \qquad (2.7)$$

To achieve the accuracy of (2.6), and to realize all the space derivatives of (2.2) and (2.3), Yee positioned the components of $\mathbb{E}$ and $\mathbb{H}$ about a unit cell of the lattice as shown in Fig. 2.1.
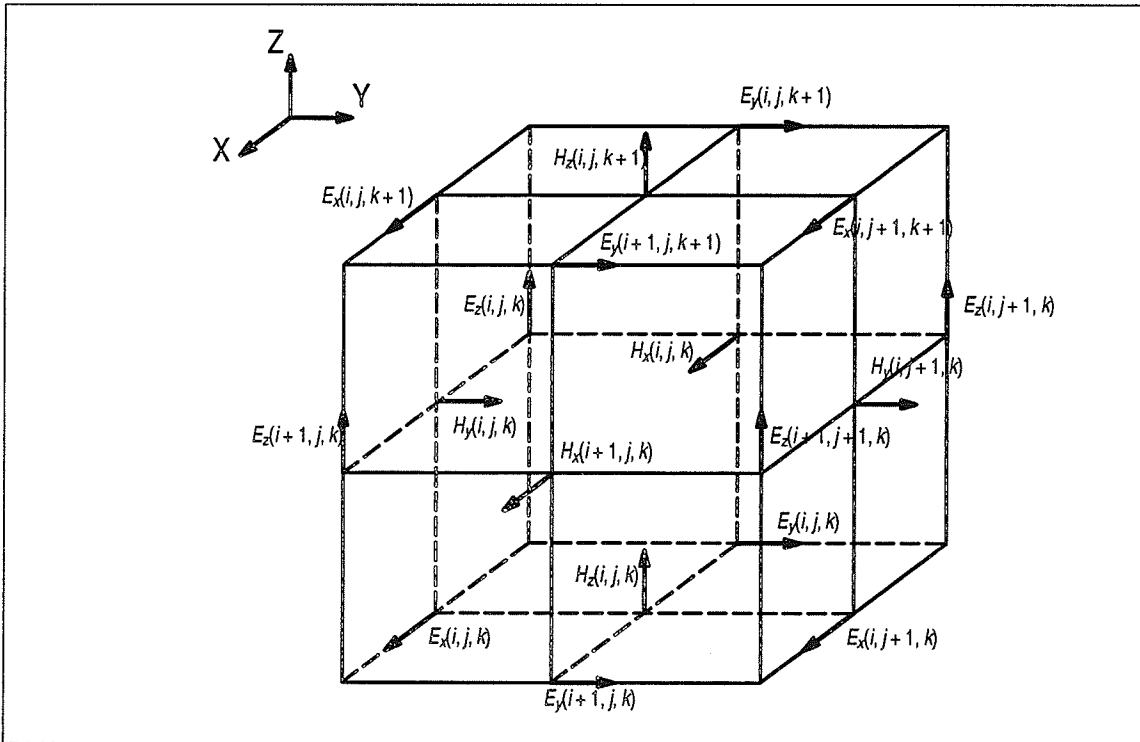
Fig. 2.1   Position of the Field Components about a Unit Cell of the Yee Lattice.

To achieve the accuracy of (2.7), he evaluated $\mathbf{E}$ and $\mathbf{H}$ at alternate half time steps. The results of these assumptions is the following system of finite–difference equations[1] for the systems of (2.2) and (2.3),

$$H_x^{n+\frac{1}{2}}(i,j+1/2,k+1/2)$$

$$= H_x^{n-\frac{1}{2}}(i,j+1/2,k+1/2) + \frac{\delta t}{\mu(i,j+1/2,k+1/2)\,\Delta} \cdot \begin{bmatrix} E_y^n(i,j+1/2,k+1) - E_y^n(i,j+1/2,k) + \\ E_z^n(i,j,k+1/2) - E_z^n(i,j,+1,k+1/2) \end{bmatrix} \quad (2.8a)$$

$$H_y^{n+\frac{1}{2}}(i+1/2,j,k+1/2)$$

$$= H_y^{n-\frac{1}{2}}(i+1/2,j,k+1/2) + \frac{\delta t}{\mu(i+1/2,j,k+1/2)\,\Delta} \cdot \begin{bmatrix} E_z^n(i+1,j,k+1/2) - E_z^n(i,j,k+1/2) + \\ E_x^n(i+1/2,j,k) - E_x^n(i+1/2,j,k+1) \end{bmatrix} \quad (2.8b)$$

$$H_z^{n+\frac{1}{2}}(i+1/2,j+1/2,k)$$

$$= H_z^{n-\frac{1}{2}}(i+1/2,j+1/2,k) + \frac{\delta t}{\mu(i+1/2,j+1/2,k)\,\Delta} \cdot \begin{bmatrix} E_x^n(i+1/2,j+1,k) - E_x^n(i+1/2,j,k) + \\ E_y^n(i,j+1/2,k) - E_y^n(i+1,j+1/2,k) \end{bmatrix} \quad (2.8c)$$

$$E_x^{n+1}(i+1/2,j,k) = \begin{bmatrix} 1 - \frac{\sigma(i+1/2,j,k)\,\delta t}{2\epsilon(i+1/2,j,k)} \\ \overline{1 + \frac{\sigma(i+1/2,j,k)\,\delta t}{2\epsilon(i+1/2,j,k)}} \end{bmatrix} E_x^n(i+1/2,j,k) + \frac{\delta t}{\begin{bmatrix} 1 + \frac{\sigma(i+1/2,j,k)\,\delta t}{2\epsilon(i+1/2,j,k)} \end{bmatrix}\epsilon(i+1/2,j,k)\Delta}$$

$$\cdot \begin{bmatrix} H_z^{n+\frac{1}{2}}(i+1/2,j+1/2,k) - H_z^{n+\frac{1}{2}}(i+1/2,j-1/2,k) + \\ H_y^{n+\frac{1}{2}}(i+1/2,j,k-1/2) - H_y^{n+\frac{1}{2}}(i+1/2,j,k+1/2) \end{bmatrix} \quad (2.9a)$$

$$E_y^{n+1}(i,j+1/2,k) = \begin{bmatrix} 1 - \frac{\sigma(i,j+1/2,k)\,\delta t}{2\epsilon(i,j+1/2,k)} \\ \overline{1 + \frac{\sigma(i,j+1/2,k)\,\delta t}{2\epsilon(i,j+1/2,k)}} \end{bmatrix} E_y^n(i,j+1/2,k) + \frac{\delta t}{\begin{bmatrix} 1 + \frac{\sigma(i,j+1/2,k)\,\delta t}{2\epsilon(i,j+1/2,k)} \end{bmatrix}\epsilon(i,j+1/2,k)\Delta}$$

$$\cdot \begin{bmatrix} H_x^{n+\frac{1}{2}}(i,j+1/2,k+1/2) - H_x^{n+\frac{1}{2}}(i,j+1/2,k-1/2) + \\ H_z^{n+\frac{1}{2}}(i-1/2,j+1/2,k) - H_z^{n+\frac{1}{2}}(i+1/2,j+1/2,k) \end{bmatrix} \quad (2.9b)$$

---

1. $\sigma E^{n+1/2} \approx \sigma \left(E^{n+1} + E^n \right) / 2$

$$E_z^{n+1}(i,j,k+1/2) = \left[\frac{1 - \frac{\sigma(i,j,k+1/2)\ \delta t}{2\epsilon(i,j,k+1/2)}}{1 + \frac{\sigma(i,j,k+1/2)\ \delta t}{2\epsilon(i,j,k+1/2)}}\right] E_z^n(i,j,k+1/2) + \frac{\delta t}{\left[1 + \frac{\sigma(i,j,k+1/2)\ \delta t}{2\epsilon(i,j,k+1/2)}\right]\epsilon\ (i,j,k+1/2)\Delta}$$

$$\cdot \left[\begin{array}{l} H_y^{n+\frac{1}{2}}(i+1/2,j,k+1/2) - H_y^{n+\frac{1}{2}}(i-1/2,j,k+1/2) + \\ H_x^{n+\frac{1}{2}}(i,j-1/2,k+1/2) - H_x^{n+\frac{1}{2}}(i,j+1/2,k+1/2) \end{array}\right] \qquad (2.9c)$$

with this system of equations the new value of a field vector component at any lattice point depends only on its previous value and on the previous values of the components of the other field vector at adjacent points. Hence, at each time step, the system of equations to update the field components is fully explicit, so that there is no need for setting up or solving a system of linear simultaneous equations.

2.1.2. EM Wave Tracking Procedure

Figure 2.2 shows the time–domain wave tracking procedure by the FDTD technique and also summarizes the basic elements of the FDTD space lattice. A region of space containing an arbitrary structure is selected where the field values are to be computed. This region is bounded by lattice truncation planes that are to be transparent to waves scattered away from the structure being modeled. The modeling of the structure inside the FDTD lattice is done by allocating the corresponding physical parameters that characterize the structure at locations defined by the grid nodes matching with the structure geometry. Initially, all the fields are set to zero within the region. An incident plane wave is assumed to enter the region at that time. This plane wave will propagate inside the modeled region by implementing the march–in–time procedure of the finite–difference analog of Maxwell's curl equations of (2.8) and (2.9). Time stepping continues as the numerical analogue hits the structure embedded within the sampled region. Waves scattered away from the structures ideally will propagate through the lattice truncation planes with minimum reflections modeling in this case an open space region. All electromagnetic phenomena such as induction of surface currents, scattering and multiple scattering, field penetration into cavities are modeled at each time step by the action of the curl equation analog. Self–consistency of these modeled phenomena is generally assured if their spatial and temporal variations are well resolved by the

space and time sampling process. Time stepping is continued until the desired late–time pulse response or steady–state behavior is achieved. No special handling of electromagnetic boundary conditions at the media interface is required because the curl equations generate these conditions naturally. In this case, inhomogeneities or fine details of the structure can be modeled with a maximum resolution of one unit cell. Curved surfaces are, generally, modeled by stepped edge surfaces when using the traditional FDTD meshing procedure, while at other cases specialized cells that take into account curved surfaces are used. Illustration of such modeling procedures will be presented later in this chapter.
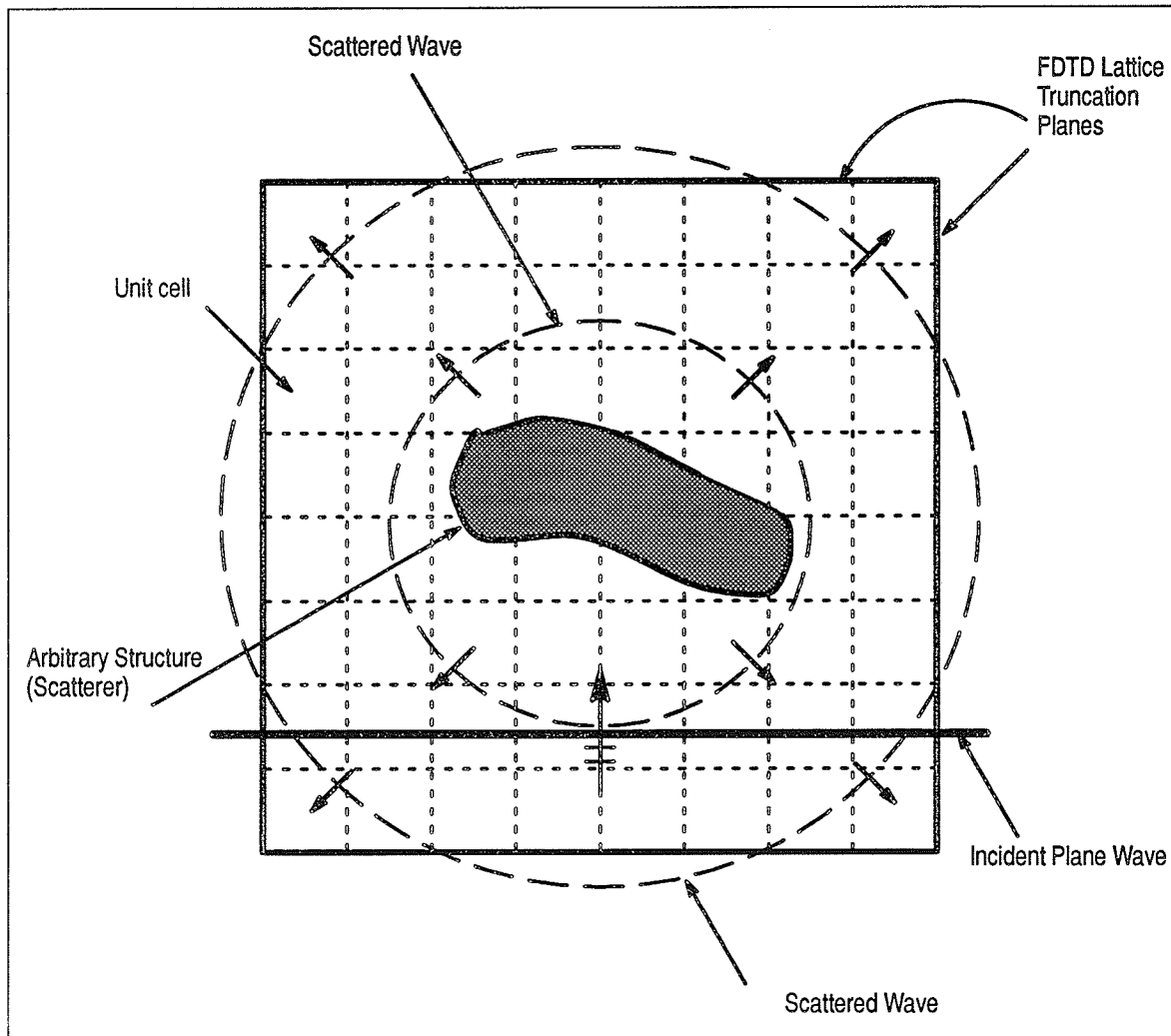
Fig. 2.2   Plane wave scattering by an arbitrary structure inside a FDTD lattice.

2.1.3. Numerical Stability

The accuracy of the computed field quantities, as well as, the stability of time stepping algorithm in FDTD is very much related to the spatial step Δ and time step increment δt, respectively. The choice of Δ and δt is such that the velocity of the numerical signals in the FDTD lattice should not be less than the velocity of light in the medium being modeled. This is satisfied in the following relation,

$$c_{max}.\delta t \leq \left[\frac{1}{\Delta x^2} + \frac{1}{\Delta y^2} + \frac{1}{\Delta z^2} \right]^{-\frac{1}{2}} \qquad (2.10)$$

c_{max} being the maximum wave phase velocity expected within the model. For a uniformly grided mesh $\Delta = \Delta x = \Delta y = \Delta z$. To insure the accuracy of the computed spatial derivatives of the electromagnetic fields, Δ must be small compared to the smallest wavelength. A value of $\Delta \leq \lambda/20$ [11] is suggested, which will provide an uncertainty in the computed field magnitudes to less than $\pm 2\%$. Also Δ should be small enough to accurately model in detail the object being modeled.

2.1.4. Numerical Dispersion

Numerical dispersion is also a factor in FDTD modeling that must be accounted to understand the operation of the algorithm and its accuracy limits. A detailed analysis of this phenomena is reported in [12] by A. Taflove. The numerical algorithm for Maxwell's curl equations represented by the finite–difference equations of (2.8) and (2.9) causes the phase velocity of the numerical modes in the FDTD lattice to vary with modal wavelength, direction of propagation, and lattice discritization. Such numerical dispersion can lead to non-physical phenomena, such as pulse distortion, artificial anisotropy, and pseudorefraction.

When comparing the numerical dispersion relation, and the analytical dispersion relation for a plane wave in a continuous lossless medium, Taflove concluded that the numerical dispersion in FDTD can be reduced to any desired degree if only a fine–enough FDTD gridding is used. He also suggested that pulse distortion can be bounded by obtaining the Fourier spatial frequency spectrum of the desired pulse, and selecting a grid cell size such that the principle spectral components are resolved with at least 10 cells per wavelength.

Such grid division will limit the spread of numerical phase velocities of the principle spectral components to less than 1%, regardless of the wave propagation angle in the grid.

Numerical dispersion can also lead to pseudorefraction of propagating modes if the cell size inside the FDTD lattice is a function of position inside the lattice. Such variable cell gridding will also vary the grid resolution of propagating numerical modes, hence perturbing their modal phase velocity distribution that will lead to nonphysical reflection and refraction of propagating modes at interfaces of grid regions having different cell sizes. Such a phenomena will be similar to that of physical waves undergoing reflection and refraction at interfaces of dielectric media having different refraction indices. Numerical examples on the use of non–uniform gridding in a FDTD lattice will be presented later in this thesis.

2.1.5. Lattice Zoning and Plane wave Excitation

The FDTD code developed is based on the formulation explained in [13]. This formulation involves the division of the FDTD lattice space into two distinct regions separated by rectangular surfaces which serves to connect the fields in each region as shown in Fig. 2.3. Region (1) of the lattice is denoted as the total–field region where all computed field quantities are comprised of the sum of the incident and the scattered fields. The interacting structure of interest is embedded inside this region. External to region (1) is region (2) of the FDTD lattice and is denoted as the scattered field region. Here it is assumed that all computed fields are comprised only of the scattered field. The outer lattice planes bounding region (2) are the lattice truncation planes where absorbing boundary wall algorithms is to be implemented to simulate free space radiation.

The incident wave, generated along one edge of the surface connecting the two regions, propagates through the total field region and is subtracted out the other end. Therefore the only components of the E and H fields to reach the scattered volume are those which are scattered off the scatterer.

The above formulation allows the excitation of plane wave of arbitrary incidence and polarization, which require very small storage, and does not cause any spurious wave reflections.
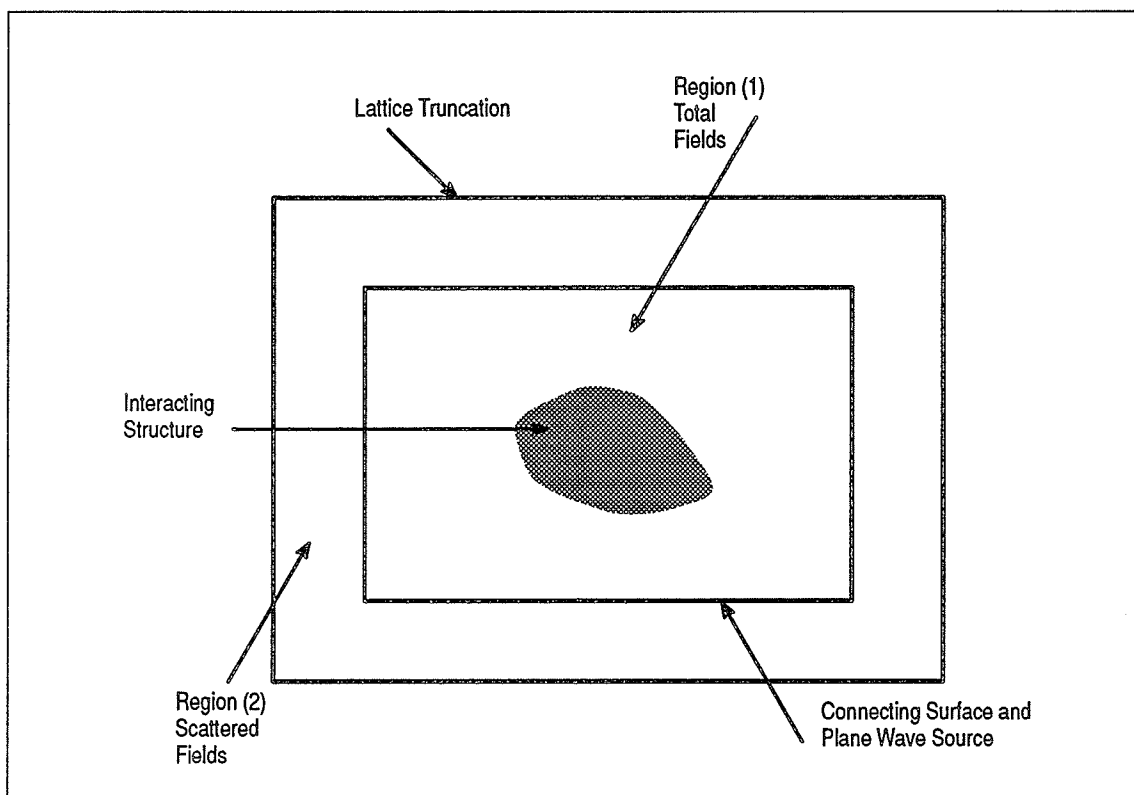
Fig. 2. 3   Division of FDTD Lattice into Total–fields and Scatterer–field Regions.

2.1.6. Absorbing Boundary Conditions (ABC)

An important drawback to the FDTD method for the case of open space problems is the fact that the radiation condition is not implicit, *i.e.* outgoing waves if left alone, would not simply disappear of the end of the grid defined by **E** and **H** arrays, but would reflect back into the scattering object as if they had hit a 'wall' defined by the edge array. The field at the lattice truncation planes cannot be computed using the central–differencing approach of (2.8) and (2.9) due to the absence of known field data outside the lattice truncation. Hence, an auxiliary lattice truncation condition is necessary. This condition must be consistent with Maxwell's equations in that the lattice truncation planes will be transparent to any outgoing waves scattering away from the modeled structure.

Different approaches to provide 'soft' lattice truncation where fields incident on the boundary walls are absorbed are used. Taylor *et al.* [14] used space extrapolation, where fields at nodes located inside the lattice are used to compute the field at the walls. Taflove and Brodwin [15] used averaged extrapolation. They simulated the propagation of an outgo-

ing wave from the lattice plane adjacent to the truncation to the lattice plane at the truncation in a number of time steps corresponding to the propagation delay. Merewether, Kunz and Lee [16,17] used the far field approximation. Applying the technique on a scattered field FDTD formulation, they assumed that the fields at the nodes will follow the $E = f (t - r/c)/r^{1/2}$ relation. Enyquist and Majda [18] showed that the required lattice truncation condition is really a radiation condition in the near field. Mur [13] employed the Enyquist and Majda's first and second order absorbing conditions which are the first one and two terms of Pade's expansion of the exact absorbing boundary condition.

In this thesis two types of 'soft' lattice truncation algorithm are studied, the averaged extrapolation algorithm which is further improved using the super–absorbing technique of [19], and the one–way wave equation procedure used in [13].

2.1.7. Curved Surface Modeling

The FDTD algorithm was originally introduced in cartesian coordinate system where the differential operators occurring in Maxwell's equations take their simplest form than in any other system. The use of orthogonal grids produces very accurate results for cases when surfaces of the modelled target match with the FDTD grid. Furthermore, when working with plane waves, cartesian coordinates constitute a natural system where such waves are expressed, i.e. plane waves are eigenmodes of the wave equation when solved on a cartesian grid. This minimizes dispersion and/or anisotropy effects that might be introduced by the numerical approximation. Also, one major advantage of using the orthogonal in FDTD algorithm lies in the regularity of the nodal coordinates, where the index numbers of each mode contain the nodal coordinates. The non–orthogonal element grid requires the storage of coordinates of all the nodes, which is demanding on memory, especially for three–dimensional problems.

A major drawback that appears in the exclusive use of rectilinear coordinates is when the modelled target have curved features. Traditionally, curved surfaces, in an orthogonal grid, are modelled by 'staircasing' Fig. 2.4. This might give poor approximation to the boundary shape unless very fine discritizations are used.
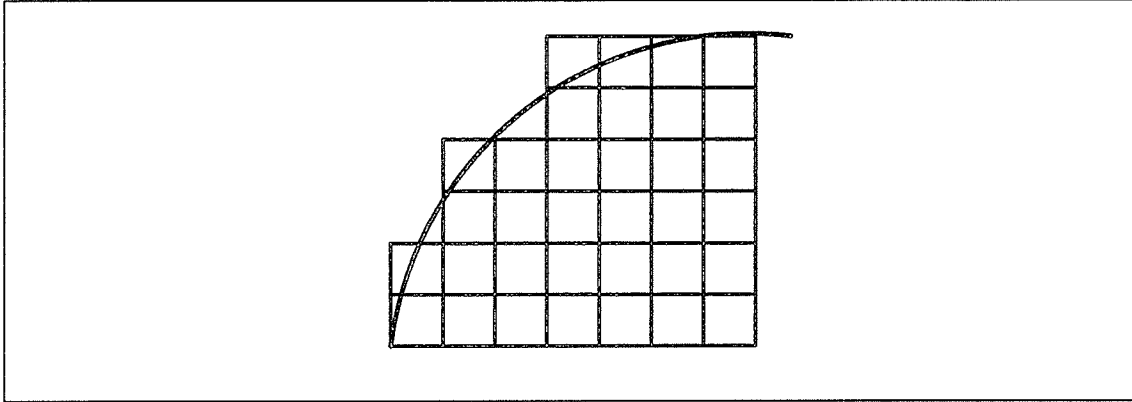
Fig. 2.4   'staircase' model of a curved surface in FDTD.

Cavities having curved surfaces will have their resonant frequencies slightly shifted when modelled using 'staircasing' technique [20]. To model curved features of scatterers in FDTD more accurately R. Holland [21] and M. Fusco [22] derived the FDTD algorithm in curvilinear coordinates by considering that Maxwell's equations are vector equations that are valid in any coordinate system. Others [23], used irregular non–orthogonal grids as the FDTD lattice mesh to model curved surfaces more smoothly. Such procedure resulted in more accurate computations, as well as, an increase in complexity when compared to the conventional FDTD algorithm. Recently, a variant of 'staircasing' has been developed [24] [7] where the cartesian mesh in the lattice is retained, and cells that are adjacent to the scatterer are deformed to take into account the proper scatterer geometry. In [24] Taflove *et al.* introduced a modified FDTD cell which is based upon Maxwell's curl equations in integral form. Curved surfaces are accounted by incorporating field behavior into contour and surface integrals implementing Ampere's law and Faraday's law at selected meshes, and by deforming contour paths as required to conform surface curvature as shown in Fig. 2.5.

Cangellaris *et al.* [7] used the Conformal Boundary Element method to model geometries with curved surfaces. This technique is applied in a way that relaxes the large memory requirement by limiting the irregularly shaped elements to the boundary of the scatterer only. This procedure can be explained briefly by considering the modeling of a conducting cylinder. The cylinder is positioned on a rectangular mesh shown in Fig. 2.6, the cylindrical contour intersects the mesh at points that will be the nodes of zero electric field in a *TM* mesh case where the mesh nodes will be the electric nodes. Then the new conformal cells will be
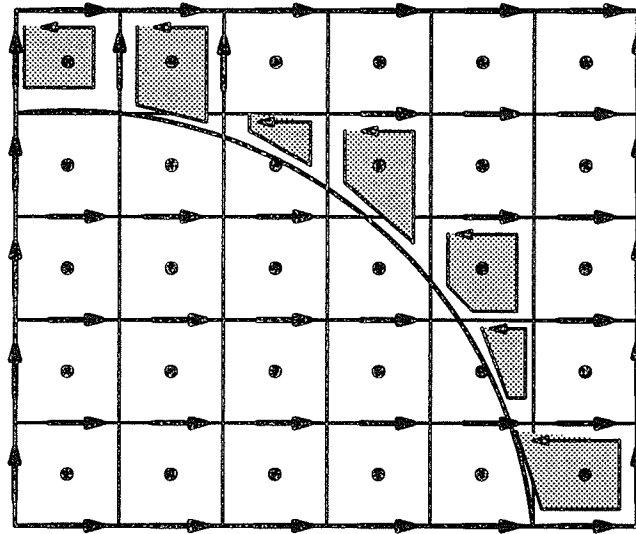
Fig. 2.5   Cell deformation in vicinity of a curved boundary. (contour integration technique)

those made from nodes on the body contour together with some of the neighboring electric nodes on the regular mesh. These electric nodes will be used for the computation of the magnetic fields near the cylinder's surface. Other field components needed for the regular algorithm procedure are obtained through either extrapolation or interpolation procedures. In this case, the uniform rectangular mesh is used everywhere in the computational domain except at the vicinity of the body contour. Only few variety of quadrilateral elements are needed to conform to the scatterer geometry.
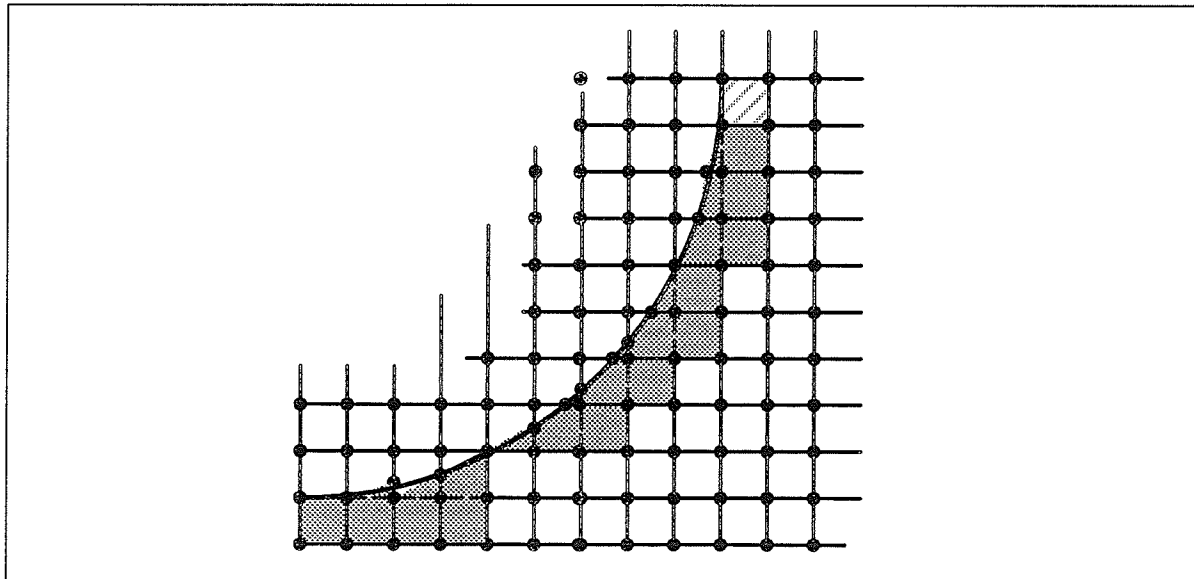
Fig. 2.6   Conformal Boundary Method for modeling curved surfaces.

2.2. Literature Survey:

In 1966 K.S. Yee, who originally proposed the FDTD technique, used the FDTD method to solve Initial Boundary value problems in isotropic media in a 2–dimensional space. He solved for the scattering of an electromagnetic pulse by a perfectly conducting cylinder [10]. Yee truncated his FDTD lattice with conducting walls which resulted in multiple scattering to occur. Later Taylor *et. al* [14] applied Yee's algorithm to study the scattering of electromagnetic pulse in a time–varying inhomogeneous media. They used Maxwell's equations in the cylindrical coordinate system. Merwether [16] used it to compute transient currents induced on a metallic body of revolution by an electromagnetic pulse (EMP). Both latter researchers applied Absorbing Boundary Conditions (ABC) to truncate the FDTD lattice walls.

The FDTD method was also used for closed region problems. Choi and Hoefer [25] used it to obtain the resonance frequencies of inhomogeneous lossless cavities and the propagation phase constant of various lossless microwave structures. FDTD method was also used to study a number of waveguide related problems [26,27]. The dispersion behaviour of waveguide–shielded microstrip line was investigated in [28]. Also the study of TE_o and TM_o modes in dielectric resonators was done in [29].

The use of FDTD for solving electromagnetic coupling problems has progressed very rapidly with the advent of computer technology in terms of high speed and large memory computers. One main application of FDTD is to compute the transient response of complicated structures illuminated by pulsed plane waves. These transient responses are, sometimes, obtained to study the effect of lightning or EMP on structures . A bulk of such applications was done by R. Holland [30] in the development of THREDE code which is based on a scattered field formulation of FDTD. Additional work was also done to study the response of slowly dying electromagnetic pulse on complex structures [17,31–33]. These researchers showed that computations from FDTD were accurate when compared with measured data.

On other instances the transient response data obtained from FDTD computations was used to compute steady state information over a wide range of frequencies by the use

of Fourier transformation. C. Britt [34] computed the Radar Cross–section (RCS) of a circular cylinder, sphere and other three–dimensional geometries from the FDTD transient response computations and using a Gaussian pulse excitation. R. Lubbers *et. al.* [35] presented an efficient method to transform FDTD results to the far zone in the time–domain and then used FFT to obtain the frequency–domain data for number of frequencies. K.S. Yee *et. al.* [36] also presented a shceme to extrapolate FDTD calculated scattered fields to the far zone. The computation of the frequency response data requires the running of the FDTD code for late times to insure that all resonance phenomena inside the lattice has died.

The same concept in computing the frequency response data from time–domain information was applied successfully to microstrip structures. K. Mei *et. al* studied the characteristics of microstrip discontinuities and computed their corresponding dispersion characteristics over a large range of frequencies [37,38]. Sheen *et. al.* [39] applied the same technique for the analysis of planar microstrip circuits. Their results were very accurate when compared with measured data. Microstrip patch antennas were also analyzed in [40]. W. Ko and R. Mittra [41] combined FDTD with Prony's method in Microstrip circuit analysis to extrapolate the long time record required fo accurate frequency–domain scattering parameters from a relatively short FDTD time record.

Taflove and Browdwin [15] used a different approach to compute steady–state data. They used a continuous sinusoidal plane wave excitation that is switched on through out the FDTD computation. The computation will continue until steady–state fields are reached and all the fields in the sampling region exhibit a sinusoidal repetition. The field values are obtained by observing the peak positive and negative excursions of the last cycle. Taflove *et. al* applied this technique to variety of electromagnetic problems. He studied the electromagnetic field penetration into complex geometries using FDTD and MoM/FDTD approaches [42,43]. Taflove and Umashankar proposed the FDTD method as a technique to analyze electromagnetic scattering of large complex objects and to compute its corresponding RCS [44–46]. A comparative study between the single freuency excitation and the pulsed excitation for RCS computations using FDTD is done in [47].

FDTD technique was also used in Biomedical engineering studies. Chen and Gandhi calculated the electromagnetic absorption in the human tissues. They also computed the currents induced in an anatomically based model of a human when exposed to EMP [49–51].

The FDTD method was also used for antenna radation applications. Analysis of electromagnetic of electromagnetic wave radiation from systems containing horn and Microstrip antennas was done in [52–54].

Although the FDTD method has proven to be a practical and efficient method in analyzing a wide range of electromagnetic coupling problems, it has some limitations that are enforced by the use of the Yee cell Fig.–1. Such limitations is the modeling of thin wires and struts whose radii are smaller than the FDTD Yee cell dimension. Also there is the modeling of narrow slots and apertures in complex geometries that involves cavities and gaps. A number of researchers proposed different type of approaches that takes care of such inefficiency inherent in the Yee cell. Holland and Simpson introduced the "in–cell inductance" concept to study the EMP coupling to thin struts and wires [55]. Others proposed a thin–slot formalism for the FDTD method [56–59]. Taflove and Umshankar introduced a modified FDTD cell which is based upon Ampere's law and Faraday's law in integral form [60,61]. With such a technique, the presence of wires, slots, and curved surfaces can be accounted by incorporating appropriate field behavior into contour and surface integrals implementing Ampere's law and Faraday's law at selected meshes, and by deforming contour pathes as required to conform surface curvature.

Complex inhomogenuities were also treated in some applications of the FDTD method such cases as anisotropic media with the diagonalized or off–diagonalized tensor property [45]. The propagation of transients in dispersive dielectric media is studied in [62] by using the FDTD method to solve the time–domain Maxwell's equations in Debye media [63]. A frequency–dependent FDTD formulation ($(FD)^2TD$), where the permittvity, permeability, and conductivity of a media are assumed to be frequency dependent is developed by extending the traditional FDTD formulation to include a discrete time–doamin convolution, which is efficiently evaluated using recurssion [64,65].

A review of the formulation and application of the FDTD method for numerical modeling of EM wave interactions with arbitrary structures has also appeared in the literature [11,12].

CHAPTER III

STABILITY STUDY

3.1. Absorbing Boundary Conditions.

In open space problems in FDTD, the lattice truncation planes have to be invisible to all waves incident on these planes. To obtain such a situation Absorbing Boundary Conditions (ABC) algorithm have to be applied on these truncation planes. In FDTD it is always the goal to use as minimum number of cells as possible that will economize the computer requirements for the FDTD implementation. The total number of FDTD cells can be minimized by using the largest possible cell size for target modeling and the minimum number of cells external to the target. The required number of cells between the target and the absorbing boundary depends on the quality of the absorbing boundary condition used, the size of the target and its scattering nature, and the size of the cells. A detailed study of ABC is done in [66,67].

In this work, two types of absorbing boundary conditions are examined. The first type is the averaged extrapolation algorithm which is a local ABC where only the fields at the neighboring space and time nodes are needed to estimate the field values lying on the lattice truncation planes [15]. The procedure is illustrated using the one–dimensional lattice of Fig. 3.1, for a time–step relation $c\delta t = \Delta$

$$F^n(M) = F^{n-1}(M - 1) \tag{3.1}$$

equation (3.1) simulates the free–space propagation of the field function F from the location $M - 1$ to the truncation point at M in the one time step which is the numerical propagation delay imposed by the time–step relation. Equation (3.1) describes an exact absorbing condition in one–dimension where all waves are absorbed at location M without reflection. To simulate the truncation of this lattice in an infinite half space of refractive index r ($r = \sqrt{\epsilon_r}$;

ϵ_r is the relative dielectric of the half space medium) waves inside the lattice will now propagate with a velocity v such that $c = r.v$. The corresponding time–step relation will be $r.v.\delta t = \Delta$ implying that the wave will propagate a distance of one spatial step in r time steps. Hence eq. (3.1) can be written as,

$$F^n(M) = F^{n-r}(M - 1) \qquad (3.2)$$
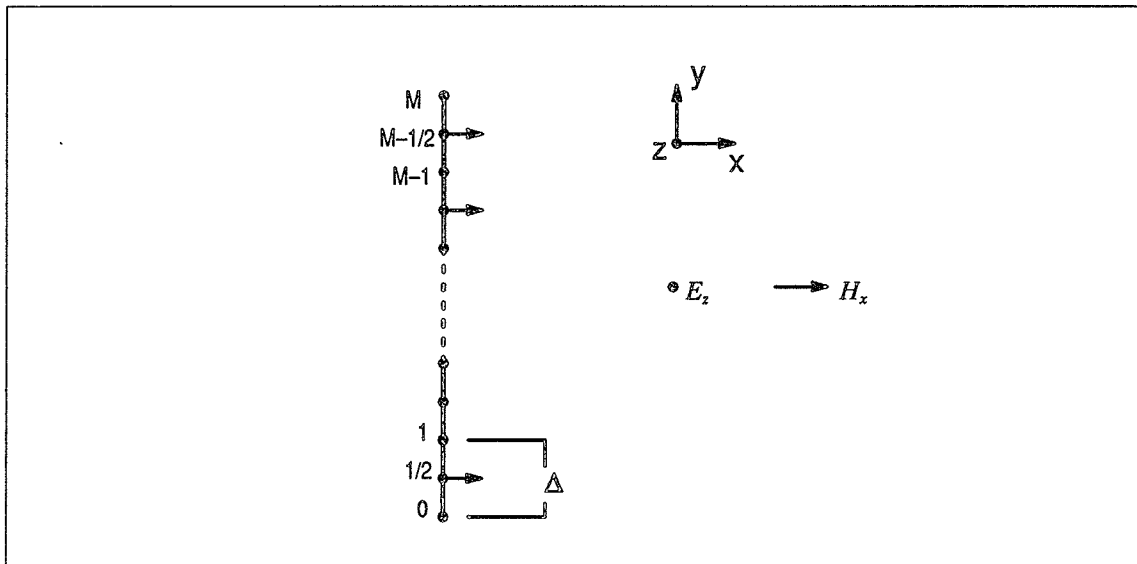
Fig. 3.1   One–dimensional lattice, illustrating averaged extrapolation ABC at M.

In this work, this procedure is implemented in two–dimensional and three–dimensional free–space, and using a time–step relation $\dfrac{c\delta t}{\Delta} = \dfrac{1}{2}$ which also satisfies the stability criterion of Yee's algorithm eq. (2.10). In this case, oblique incidence is accounted for by averaging the field values at the FDTD nodes located in the vicinity of the node in question at the truncation plane as shown in Fig. 3.2. The averaged extrapolation algorithm is considered to be of first–order ABC.

This absorbing boundary condition is further improved by using the super absorbing condition [19] which is a predictor–corrector technique. With this technique, the leading error of the conventional local ABC can be cancelled by a simple algorithm, so that the absorb-

ing quality of the boundary condition can be greatly improved. It is found that by applying the same kind of boundary condition on the tangential H field next to the boundary, and comparing it with those H values calculated from the difference equation of eq. (2.8) (the boundary E's used are obtained from the ABC one time step earlier), these two H fields will always have the property that errors contained in them due to the approximation in the ABC will have opposite signs and magnitudes of a known ratio. Using the corrected values of the H fields the E fields are updated to more accurate values.

$$E^n(0,j) = \frac{1}{3}\left[\, E^{n-2}(1,j+1) + E^{n-2}(1,j) + E^{n-2}(1,j-1)\,\right]$$
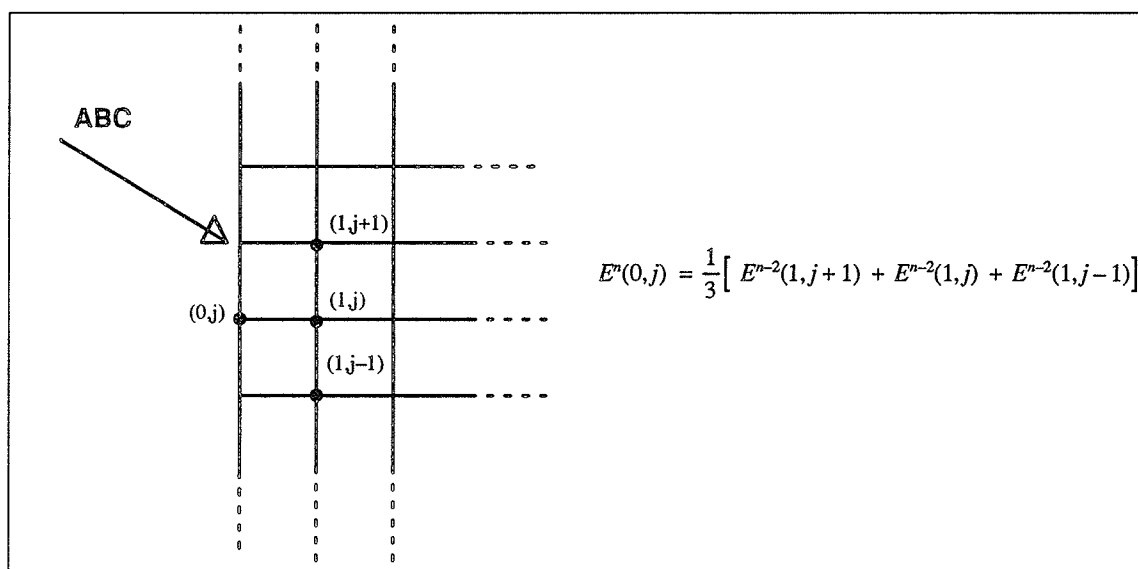
Fig. 3.2   Averaged Extrapolation Absorbing Boundary Conditions (two–dimensions).

The second absorbing boundary algorithm examined in this work is based on the theory of approximate One–way wave equation, which is a partial differential equation which permits wave propagation only in certain direction. G. Mur [13] introduced a simple and successful finite difference scheme for implementing the One–way wave equation to compute field components at the FDTD lattice walls.

Following the explanation in [66,67], the absorbing boundary conditions used are based on general second–order One–way wave equations. The derivation of these equations follows from the application of general rational function approximation to $\sqrt{1-s^2}$ on the in-

terval [−1,1]. Considering the two–dimensional wave equation in cartesian coordinates,

$$LU = D_x^2 U + D_y^2 U - \frac{1}{c^2} D_t^2 U = 0 \qquad (3.3)$$

where D_x^2, D_y^2, and D_t^2 denote second partial derivatives with respect to x, y, and t, respectively. Factoring the wave operator, L,

$$LU = L^+ L^- U = 0 \qquad (3.4)$$

where L^- and L^+ are defined as,

$$L^- \equiv D_x - \frac{D_t}{c} \sqrt{1-s^2}, \qquad (3.5a)$$

$$L^+ \equiv D_x + \frac{D_t}{c} \sqrt{1-s^2} \qquad (3.5b)$$

where, $s = \dfrac{cD_y}{D_t}$

Engquist and Majda [18] showed that at a planer boundary at $x=0$, an application of L^- to the wave function U, will exactly absorb plane waves incident at any angle which travel in the $-x$ direction. Hence, applying

$$L^- U = 0 \qquad (3.6)$$

at $x=0$ will result in an exact absorbing boundary condition that absorbs waves originating from the interior of the spatial FDTD domain. The L^+ operator will function in a similar manner but for waves travelling in the $+x$ direction and hitting the other lattice wall. The presence of the radical in (3.5a), and (3.5b) prohibits the direct implementation of (3.6) as an absorbing condition for dimensions greater than one.

Algebraic approximation of the radical in (3.5) produce absorbing boundary conditions that can be implemented numerically with finite difference schemes. The resulting boundary conditions are not exact causing small amount of reflections when waves pass through the boundary. The substitution for the radical in (3.5), proposed first in [18],

$$\sqrt{1-s^2} \approx 1 - \frac{1}{2}s^2 \tag{3.7}$$

gives the following absorbing boundary condition, when multiplying by D_t, which can be implemented at the boundary, $x=0$,

$$U_{xt} - \frac{1}{c}U_{tt} + \frac{c}{2}U_{yy} = 0 \tag{3.8}$$

The ABC in [67] works well when the grid truncation boundaries are sufficiently distant so that the scattered waves hit the boundaries at near normal incidence.

In three–dimensional space eq. (3.8) will be written as,

$$U_{xt} - \frac{1}{c}U_{tt} + \frac{c}{2}U_{yy} + \frac{c}{2}U_{zz} = 0 \tag{3.9}$$

equation (3.8) and (3.9) are used in the FDTD algorithm by substituting U with the corresponding field components and applying central different schemes on the derivatives.

● *Numerical Tests:*

The FDTD code initially developed, used the averaged extrapolation algorithm of equation 3.1 as ABC on the lattice truncation planes, and was further improved by using the super absorbing procedure. The spatial distance between the modeled target inside the FDTD lattice and the lattice truncation planes affect the performance of the ABC on these planes. Figures 3.3, 3.4 show the transient response of the conducting sphere introduced earlier. These responses are computed for two lattice sizes (60 × 30 × 60) and (80 × 40 × 80) and are compared with the Rayleigh–Mei classical solution.

In Fig. 3.3, which is the response at the illuminated pole of the sphere, a minor difference is observed in the response using either lattice dimensions. On the other hand, Fig. 3.4 shows the shadow region transient response of the sphere. A relatively significant change is observed between the two lattices computations. This change can be attributed to more

reflections from the lattice truncation planes, in a region where the incident field is minimum, when using the smaller size lattice.
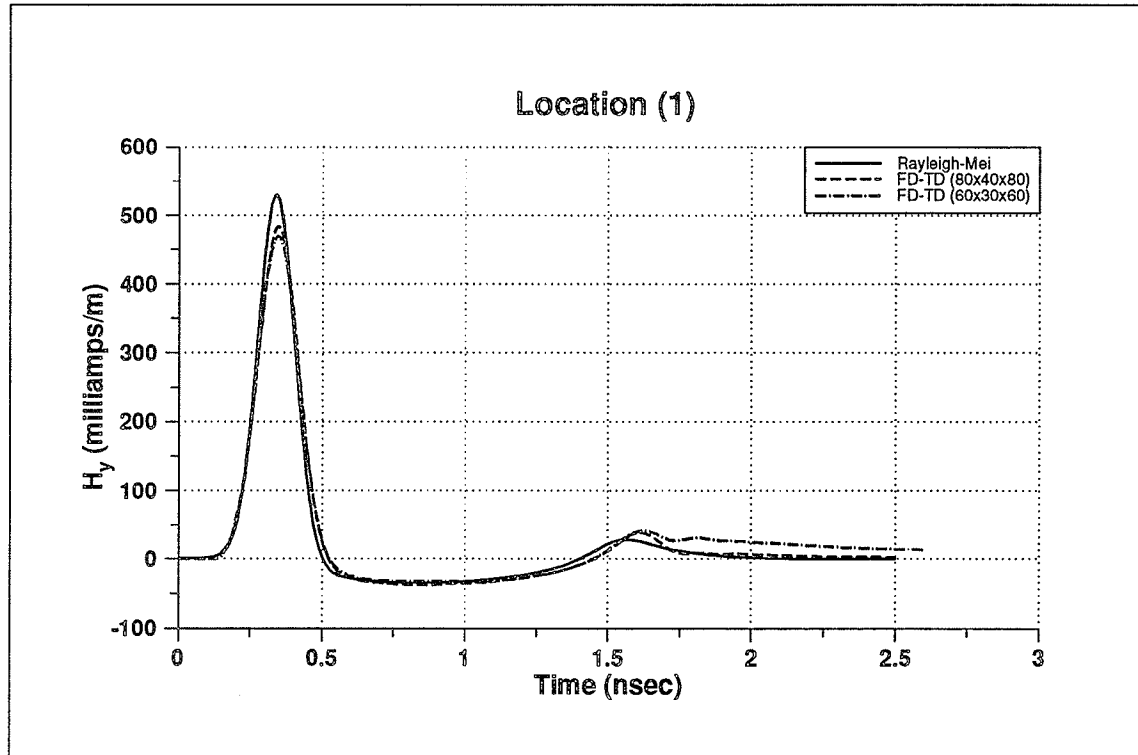
Fig. 3.3   Transient Response of a conducting sphere. (Averaged Extrapolation ABC)

The "One–Way Wave Equation" ABC procedure of equation 3.9 is also investigated. It is implemented on a *TM* two–dimensional version of the FDTD code. In addition, the super absorbing algorithm is also implemented to get an optimum accuracy for the current implementation.

To test the new absorbing boundary algorithm the transient response of a conducting circular cylinder illuminated by a Gaussian shape plane wave is calculated. The data is compared with those computed using the averaged extrapolation algorithm. The circular cylinder having a radius equals to $27.5cm$ $(22 \times \Delta x)$ and shown in Fig. 3.5, is mapped into a 100×100 FDTD lattice of spatial step size $\Delta = .0125m$ and a time step size $\delta t = \dfrac{\Delta}{2c}$ where c is the speed of light.

The benchmark data is obtained by computing the cylinder transient response in a 200×200 FDTD mesh having the same spatial and time step sizes as indicated above. Figures 3.6 show the transient response of the cylinder at locations indicated in Fig. 3.5. These results show an improvement in the accuracy achieved by using the " super–absorbing one–way wave equation " algorithm as compared to the averaging technique.
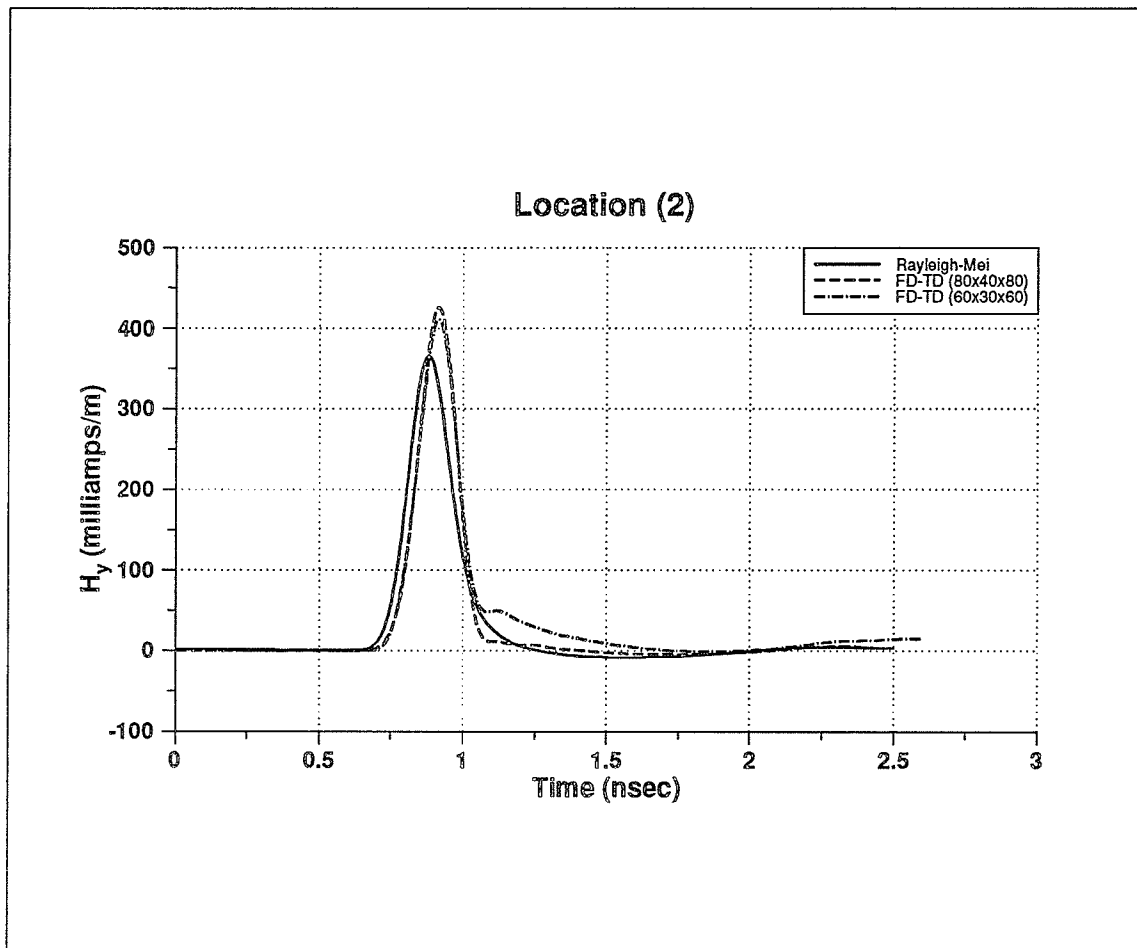
Fig. 3.4   Transient Response of a conducting sphere. (Averaged Extrapolation ABC)
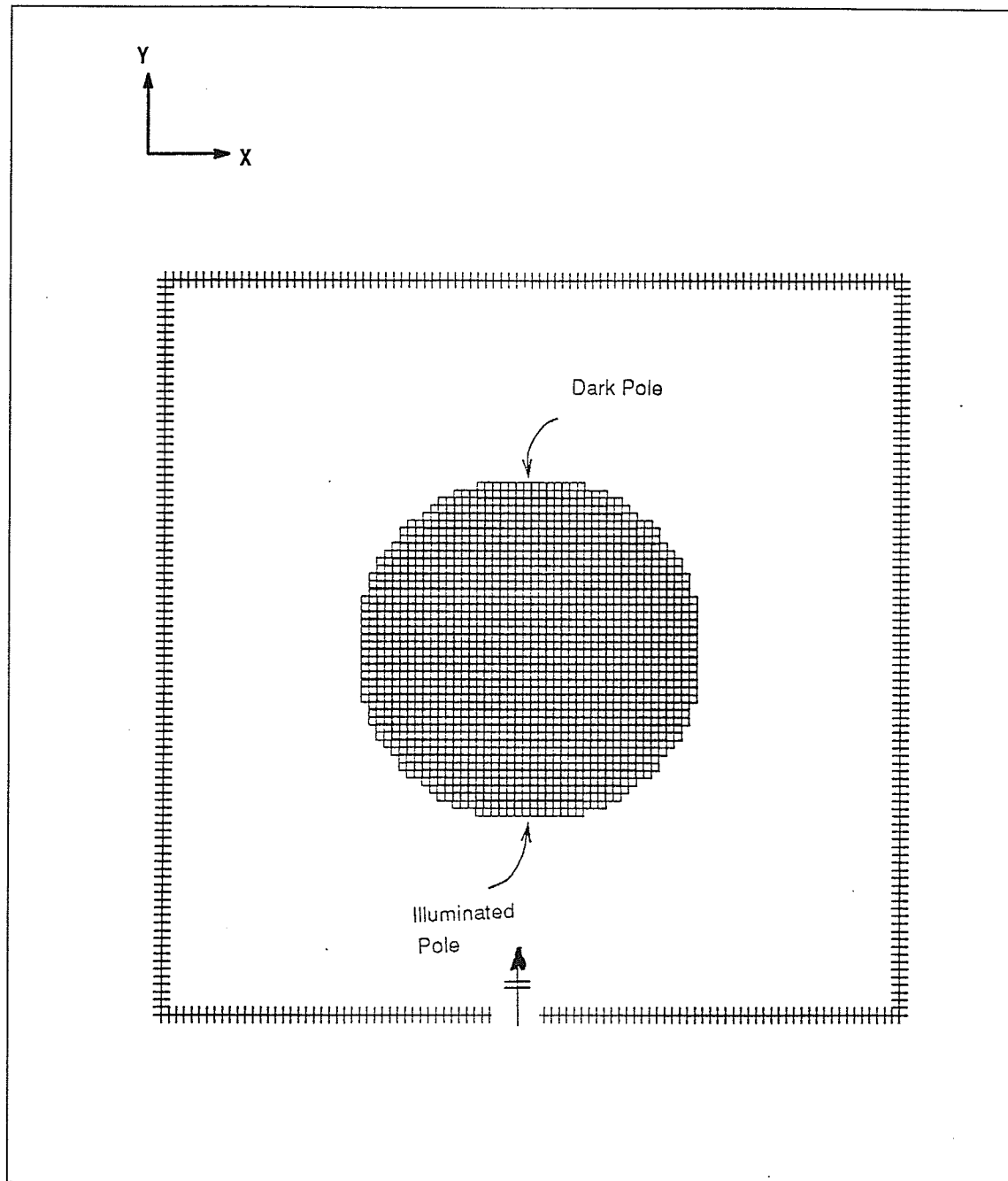
Fig. 3.5 Geometry of a circular cylinder inside a 2–D FDTD Lattice.

(a) illuminated pole.

(b) dark pole.
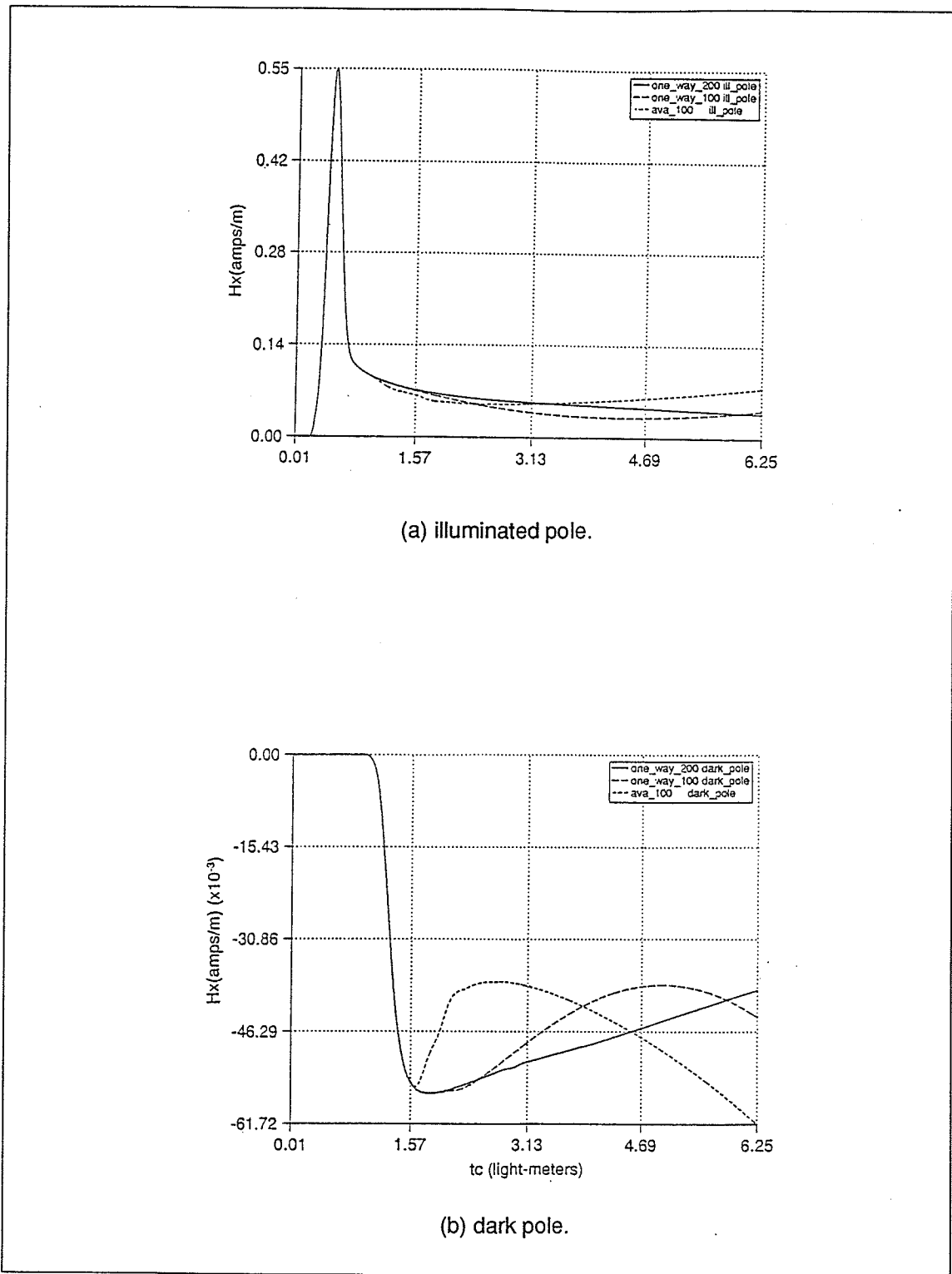
Fig. 3.6   Transient Response of a Conducting Circular Cylinder illuminated by a Gaussian plane Wave.

3.2. Grid Size.

As described in the last chapter, FDTD is a direct solution of Maxwell's time–dependent curl equations. A second–order accuracy is achieved when a central finite–difference approximation for the space and time derivatives of these equations is used. The stability of the time stepping algorithm, and hence the accuracy of the computed field quantities are related to the spatial step Δ and the time step increment δt, respectively. The choice of these two parameters have to satisfy the stability criterion of (2.10).

The selection of the spatial step Δ is also restricted by the type and the characteristics of the incident plane wave launched at the target inside the FDTD lattice. It is suggested [11] that the spatial step Δ should be at least $\dfrac{\lambda_{min}}{10}$, where λ_{min} is the wavelength of the highest frequency having a relatively significant magnitude in the incident plane wave spectrum.

Satisfying such a spatial step requirement will eliminate significantly any distortion of the incident plane wave form, as well as, any other scattered waves from the target embedded in the FDTD lattice during the time–stepping procedure. The choice of the spatial step Δ is also made such that the target in question will be modeled in fine details, enough to allow all the physical phenomena to occur accurately. One example to such fine modeling is the case of curved surfaces which is modeled by a stepped edge surface when using the Yee FDTD unit cell. This cell has to be small enough in size to model the curved surface accurately as shown in Fig. 3.7.

● *Numerical Tests:*

To illustrate the relation between the accuracy of the FDTD method and the spatial step Δ, which is the size of a cubic unit cell inside a FDTD lattice, the propagation of a Gaussian pulse plane wave is investigated. Figure 3.8 shows snap shots of the electric field component inside a uniformly gridded lattice for different values of Δ. This figure shows the
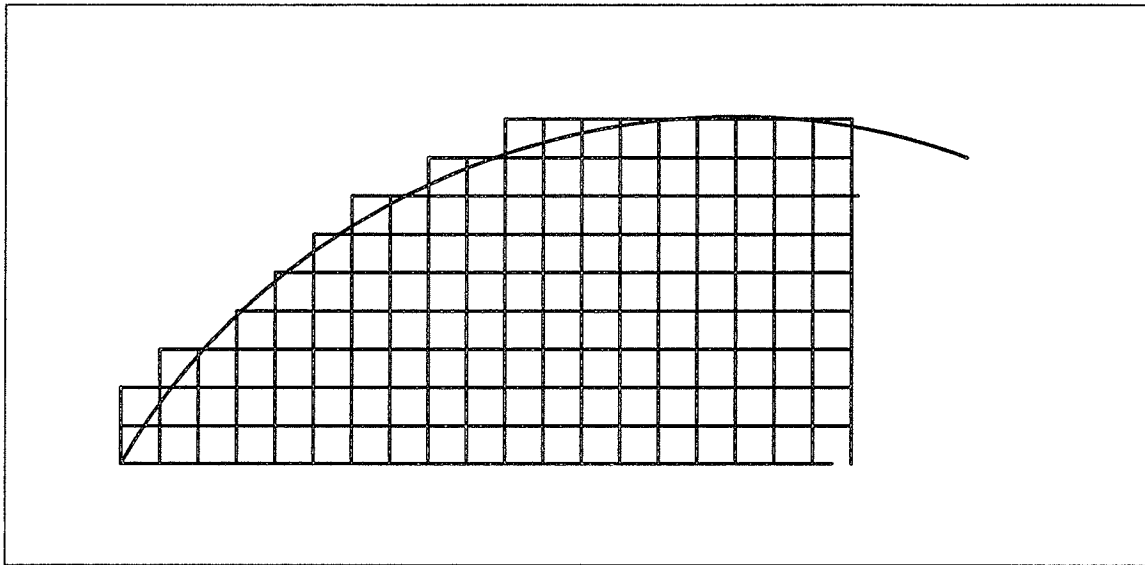
Fig. 3.7   Modeling of curved surfaces using the FDTD Yee cell.
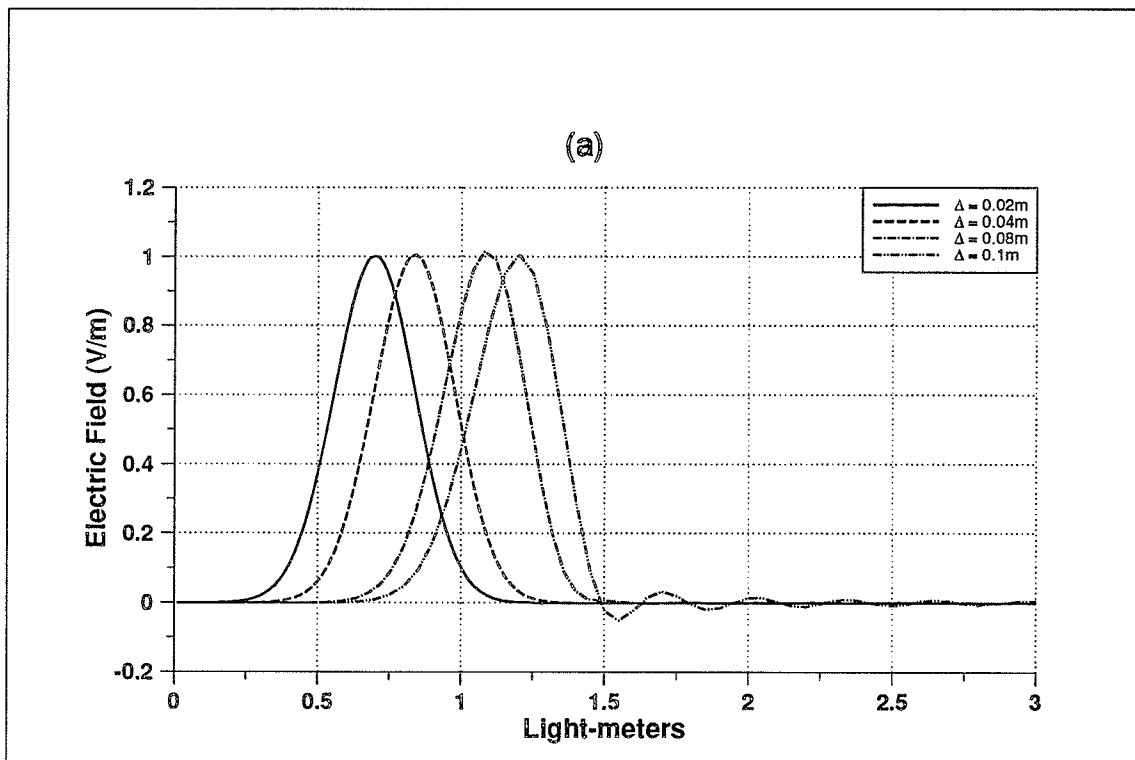
Fig. 3.8a   Propagation of a Gaussian Pulse in a FDTD lattice for different values of Δ.

(b)
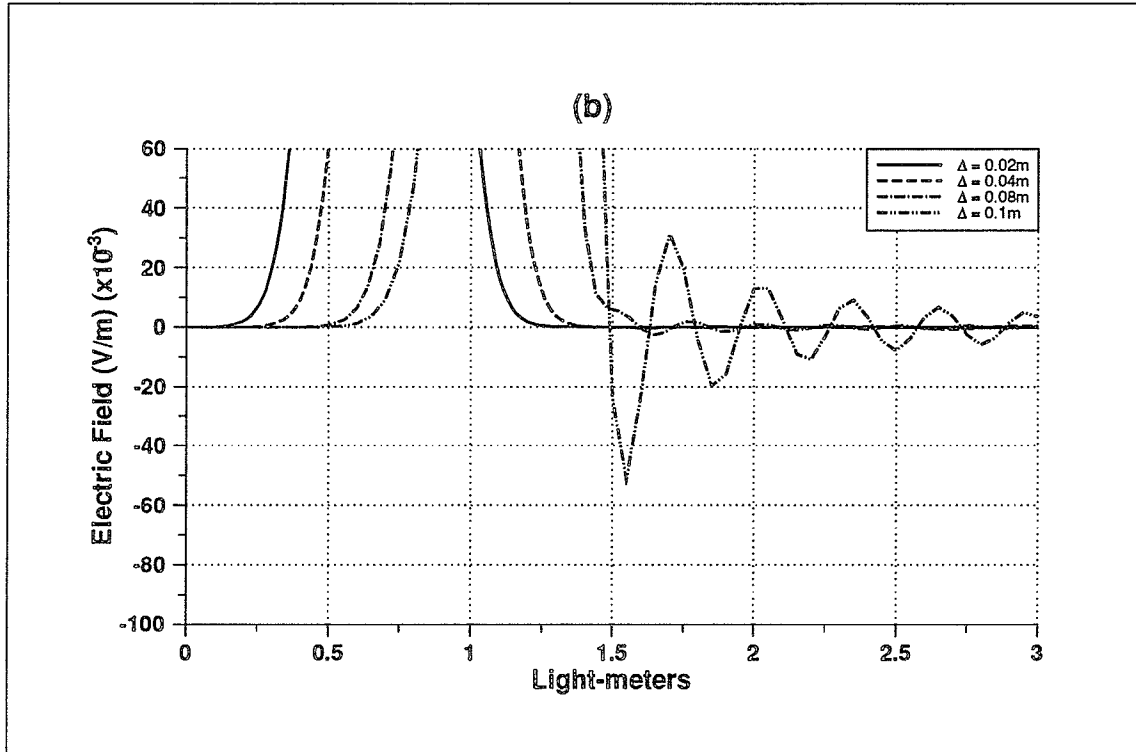
Fig. 3.8b   Propagation of a Gaussian Pulse in a FDTD lattice for different values of Δ (zoomed in).

dispersion of the Gaussian pulse , as well as, ringing when large values of Δ are used. Figure 3.9 shows the model of a conducting sphere inside a FDTD lattice with spatial step Δ = .003*m* . The transient response of the sphere, illuminated by a Gaussian pulse plane wave, is computed at locations (1) and (2) on the sphere. A lattice size of (60 × 60 × 60) is used to model the full sphere, however, at other occasions the sphere symmetry is utilized and a lattice size of (60 × 30 × 60) is used. Two Gaussian pulse widths are tested for a constant spatial step Δ . Figures 3.10–3.13 shows the corresponding transient response at locations indicated on Fig. 3.9 of the sphere model obtained by FDTD method and compared with the Rayleigh–Mei classical solution of scattering from a sphere. The averaged extrapolation algorithm is used as ABC on the lattice walls.

In Fig. 3.10 an obvious level of distortion in the transient response resulted when the narrower Gaussian pulse is used as compared to that of Fig. 3.11. A similar phenomena is observed in Fig. 3.12 as compared to that of Fig. 3.13. Based on the earlier illustration, such a distortion in the transient response can be attributed to the poor sampling of the narrower Gaussian pulse as a result of using a spatial step of $\Delta = .003m$
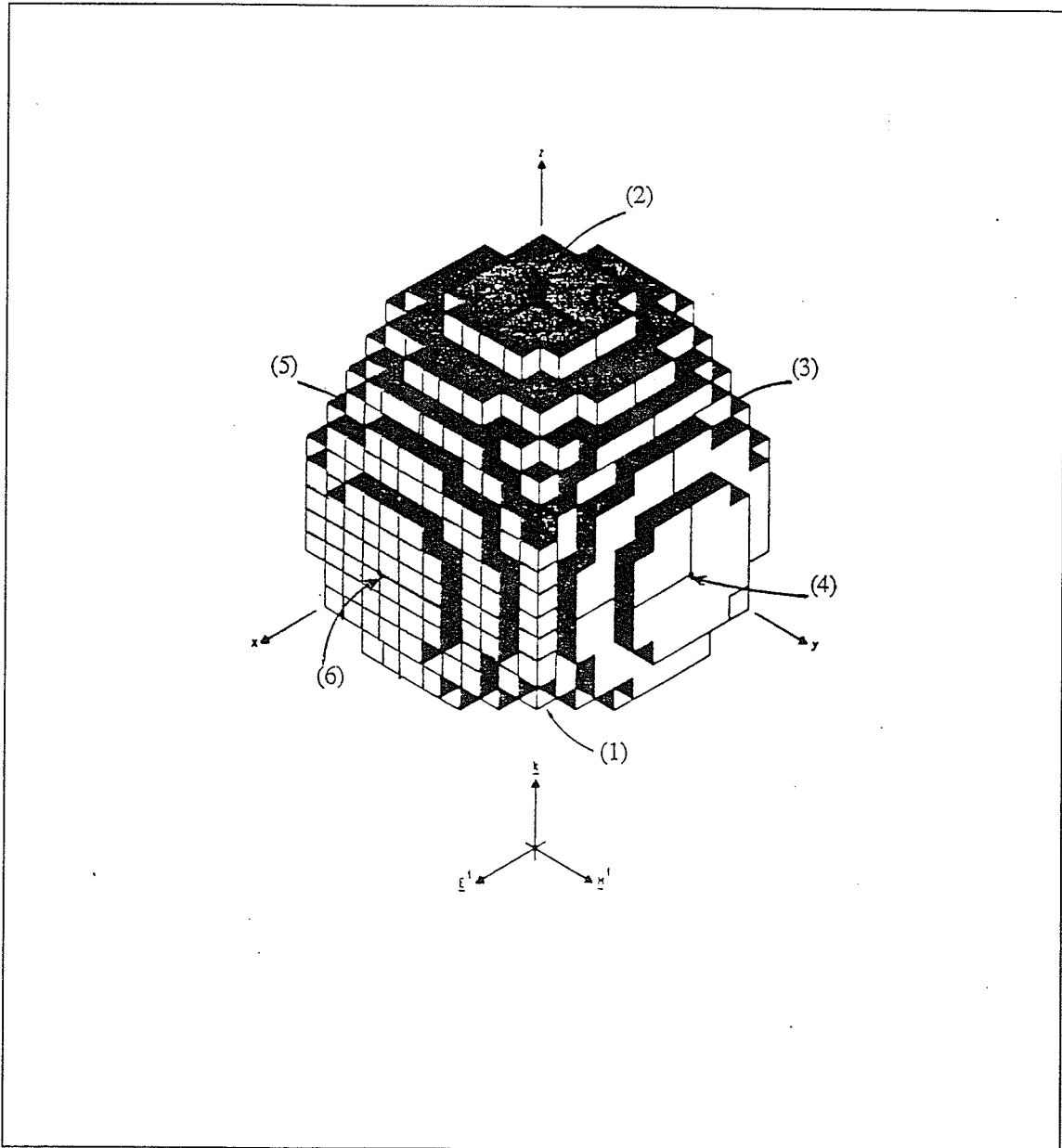
Fig. 3.9   Sphere model inside a three–dimensional FDTD lattice.

Location (1)
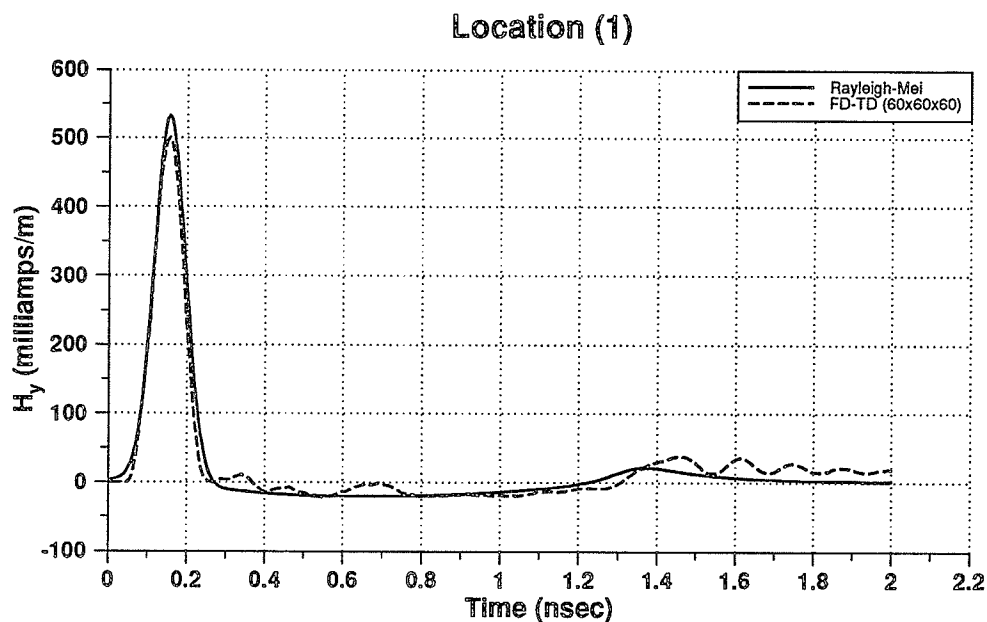
Fig. 3.10   Transient Response of a conducting sphere: Narrow Gaussian pulse case.

$$E_x(t) = 100Exp\Big((t - 2.15 \times 10^{-10})/ 0.0625 \times 10^{-9}\Big)^2 \ V/m, \quad \Delta = .003m, \quad (60 \times 60 \times 60)$$

Location (1)
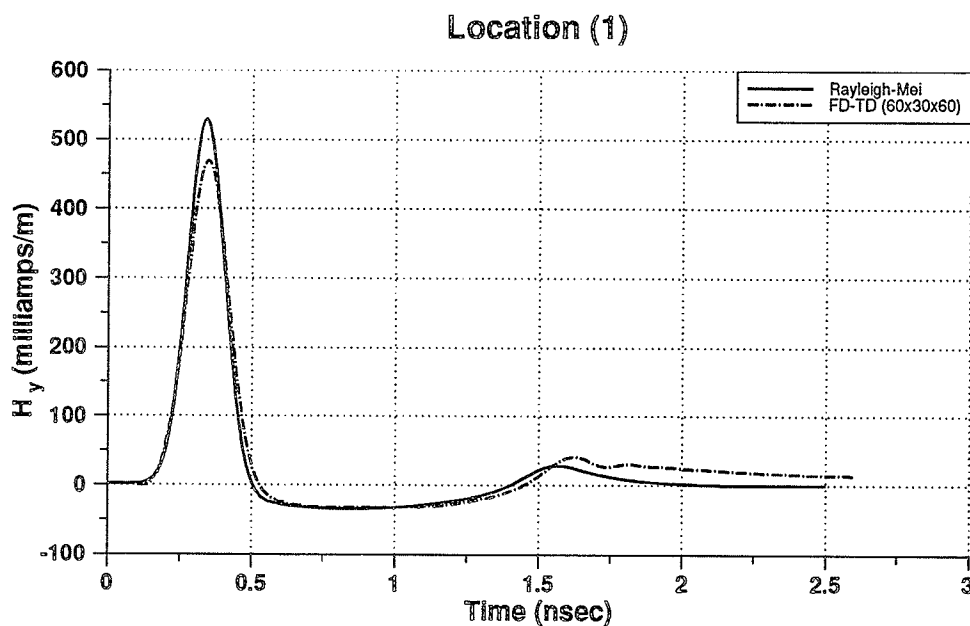
Fig. 3.11   Transient Response of a conducting sphere: Wide Gaussian pulse case.

$$E_x(t) = 100Exp\Big((t - 1.52 \times 10^{-8})/ 0.1 \times 10^{-9}\Big)^2 \ V/m, \quad \Delta = .003m, \quad (60 \times 30 \times 60)$$

Location (2)
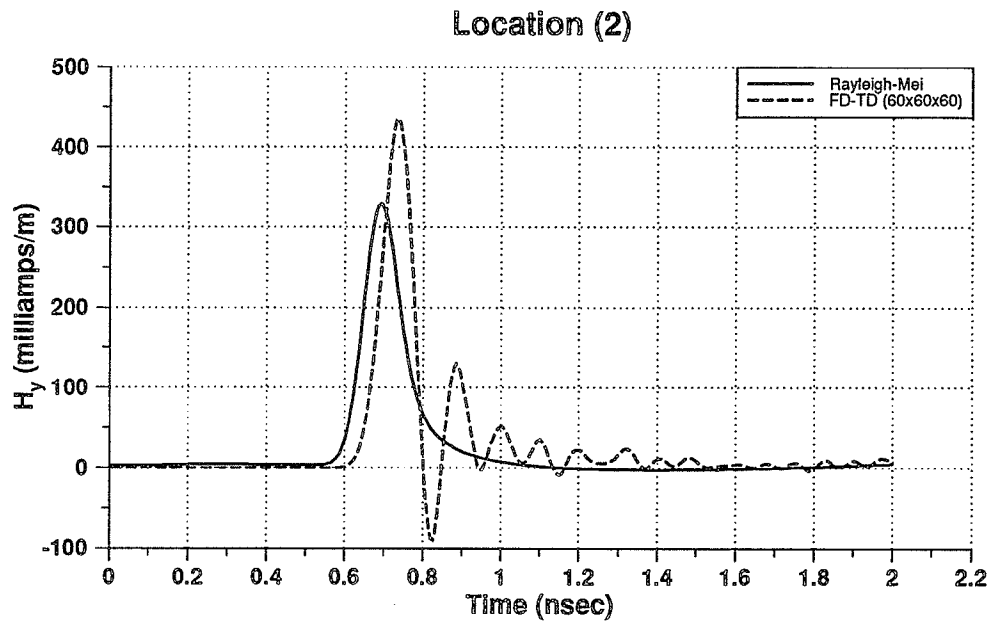
Fig. 3.12   Transient Response of a conducting sphere: Narrow Gaussian pulse case.

$$E_x(t) = 100 Exp\left((t - 2.15 \times 10^{-10})/ 0.0625 \times 10^{-9}\right)^2 \ V/m, \quad \Delta = .003m, \quad (60 \times 60 \times 60)$$

Location (2)
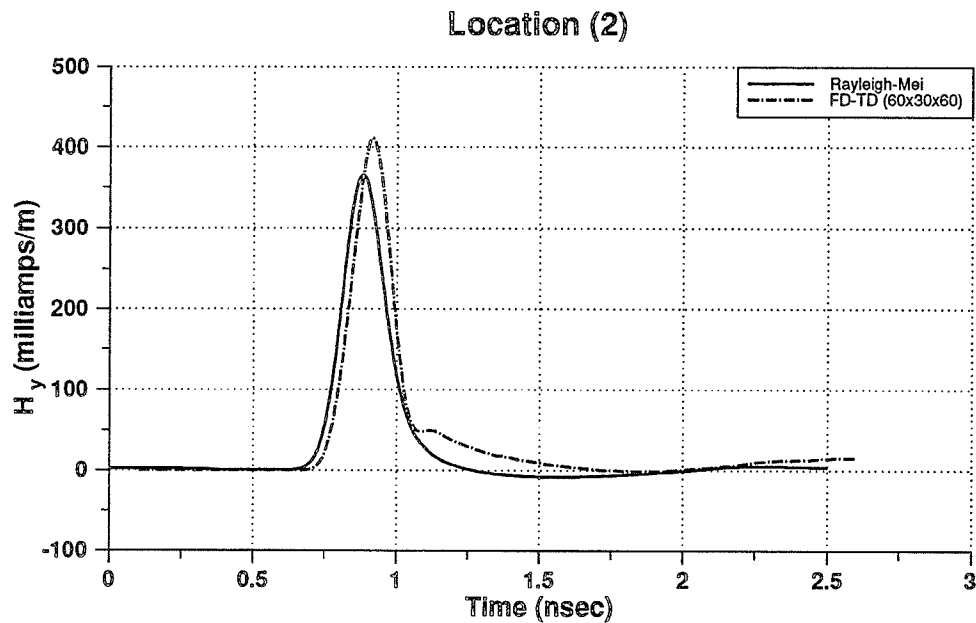
Fig. 3.13   Transient Response of a conducting sphere: Wide Gaussian pulse case.

$$E_x(t) = 100 Exp\left((t - 1.52 \times 10^{-8})/ 0.1 \times 10^{-9}\right)^2 \ V/m, \quad \Delta = .003m, \quad (60 \times 30 \times 60)$$

3.3. FDTD Grid Characteristics

Most of the electromagnetic civil and military applications involve structures that are complex in their geometry and their material composition. These geometries may contain very fine geometric details such as lapped joints and cracks, or they may be coated with a lossy material to reduce field penetration or RCS of these structures in some applications. Using FDTD method, different approaches were followed by researchers to model such structures accurately to include their geometric details. One approach is the use of subcell modelling techniques, where specialized cells are designed to model accurately the physics of a specified geometry. Such approach was followed by Taflove et. al. [61] where he used the Faraday's law in integral form to model wires, curved surfaces and gaps in conductors of sizes that are less than the size of a Yee cell inside the FDTD lattice. Demarest [57] used Babient's principle in conjunction with the FDTD method to model slots in conducting structures. He also used Faraday's and Ampere's laws in integral form to model thin dielectric slabs, conductor backed dielectric slabs, and cracks in dielectric structures [68].

In the modeling of lossy structures or conducting structures with lossy coating, some researchers followed the approach of substituting the lossy material with a surface Impedance Boundary Condition (SIBC) analogue. Maloney [69] developed a SIBC to replace a lossy dielectric half–space, a line current over a lossy dielectric half space, and wave propagation in parallel plate waveguide with lossy walls. Beggs et. al.[70] implemented a constant SIBC and a dispersive SIBC that is applicable over a large frequency bandwidth and over a large range of conductivities to replace lossy dielectric objects. Recently, Maloney and Smith [71] also presented a subcell model to include thin material sheets in the FDTD method. This subcell model removed the normal restriction which sets the spatial grid increment to be at least as small as the smallest geometric feature in the solution space. On the other hand others modelled lossy thin sheets by sheet impedances [72,73].

Non–uniform gridding in the FDTD lattice is another procedure used to model structures with very fine geometric details or structures that contain sharp discontinuities where the fields become highly non–uniform in the vicinity of the discontinuities. A non–uniform FDTD mesh, consisting of a coarse and a relatively fine mesh, is an alternative modeling procedure to using a uniform fine FDTD mesh that will be expensive in terms of computer

requirements. Kunz and Simpson [74] introduced an expansion technique in conjunction with the FDTD method to model small local objects. They first calculated the fields in a volume with a coarse grid, then used spatial and time interpolation of these fields to obtain tangential electric field components on the boundary of a subgridded volume which was analyzed in a second run. Zivanovic *et. al.* [75] used a similar procedure but instead of making two separate calculations, the calculations in the coarse grid are coupled with those in the fine grid through the use of Maxwell's equations in a single computer run. Xiao *et. al.* [76] analyzed a grading scheme where the mesh size is gradually changing in either the x– or y–directions or in both directions simultaneously. They claim that applying such a non–uniform gridding, using the traditional FDTD Yee scheme, will result in first order errors in the computed fields. They improved the accuracy of this gridding scheme to second order by analytical cancellation of the first order error terms.

In the following section a numerical demonstration to investigate the accuracy and limitations of using non–uniform gridding inside a FDTD mesh. The FDTD code used allows non–uniform gridding along any of the three cartesian coordinate axis in the FDTD lattice [77]. In this investigation, the propagation of a Gaussian pulse plane wave in one– and three– dimensional FDTD code is done.

3.3.1. One–dimensional Case

The non–uniform gridding procedure is first tested on a one dimensional FDTD algorithm. To insure stability the following inequality is to be satisfied,

$$\delta t \leq \frac{\Delta x}{c} \tag{3.10}$$

where Δx and δt are the spatial and time increments, respectively, and c is the speed of light in free space.

An axis of 100 nodes is considered to investigate the propagation of electromagnetic wave in one–dimensional FDTD algorithm. Figure 3.14 shows snapshots of a Gaussian pulse, having a peak value of 100 V/m, at nodes $i = 15$, $i = 50$, and $i = 85$ along a uniformly grid FDTD axis, i being the node index. These snapshots are computed for different values of time step increment δt and for a spatial step $\Delta x = 0.01m$. It is observed from Fig.

3.14 that the magnitude of the Gaussian pulse peak varies for different values of δt, where the correct magnitude of the Gaussian peak is noted for $\delta t = \dfrac{\Delta x}{2c} = \dfrac{0.005}{c}$.
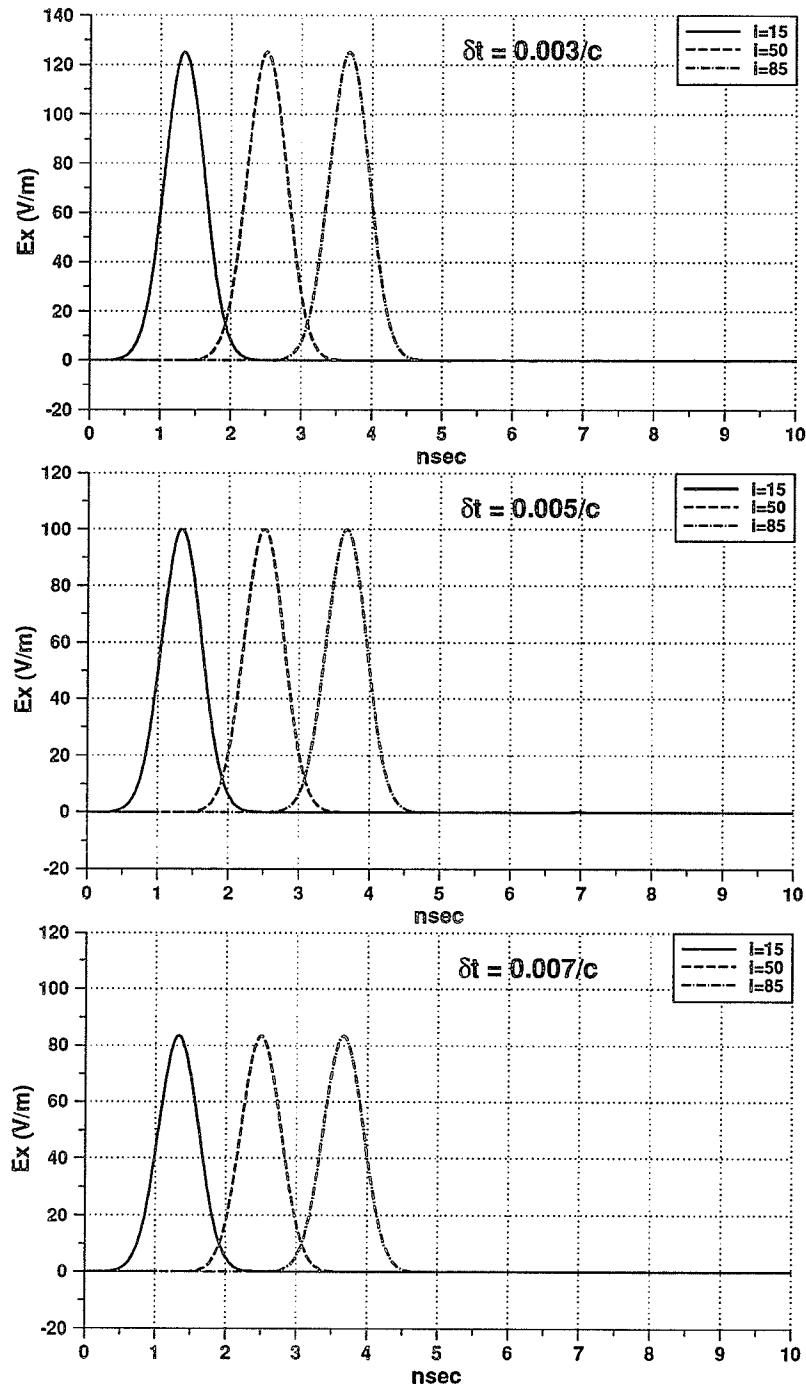

Figure 3.14 Snapshots of a Gaussian pulse inside a uniform grid of a one–dimensional FDTD axis computed for different values of δt. (100 nodes axis, $\Delta x = 0.01m$)

In addition, there was no distortion in the pulse shape and the 'bell' shape of the Gaussian pulse is maintained along the FDTD grid for the different time step values used.

A non–uniform grid discritization shown in Fig. 3.15 (grid_1) is considered. In this case the grid is divided as follows,

$\Delta x = 0.01m, \quad i = 1, \ 41$

$\Delta x = 0.008m, \quad i = 41, \ 60$

$\Delta x = 0.01m, \quad i = 60, \ 100 \cdot$

Figures 3.16 show snapshots of the Gaussian pulse at nodes inside the one–dimensional grid computed for different values of δt. Correct waveforms resulted also for the time step $\delta t = \dfrac{\Delta x}{2c} = \dfrac{0.005}{c}$. Unstable solution occurred for $\delta t = 0.008/c$. Figure 3.17 (grid_2) shows a second example of non–uniform gridding being examined. The 100 nodes axis is divided symmetrically at $i = 50$, such that,

$\Delta x = 0.01m, \quad i = 1, \ 20$

$\Delta x = 0.01$ to $1.0797 \times 10^{-3}m, \quad i = 20, \ 50$ at a ratio $l = 0.92611$ between adjacent spatial steps. The corresponding snapshots of the Gaussian pulse are shown in Figs. 3.18 computed for different values of δt. In this case the stability of the solution is restricted by the smallest spatial step in the grid that also resulted in an increase in the peak values of the wave forms while maintaining the shape of the Gaussian. Using $\delta t > \dfrac{1.2 \times 10^{-3}}{c}$ resulted in an unstable solution. Figure 3.19 (grid_3) shows a third example of a non–uniform gridding. The axis is divided symmetrically at $i = 50$, such that,

$\Delta x = 0.01m, \quad i = 1, \ 20$

$\Delta x = 0.01$ to $0.00511m, \quad i = 20, \ 50$ at a ratio $l = 0.97716$ between adjacent spatial steps. Figures 3.20 show the snapshots of the Gaussian pulse at nodes on the grid axis computed for different values of δt. Unstable solution occurred for values of $\delta t > 0.006/c$.
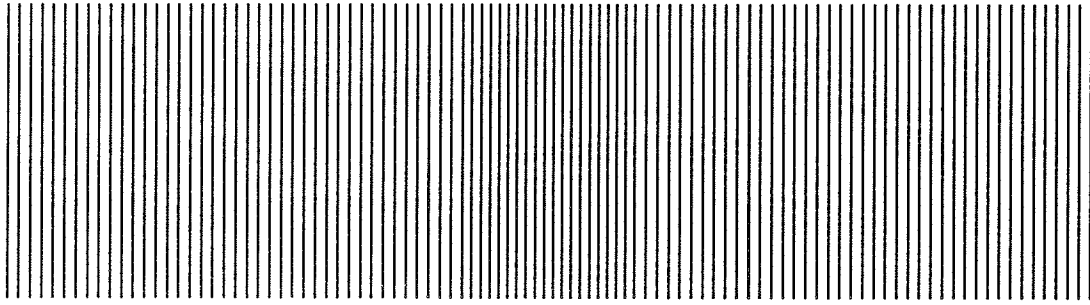
$$\Delta x = 0.01m, \quad i = 1, \ 41$$

$$\Delta x = 0.008m, \quad i = 41, \ 60$$

$$\Delta x = 0.01m, \quad i = 60, \ 100 \ ,$$

Figure 3.15   A non–uniform grid discritization of a one–dimensional FDTD axis (grid_1).
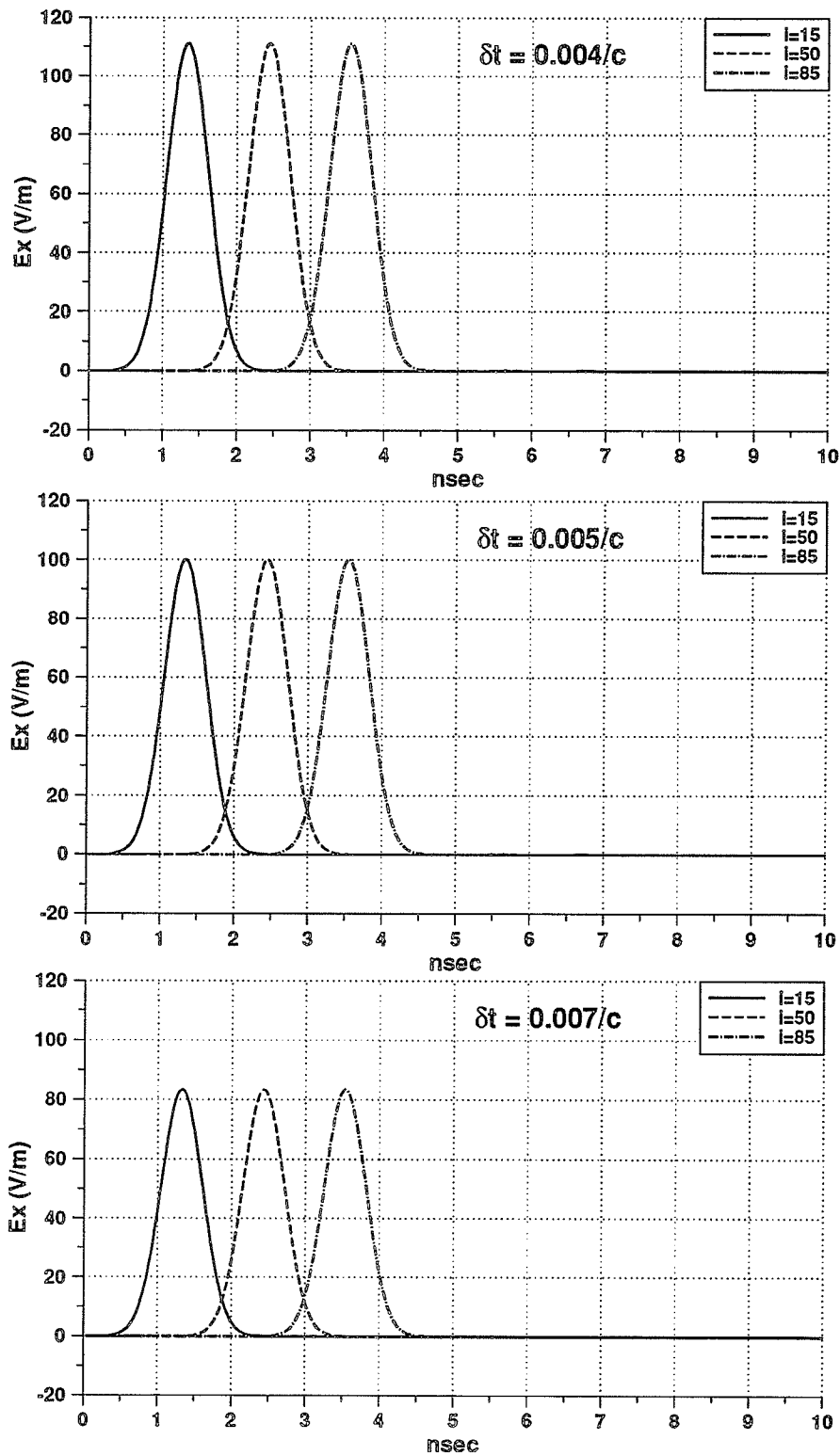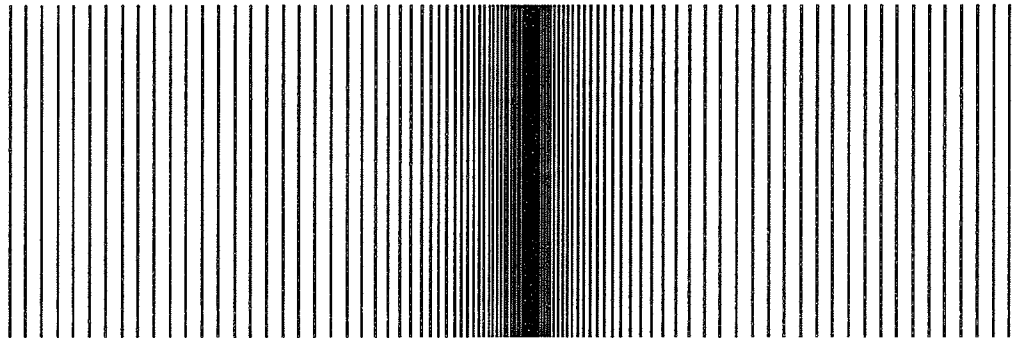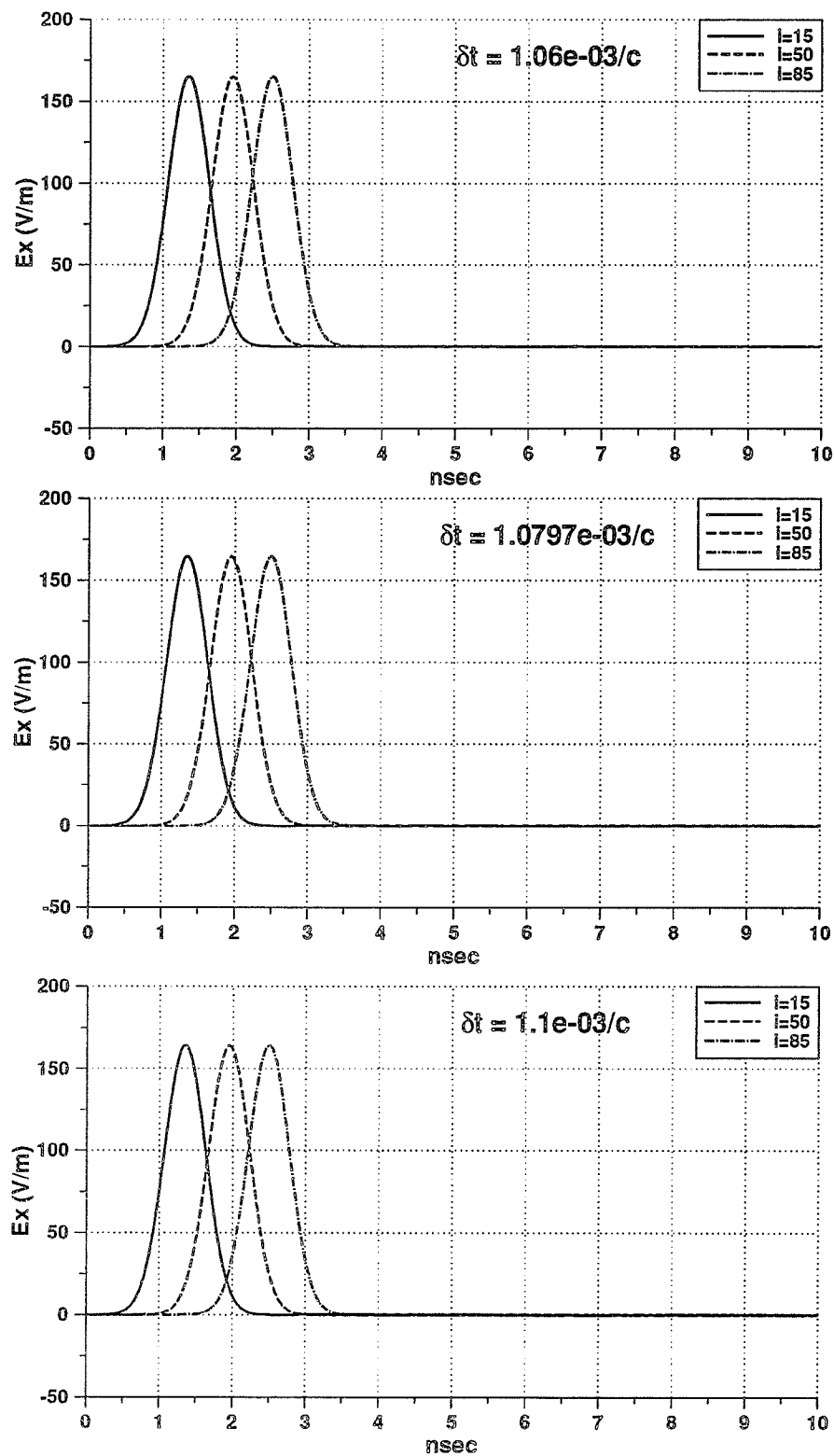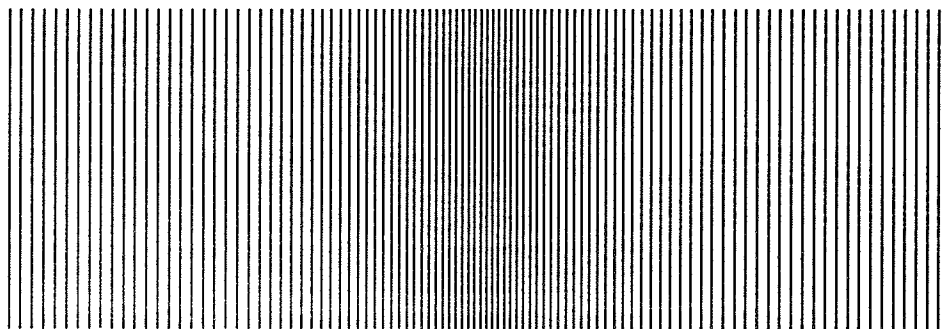
Figure 3.16   Snapshots of a Gaussian pulse inside grid_1 of Fig. 3.15 computed for differ-
ent values of δt.

The 100 nodes axis is divided symmetrically at $i = 50$, such that,

$\Delta x = 0.01 m, \quad i = 1, \ 20$

$\Delta x = 0.01 \rightarrow 1.0797 \times 10^{-3} m, \quad i = 20, \ 50$ at a ratio $l = 0.92611$ between adjacent spatial steps.

Figure 3.17   A non–uniform grid discritization of a one–dimensional FDTD axis (grid_2).

Figure 3.18   Snapshots of a Gaussian pulse inside grid_2 of Fig. 3.17 computed for differ-
ent values of δt.

the axis is divided symmetrically at $i = 50$, such that,

$\Delta x = 0.01m, \quad i = 1, \ 20$

$\Delta x = 0.01 \rightarrow 0.00511m, \quad i = 20, \ 50 \quad$ at a ratio $l = 0.97716$ between adjacent spatial steps.

Figure 3.19   A non–uniform grid discritization of a one–dimensional FDTD axis (grid_3).
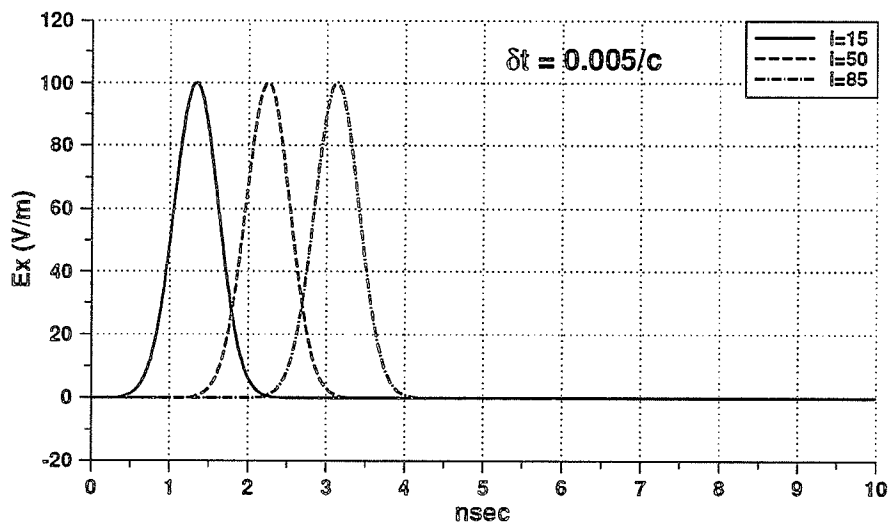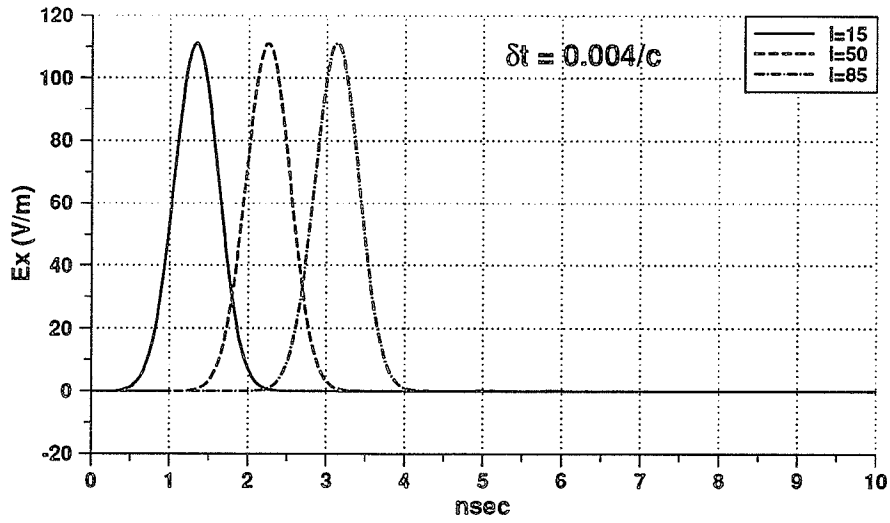
Figure 3.20   Snapshots of a Gaussian pulse inside grid_3 of Fig. 3.19 computed for differ–

ent values of δt.

3.3.2. Three–dimensional Case

The propagation of electromagnetic waves in a three–dimensional non–uniformly grid FDTD lattice is also studied. In this case the stability of the time stepping algorithm is insured by satisfying the following inequality,

$$c \, \delta t \ \leq \ \left(\frac{1}{\Delta x^2} + \frac{1}{\Delta y^2} + \frac{1}{\Delta z^2} \right)^{-\frac{1}{2}} \tag{3.11}$$

Initially, the propagation of a Gaussian pulse plane wave having a peak magnitude of $100 \ V/m$ propagating along the $z-$ direction is considered. Figure 3.21 shows snapshots of the Gaussian pulse computed at locations $(10, 10, 10)$, $(10, 10, 40)$, and $(10, 10, 70)$ respectively, inside a uniformly grid FDTD lattice having an array size of $(20 \times 20 \times 80)$. A spatial step of $\Delta = 0.01m$ is used in the FDTD mesh. As observed earlier in the one–dimensional case the peak value of the Gaussian pulse changes from the correct value $(100 \ V/m)$ while maintaining the 'bell' shape for values of $\delta t \neq \dfrac{\Delta}{2c}$. Unstable solution occurred for $\delta t > 0.006/c$. The second FDTD lattice tested is that of a non–uniform gridding along the $z-$ axis of the lattice. The lattice has the same size as before, the gridding along the $z-$ axis is as follows,

$\Delta z = 0.01m, \quad k = 1, \ 31$

$\Delta z = dl, \quad k = 31, 50$

$\Delta z = 0.01m, \quad k = 50, \ 80$

Figure 3.22 shows snapshots of the Gaussian pulse for $dl = 0.005m$ computed for different values of δt. The values of δt used provided a stable solution but caused the peak value of the Gaussian pulse to change. Unstable solution occurred for values of $\delta t > 0.004/c$. Figure 3.23 shows the corresponding Gaussian pulse snapshots for $dl = 0.007m$ computed using $\delta t > 0.0045/c$, using $\delta t = 0.005/c$ resulted in an unstable solution. Figure 3.24 shows similar computations for $dl = 0.008m$ and for $\delta t = 0.005/c$ resulting in a correct peak value for the Gaussian pulse.
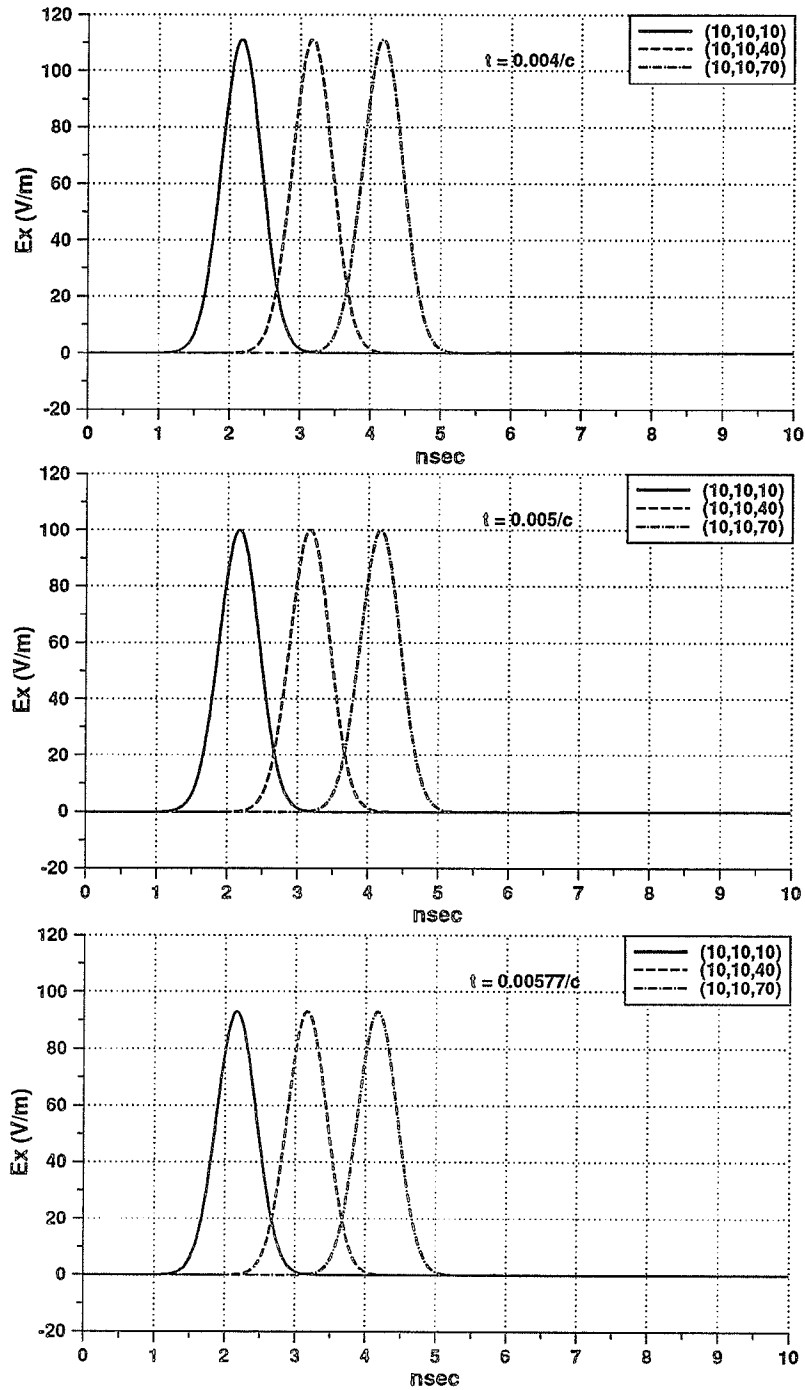
Figure 3.21   Snapshots of a Gaussian pulse propagating along the z–axis inside a

uniformly grid FDTD lattice computed for different values of δt.

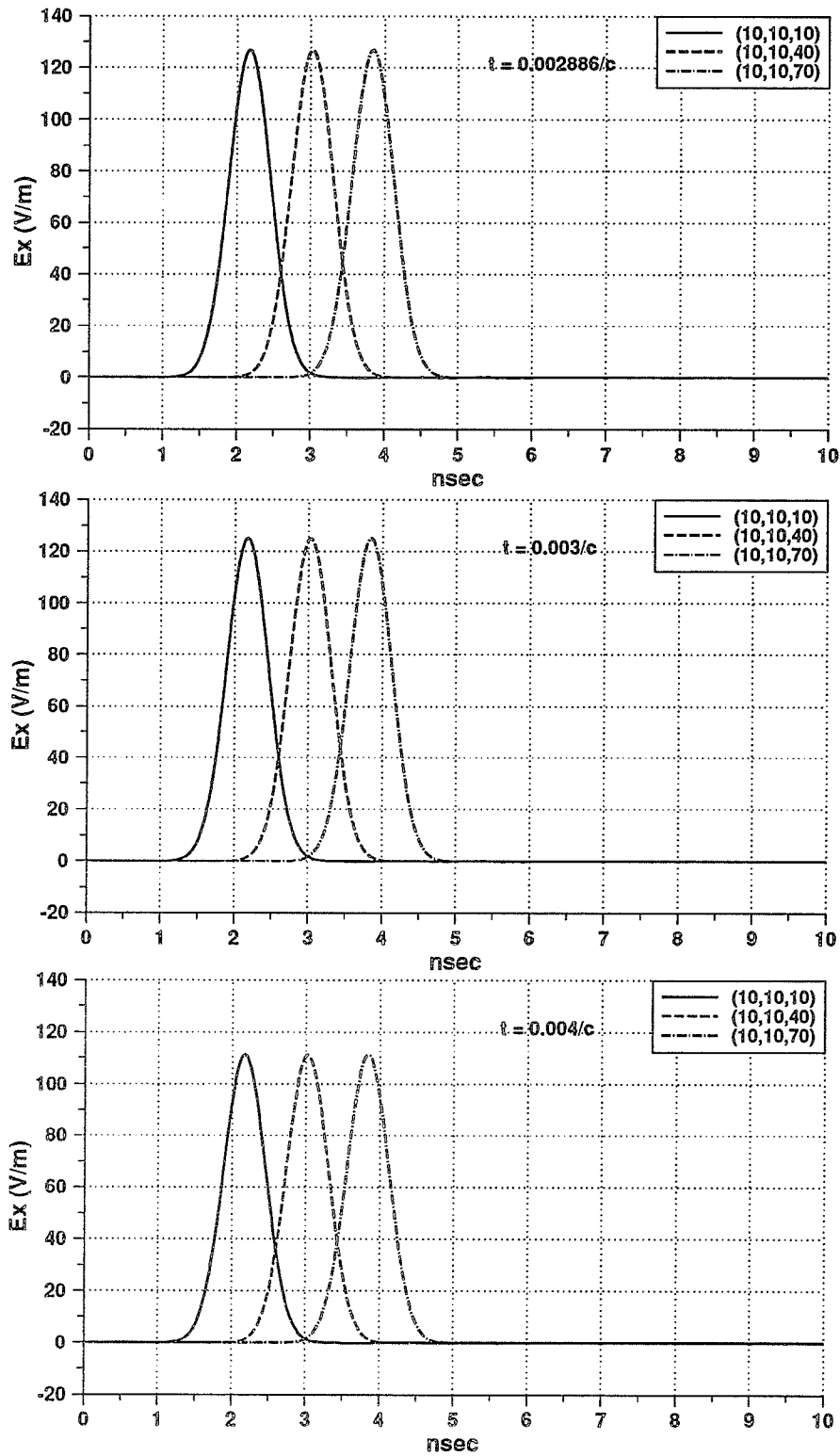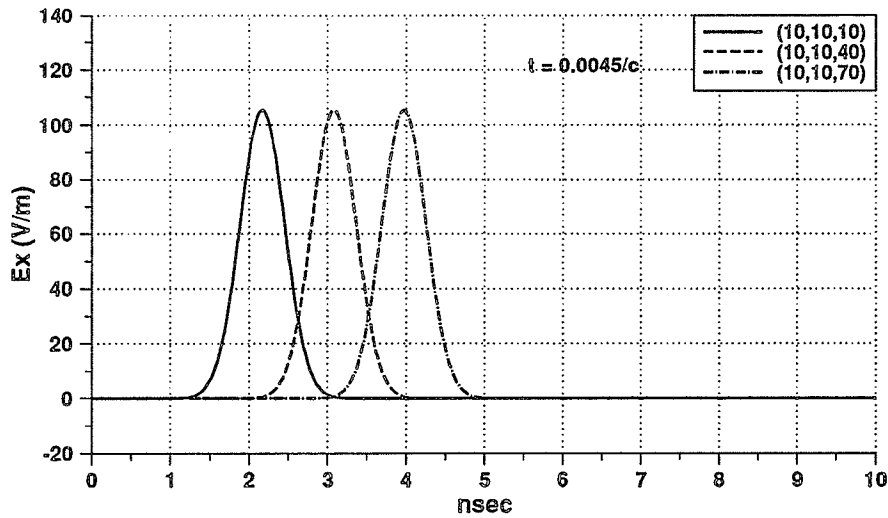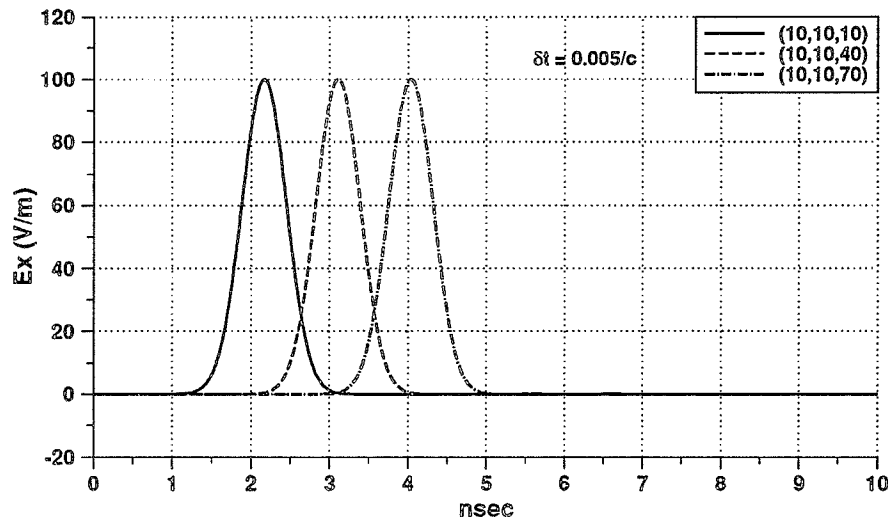[lattice size $(20 \times 20 \times 80)$, $\Delta x = \Delta y = \Delta z = 0.01m$]

Figure 3.22   Snapshots of a Gaussian pulse propagating along the z–axis inside a non–uniform grid FDTD lattice computed for different values of δt.

[lattice size $(20 \times 20 \times 80)$, $dl = 0.005m$]

Figure 3.23   A Snapshot of a Gaussian pulse propagating along the z–axis inside a
non–uniform grid FDTD lattice computed for different values of δt.

[lattice size $(20 \times 20 \times 80)$, $dl = 0.007m$]

Figure 3.24   A Snapshot of a Gaussian pulse propagating along the z–axis inside a
non–uniform grid FDTD lattice computed for different values of δt.

[lattice size $(20 \times 20 \times 80)$, $dl = 0.008m$]

Conclusions

In this section, the propagation of electromagnetic waves in one–dimensional and three–dimensional FDTD space is investigated. The propagation of a Gaussian pulse wave in a non–uniform grided FDTD axis is tested for different non–uniform gridding schemes. To insure stability in the FDTD algorithm, the time step increment has to be chosen to satisfy the Courant stability criteria taking into account the smallest spatial step size inside the FDTD lattice. Different time step increments has been used to study the performance of each of the FDTD grids. In a uniform grid, it was observed that a Gaussian pulse will propagate without any shape distortion or change in its peak value for $\delta t = \dfrac{\Delta}{2c}$. The pulse peak magnitude increased for $\delta t > \dfrac{\Delta}{2c}$ and decreased for $\delta t < \dfrac{\Delta}{2c}$ ($\Delta = \Delta x = \Delta y = \Delta z$, in the 3–dimensional case). In the case of a non–uniform grid the choice of δt is restricted by the size of the smallest spatial step in the grid. Hence, the choice of δt to insure stability might effect the magnitude values of the pulse, depending on how small is the smallest Δ relative to the largest Δ. It should be noted that although there was a change in the peak magnitude of the pulse, in a non–uniform grid, the shape of the pulse is maintained with no distortion as it propagates inside the FDTD lattice. It is expected that for EM problems where the impulse response of a structure is required, the use of a non–uniform grid will be appropriate, for the resulting response will be normalized to that of the incident pulse propagating inside the FDTD lattice.

Chapter IV

Application to Scattering Problems

As described in the literature survey of Chapter II the FDTD numerical method has been applied to a wide variety of electromagnetic scattering and antenna problems. In this chapter the FDTD method in two– and three–dimensional space is used to study the transient response of cylinders and spheres. The transient response of conducting and dielectric circular cylinders due to a step plane wave is computed and the correspondence between the transient response and the rise time of the excitation wave is investigated. The transient response of conducting and dielectric spheres illuminated by a Gaussian pulse plane wave is also computed and compared with those obtained from analytic solution. Also in this chapter, the field penetration inside a conducting box with an open top illuminated by an Electromagnetic Pulse (EMP) plane wave is computed. The effect of changing the aperture geometry and loading the box with lossy material on the field magnitude and frequency content inside the box is analyzed. Finally, the capability of the FDTD method to model thin conducting wires of different cross–sections and lengths is studied, where different thin wire modeling procedures are examined.

4.1. Transient Response of Circular Cylinders

An important simplification of the full three–dimensional FDTD algorithm case is the assumption that neither the incident plane wave excitation nor the modeled geometry has any variation in the z–direction (*i.e.* all partial derivatives with respect to z are equal to zero), Maxwell's curl equations eqs. (2.2, 2.3) reduces to two decoupled sets of scalar equations. These decoupled sets, referred to as the transverse magnetic (*TM*) mode and the transverse electric (*TE*) mode, describe two–dimensional wave interaction with objects. The related equations for each case:

– *TM* case (E_x, H_x, and H_y)

$$\frac{\partial H_x}{\partial t} = -\frac{1}{\mu}\left(\frac{\partial E_z}{\partial y}\right) \tag{4.1a}$$

$$\frac{\partial H_y}{\partial t} = \frac{1}{\mu}\left(\frac{\partial E_z}{\partial x}\right) \tag{4.1b}$$

$$\frac{\partial E_z}{\partial t} = \frac{1}{\epsilon}\left(\frac{\partial H_y}{\partial x} - \frac{\partial H_x}{\partial y} - \sigma E_z\right) \tag{4.1c}$$

– *TE* case (H_z, E_x, and E_y)

$$\frac{\partial E_x}{\partial t} = \frac{1}{\epsilon}\left(\frac{\partial H_z}{\partial y} - \sigma E_x\right) \tag{4.2a}$$

$$\frac{\partial E_y}{\partial t} = -\frac{1}{\epsilon}\left(\frac{\partial H_z}{\partial x} + \sigma E_y\right) \tag{4.2b}$$

$$\frac{\partial H_z}{\partial t} = \frac{1}{\mu}\left(\frac{\partial E_x}{\partial y} - \frac{\partial E_y}{\partial x}\right) \tag{4.2c}$$

Recently, the interest in the transient response of complex structures illuminated by slowly decaying transient pulses, resulting from lightning or nuclear bursts, has increased with the development of few technologies. These developments include the use of advanced composite materials which provided less shielding than conventional metallic structures, and the increased use of low power level semiconductors for circuits.

In the following study the field transient response of both conducting and dielectric circular cylinders illuminated by a plane wave having a step function waveform in the time-domain is computed. The choice of such a plane wave is made because of its close similarity with the EMP resulting from lightning or nuclear bursts which have a fast rise time and a slow decay in its field magnitude. The conducting cylinder may represent in this case metallic wires in electric circuits, while dielectric cylinders may represent guiding dielectric structures such as optical fibers. A two–dimensional space FDTD algorithm will be used to model the circular cylinders, and the correspondence between the transient response and the rise time of the excitation wave will be investigated [78].

4.1.1. Results and Discussion

The transient response of a circular cylinder illuminated by a step function plane wave is computed in a *TM* FDTD grid space. The circular cylinder considered, having its axis parallel to the z–axis, has a radius of *37.5cm* and is mapped into *298 × 298* FDTD grid mesh of spatial step size $\Delta x = \Delta y = 0.0125m$. A time step size of $\delta t = \dfrac{\Delta x}{2c}$ is used, where

c the speed of light in free space. Since such a scattering problem is an open space problem, the walls of the FDTD mesh are terminated with ABC. Thus, the fields scattered away from the illuminated structure are absorbed with minimal reflections. The algorithm used to implement such ABC is that of the 'One–Way' wave equation [13] and it is further improved using super ABC of [19]. The circular cylinder is mapped into the FDTD mesh where its curved surface is sampled as a stepped edge surface as shown in Fig. 4.1. The excitation plane wave used to illuminate the cylinder is a z–polarized plane wave propagating in the $+y$–direction. The wave form of the plane wave has a unit step like shape,

$$E_z(t) = \left[1 - Exp(-At)\right] \quad (V/m) \tag{4.3}$$

where different values of A corresponding to different rise times are considered. The resulting waveforms are shown in Fig. 4.2.
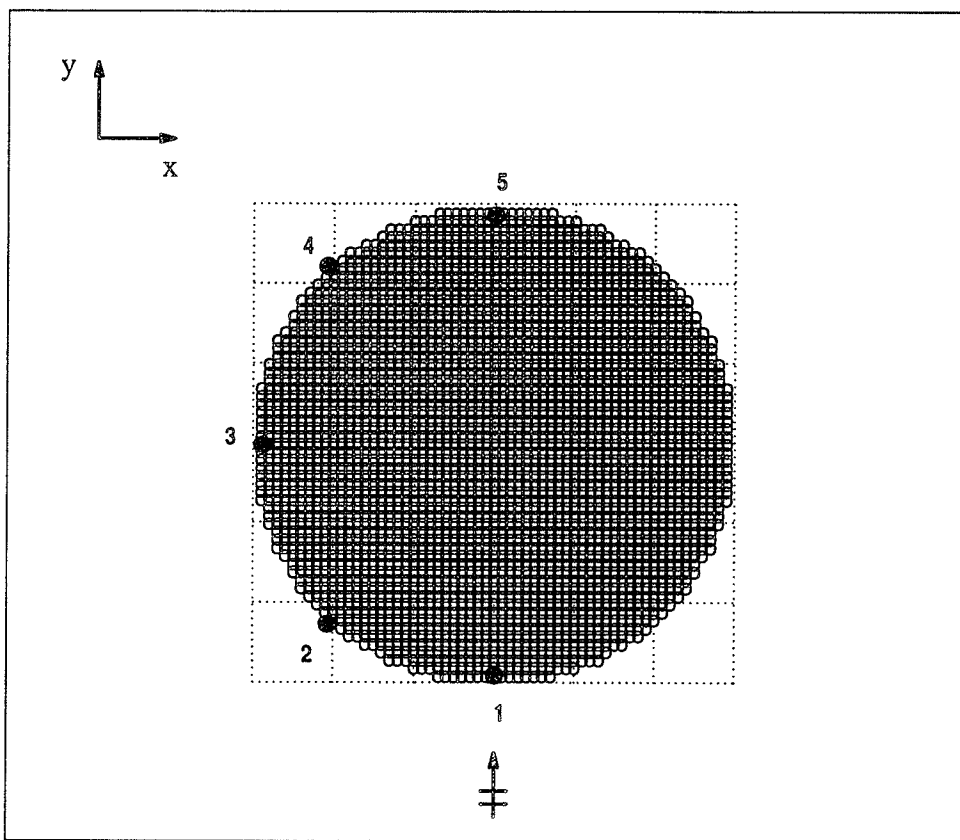

Figure 4.1   Circular Cylinder in a FDTD mesh.

i) *Conducting Circular Cylinder.*

The conducting surface of the cylinder is simulated by setting the electric fields tangent to that surface to zero ($E_{z\,\tan}$ = 0) at all time steps. An incident plane wave is launched normally onto the cylinder. Fig. 4.3 shows the propagation of the step like plane wave in the presence of the conducting cylinder, where the E_z field component is plotted at different time steps. The magnetic field transient response at positions (*1*) to (*5*) indicated in Fig. 4.1 are computed for different values of *A* and are shown in Fig. 4.4. These positions, *i.e.* (*1*) to (*5*), are located approximately one–half cell from the cylinder surface. At observation points (*1*) and (*2*) in the illuminated region of the cylinder the effect of varying the rise time of the excitation function can be seen clearly at the early times of the corresponding responses. At location (*1*) of the cylinder the field response at the early time rises to approximately twice the incident field[2] and then continue with an increasing value exceeding that of the incident wave. This can be attributed to the incident excitation illuminating continuously the conducting cylinder causing an accumulation of charges on the cylinders surface. Also, imposing the $E_{z\,\tan}$ = 0 on the cylinders surface (infinite conductivity) contributed to this phenomena as well. In the shadow region of the cylinder (*4 & 5*) the fields on the cylinder are due to creeping currents launched from the illuminated region, hence, the effect of the rise time of the incident plane wave is being damped due to radiation as can be seen in the corresponding early time responses. At late times the field magnitude at (*3, 4 & 5*) increased steadily due to the charge accumulation. Such a situation of continuous increasing field response exists only in a case of a step plane wave excitation where infinite energy is available.

---

2. $2H_y^{inc} = 2E_x^{inc}\,/\,\eta_o\,=\,2\,/\,(120\pi\,)\,=\,5.3\;mA/m$

Figure 4.2   Waveform of the incident plane wave
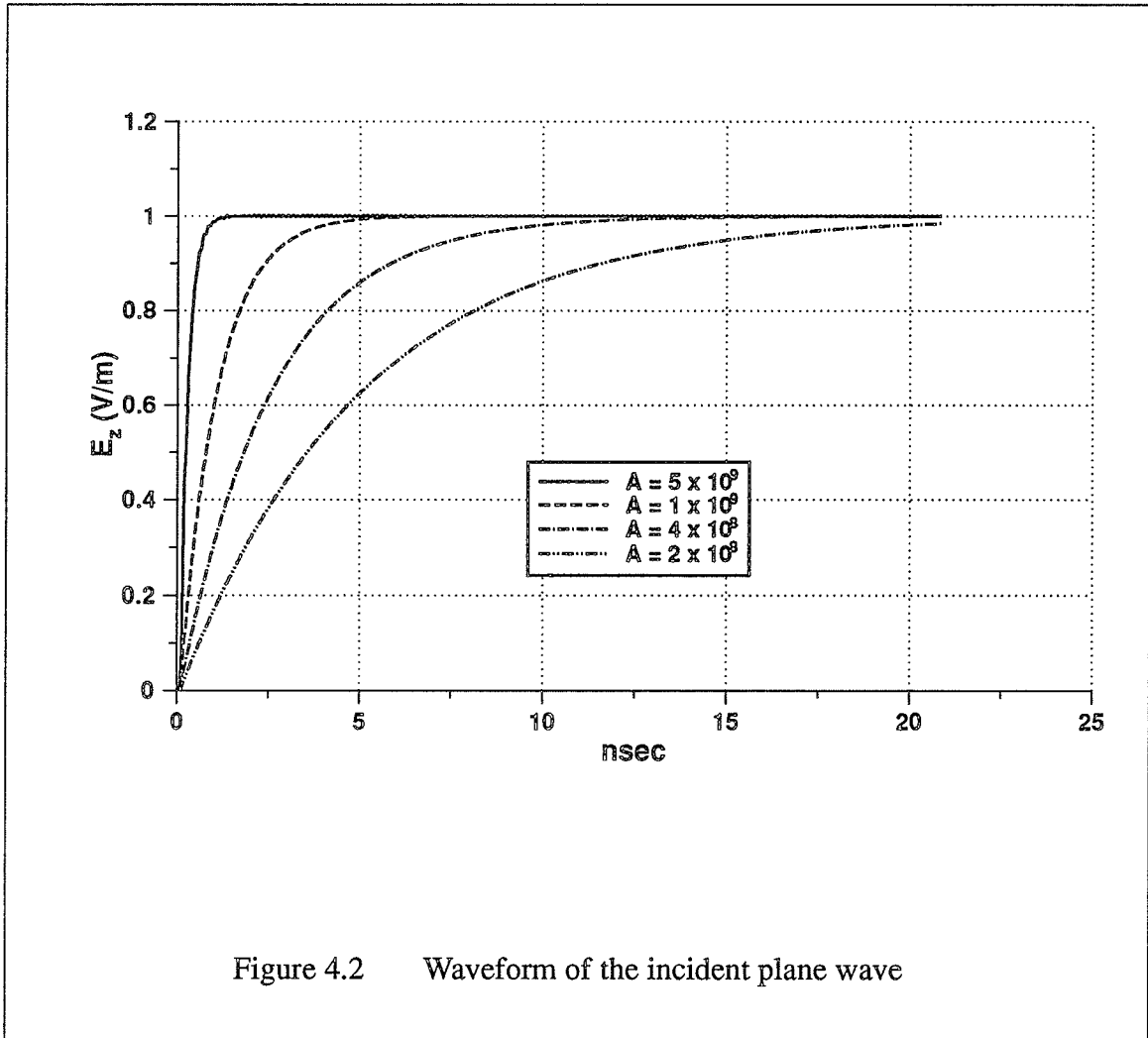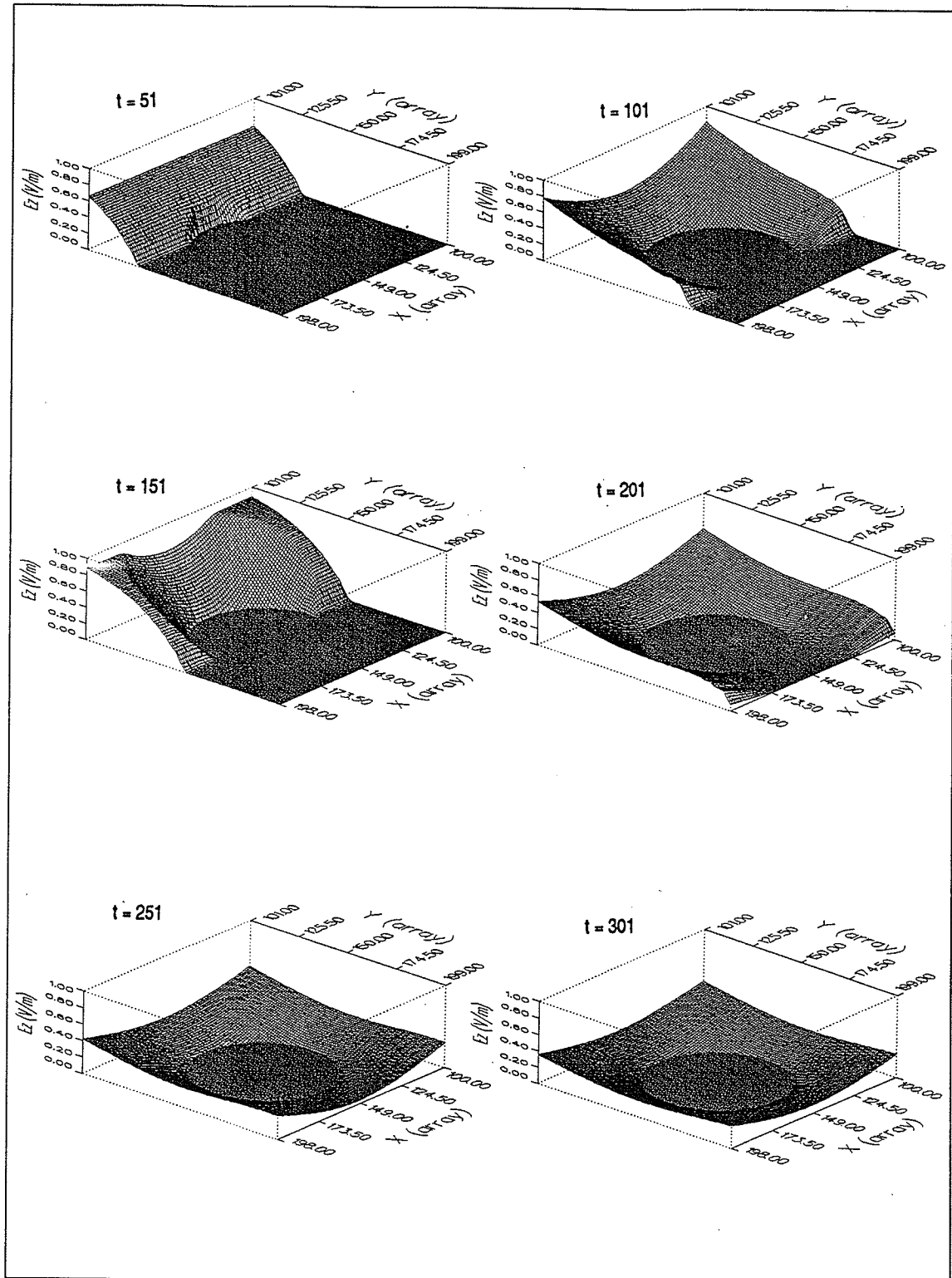
Figure 4.3   Propagation of a plane wave in the presence of a conducting circular

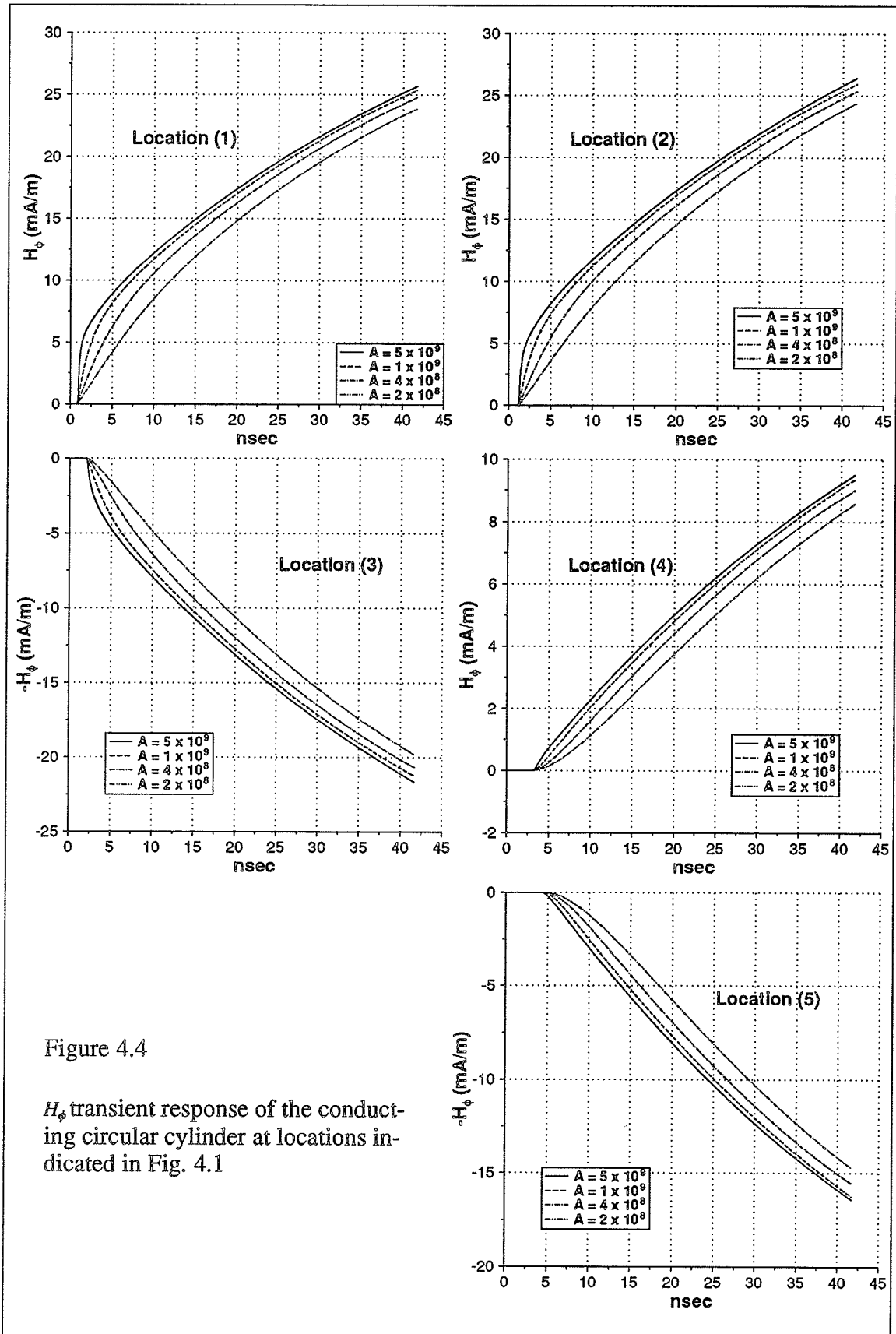cylinder. $(A = 1 \times 10^9)$; $\Delta x = 0.0125m$, $\delta t = \dfrac{\Delta x}{2c}$

Figure 4.4

H_ϕ transient response of the conducting circular cylinder at locations indicated in Fig. 4.1

ii) *Dielectric Circular Cylinder.*

The scattering of a dielectric circular cylinder by a step like plane wave is also considered. The cylinder is chosen to have an $\epsilon_r = 4$. Fig. 4.5 shows the propagation of the plane wave in the presence of the dielectric cylinder, where the E_z field component is plotted at different time steps. The magnetic field transient responses, shown in Fig. 4.6, are again computed for different values of A and at positions indicated in Fig. 4.1. The effect of different rise time values A of the excitation function on the early time field response can be seen clearly at the indicated locations. For $A = 5 \times 10^9$, corresponding to the fastest rise time, a ringing behavior occurred at the early time response of the cylinder due to the spatial resolution of the FDTD lattice not being fine enough to sample accurately the higher frequencies contained in the $A = 5 \times 10^9$ excitation pulse spectrum. This ringing behavior can be eliminated by using a spatial step $\Delta \approx \lambda_{min} / 20$, where λ_{min} is the wavelength of the highest frequency in the incident pulse frequency spectrum. For other values of A the FDTD lattice spatial resolution was adequately fine. At late times, where the incident pulse reaches a steady value of $E_z = 1.0 \ V/m$, the field response at locations (*1 & 5*) reaches a steady value of $H_\phi \approx 2.65 \ mA/m$, and $H_\phi \approx 0 \ mA/m$ at location (*3*) as expected[3]. Also, an observation can be made from the transient responses at observation points (*1*) and (*5*). The ringing at late times are approximately *10ns* apart, which is the time needed for a monochromatic pulse traveling in a medium having an $\epsilon_r = 4$ to cross twice the cylinder diameter (*1 → 5 → 1*). No accumulation of charges is observed since the conductivity $\sigma = 0$.

The field transient response of a circular cylinder illuminated by a plane wave having a step function waveform in the time–domain is computed using two–dimensional FDTD code. Both cases of conducting and dielectric circular cylinders were studied and the correspondence between the transient response and the rise time of the excitation wave at different observation points on the cylinders surfaces were investigated. An accumulation of charges causing a steady increase in the field response of the conducting cylinder is related to the cylinder having infinite conductivity and the excitation wave having infinite energy.

---

3. $H_\phi \ |_{(1)} = -\sin\phi \ |_{\phi = -90^o} \cdot H_x^{inc} = \dfrac{E_z^{inc}}{\eta_o} = (120 \ \pi \ )^{-1} = 2.65 \ mA/m. = -H_\phi \ |_{(5)}$

$H_\phi \ |_{(3)} = -\sin\phi \ |_{\phi = 0^o} \cdot H_x^{inc} = 0.$
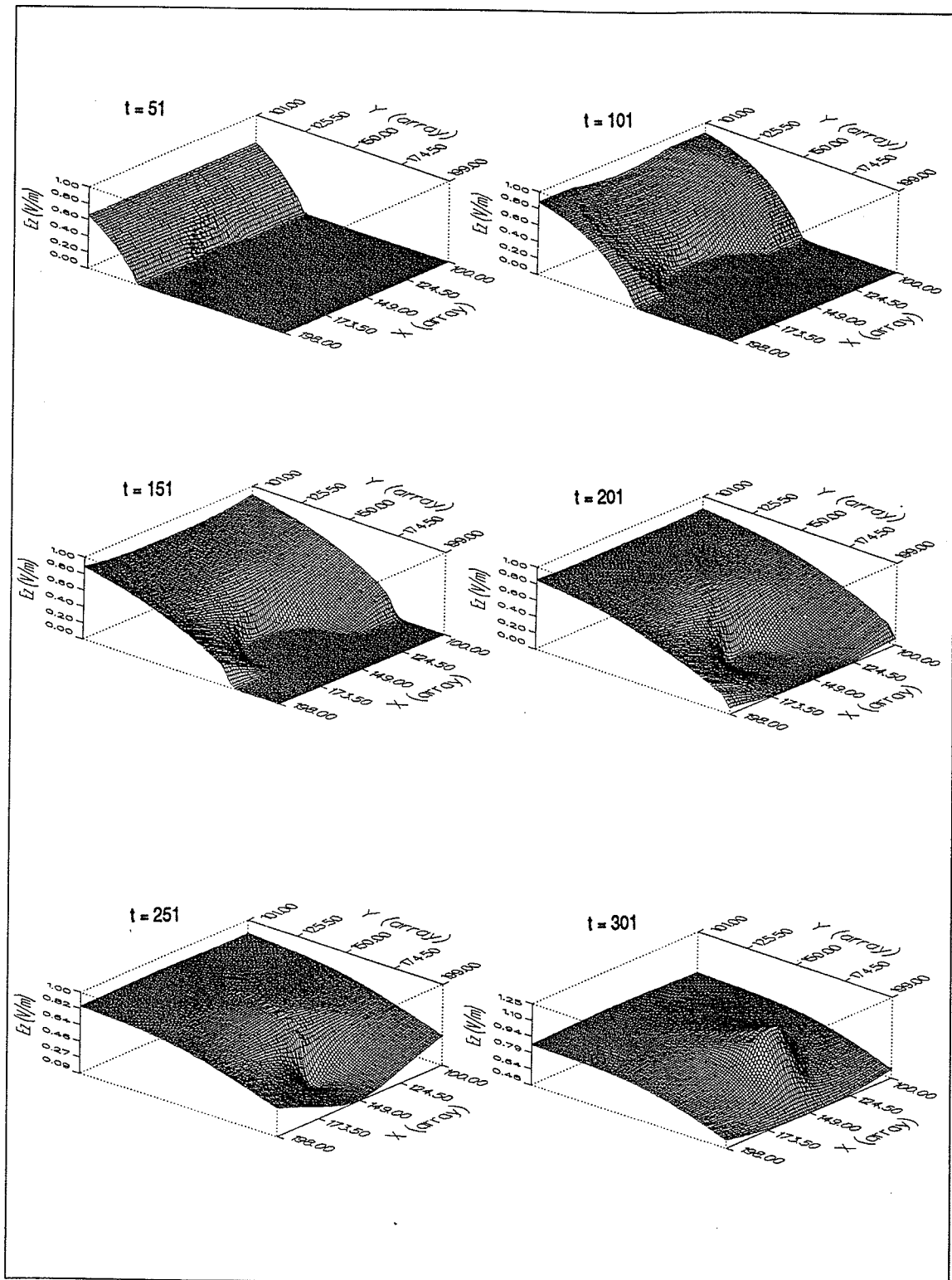

Figure 4.5   Propagation of a plane wave in the presence of a dielectric circular

cylinder, $\epsilon_r = 4$. $(A = 1 \times 10^9)$; $\Delta x = 0.0125m$, $\delta t = \dfrac{\Delta x}{2c}$
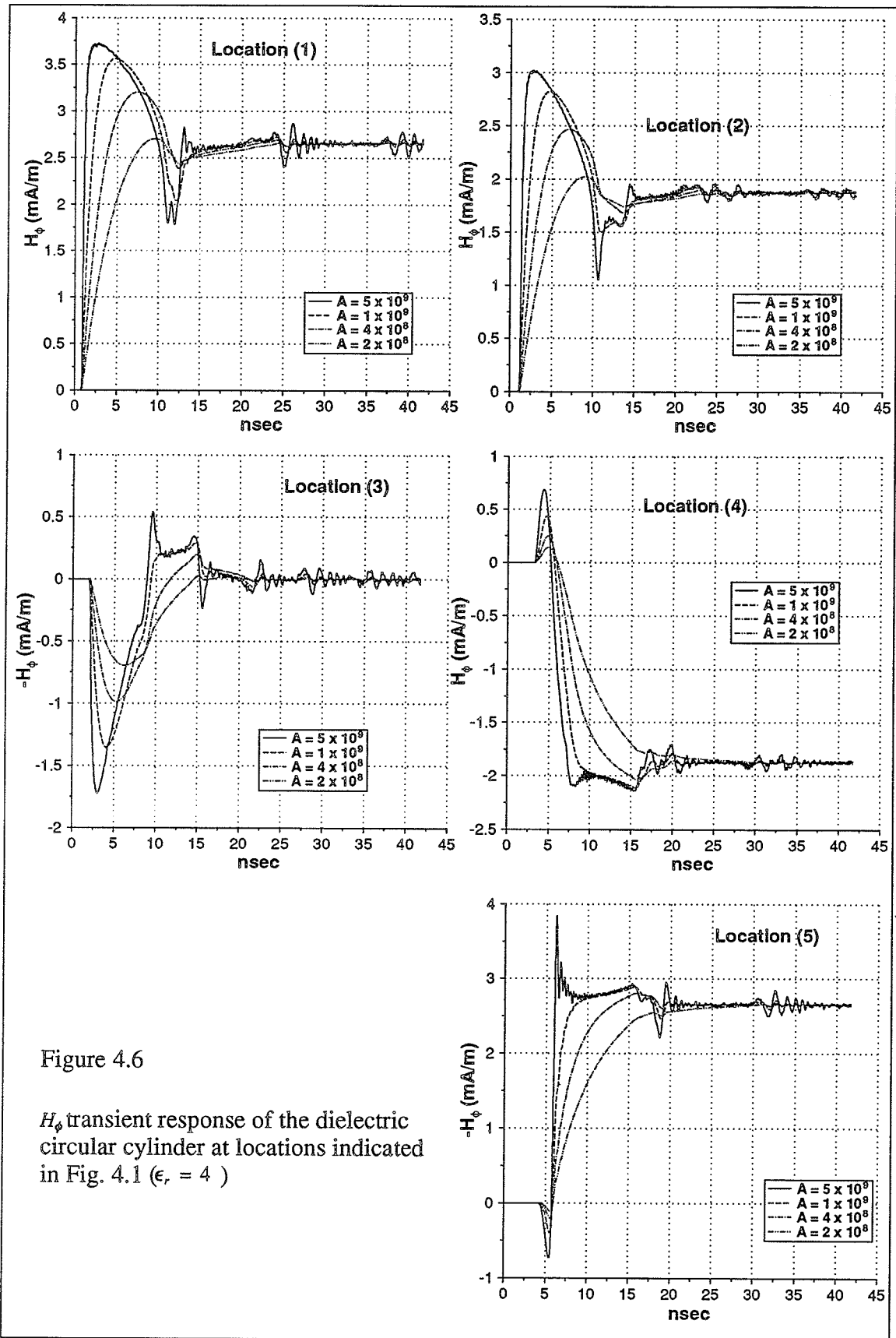
Figure 4.6

H_ϕ transient response of the dielectric circular cylinder at locations indicated in Fig. 4.1 ($\epsilon_r = 4$)
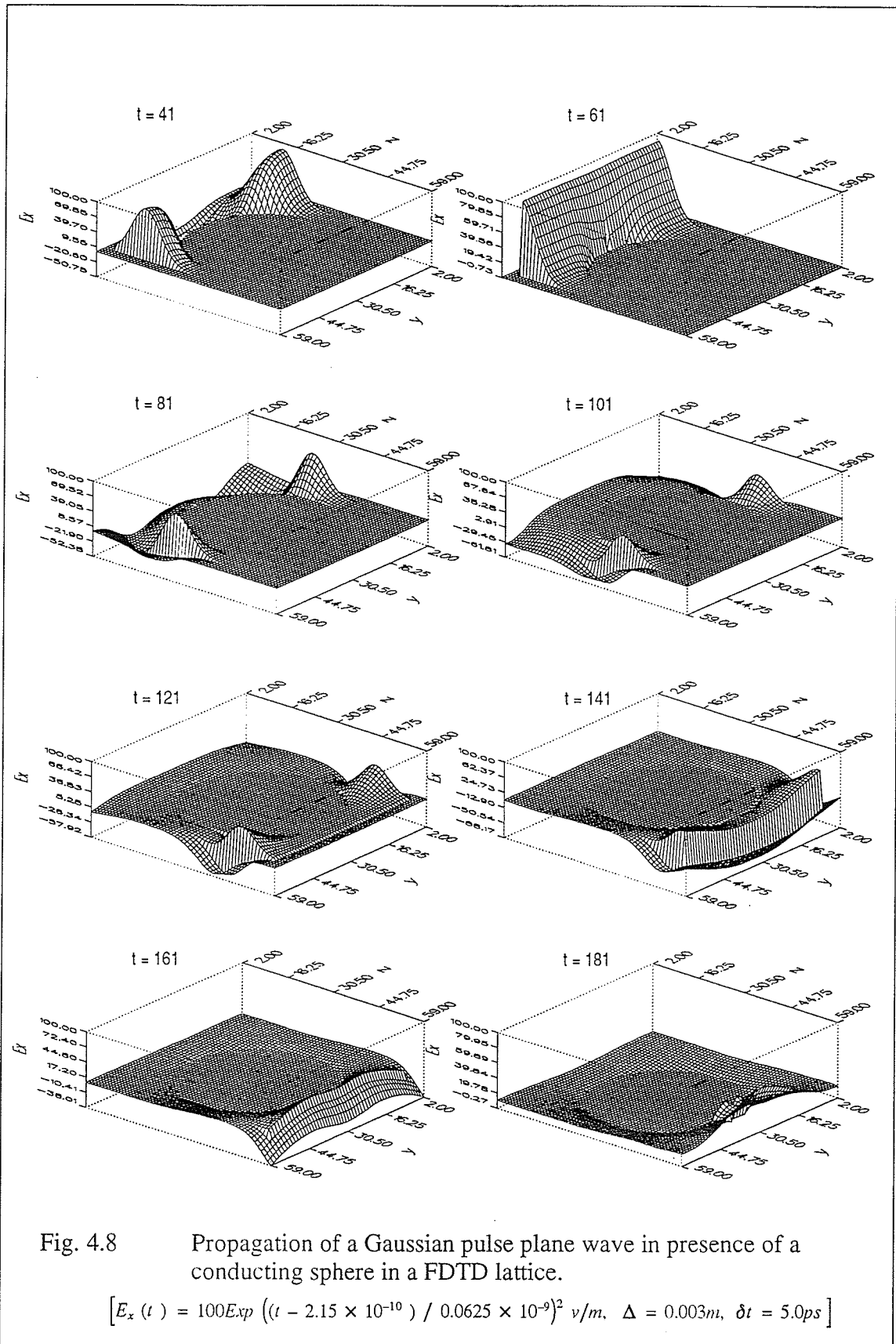
4.2. Transient Response of a Sphere

In electromagnetic scattering and radar cross section (RCS) computations the geometry of a sphere has been the attractive geometry on which new analytical and numerical techniques are generally evaluated by considering it as the test geometry that has a closed form solution. In addition, the similarity between the sphere geometry and several electromagnetic applications (sections of an aircraft and human body, rain drops, . . .) has made the sphere geometry as the popular choice for electromagnetic analysis.

In this section, the implementation of the FDTD technique in a three–dimensional space is illustrated by computing the transient fields of a sphere illuminated by a Gaussian pulse plane wave. The computed responses of a conducting and a dielectric sphere are compared with those obtained from analytical solution.

4.2.1. Results and Discussion

The geometry of the sphere considered has a radius $a=6.0cm$ and is mapped into a uniform ($60 \times 60 \times 60$) FDTD lattice. Figure 4.7 shows the sphere model used by the FDTD code and is located at the center of the lattice. The Sphere model is 40 cells through the diameter. The spatial dimension of the FDTD cell is set to $\Delta = 0.003m$, and a time increment of $\delta t = \dfrac{\Delta}{2c}$ is used, where c is the speed of light in free space. Figure 4.7 also defines the coordinate system and the incident field polarization used in the FDTD code. The sphere is illuminated by a plane wave of Gaussian field distribution propagating in the $z-$direction. The transient response due to the incident pulse is obtained at different observation points on the sphere structure. To validate the results obtained by the FDTD code, the computed results are compared with similar results computed using the Rayleigh–Mei solution for a sphere [79]. It should be noted that the Rayleigh–Mei expressions are in frequency–domain. time–domain data is obtained using the inverse Fourier Transformation. Applying the convolution theorem on the Rayleigh–Mei data and on an incident plane wave identical to that used in the FDTD code the proper transient responses are obtained, this procedure is explained in Appendix A. The cases of a perfectly conducting and dielectric sphere are considered [80,81].

i) *Conducting Sphere.*

The conducting sphere is illuminated by assigning a very high conductivity ($\sigma = 99 \times 10^{25}$ s/m) at the nodes representing the sphere. Figure 4.8 shows the propagation of the Gaussian pulse plane wave in the presence of the conducting sphere. The E_x field component at a plane passing through the middle section of the sphere is plotted for different time steps.

Fig. 4.7 FDTD model of a sphere with the incident field and observation Points indicated.

Figure 4.9(a–c) compares the FDTD and the Rayleigh–Mei solutions for the transient tangential magnetic field component at locations on the sphere indicated in Fig. 4.7 showing

a good agreement between the two procedures. At the illuminated pole (location *1*) the field response reached a peak value of approximately *0.53 A/m* which is twice the incident field value. The response at later time, after the pulse has passed the sphere, is due to the surface currents on the sphere bouncing back to location (*1*) with a lower magnitude due to radiation. The slight disagreement in Fig. 4.9b between the two solutions is due to the location of observation point (2) in the shadow region of the sphere where the incident field is minimum, and also due to the simulation of the curved surface of the sphere by a stepped edge surface which introduced diffracted fields that interfered with the main field computations.

Fig. 4.8   Propagation of a Gaussian pulse plane wave in presence of a conducting sphere in a FDTD lattice.

$$\left[E_x\,(t\,) \;=\; 100 Exp\,\left((t - 2.15 \times 10^{-10}\,) \,/\, 0.0625 \times 10^{-9}\right)^2\; v/m,\quad \Delta \;=\; 0.003m,\quad \delta t \;=\; 5.0 ps \right]$$

66

location (1) $(\theta = \pi, \phi = -\pi / 2)$

(a)

location (2) $(\theta = 0, \phi = \pi / 2)$

(b)

location (4) $(\theta = \pi / 2, \phi = \pi / 2)$

(c)
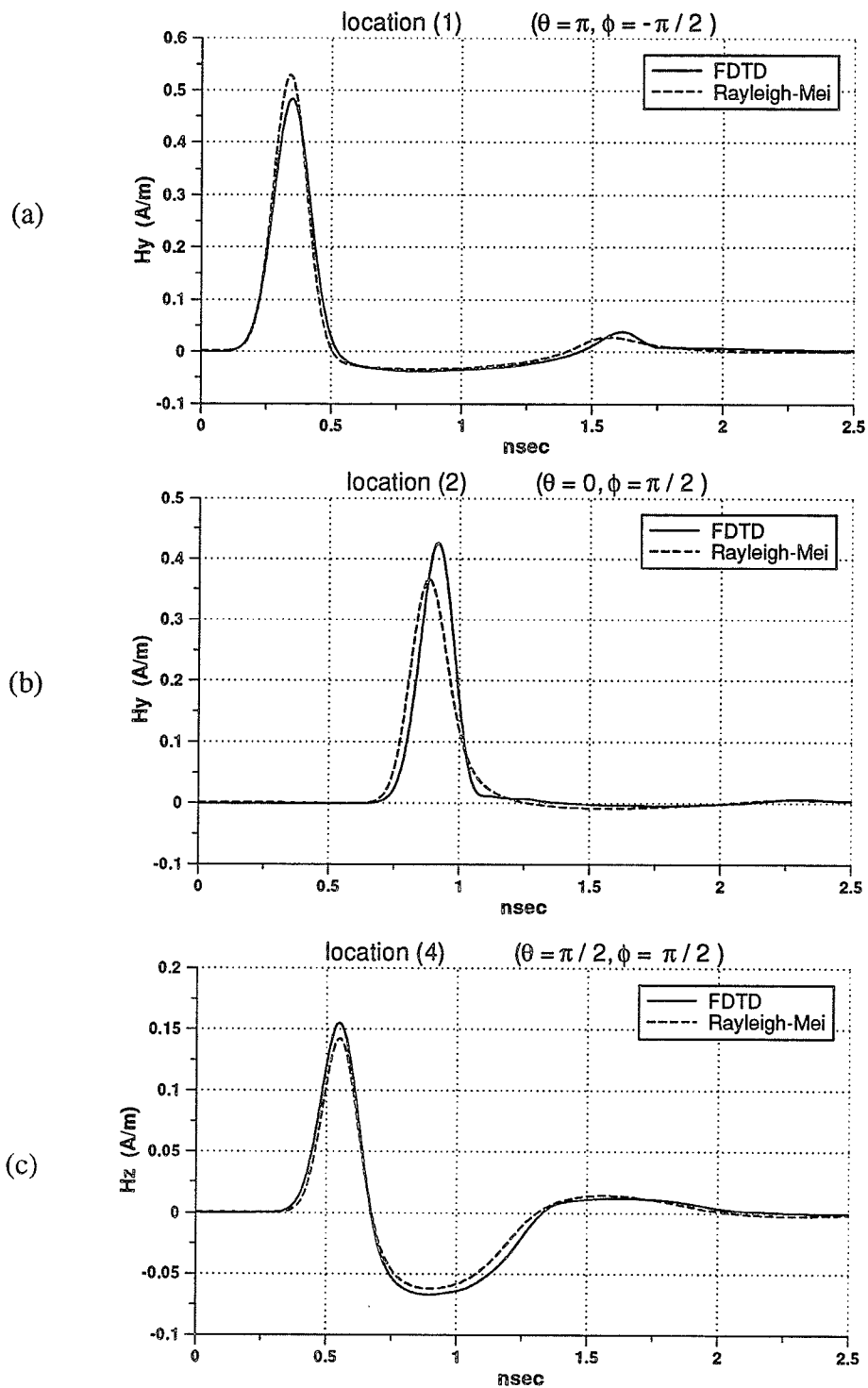
Fig. 4.9   Transient response of a conducting sphere.

$$\left[E_x (t) = 100 Exp \left((t - 1.52 \times 10^{-8}) / 0.1 \times 10^{-9} \right)^2 \ v/m, \quad \Delta = 0.003m, \quad \delta t = 5.0 ps \right]$$

ii) Dielectric Sphere.

The same sphere geometry of Fig. 4.7 is again used but with the physical parameters as ϵ_r, $\mu = 1$, and $\sigma = 0$. Figure 4.10 shows the scattering of a Gaussian pulse plane wave by the dielectric sphere. In this figure the E_x field component at a plane in the middle section of the sphere, with $\epsilon_r = 5.0$, is plotted for different time steps. From these surface plots the penetration of the electromagnetic fields inside the dielectric sphere is at lower speed than the original pulse in free space. Also, due to the curvelinear geometry of the sphere a focusing phenomena is observed where a peak value of $E_z \approx 200$ V/m ($E_z^{inc} = 100$ V/m) is also observed at time step $t = 181$. The trapped wave inside the sphere (after the incident pulse has passed the sphere) will keep bouncing back and forth due to the media mismatch at the dielectric sphere–free space interface. This phenomena is recorded in Fig. 4.11a showing the field response at location (*1*). The trapped wave will eventually attenuate due to the radiation to free space each time the trapped wave hits the dielectric sphere–free space interface. Figure 4.11(a–c) compares the FDTD and the Rayleigh–Mei solutions for the transient tangential magnetic field component at locations on the sphere, with $\epsilon_r = 5.0$, showing a good agreement between the two computations.

Fig. 4.10   Propagation of a Gaussian pulse plane wave in presence of a dielectric sphere in a FDTD lattice. ($\epsilon_r = 5.0$, $\mu_r = 1.0$, $\sigma = 0$)

$$\left[E_x(t) = 100 Exp\left((t - 2.15 \times 10^{-10}) / 0.0625 \times 10^{-9} \right)^2 \, v/m, \quad \Delta = 0.003m, \quad \delta t = 5.0ps \right]$$

t = 201

t = 221

t = 241

t = 261

t = 281

t = 301

t = 321

t = 341

Fig. 4.10 contd.

Fig. 4.11 Transient response of a dielectric sphere. ($\epsilon_r = 5.0$, $\mu_r = 1.0$, $\sigma = 0$)

$$\left[E_x(t) = 100 Exp\left((t - 1.52 \times 10^{-8}) / 0.1 \times 10^{-9} \right)^2 \, v/m, \quad \Delta = 0.003m, \quad \delta t = 5.0ps \right]$$
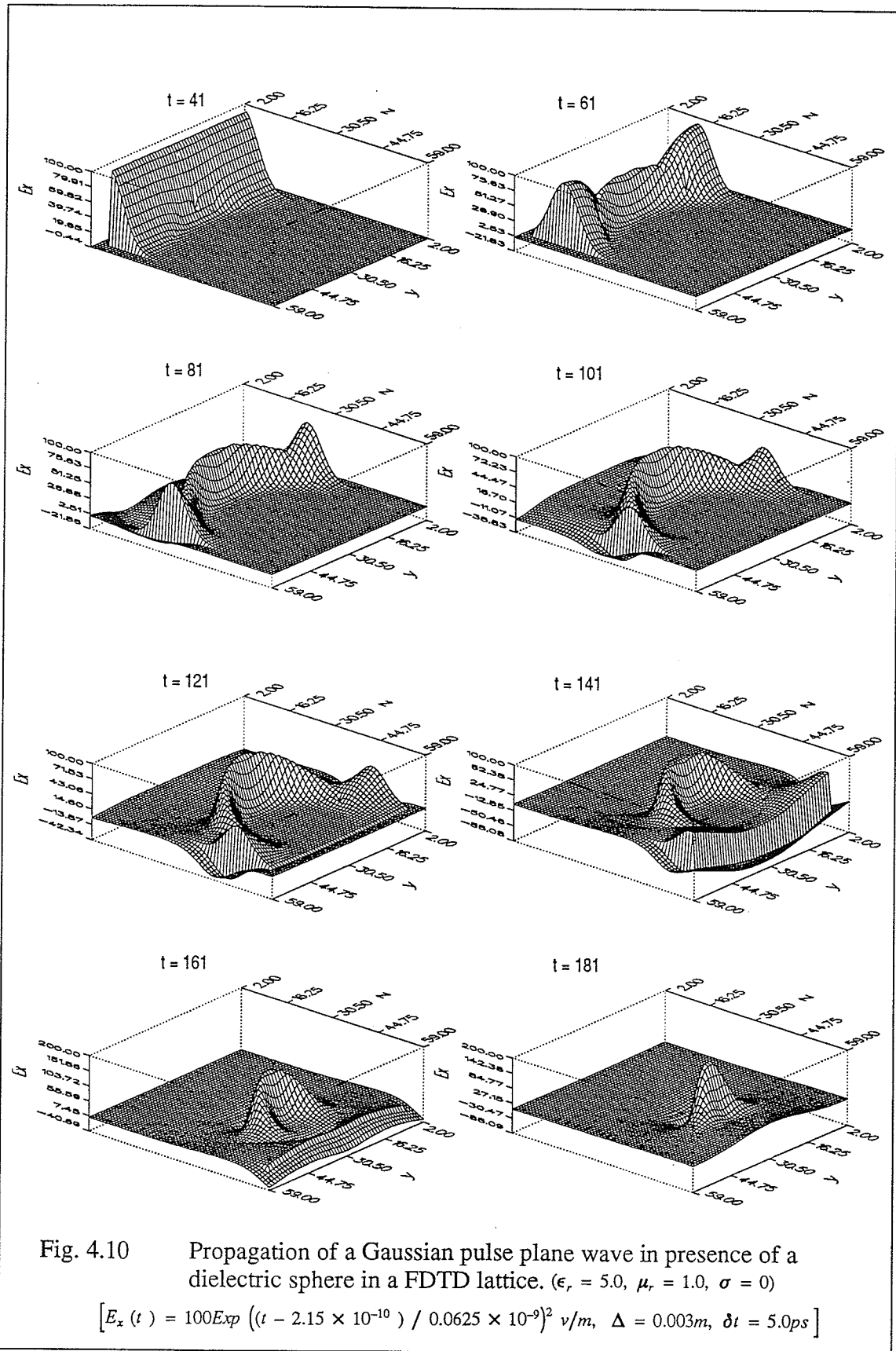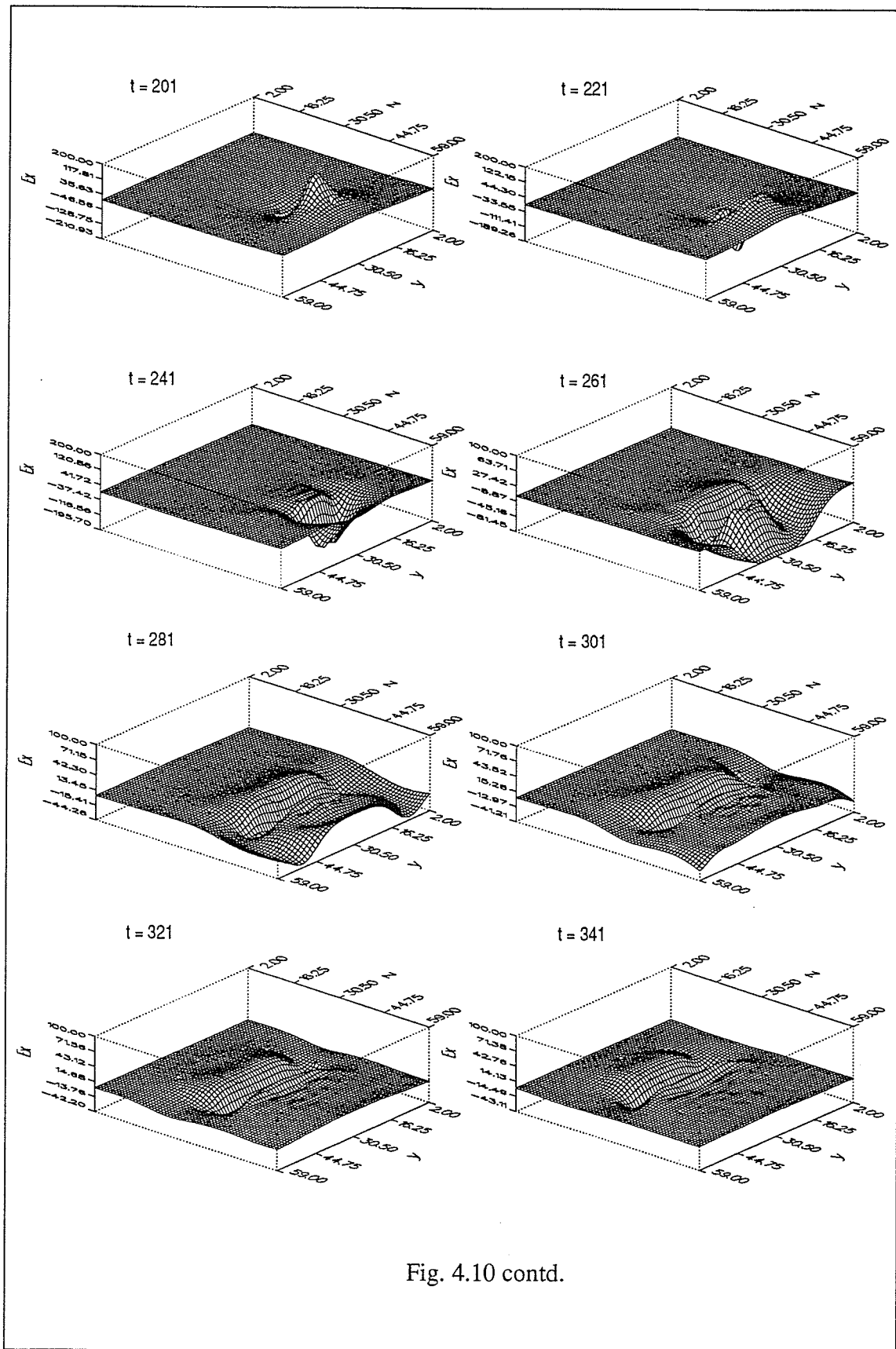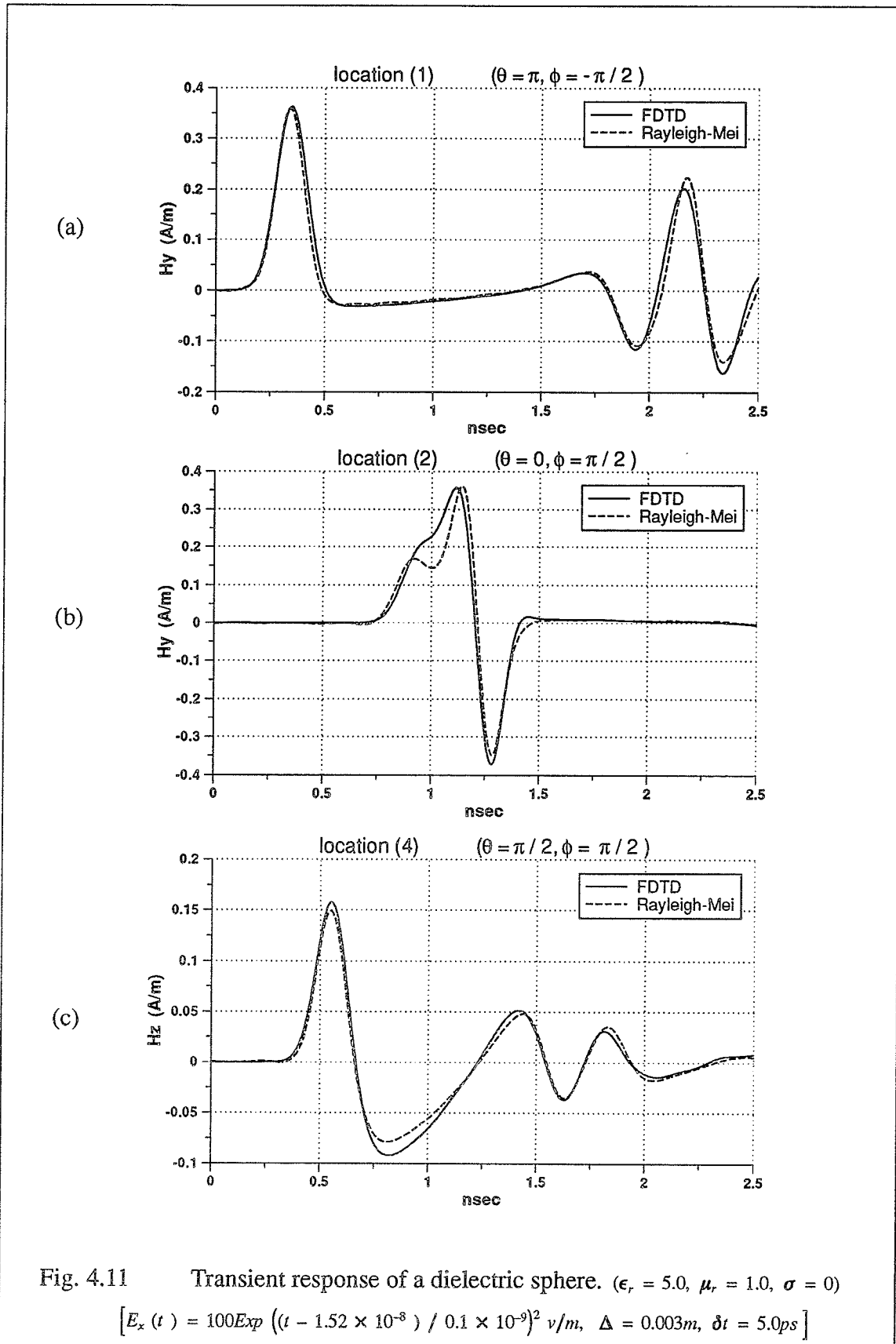
The transient response on the surface of a sphere illuminated by a Gaussian pulse plane wave, is computed for the cases of a conducting and dielectric spheres using the FDTD method. The results are compared with the analytic solution of Rayleigh and Mei with the aid of inverse Fourier transformation. A good agreement between the results obtained by the two methods is observed. The discrepancy in the two solutions observed at the shadow region of the conducting sphere can be attributed to the simulation of the curved surface of the sphere by a stepped edge surface which introduced diffracted fields that interfered with the main field computations. Also, the relatively low magnitude of the incident field in the shadow region allowed fields reflected from the lattice boundary to further degrade the field computation in that region.

4.3. Study of Transient Field Penetration inside a Conducting Box.

The effect of impulsively excited electromagnetic bursts, resulting from lightning or man made sources, on electronic equipment, devices and installations have raised the interest in electromagnetic transient response field penetration and coupling into complex structures. The analysis of electromagnetic interaction with such complex structures is difficult to achieve analytically since, generally, the geometry of such structures will not match with the known orthogonal coordinate system. In this case the problems will be limited to structures whose surface coincide with the coordinate surface of a separable coordinate system.

With the advent of digital computers capabilities that can keep track of the geometrical details of a body in addition to any associated numerical computations, developed numerical techniques capable of solving electromagnetic interaction problems are only limited by the characteristics of the formulation, the storage capability and speed of the computer. The problem of the penetration and coupling of electromagnetic energy through apertures has been studied extensively by many researchers that used both analytic and numerical techniques [82–84] using the Method of Moments (MoM) [85]. The Finite Difference–Time Domain (FDTD) numerical technique is also used to study electromagnetic penetration and coupling problems [42,43,61,98].

In this section the transient electromagnetic field penetration inside a cubic conducting box with an open top illuminated by a doubly–exponential plane wave is investigated using the FDTD numerical method. This investigation also involved the study on the effect of modifying the conducting box aperture, as well as, the addition of absorbing materials on the transient field inside the box which includes transient and spectral information.

i) Modeling of Structures.

Generally, modelling of structures inside the FDTD lattice is done by allocating the corresponding physical parameters that characterize the structure at locations defined by the grid nodes matching with the structure geometry. Structures made up of conducting plane surfaces are modelled by setting the electric field components lying in these planes to zero at all times. Open planer surfaces having a small physical thickness are modelled as 'infinite-

ly thin' conducting sheets. Curved surfaces are modelled inside the FDTD lattice either by a stair case surface or by using techniques that allocate specialized cells to conform with the surface curvature [7,24]. In the case of inhomogenoeus structures, no special handling of electromagnetic boundary conditions at the media interface is required, because the curl equations generate these conditions naturally.

The FDTD method can be used in an efficient way if structures involved have geometrical symmetry. Utilizing such symmetry will reduce the memory storage requirement that will reduce, in turn, the computation time of the problem. The symmetry conditions applied inside the FDTD lattice is done by implementing the concept of electric walls ($E_{\tan} = 0$) or magnetic walls ($H_{\tan} = 0$) as the planes of symmetry in the modeling procedure. The choice of either magnetic or electric walls as symmetry planes will depend on the polarization of the incident plane wave used to illuminate the modelled target. The characteristics of the electric and magnetic walls and the procedure to implement them is illustrated in Fig. 4.12.
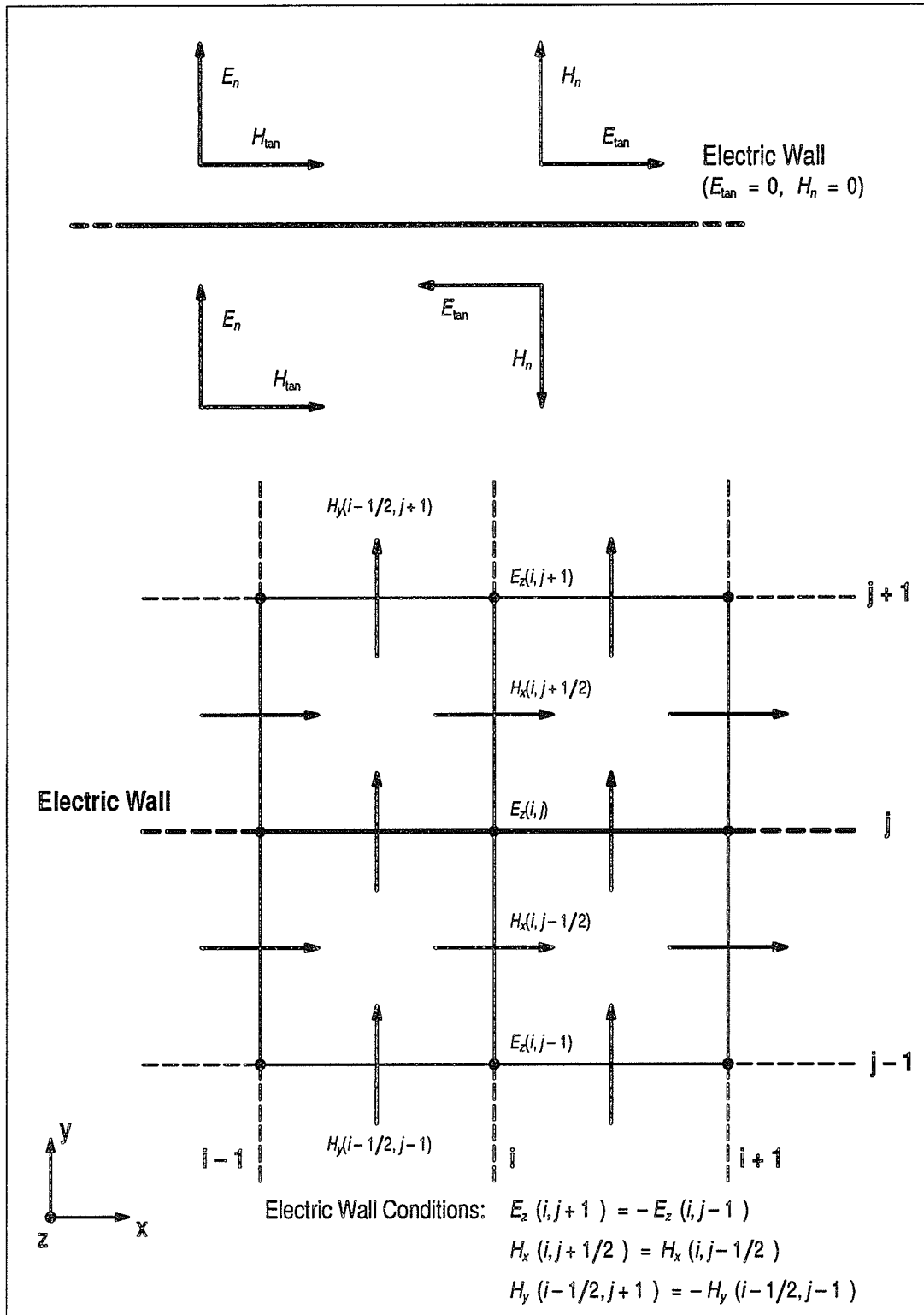
Fig. 4.12a Conditions and procedure for implementing an Electric Wall. (*TM*, 2–d case)
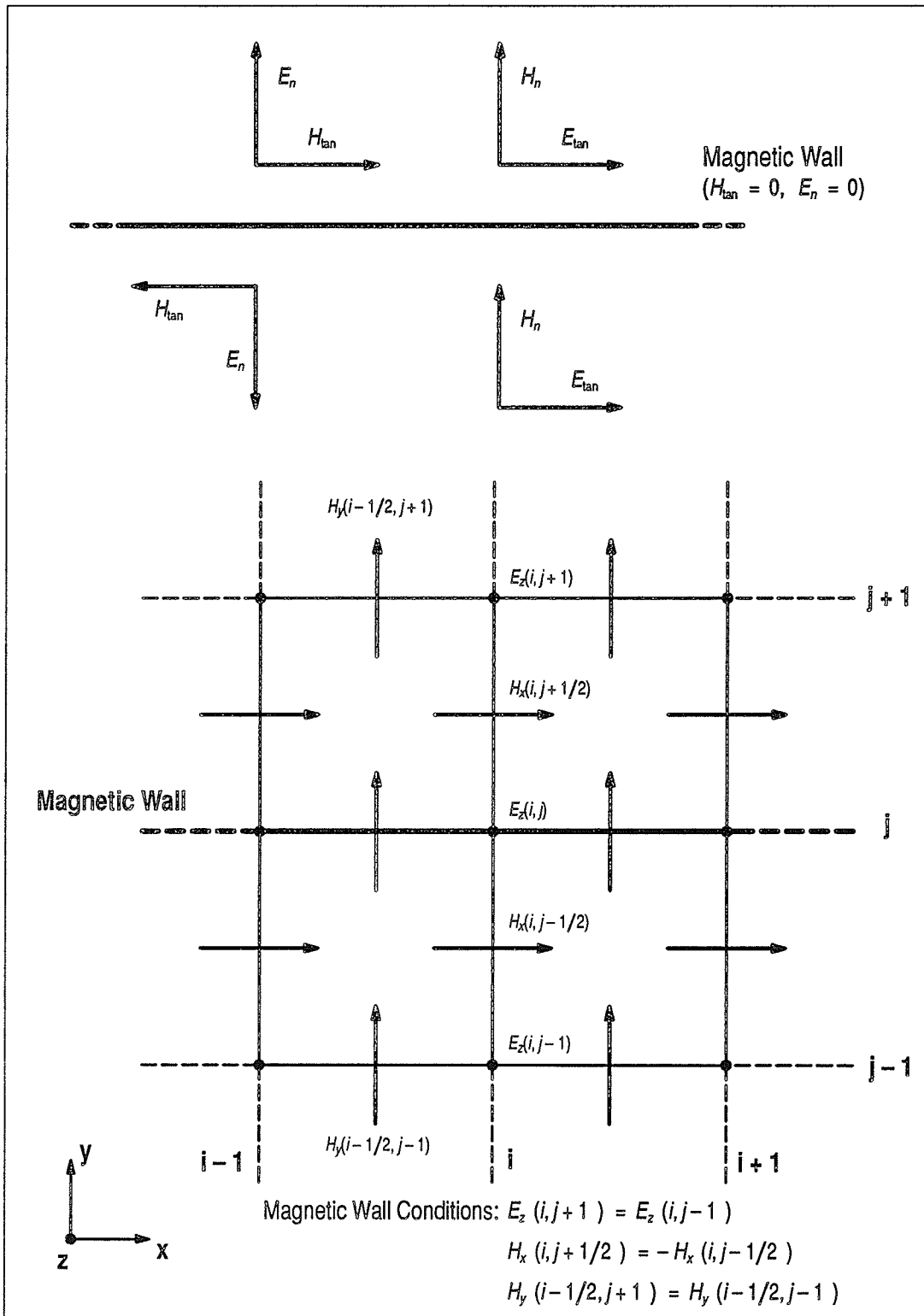
Fig. 4.12b   Conditions and procedure for implementing a Magnetic Wall. (*TM*, 2–d case)

4.3.1. Numerical Results and Discussion

The electromagnetic transient field penetration inside a cubic conducting box with an open top is studied using the FDTD method. The geometry and dimensions of the conducting box is shown in Fig. 4.13. The box structure is illuminated by an x–polarized plane wave having a doubly–exponential time distribution, and is propagating in the $+\hat{a}_z$ direction. The plane wave time distribution is expressed by

$$E_x(t) = AV\ t\ (\ e^{at} - e^{bt}\ )\ \ Volts/m \tag{4.4}$$

where

$$AV = 9 \times 10^9\ V/(m.sec)$$

$$a = -6 \times 10^8\ sec^{-1}$$

$$b = -9 \times 10^8\ sec^{-1}$$
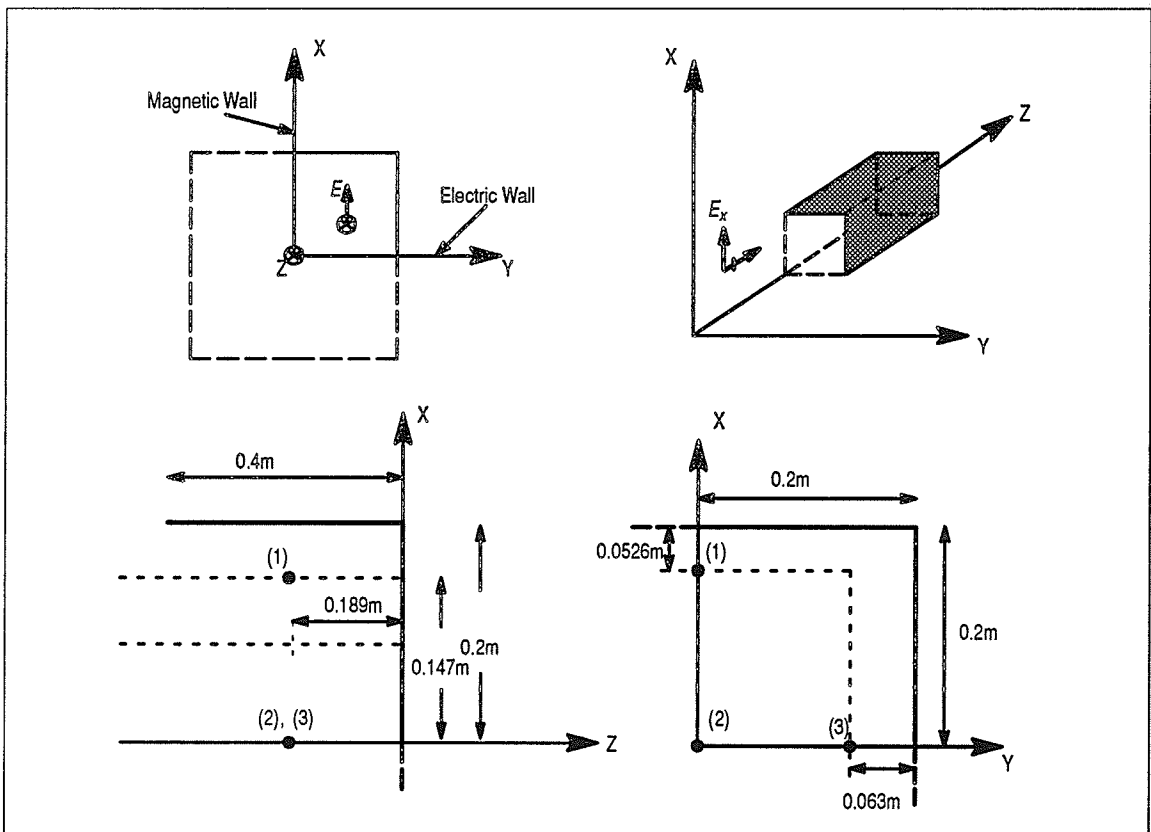
Fig. 4.13   Geometry of a cubic box with an open top.

the corresponding wave form together with its frequency spectrum are shown in Fig. 4.14 The symmetry inherent in the box geometry is utilized and only one–quarter of the box is modelled inside the FDTD lattice. Considering the polarization of the incident plane wave, electric and magnetic walls are used as symmetry planes as shown in Fig. 4.13. The conducting box is mapped with a 'zero' wall thickness into a uniform FDTD lattice of $(40 \times 40 \times 80)$ array size. A spatial increment of $\Delta = .02105m$, and a time increment of $\delta t = \dfrac{\Delta}{2c}$ are used. The FDTD lattice zoning procedure of [13] that separates the lattice into total–field and scattered–field regions is adopted.
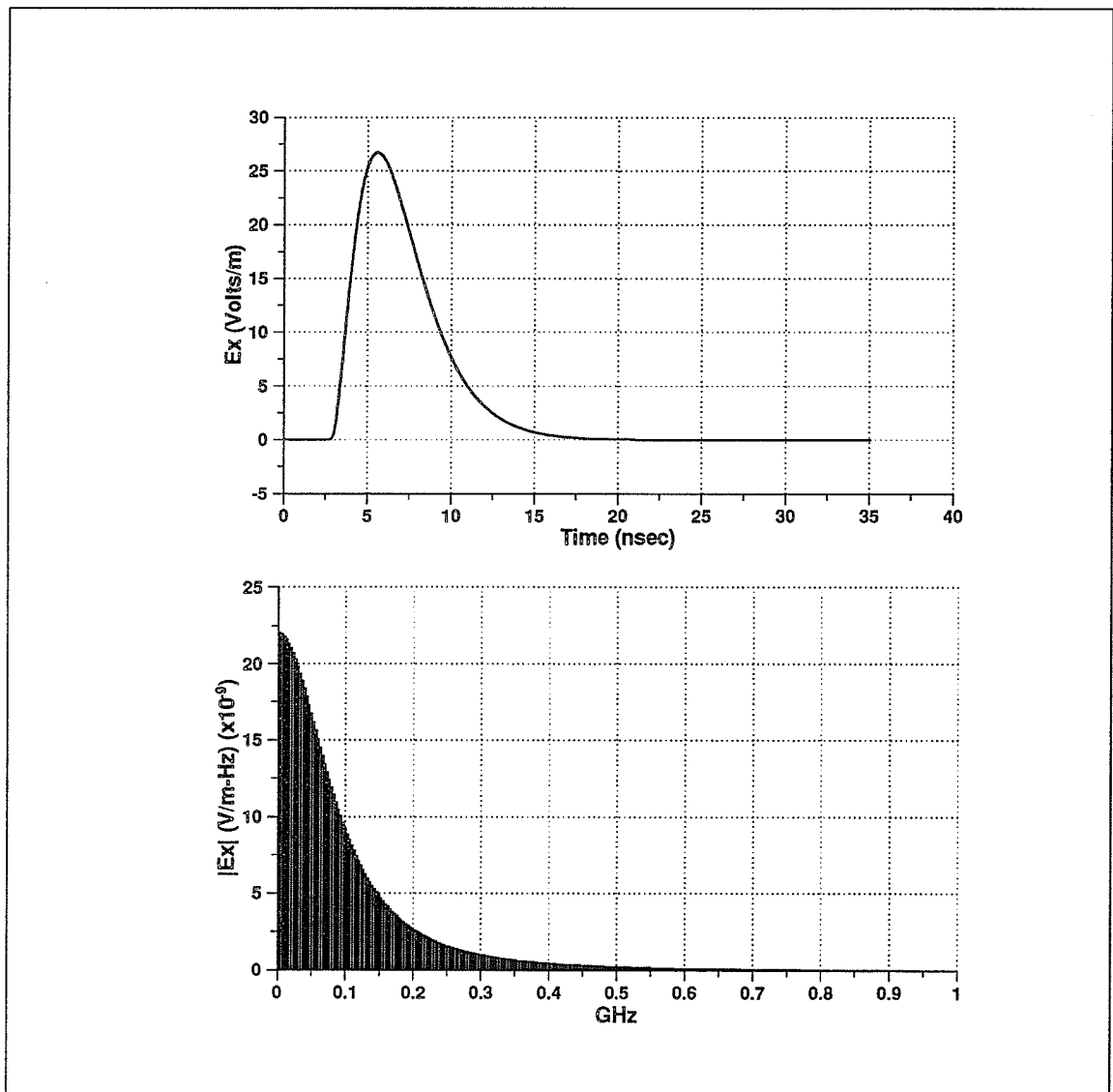
Fig. 4.14 Wave form and frequency spectrum of the incident excitation plane wave. (Doubly–Exponential).

ii) Conducting Box

The E_x transient field components are computed at locations inside the conducting box shown in Fig. 4.13. Figure 4.15 shows the E_x transient response at locations (1), (2) and (3) inside the box due to the doubly-exponential plane wave illumination. At location (1), the magnitude of the field response is the largest due to the plane wave x–polarization that caused higher diffracted field magnitudes to occur at the box edge closer to location (1). Figure 4.16 shows the frequency response of the field at location (2) obtained using the Discrete Fourier Transformation (DFT) procedure (Appendix B). The half wave length resonance of the conducting box used ($f_o \approx \left(\dfrac{c}{2l}\right) = 0.375GHz$) is also observed in Fig. 4.16.

Our numerical experiment involves the study on the effect of modifying the conducting box aperture on the transient field penetration inside the box when illuminated by a doubly–exponential plane wave which is similar in wave form to Electromagnetic Pulse (EMP) resulting from lightning or man made sources. The aperture geometries involved in this analysis are shown together with their corresponding dimensions and aperture areas in Fig. 4.17. The choice of these aperture geometries is based on the knowledge that the main source of fields inside the conducting box are those due to the diffraction of fields on the box edges. Hence, the length and orientation of such edges are the variable parameters in this study. In Fig. 4.17 the modified aperture boxes are denoted by 'box_a', 'box_b', 'box_c', 'box_d', and 'box_e' respectively, 'box' corresponds to the unmodified aperture conducting box.

Figure 4.18a shows the E_x transient field response at location (2) inside the conducting box for different aperture geometries. This figure shows that the field magnitude is reduced significantly at the early time of the response especially with 'box_b' design corresponding to a smaller aperture area. Although using these aperture geometries has resulted in reduced transient field magnitude at the early time as compared to 'box', they also resulted in resonance phenomena with different transient field decay rates for each of the box geometries used. 'box_b' geometry, which has the smallest aperture area as compared to that of 'box' and 'box_a', resulted in the slowest transient field decay rate. This behavior can be explained in that the stored energy within 'box_b' takes longer time to dissipate in the form of radiation losses which is the only loss involved in this study. To investigate the effect of

aperture areas and geometries used on the transient field decay rate inside the boxes, the time–stepping is continued for a sufficiently long time whereby all field resonance behavior would have died down. Figure 4.18b shows the E_x transient response at observation point (2) of the box geometries in Fig. 4.18a computed for relatively long time. From these figures one can observe that the aperture geometries that resulted in the reduction in the magnitude of the early time field response resulted also in a slower resonant field decay, specifically, for the 'box_b' case.

Using the Discrete Fourier Transformation (DFT), the frequency response at location (2) inside the box geometries considered are calculated and are shown in Fig. 4.19. These plots show that the cubic conducting boxes became more frequency selective with aperture geometry modified.
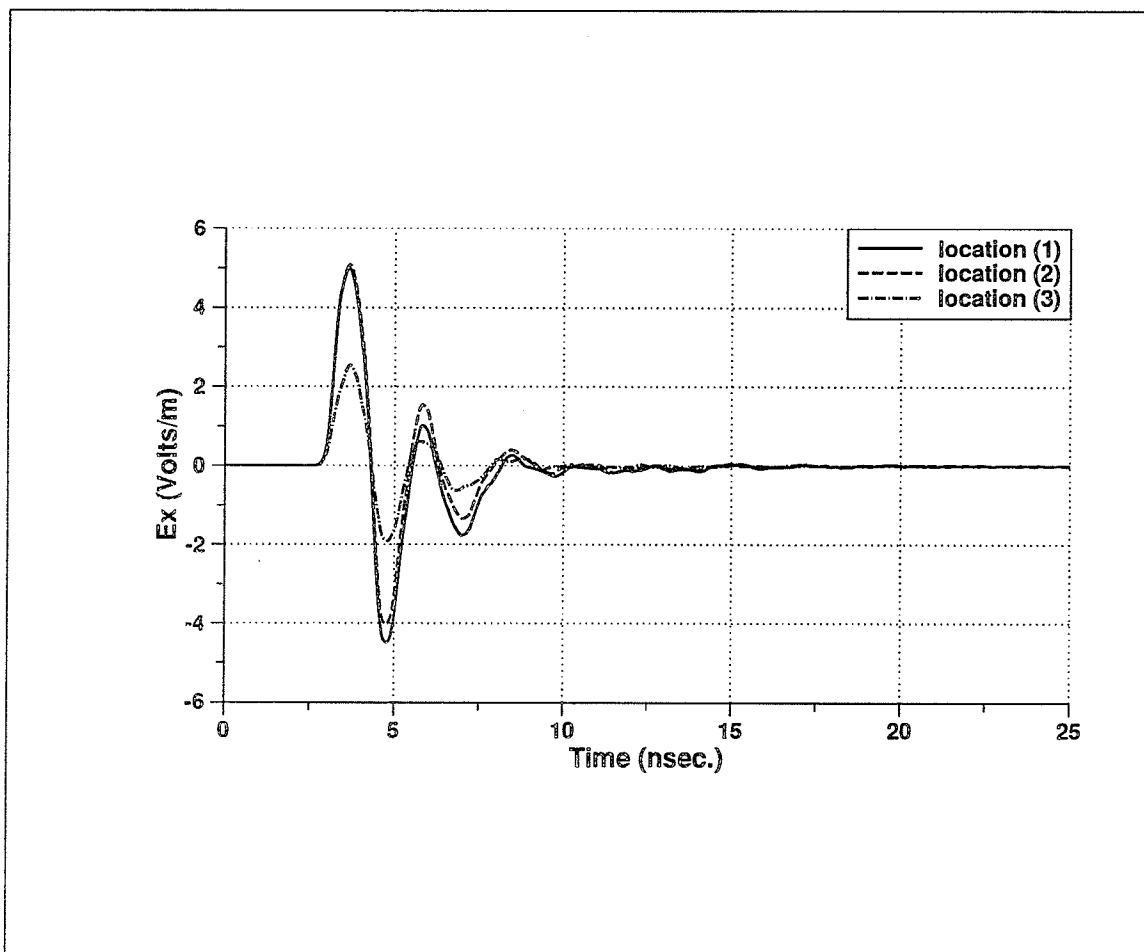
Fig. 4.15   transient response inside the conducting cubic box at locations (1), (2), and (3).
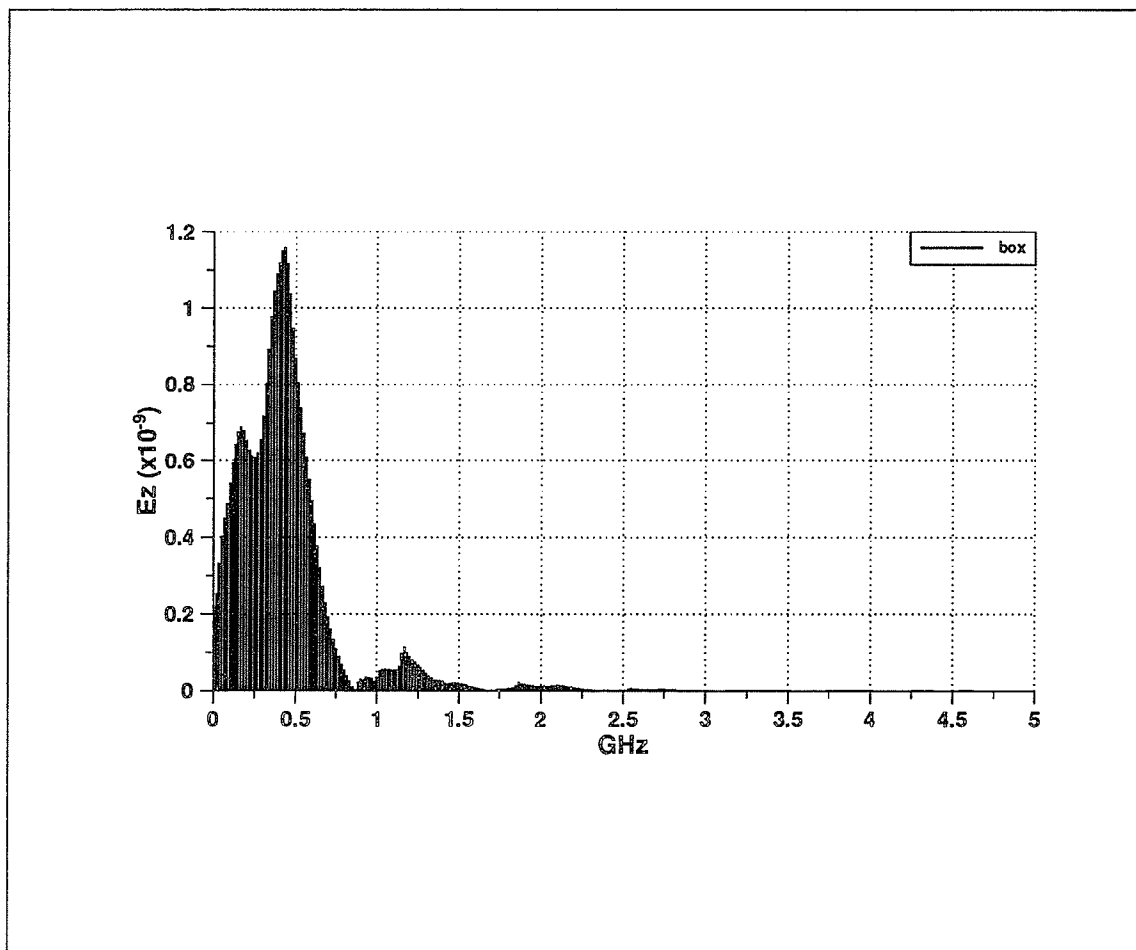
Fig. 4.16   Frequency field response of the conducting cubic box at location (2).
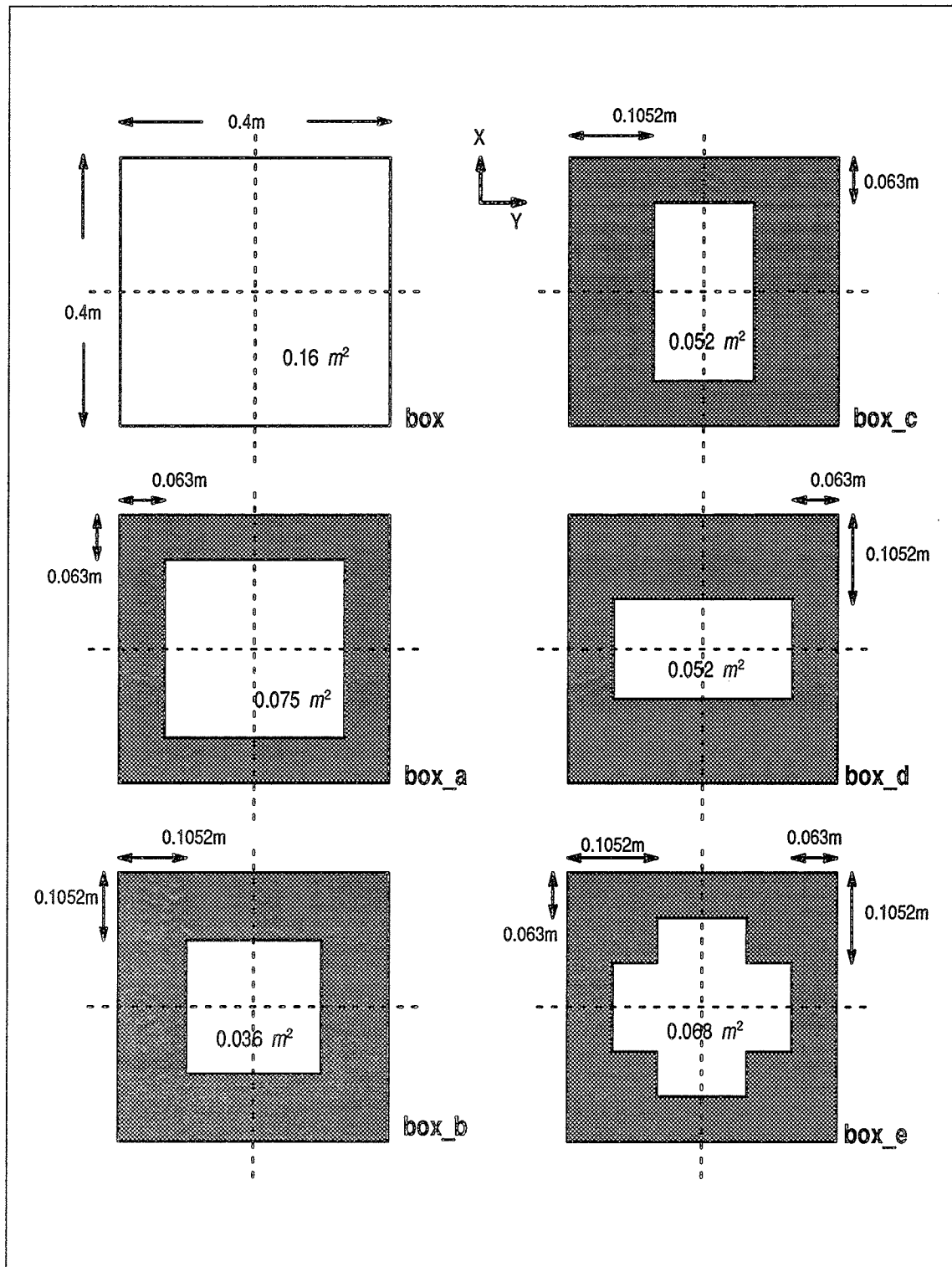
Fig. 4.17   Aperture geometries and dimensiona of the modified boxes.
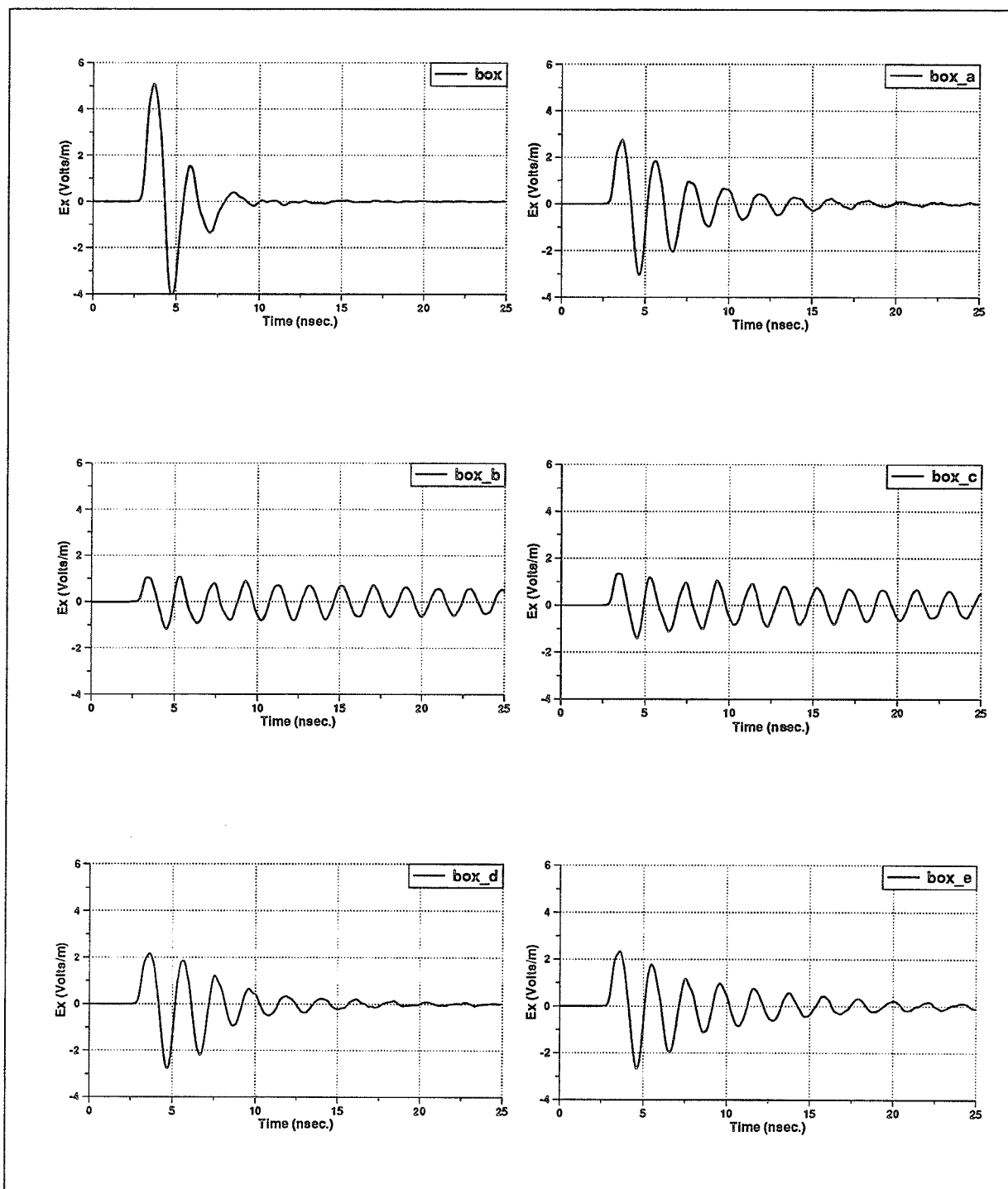
Fig. 4.18a E_x transient response inside the conducting boxes of Fig. 4.17 at location (2).
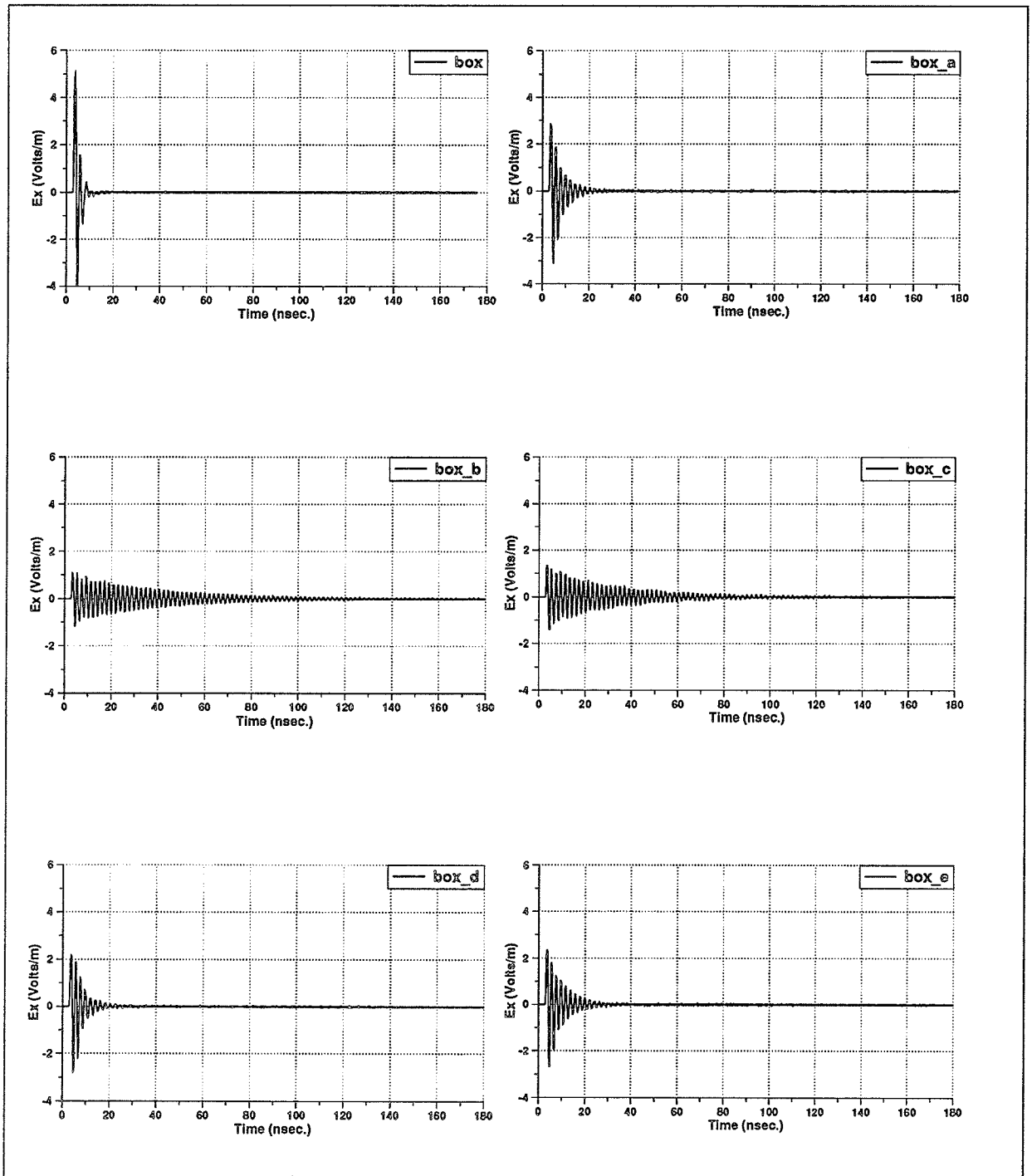
Fig. 4.18b E_x transient response inside the conducting boxes of Fig. 4.17 at location (2) computed for a relatively long time.
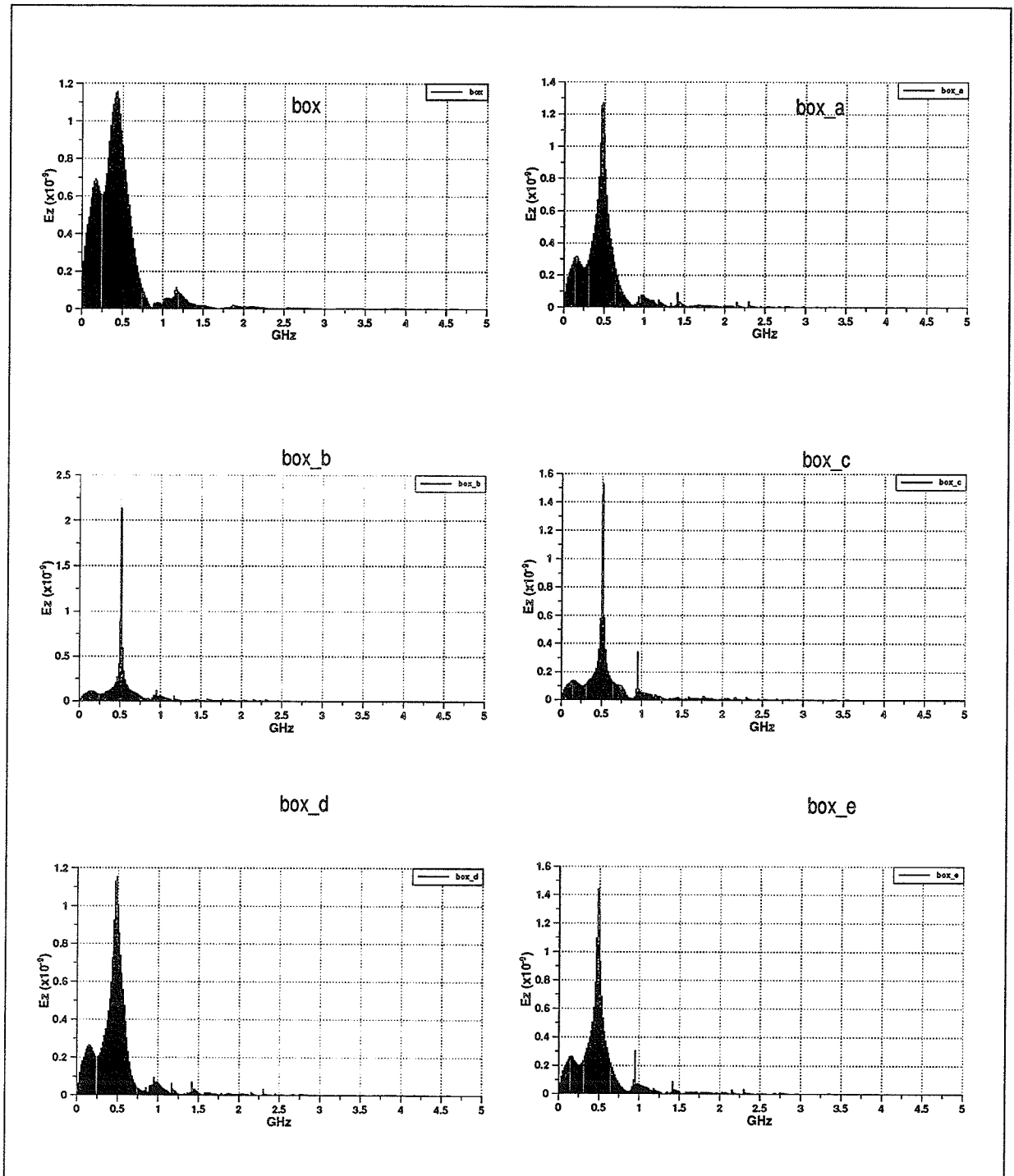
Fig. 4.19   Frequency response of the field at location (2) inside the box geometries of Fig. 4.17 $\left(\Delta f = 16.6 MHz\right)$

iii) Addition of Absorber Material.

In this sub–section, the study of field penetration inside a conducting box is extended to include the effect of adding absorbing material on the walls of the conducting box.

The addition of absorbing material on the inner and outer walls of the conducting box is another parameter considered to reduce the field magnitude inside the conducting box [86,87]. The absorber material modeled is that similar to an Eccosorb lossy material used in anechoic chambers and have the following physical parameters:

$$\epsilon_r = 10$$

$$\mu_r = 1.3$$

$$Loss\ Tangent\ \left(Tan\delta\right) = 0.3$$

$$\sigma = \left(5.5 \times 10^{-11}\right)\left(\epsilon_r\ Tan\delta\right).f\ ; \qquad 1GHz \leq f \leq 30GHz$$

The absorbing layer is modeled in the FDTD code by setting the corresponding parameters of the absorber to each cell in the FDTD lattice comprising the absorber geometry with $\sigma = 0.165\ s/m$ for $f = 1GHz$. An absorber layer of one FDTD cell $\left(\approx 2.1cm\right)$ is used.

Four cases of the conducting box with an absorber layer on its surfaces are studied. The first case where an absorber layer is added on the conducting part of the box top as shown in Fig. 20a and is referred to as 'absrb_1' case. The second case is similar to that of 'absrb_1' but with the absorber layer covering all the top surface of the conducting box as shown in Fig. 20b and is referred to a 'absrb_2' case. The third case is similar to 'absrb_1' case but with all the inner walls of the conducting box covered with a one cell thick absorber and is referred to as 'absrb_3' case. 'absrb_4', which is the fourth case investigated, correspond to the 'absrb_2' case but with the inner walls covered with a one cell thick absorber.
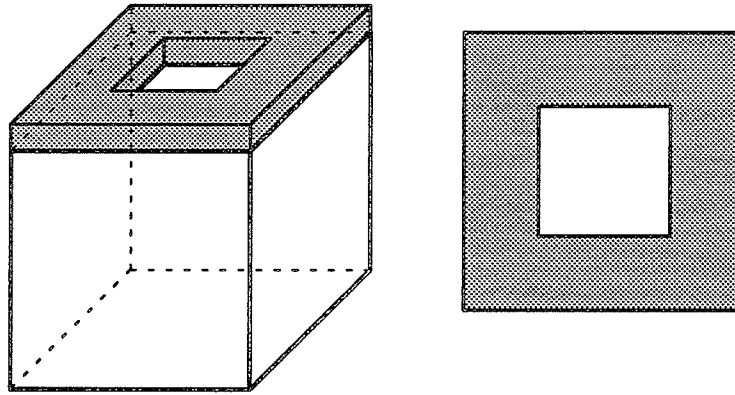
Figure 4.20a   Box with absorber material 'absrb_1' case
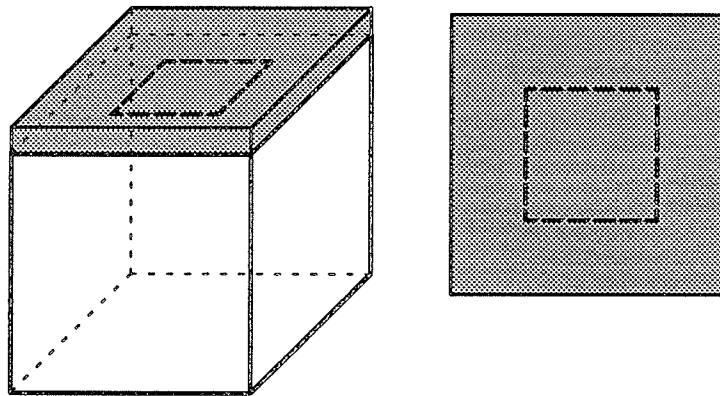$$\left(\epsilon_r = 10, \ \mu_r = 1.3, \ \sigma = 0.165\right)$$

Figure 4.20b   Box with absorber material 'absrb_2' case
$$\left(\epsilon_r = 10, \ \mu_r = 1.3, \ \sigma = 0.165\right)$$

The above four cases are applied to the conducting boxes of modified aperture geometry of Fig. 4.17 . Using the FDTD code the field transient response at location (2) inside the conducting boxes illuminated by the doubly exponential plane wave of eq. (4.4) is calculated. Figure 4.21 shows the E_x transient field response for the four absorber cases applied on 'box_a' geometry. For the 'absrb_1' case, there is no change at early time but it resulted in a faster decay of the field magnitude, and is decayed even faster when adding absorber layers at the inner box walls in the 'absrb_3' case. Covering all the top side of the conducting box with an absorber layer, 'absrb_2' case, resulted in a significant decrease of the transient field at early time but resulted in a field resonance behavior at later times. The addition of absorbers at the inner walls, 'absrb_4' case, damped those resonant behavior in a relatively short duration. The corresponding frequency response for each of the absorber cases is shown on Fig. 4.22. It is observed that the addition of absorber material resulted in a shift in the frequency spectrum to lower frequency values. Figure 4.23 shows the E_x transient response at location (2) inside 'box_b' for the four absorber cases described earlier. It is observed that for the absorber cases 'absrb_3' and 'absrb_4', corresponding to the addition of absorber layer on the inner walls of the conducting box, the resonance behavior is damped in a relatively short time as the fields bounce back and forth on the inner lossy walls of the conducting box. Figure 4.24 shows the corresponding frequency spectrum of E_x transient field responses inside 'box_b' of Fig. 4.23.

Figures 4.25, 4.27, and 4.29 shows similar computations of the E_x transient response at location (2) inside 'box_c', 'box_d' and 'box_e' respectively, for the four absorber cases, and the corresponding frequency spectrum plots are shown in Figs. 4.26, 4.28, and 4.30 respectively. Similar behavior for the addition of absorbing material is observed, in these box designs, to that of 'box_a' of Figs. 4.21 and 4.22.
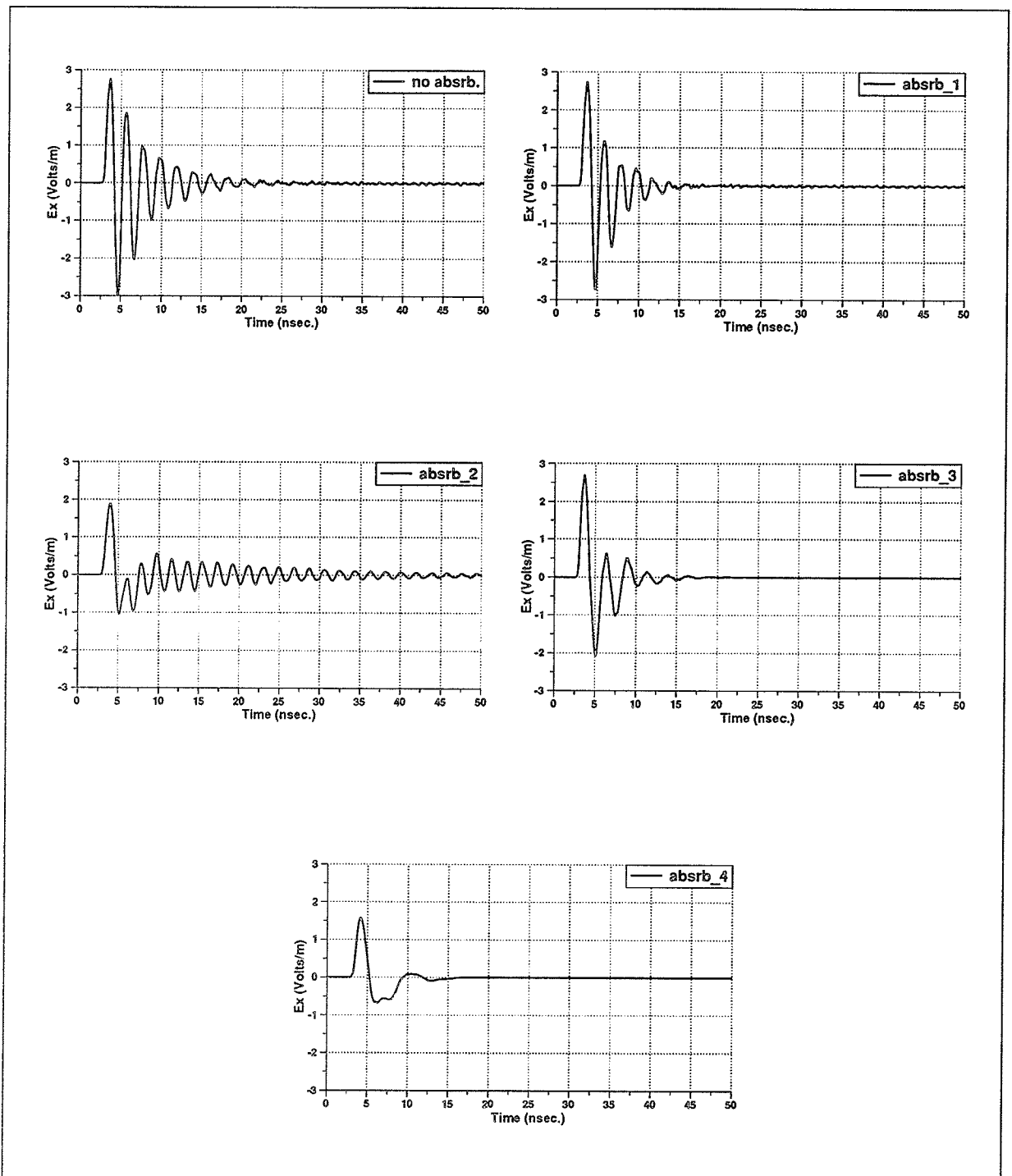
Fig. 4.21 E_x transient response at location (2) inside 'box_a' for all absorber cases.
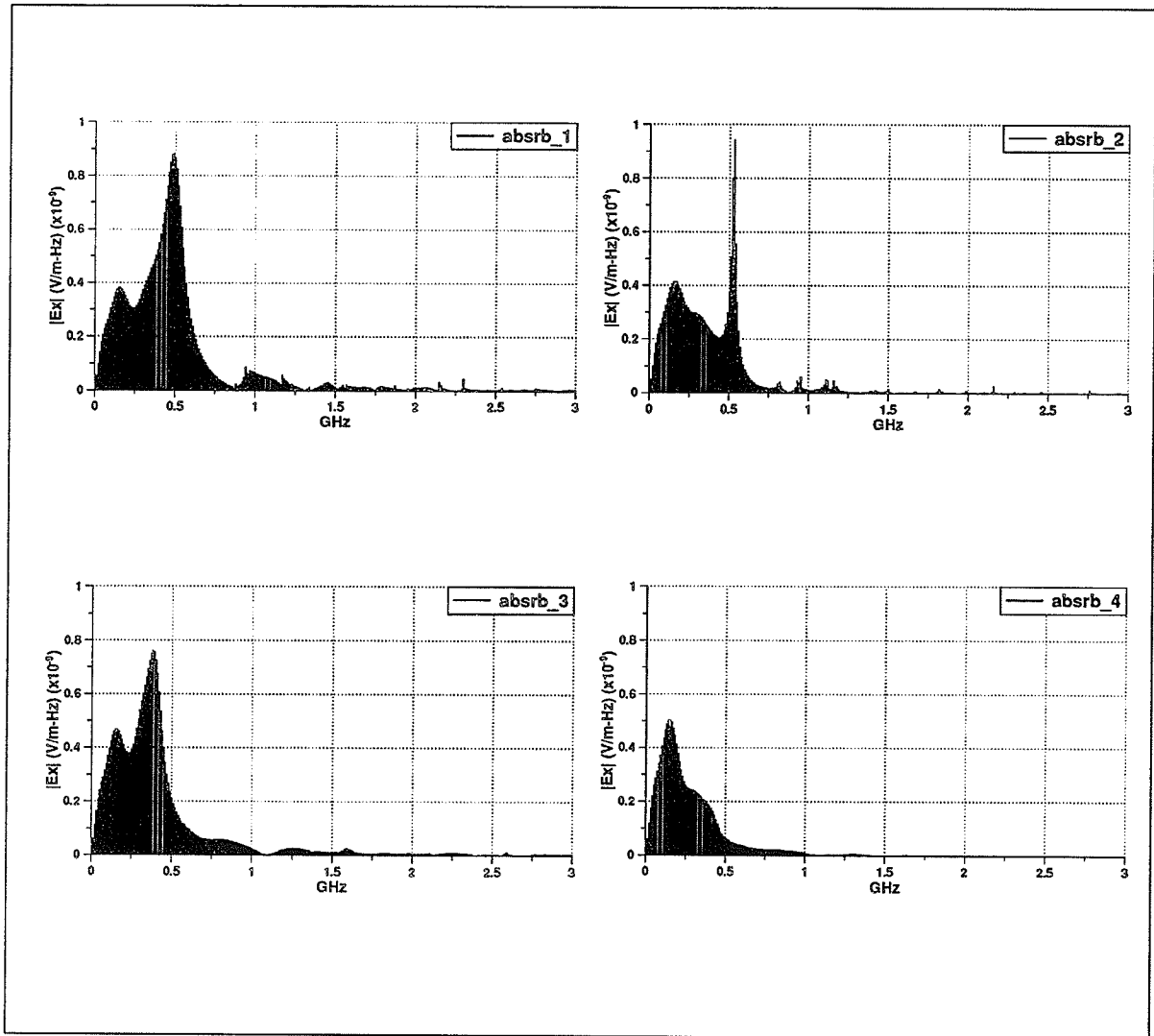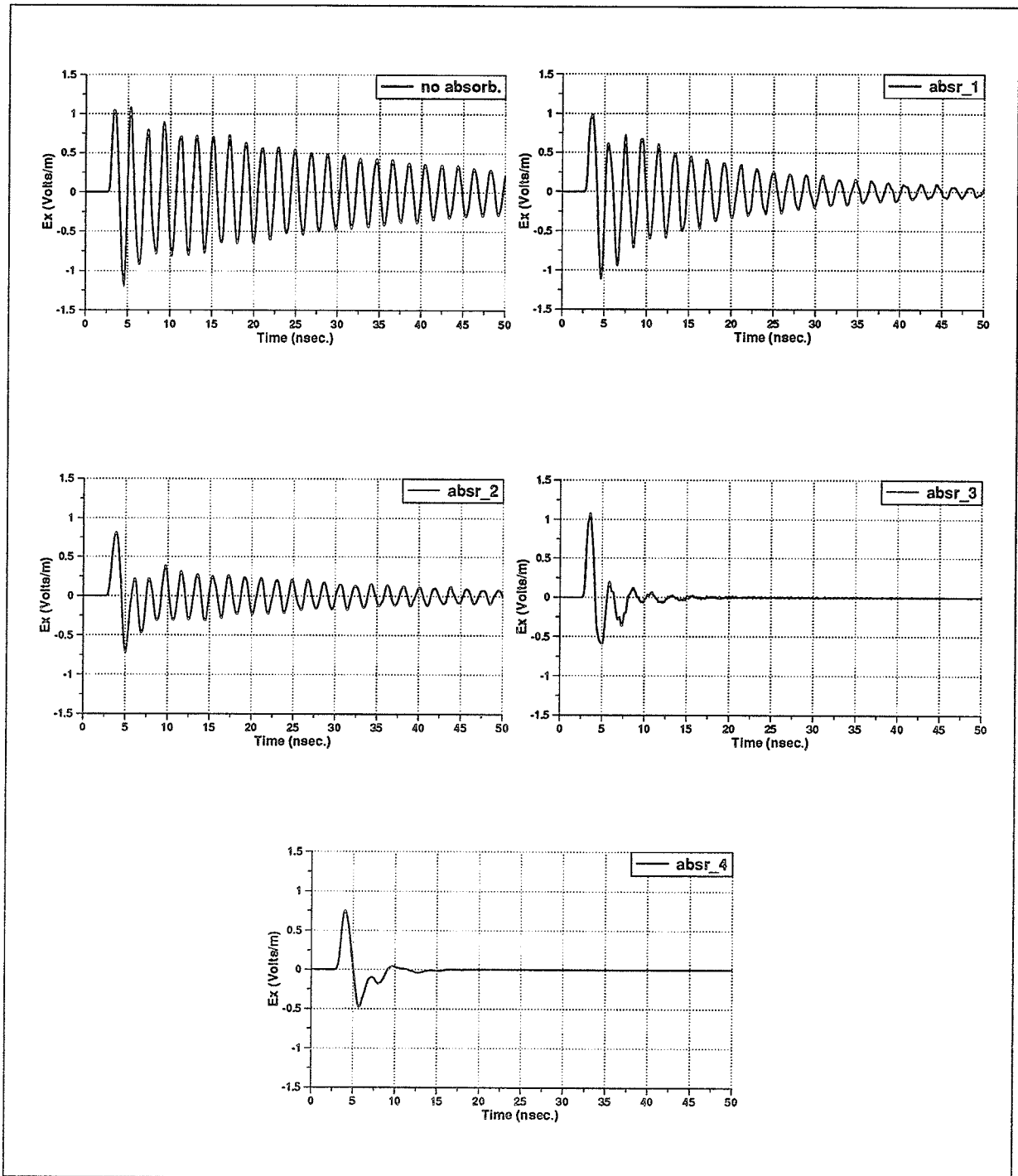
Fig. 4.22 E_x field frequency response at location (2) inside 'box_a' for all the absorber

cases. $\left(\Delta f \,=\, 10 MHz \right)$

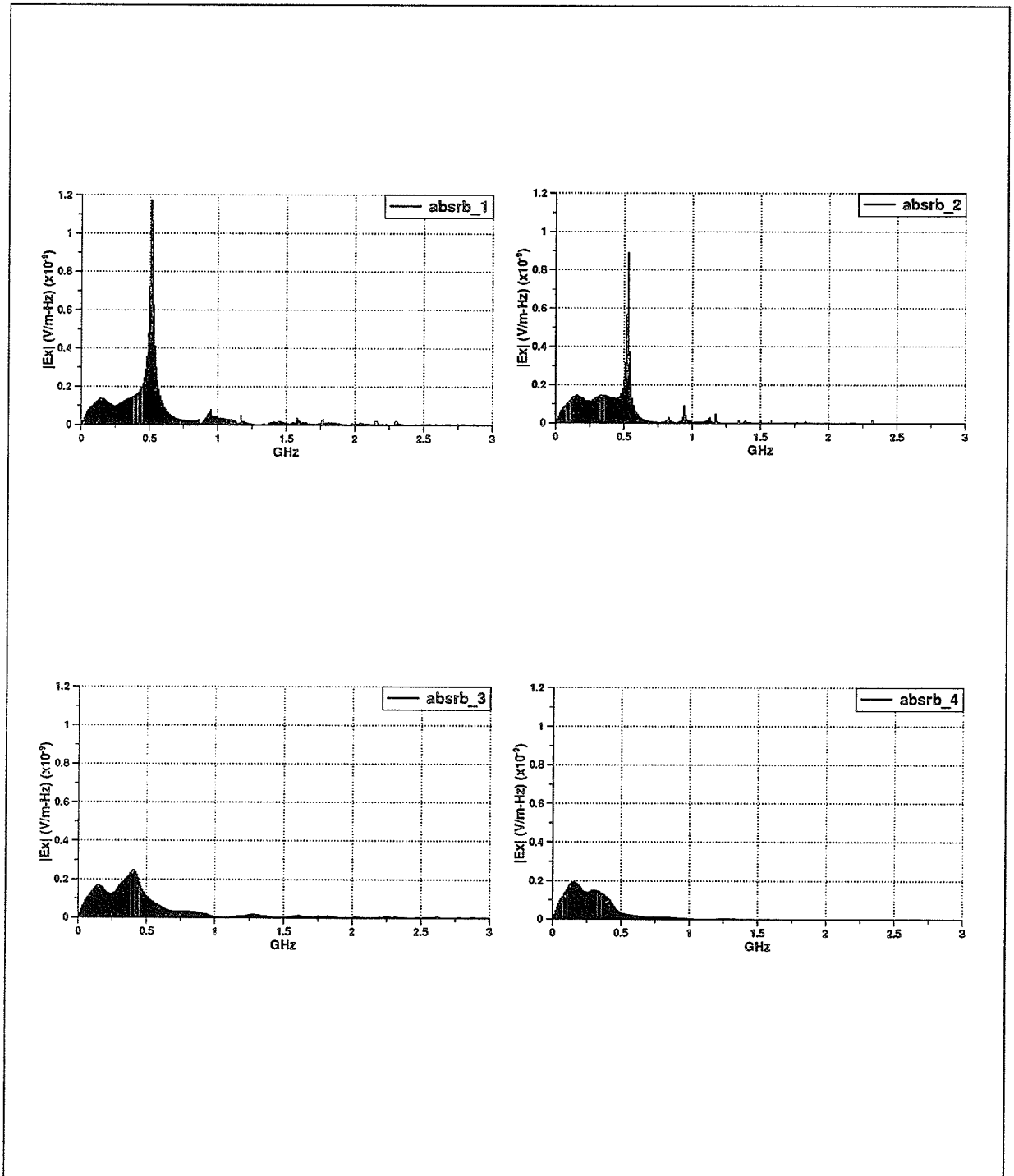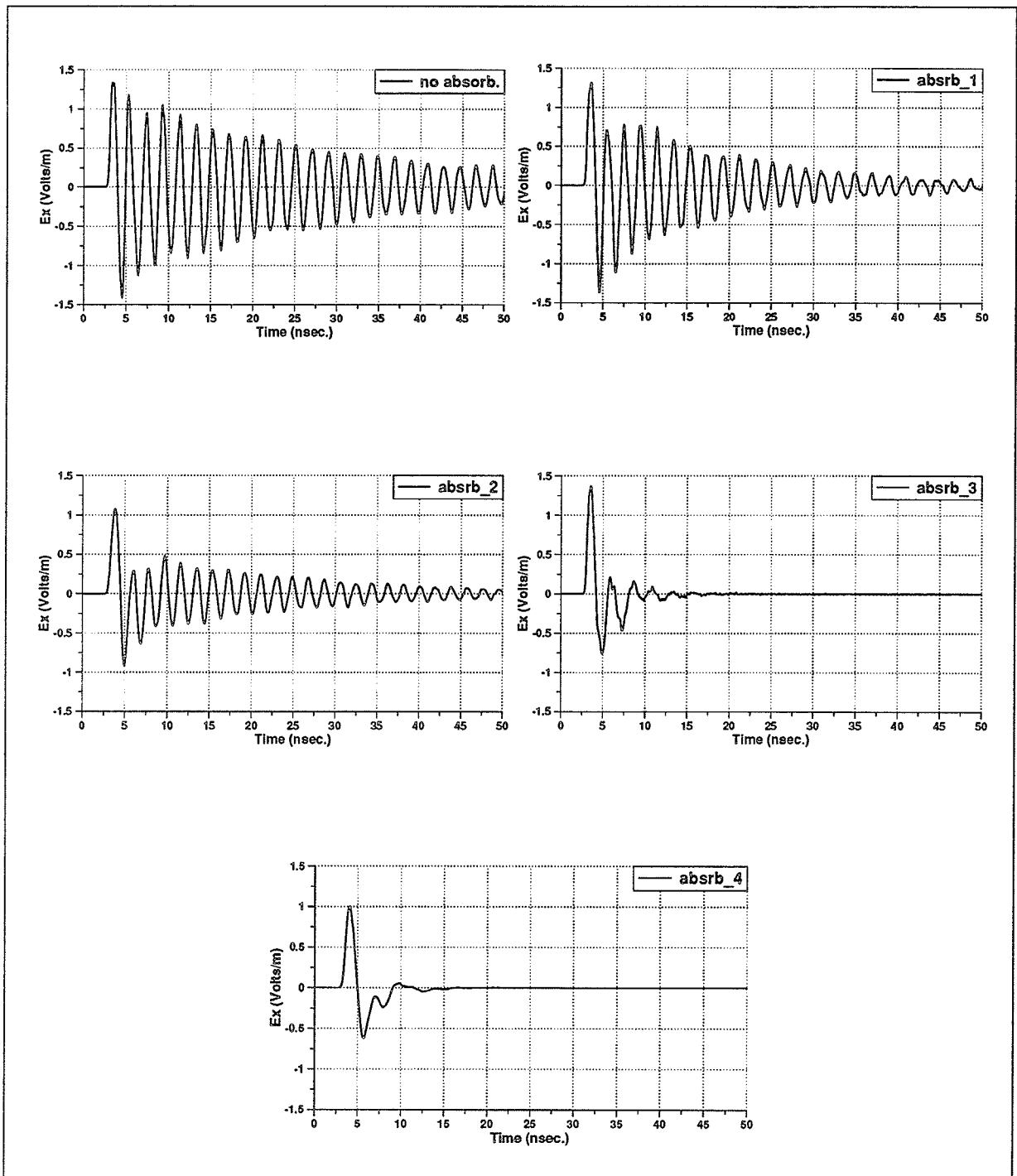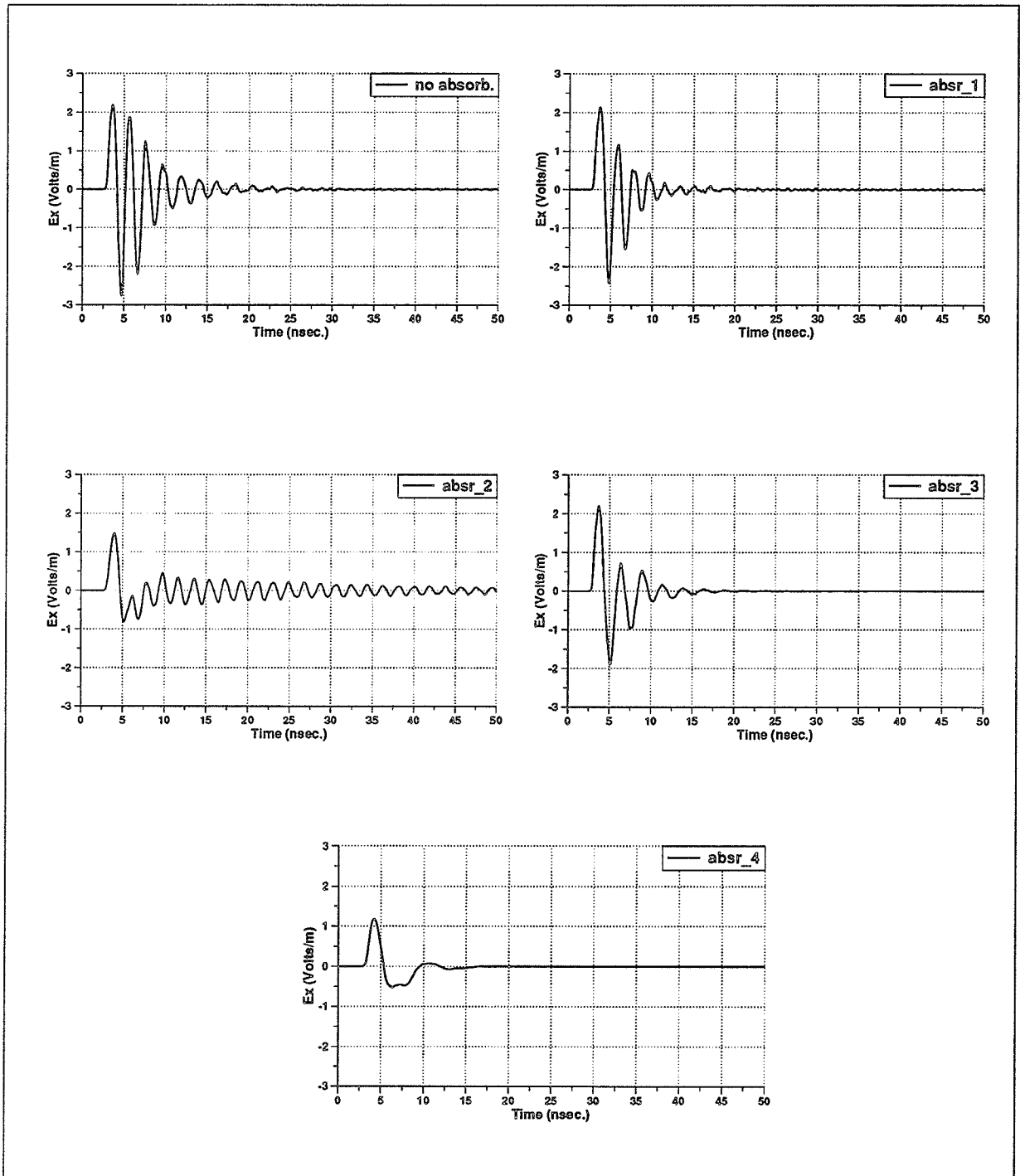Fig. 4.23 E_x transient response at location (2) inside 'box_b' for all absorber cases.

Fig. 4.24 E_x field frequency response at location (2) inside 'box_b' for all the absorber cases. $\left(\Delta f = 10MHz\right)$

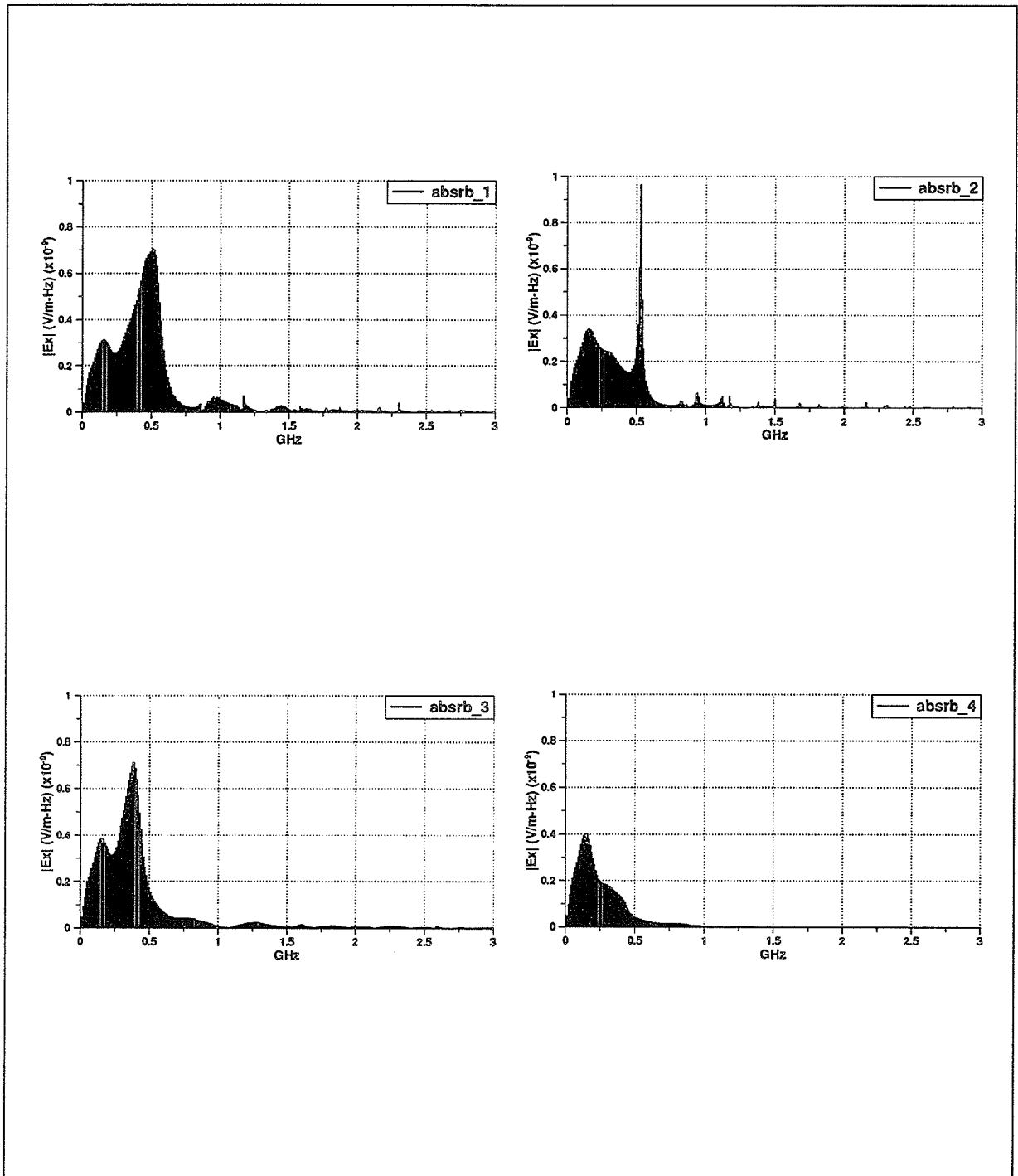Fig. 4.25 E_x transient response at location (2) inside 'box_c' for all absorber cases.
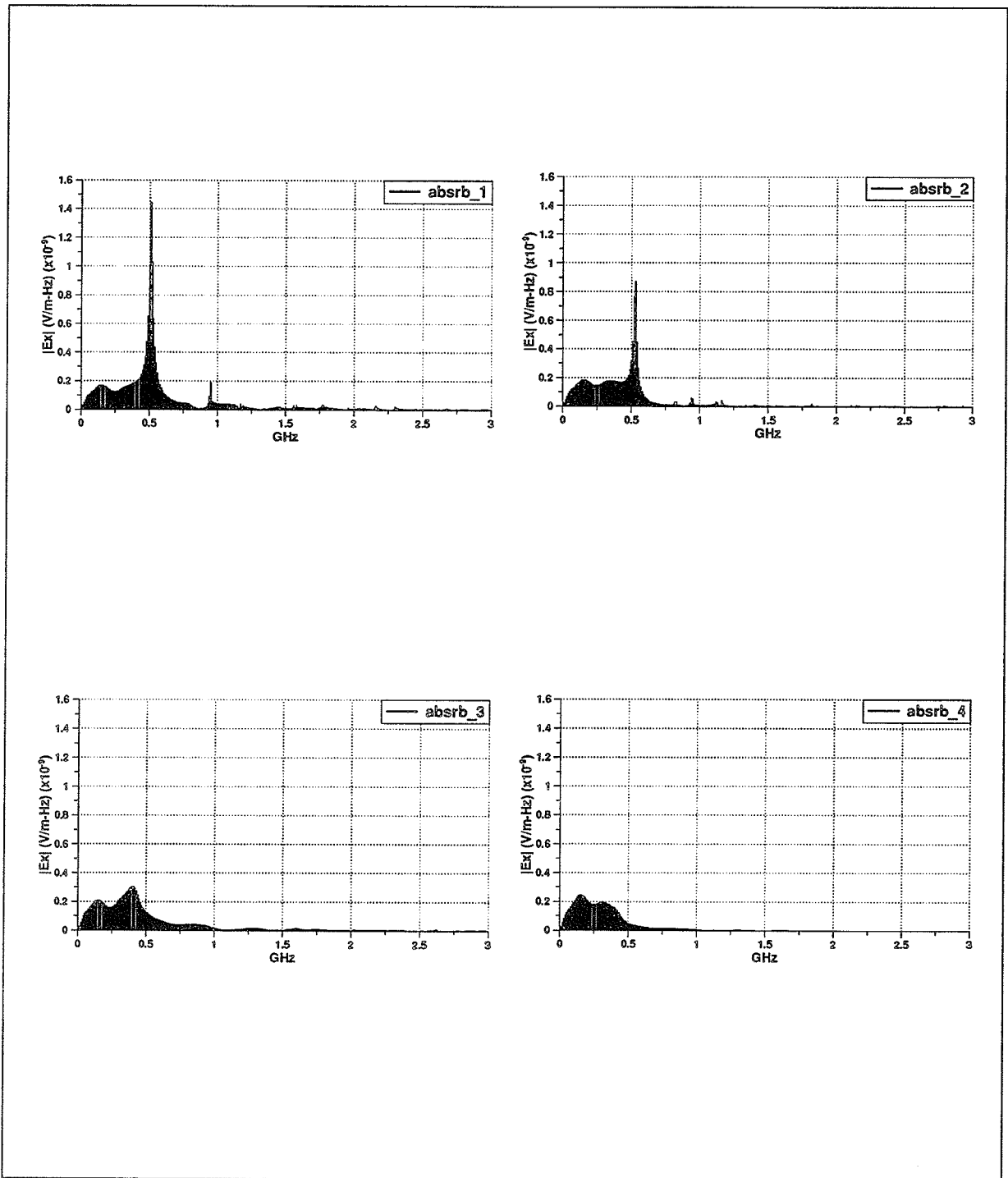
Fig. 4.26 E_x field frequency response at location (2) inside 'box_c' for all the absorber cases. $\left(\Delta f = 10MHz\right)$
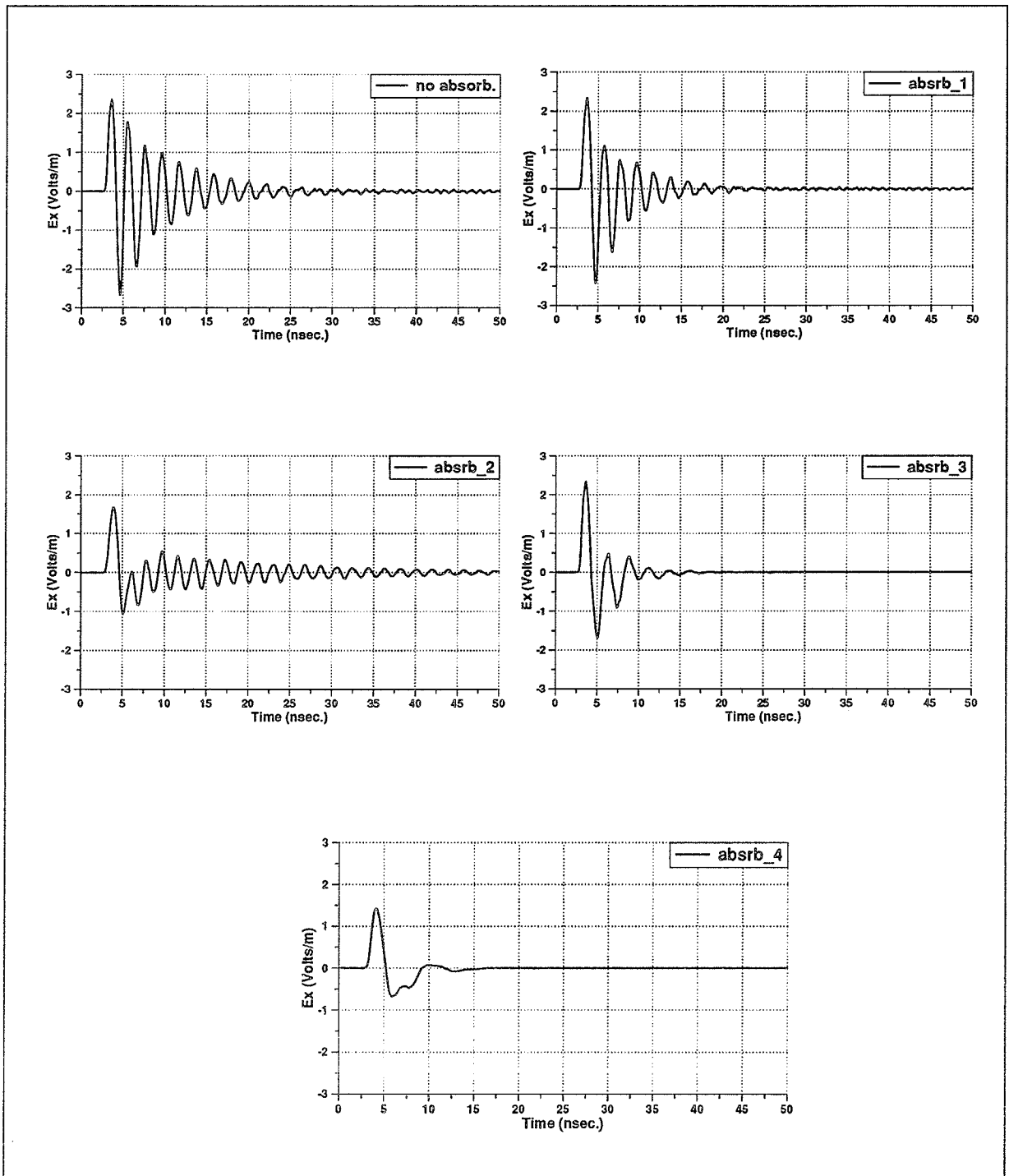
Fig. 4.27 E_x transient response at location (2) inside 'box_d' for all absorber cases.

Fig. 4.28 E_x field frequency response at location (2) inside 'box_d' for all the absorber

cases. $\left(\Delta f = 10 MHz\right)$

Fig. 4.29 E_x transient response at location (2) inside 'box_e' for all absorber cases.
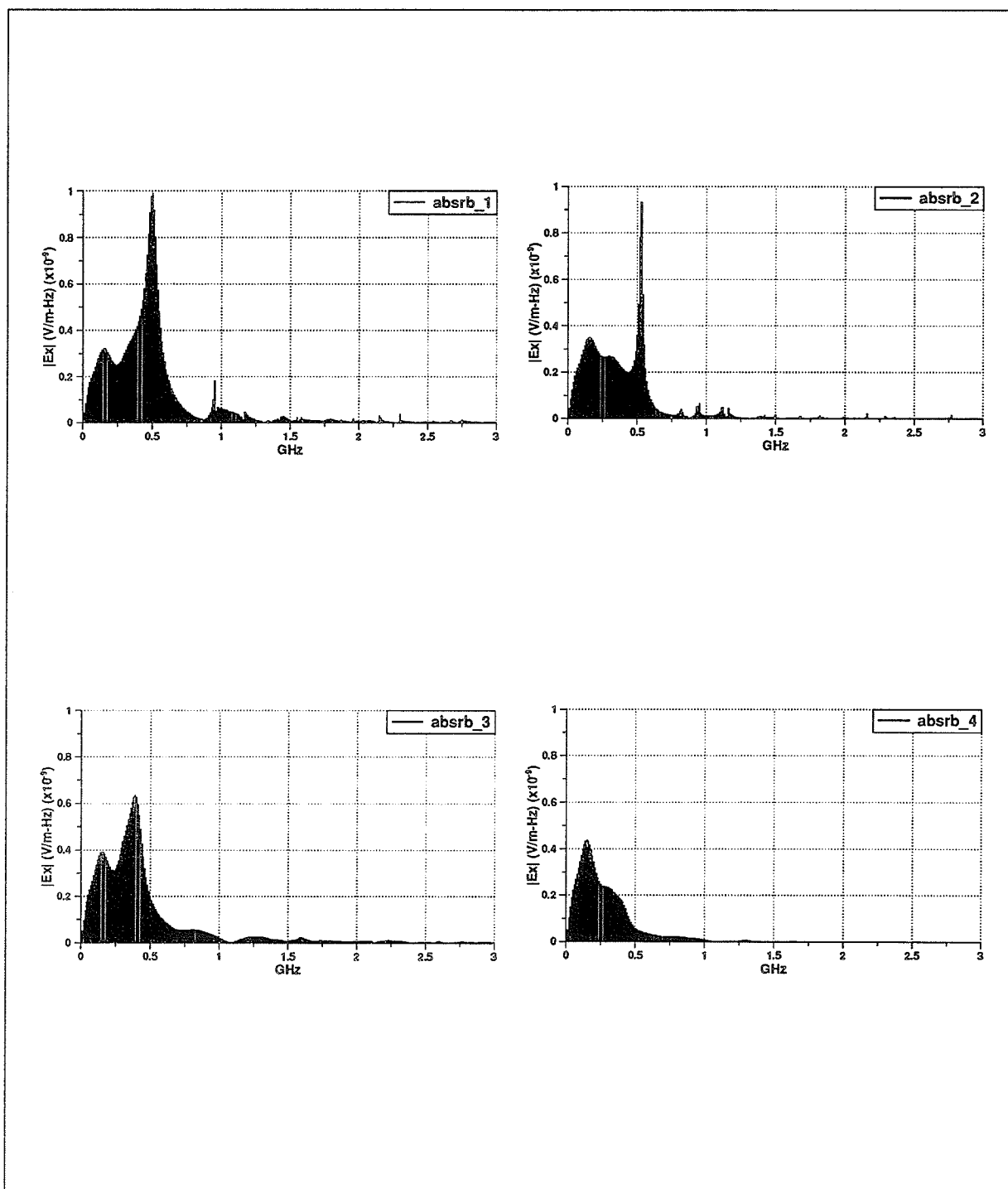
Fig. 4.30 E_x field frequnecy response at location (2) inside 'box_e' for all the absorber

cases. $\left(\Delta f = 10MHz\right)$.

Conclusions

In this section, the Finite Difference–Time Domain numerical technique was used to calculate and study the transient field response inside a cubic conducting box with an open top normally illuminated by a doubly–exponential pulse plane wave. The modeling of the conducting box was done efficiently by using electric and magnetic walls and only one–quarter of the conducting box geometry was modeled. The effect of modifying the conducting box aperture geometry on the magnitude and frequency content of the transient field penetration inside the conducting box is studied. Five aperture geometries were considered where the size and orientation of the aperture edges were the variable parameters involved in this study. The aperture edges geometry having the smaller edge size perpendicular to the polarization of the incident plane wave resulted in a significant reduction of the transient field magnitude at the early time in addition to a resonance phenomena. Also, the conducting boxes with modified aperture geometries became more frequency selective as compared with the unmodified aperture conducting box. The addition of absorbing material on the walls of the conducting box geometries analyzed was also investigated. Adding the absorbing material on the aperture wall reduced the transient field magnitude penetrating inside the box cavity, while adding the absorber at the inner walls caused the field resonance to attenuate at a faster rate.
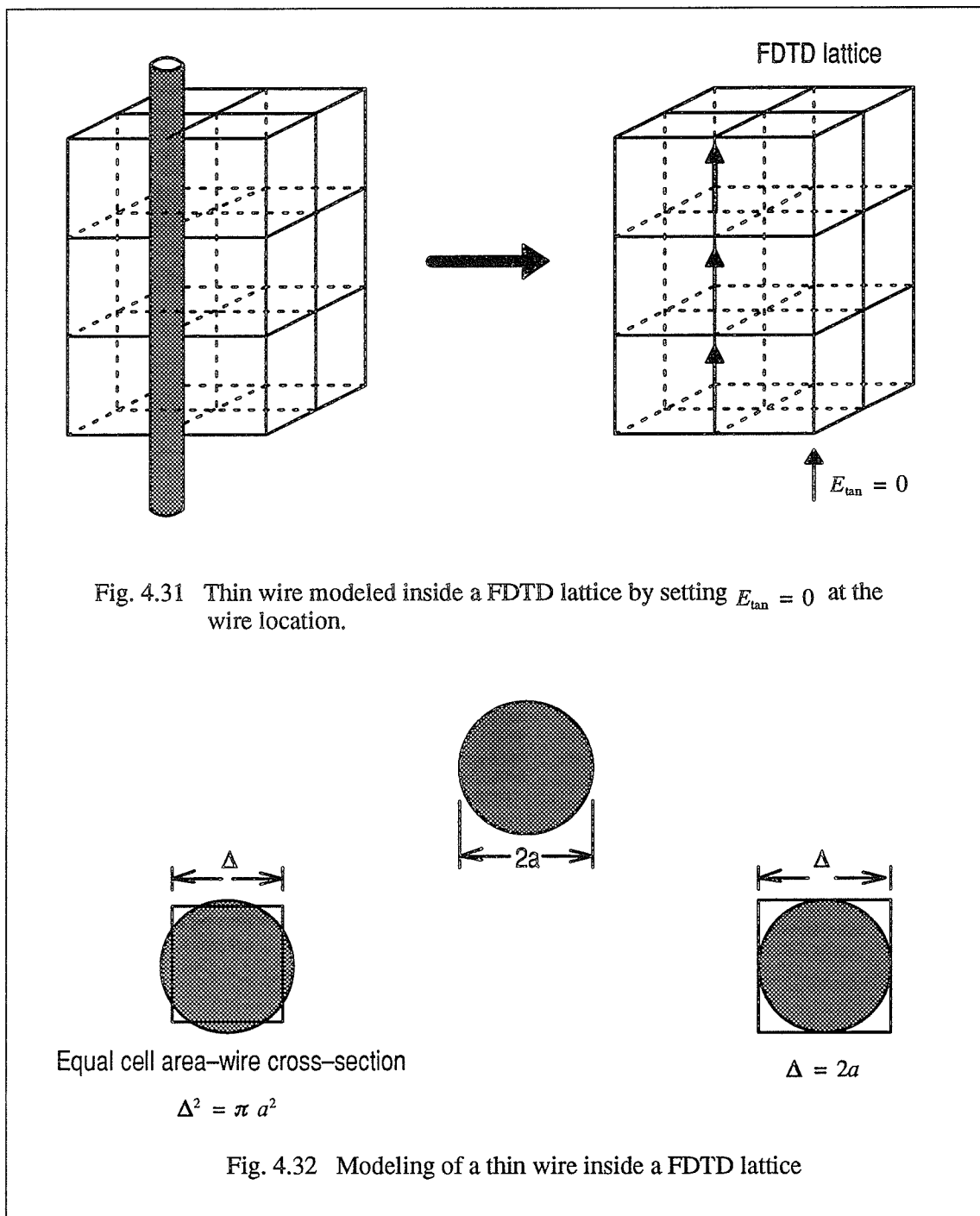
4.4. Thin Wire Modeling

i) *Review*

The FDTD method has proven to be a successful numerical technique used for solving a variety of electromagnetic scattering and coupling problems. Using Yee's cell, Fig. 2.1, geometries with complex shapes and composition are modeled in a straight forward manner inside the FDTD space lattice. On the other hand, the Yee cell fails to model thin wire structures efficiently. In this case, thin wires are modelled by setting the tangential total electric field to ($E_{tan} = 0$) zero at the wire location leaving no parameter to vary to study the influence of wire radius on the solution [88]. Such modeling is illustrated in Fig. 4.31. A second approach to model wires is to set the dimensions of the Yee cell such that the cell area will match with the cross–sectional area of the wire, or to set the dimension to be equal to the wire diameter as shown in Fig. 4.32. In this manner, relatively accurate results are obtained [89]. However, this approach will be very expensive in terms of memory storage requirements if composite geometries are involved. Thin wire subcell models [55,61] are alternative approaches that succeeded in modeling of wires efficiently. Thin wires of radii much smaller than the FDTD cell size are modelled using the thin wire subcell models. In [55], an "in–cell inductance " model of the thin wire is developed, the current distribution on the wire is obtained through the solution of a differential equation for the wire current solved concurrently with the FDTD time stepping. The wire subcell of [61] uses a Faraday's law contour integral approach to obtain a simple modification of the basic FDTD algorithm to properly model the electromagnetic field near the wire.

Taflove *et al.* [61] suggested that the extension of FDTD modeling to wires, slots, and curved surfaces can be achieved by departing from Yee's original pointwise derivative interpretation. As shown in Fig. 4.33, their new idea is based upon Ampere's law and Faraday's law in integral form implemented on an array of electrically small spatially orthogonal contours. These contours mesh (intersect) in the manner of links in a chain, providing a geometrical interpretation of the coupling of Ampere's law and Faraday's law. This meshing results in filling of the FDTD modeled space by a three–dimensional chain–link array of intersecting orthogonal contours. The presence of wires, slots, and curved surfaces can be accounted by incorporating appropriate field behavior into the contour and surface integrals

implementing Ampere's law and Faraday's law at selected meshes, and by deforming contour paths as required to conform with surface curvature. The equivalence of this procedure to the Yee algorithm in free space and its implementation to thin wire modeling is included in Appendix C.
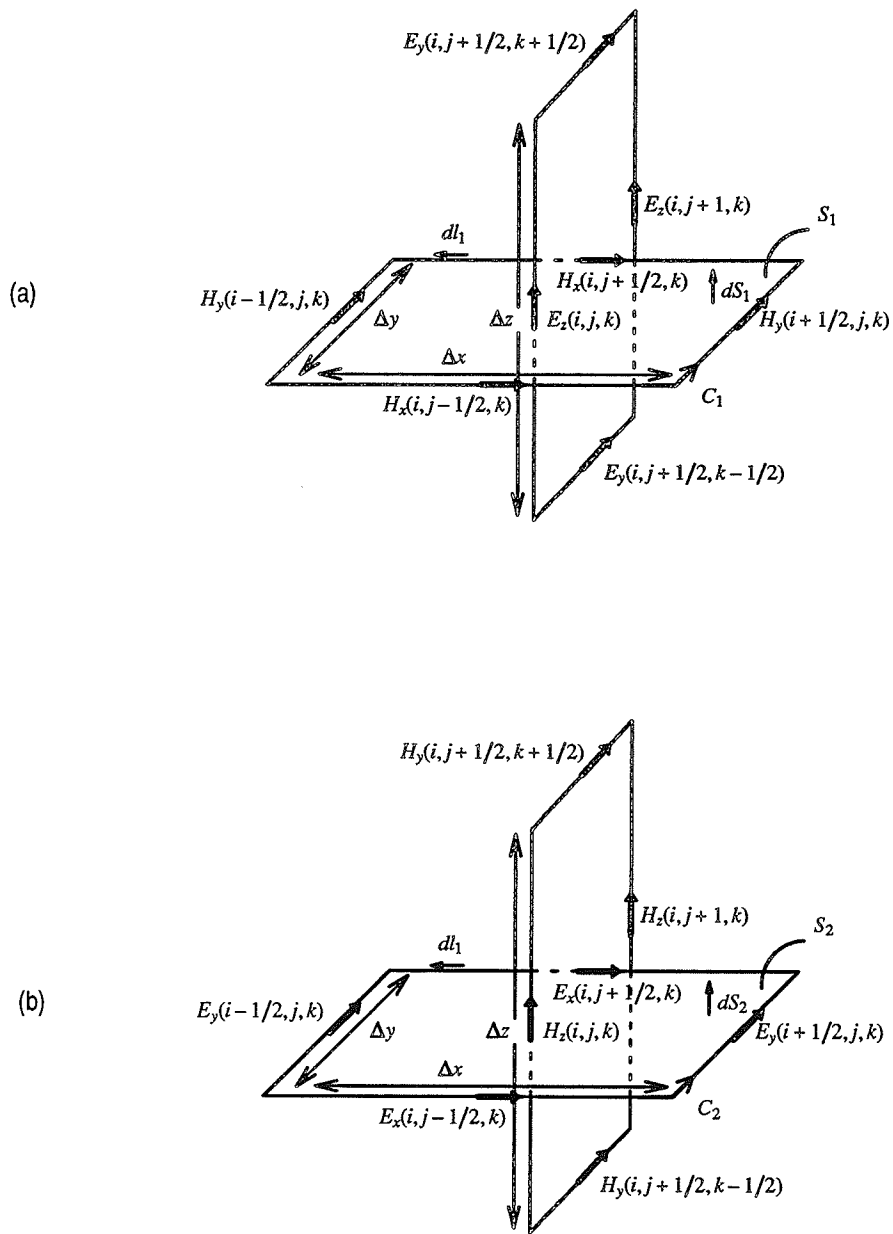

Fig. 4.31 Thin wire modeled inside a FDTD lattice by setting $E_{\tan} = 0$ at the wire location.

Equal cell area–wire cross–section

$$\Delta^2 = \pi\, a^2$$

$$\Delta = 2a$$

Fig. 4.32 Modeling of a thin wire inside a FDTD lattice

Fig. 4.33 Examples of spatially orthogonal contours in free space. (a) Ampere's law for E_z. (b) Faraday's law for H_z.

4.4.1. Numerical Tests

Most of real life scattering application structures are made of composite components (planer surfaces, boxes, coated surfaces, wires, . .), and the FDTD method has proven to be an efficient method in modeling such complex geometries. In this section, the different approaches used to model thin wires in the FDTD method will be examined. The current phase and magnitude along thin wires are computed using three of the wire modeling procedures mentioned earlier;

1– Equal–cell area–wire cross–section,

2– Contour integration,

3– $E_{tan} = 0$, at wire location.

These current magnitudes are compared with those computed using the Method of Moments (MoM) adopted by NEC [90].

ii) *Infinitely long wire (two–dimensions).*

The case of an infinitely long thin wire is considered first. Fig. 4.34 shows the computed circumferential equivalent magnetic field (H_{eq}) near a thin perfectly conducting infinitely long wire illuminated by a Sinusoidal *TM* plane wave for a wide range of wire radii at a distance $\lambda/20$ from the center of the wire. H_{eq} is the circumferential magnetic field that will produce the same wire current obtained by integrating the circumferential magnetic fields resulting from the FDTD computations as illustrated in Fig. 4.35. H_{eq} is computed using;

1– equal–cell area–wire cross–section,
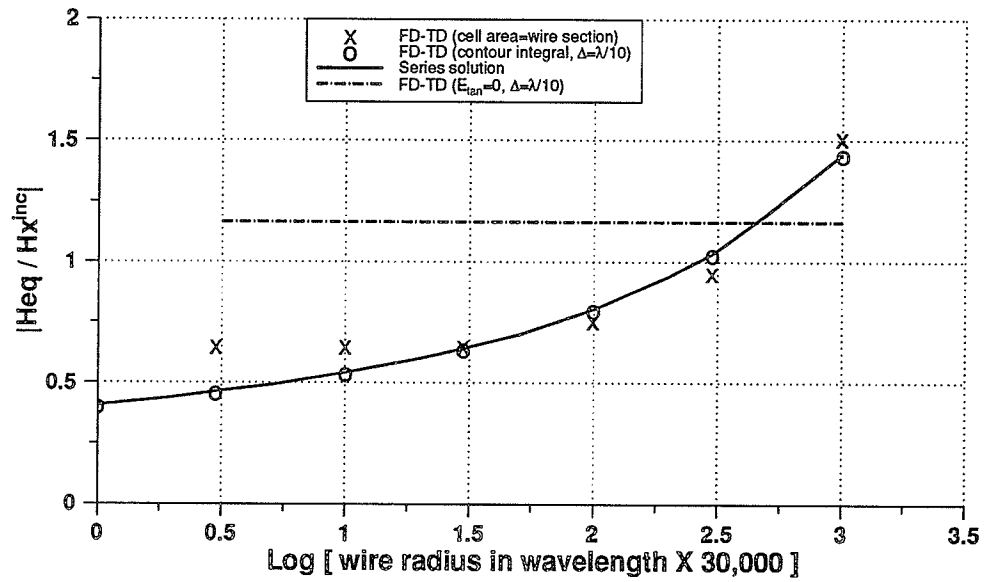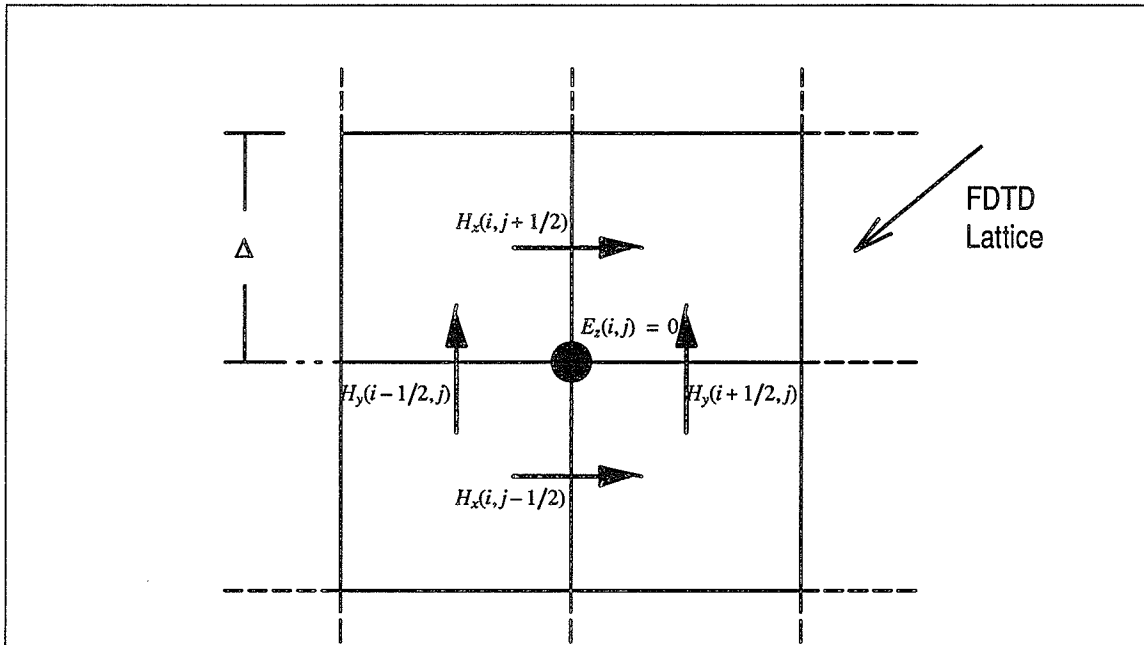
2– contour integration,

3– exact solution.

Fig. 4.34 H_{eq} circumferential magnetic field at location $\lambda/20$ from the center of an infinite wire.

$$H_{eq} \, 2\pi \, l = \Big[\, H_y(i+1/2,j) - H_x(i,j+1/2) - H_y(i-1/2,j) + H_x(i,j-1/2) \Big] \cdot \Delta$$

Fig. 4.35a Procedure to compute H_{eq} at location l from the wire at location (i, j) modeled inside a FDTD lattice. ($E_{tan} = 0$ case).

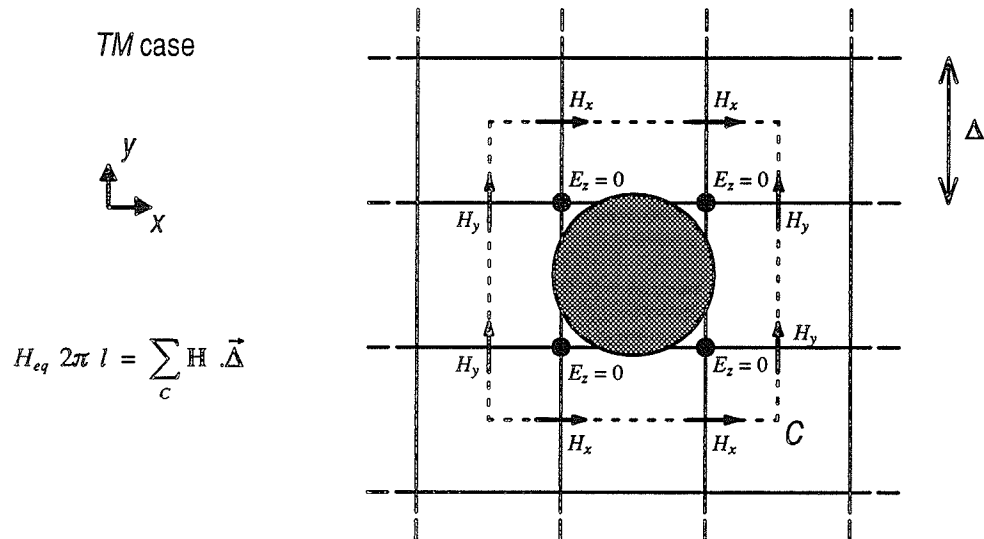$$H_{eq} \, 2\pi \, l = \sum_c \mathbb{H} \cdot \vec{\Delta}$$

Fig. 4.35b Procedure to compute H_{eq} at location l from the wire at location (i, j) modeled inside a FDTD lattice. (equal cell area–wire cross–section case).

The exact solution for the H_{eq} of a wire can be obtained using the boundary value problem solution of the scattering by a conducting cylinder, however, due to the small wire radii, special handling is required to evaluate the series solution. A cell size of $\Delta = \dfrac{\lambda}{10}$ is considered for the contour integral method. Field values obtained using the contour integral modeling matched exactly with the exact solution as reported in [61], while the equal cell area–wire cross–section modeling departed from the exact solution at small radii. On the other hand, using $E_{\tan} = 0$ on the wire modeling, the value of H_{eq} intersect the exact solution curve at a wire radius value of approximately $a = 0.014\lambda$ corresponding to a wire radius to cell width ($\Delta = \dfrac{\lambda}{10}$) ratio of $\dfrac{a}{\Delta} = 0.14$. In [55] a value of $\dfrac{a}{\Delta} = 0.5$ is suggested, corresponding to zeroing the " in–cell inductance " in the thin wire formalism in the corresponding subcell model.

iii) *finite wire (three–dimensions).*

Next, wires in three–dimensional space are considered. A perfectly conducting wire of length L and radius a along the z–direction is illuminated by a *TM* sinusoidal plane wave. The magnitude and phase of the current distribution along the wire structure are computed using the above mentioned modeling procedures and are compared with the MoM solution for the same wire geometry [91].

A FDTD cell size of $\Delta = \dfrac{\lambda}{20}$ is used for the cases of $E_{\tan} = 0$ on the wire and the contour integral wire modeling, while a $\Delta = \dfrac{\lambda}{60}$ resolution is used in the MoM modeling. Figures 4.36–4.38 show the magnitude and the phase of the computed current distribution along the wire structures of radius $a = \dfrac{\lambda}{100}$ and lengths $L = 1\lambda$, $\dfrac{3}{2}\lambda$, and 2λ . Figures 4.39–4.41 show similar wire current information but for wire structures of radius $a = \dfrac{\lambda}{200}$. It is observed that for a wire radius $a = \dfrac{\lambda}{200}$ both the equal cell area–wire cross–section and the contour integral procedures show fairly accurate values of the current magnitude as compared with the MoM solution. While for the $E_{\tan} = 0$, on the wire, modeling case less accurate val-

ues are obtained as compared to the other two procedures. For a wire radius of $a = \dfrac{\lambda}{100}$, both the equal cell area–wire cross–section and the contour integral wire modeling are fairly in good agreement with the MoM solution. On the other hand, the $E_{tan} = 0$ on the wire modeling predicted more accurate values for the current magnitude along the wire compared with the other two FDTD modeling procedures. It should be noted that in this case the wire radius to the FDTD cell size ratio $\dfrac{a}{\Delta} = 0.2$ is close to the value obtained from Fig. 4.34 in the two–dimensional case.
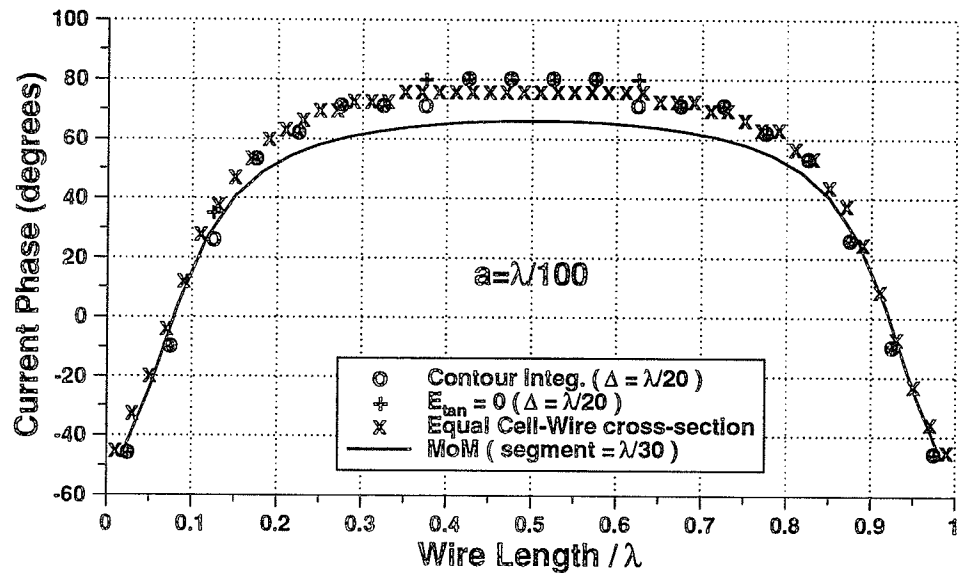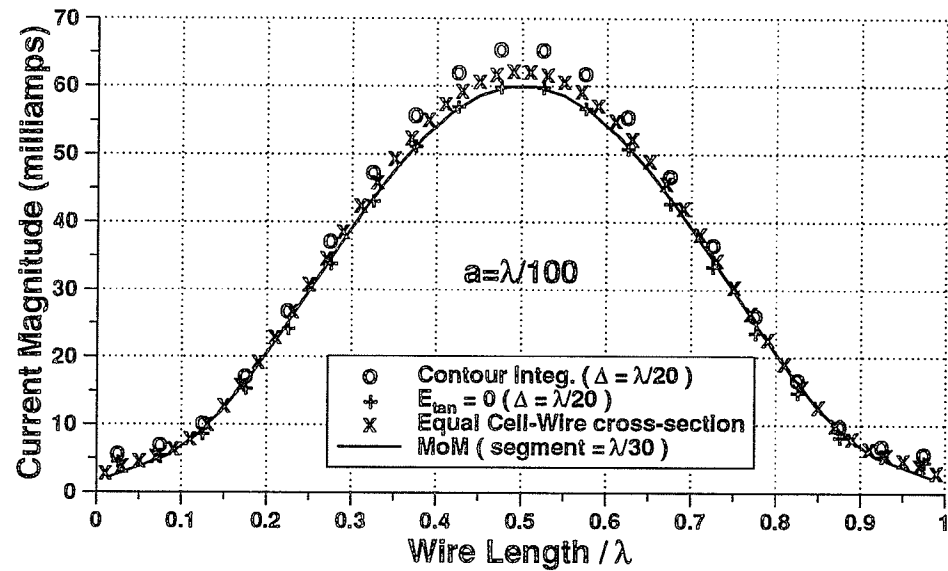
Fig. 4.36 Current magnitude and phase solutions for different FDTD thin wire modeling procedures and the MoM solution along a 1.0λ wire (*TM* illumination).

Fig. 4.37 Current magnitude and phase solutions for different FDTD thin wire modeling procedures and the MoM solution along a 3/2λ wire (*TM* illumination).

Fig. 4.38 Current magnitude and phase solutions for different FDTD thin wire modeling procedures and the MoM solution along a 2.0λ wire (*TM* illumination).

Fig. 4.39 Current magnitude and phase solutions for different FDTD thin wire modeling procedures and the MoM solution along a 1.0λ wire (*TM* illumination).
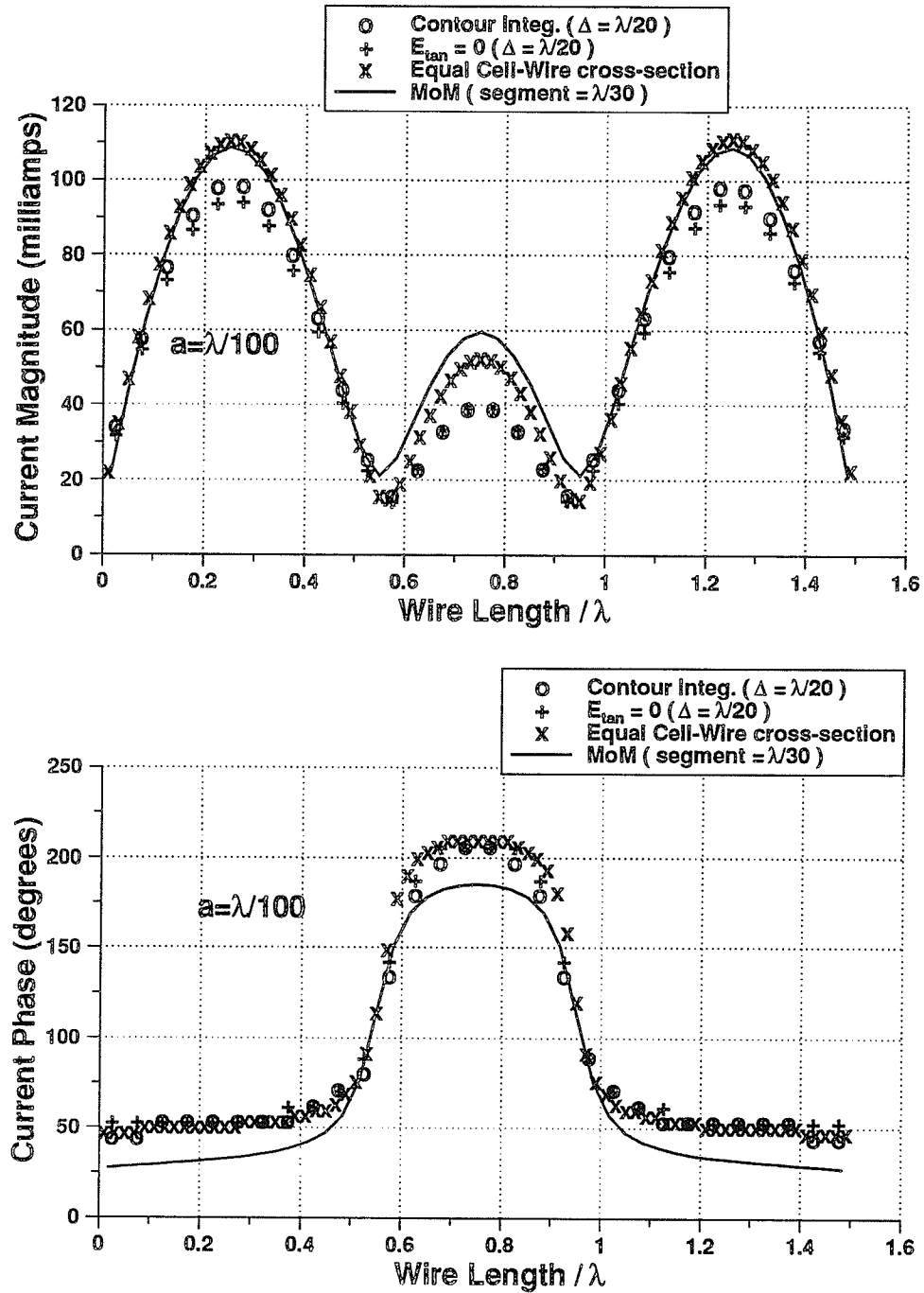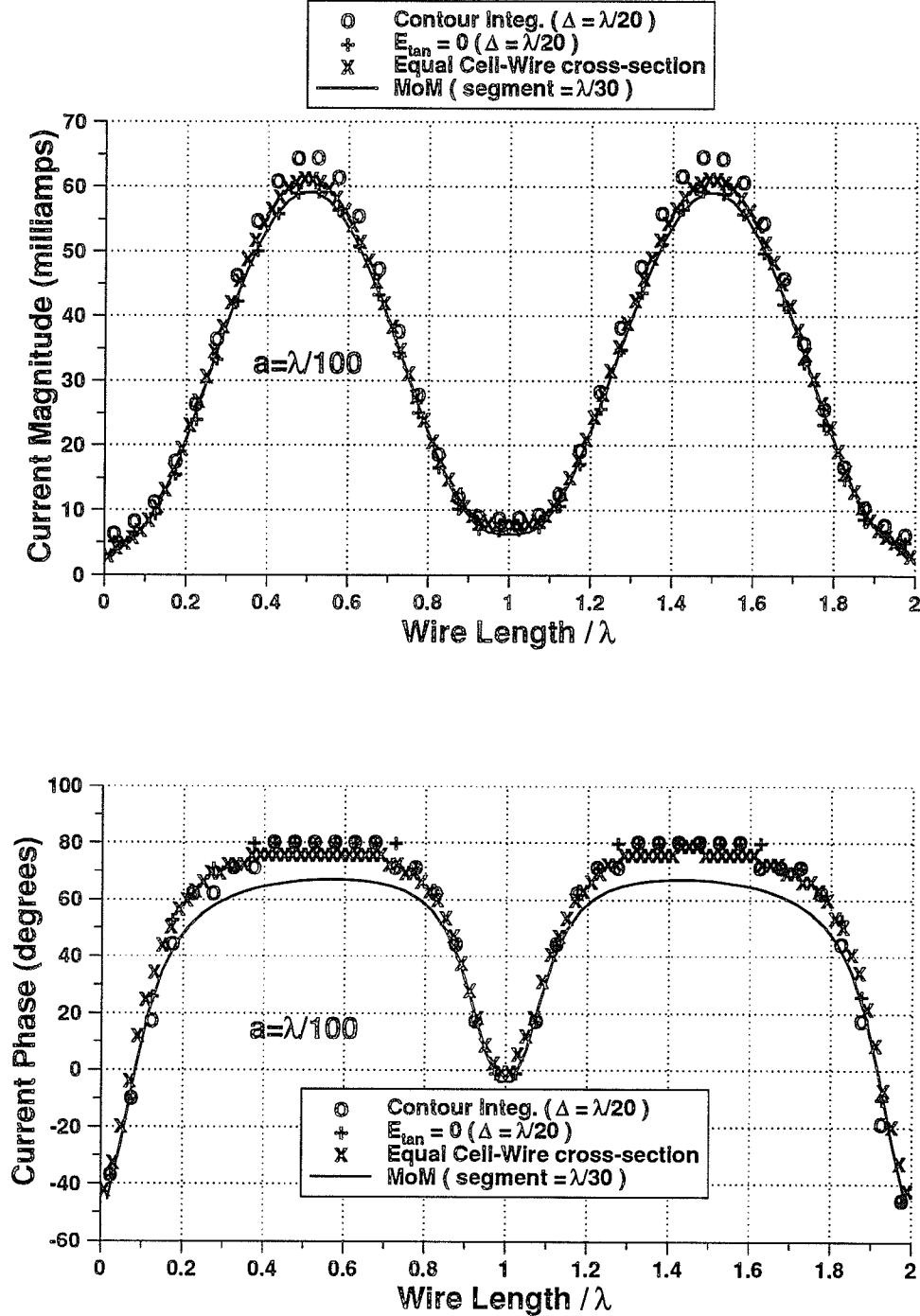
Fig. 4.40 Current magnitude and phase solutions for different FDTD thin wire modeling procedures and the MoM solution along a $3/2\lambda$ wire (*TM* illumination).

Fig. 4.41 Current magnitude and phase solutions for different FDTD thin wire modeling procedures and the MoM solution along a 2.0λ wire (*TM* illumination).
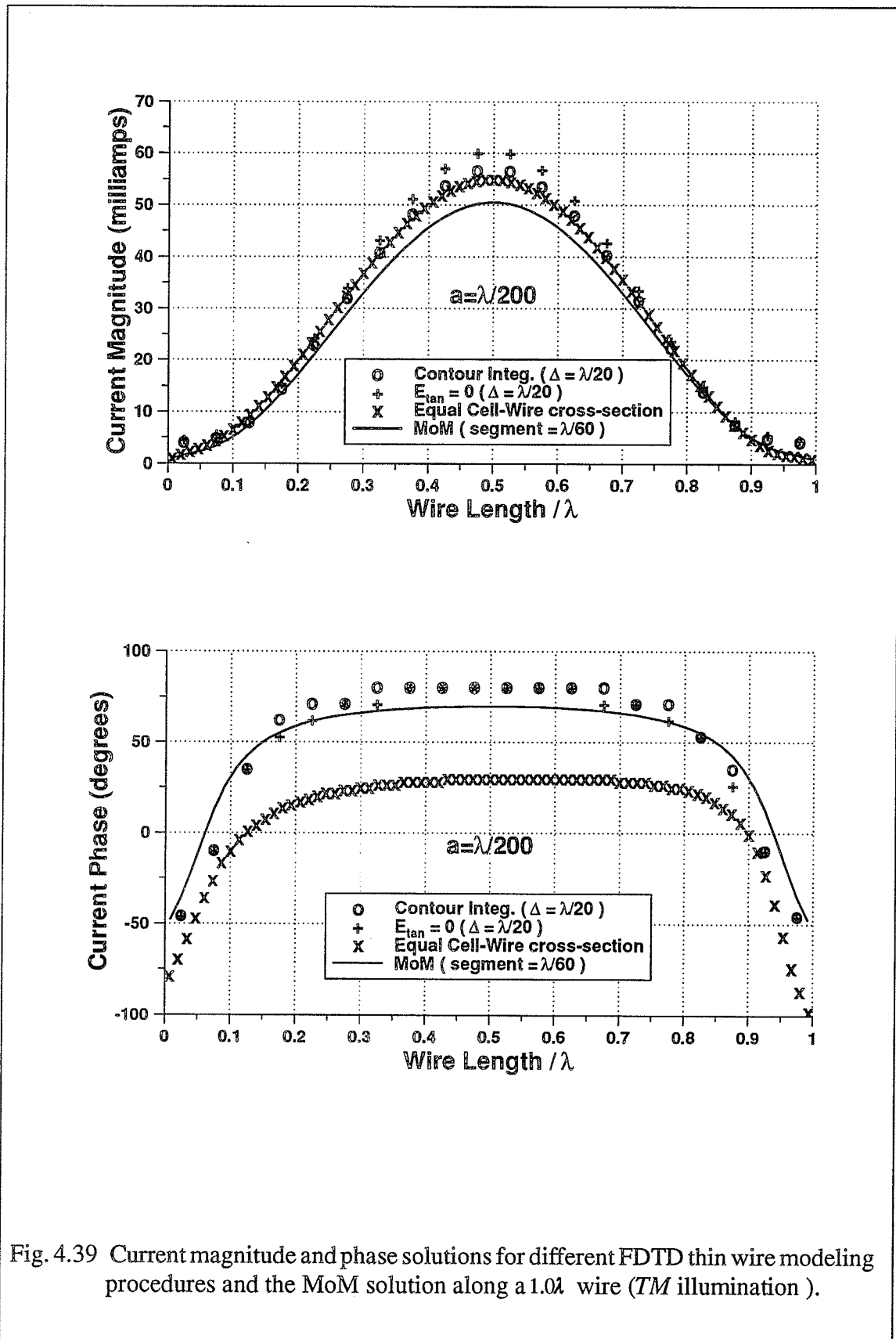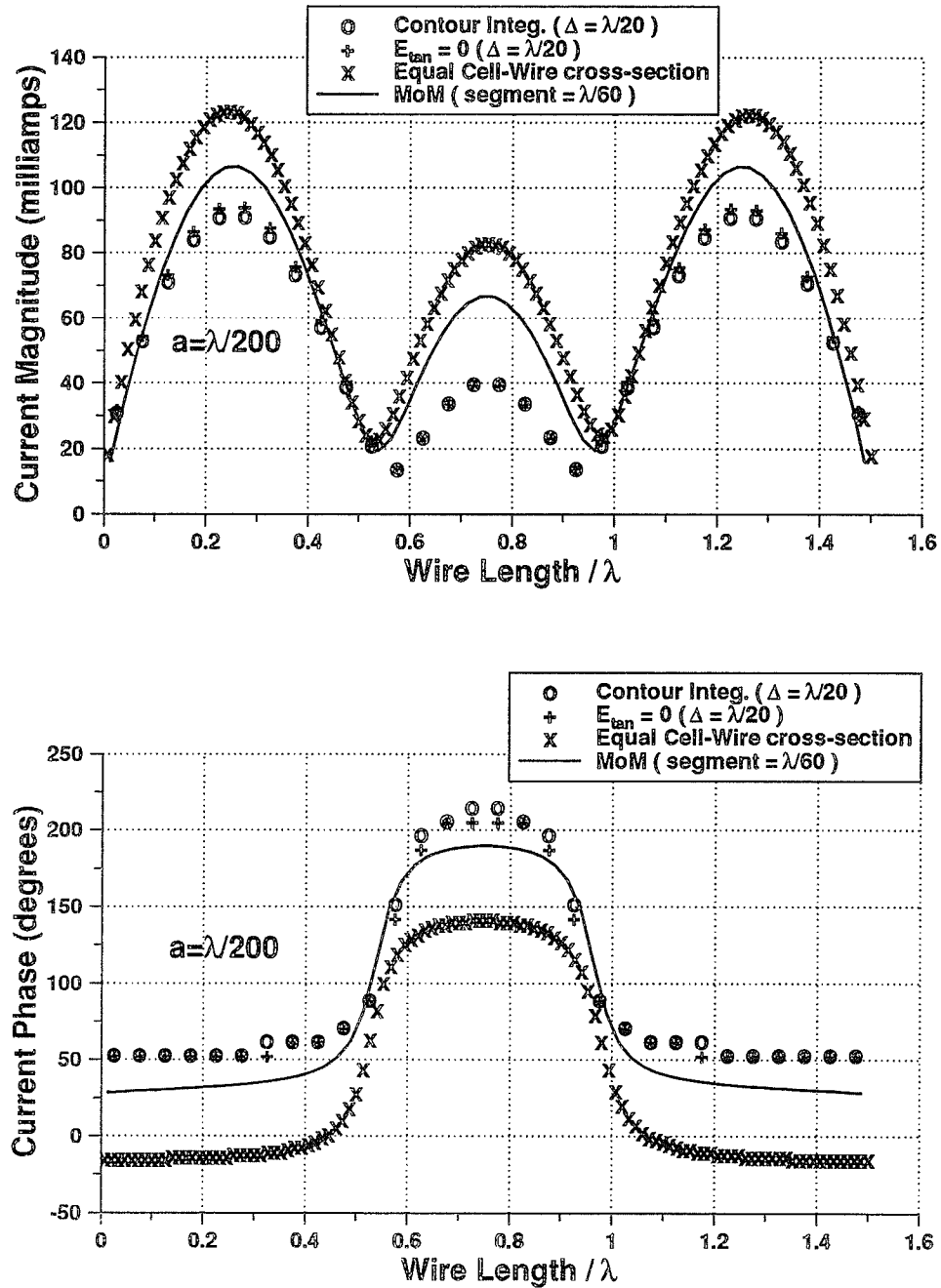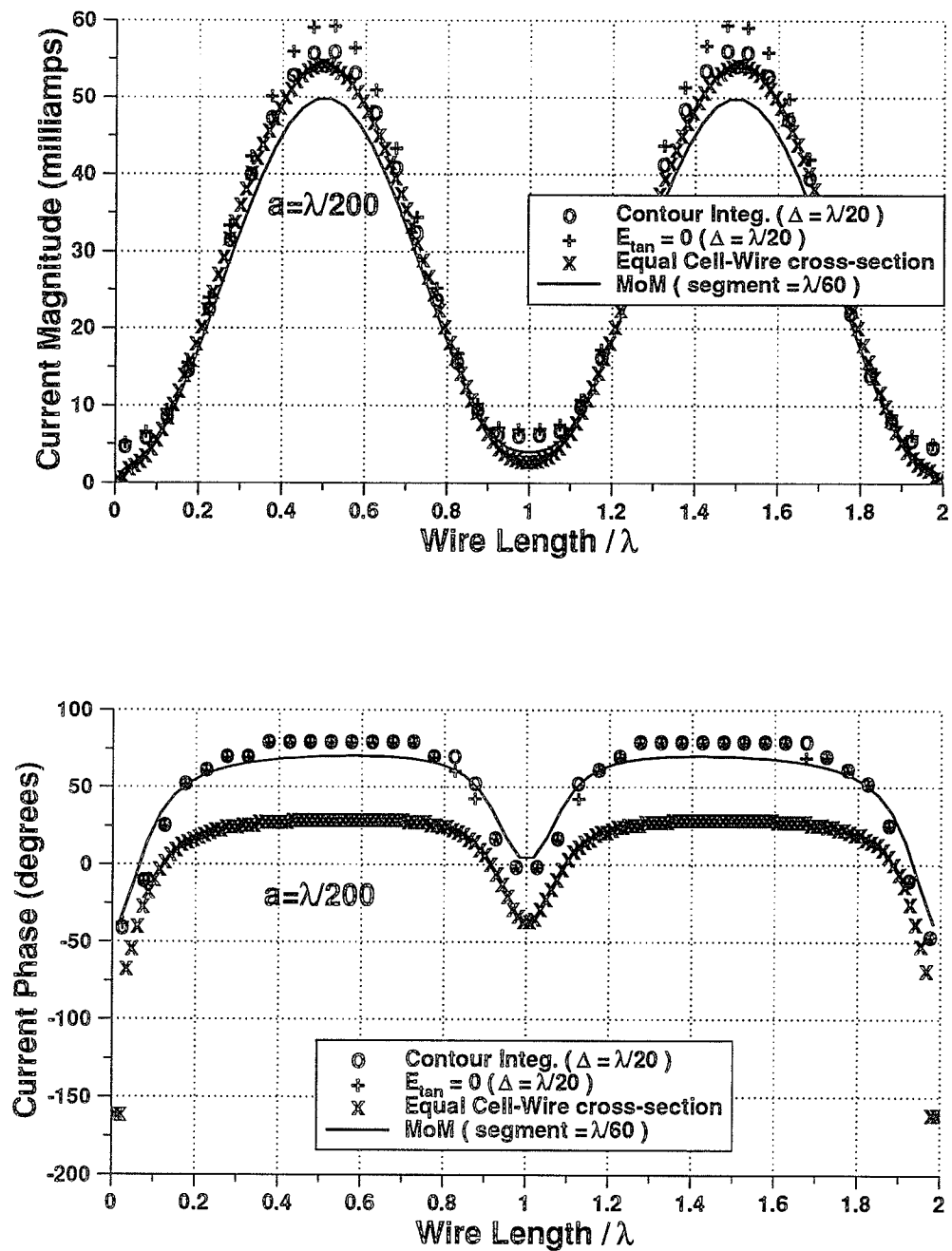
iv) Transient Response of a Wire

The capability of the thin wire modeling procedures in the FDTD method, studied in this section, to predict transient field and transient response information is also investigated. A half wavelength dipole having a radius $a = \dfrac{\lambda}{200}$ along the z–direction is illuminated by a *TM* Gaussian shape plane wave, a cell size of $\Delta = \dfrac{\lambda}{20}$ is used. Figure 4.42 shows the current transient response at the midpoint of the dipole. The dipole structure is modelled using the three wire modeling procedures involved in this study. The equal cell area–wire cross–section modeling resulted in a larger damping ratio the transient response than the other two modeling procedures. The corresponding frequency response of the current magnitude is obtained from the time information of Fig. 4.42 and is shown in Fig. 4.43. These frequency response plots are compared with that obtained from the MoM solution of an identical dipole. The MoM frequency data are scaled to include the effect of a Gaussian pulse excitation. The design frequency of our numerical experiment for this case is 1*GHz*, and the Gaussian pulse width used allows accurate current response of up to 2*GHz*. The resonant frequency of the dipole predicted by the three wire modeling procedures is very close to that obtained by the MoM solution.

The performance of different thin wire modeling procedures in the FDTD numerical technique is investigated. Current and phase magnitudes along thin dipoles are computed using the equal cell area–wire cross–section, $E_{tan} = 0$ on wire, and the contour integral modeling procedures. The computed results are compared with those obtained from the MoM solution. The equal cell area–wire cross–section procedure gave accurate results but was expensive in memory storage requirements, while the contour integral method provided an efficient and accurate wire modeling technique.
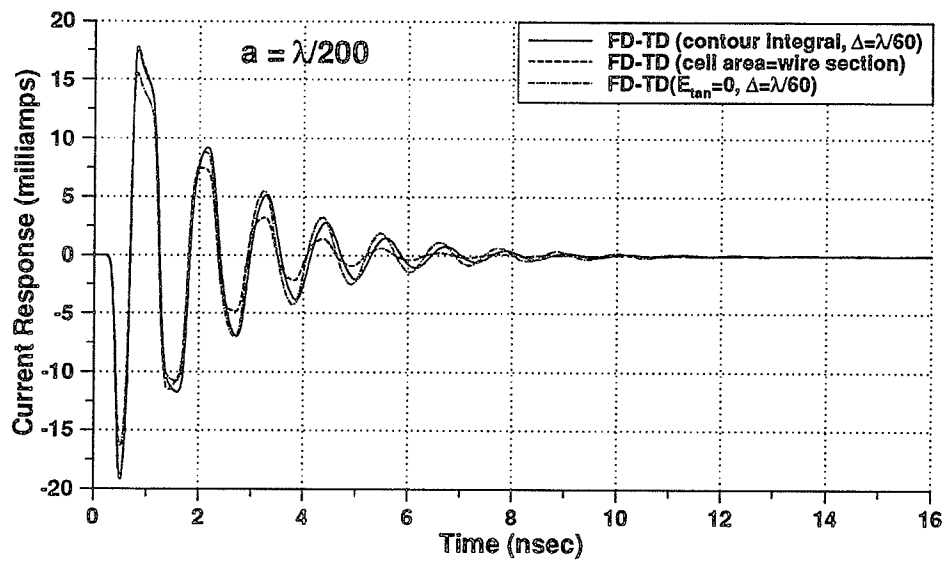
Fig. 4.42   Current response at the midpoint of a $\lambda/2$ dipole illuminated by a *TM* Gaussian plane wave computed by different FDTD thin wire modeling procedures. ($f = 1GHz$)
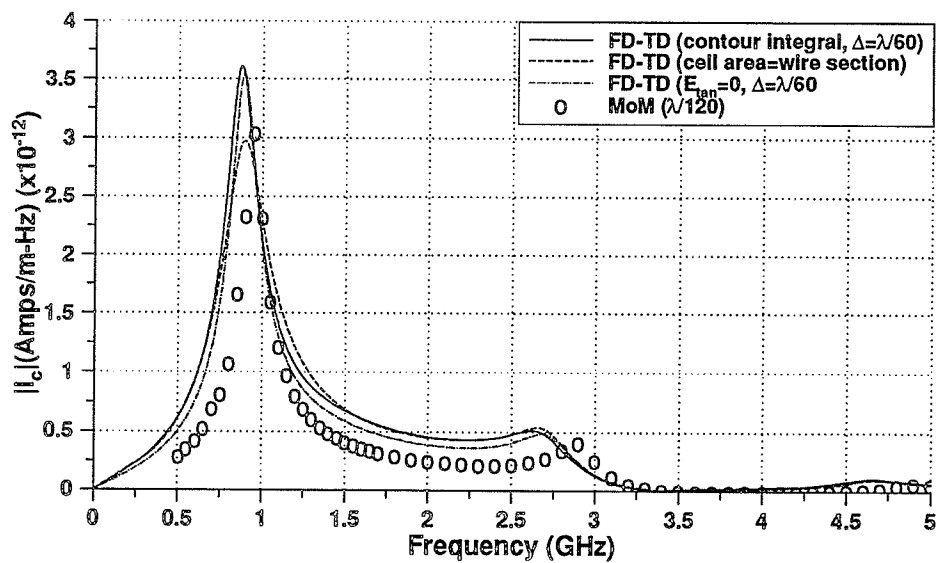

Fig. 4.43   Frequency current response of time data of Fig. 4.42 compared with the MoM solution.

CHAPTER V

APPLICATION TO ANTENNAS

The problem of radiation of electromagnetic waves by an antenna in a given environment is basically that of solving Maxwell's equations subject to the boundary conditions introduced by both the radiating antenna and its surrounding environment. solving such antenna problems have been done widely by using frequency–domain techniques (MoM, finite element, etc. .). On the other hand, the FDTD, which is a time–domain technique, has been used in the analysis of large number of electromagnetic scattering and interaction applications, as presented in Chapter II, and relatively little has been reported toward applying FDTD to model antenna radiation. Maloney *et. al.* [92] used the FDTD method to analyze radiation by axially symmetric two–dimensional problems, where he modeled cylindrical and conical monopole antennas. Katz *et. al.* [52], also used the FDTD method to model various radiating structures that included two– and three–dimensional waveguides, flared hornes and a two–dimensional parabolic reflector. Tirkas and Balanis [53] used the FDTD technique to model and predict the radiation pattern of wire and aperture antennas and were compared with measured radiation patterns.

FDTD modeling has been also extended to provide detailed characterization of microstrip antennas and circuits. Reinex and Bernard [40] used the FDTD method to analyze radiation by a microstrip patch. K. Mei *et. al.* [37,38] used the FDTD to calculate dispersive characteristics of a typical microstrip on a Gallium Arsenide substrate. A Gaussian pulse excitation is used and the effective dielectric constant and characteristic impedance over a large range of frequencies is efficiently obtained via Fourier transform of the time–domain field response. K. Mei *et. al.*, also [54] applied the FDTD to analyze a small broadband and flared antenna on a substrate. In [93] an efficient time–domain method based upon the combination of the FDTD with an appropriate periodic boundary condition, is developed and is successfully applied to time–domain characterization of a phased array of tapered slots. The FDTD method was also applied successfully on microstrip circuits in [39,94, and 95].

An important aspect of microstrip patch antennas lies in the feeding (exciting) of these structures. The location and the type of the feeding network will determine what field modes and polarization are excited by the microstrip structure. Hence, the field levels in the co–polar and cross–polar radiation patterns of the patch antenna will be directly related to the location and type of the feeding network.

In this chapter, a rectangular microstrip patch antenna is considered. This patch antenna is excited by using a transmission line of characteristic impedance Z_o located at a distance d from the center of the patch as illustrated in Fig. 5.1. The effect of scanning the transmission line along the patch length on the level of the co–polar and cross–polar radiation field patterns will be investigated for three rectangular patch dimensions.

Fig. 5.1   Rectangular microstrip patch antenna with a transmission line feed.
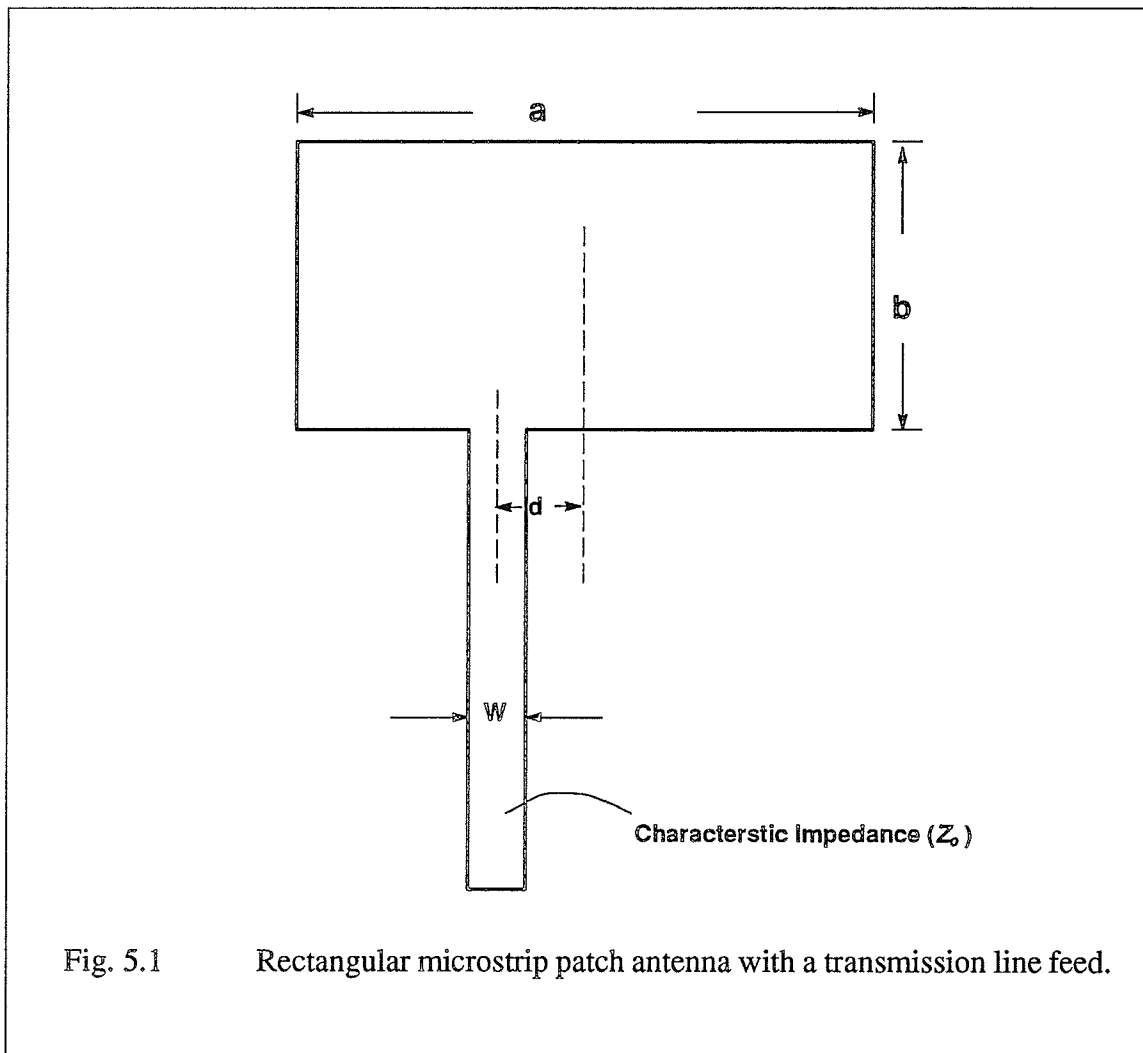
5.1. Analysis of a Rectangular Microstrip Patch Antenna.

In this section, the modeling procedure inside the FDTD lattice of the microstrip structure considered in this investigation will be presented. Also, the procedure followed in computing the circuit and radiation parameters of the microstrip structure will be discussed.

i) *Modelling Procedure.*

Figure 5.2 shows the geometry of the rectangular microstrip patch antenna and its corresponding dimensions and physical parameters considered in this analysis. The patch is mapped into a (60 × 95 × 25) FDTD lattice. The upper and side walls of the lattice are truncated with first–order 'One–Way' wave equation ABC described in Chapter III, while a conducting surface is imposed on the bottom surface of the lattice. Applying ABC on the side walls of the FDTD lattice will approximate the assumption of an infinite substrate and ground plane in this analysis. In this case, surface waves propagating inside the substrate will be absorbed at the lattice walls with no reflection nor diffraction as if the substrate is infinite in the x– and y–directions. Figure 5.3 demonstrates the modeling procedure of the rectangular patch together with the excitation transmission line in the FDTD lattice.

The excitation pulse used in this study has been chosen to be a Gaussian pulse. This choice is based on the Gaussian pulse having a smooth waveform in time, and its Fourier transform is also a Gaussian pulse centered at zero frequency. These unique properties make it a perfect choice for investigating the frequency–dependence characteristics of microstrip structures through the Fourier transform of the pulse response. The Gaussian pulse used in this investigation has the following expression.

$$E_z(t) = 100 \; Exp -\left[\left(t - 100 \times 10^{-12}\right) / \left(30 \times 10^{-12}\right)\right]^2 \; (V/m) \qquad (5.1)$$

Figure 5.4 shows the Gaussian shape waveform together with its corresponding frequency spectrum. The choice of the spatial step sizes of Δx, Δy, and Δz shown in Fig. 5.3 is done to model with sufficient accuracy

– the microstrip structure

– the fields in the dielectric substrate and above the patch

– the frequency response of the microstrip structure up to $\approx 13GHz$. ($\lambda_{min} = 30 \times \Delta x$, *i.e.* the shortest wavelength is modeled approx. by *30* spatial cells).

$$\frac{W}{h} = 2.865 \quad (\; Z_o = 49\Omega, \quad Wheeler's \; [96] \;)$$

$\epsilon_r = 2.5$

h=1.587mm

Conducting plane

a = 22.66mm

b = 19.33mm

L = 29.70mm   2d / a = 0.466

W

R   R′

Fig. 5.2   Geometry and dimensions of a rectangular patch antenna with
a transmission line feed (*2d/a = 0.466*).

$$\Delta x = 0.75583 \text{ mm} \qquad nx = 60$$
$$\Delta y = 0.74361 \text{ mm} \qquad ny = 95$$
$$\Delta z = 0.52916 \text{ mm} \qquad nz = 25$$
$$\delta t = \Delta z / 2c$$

Fig. 5.3   Modeling procedure of the microstrip rectangular patch antenna inside a FDTD lattice.
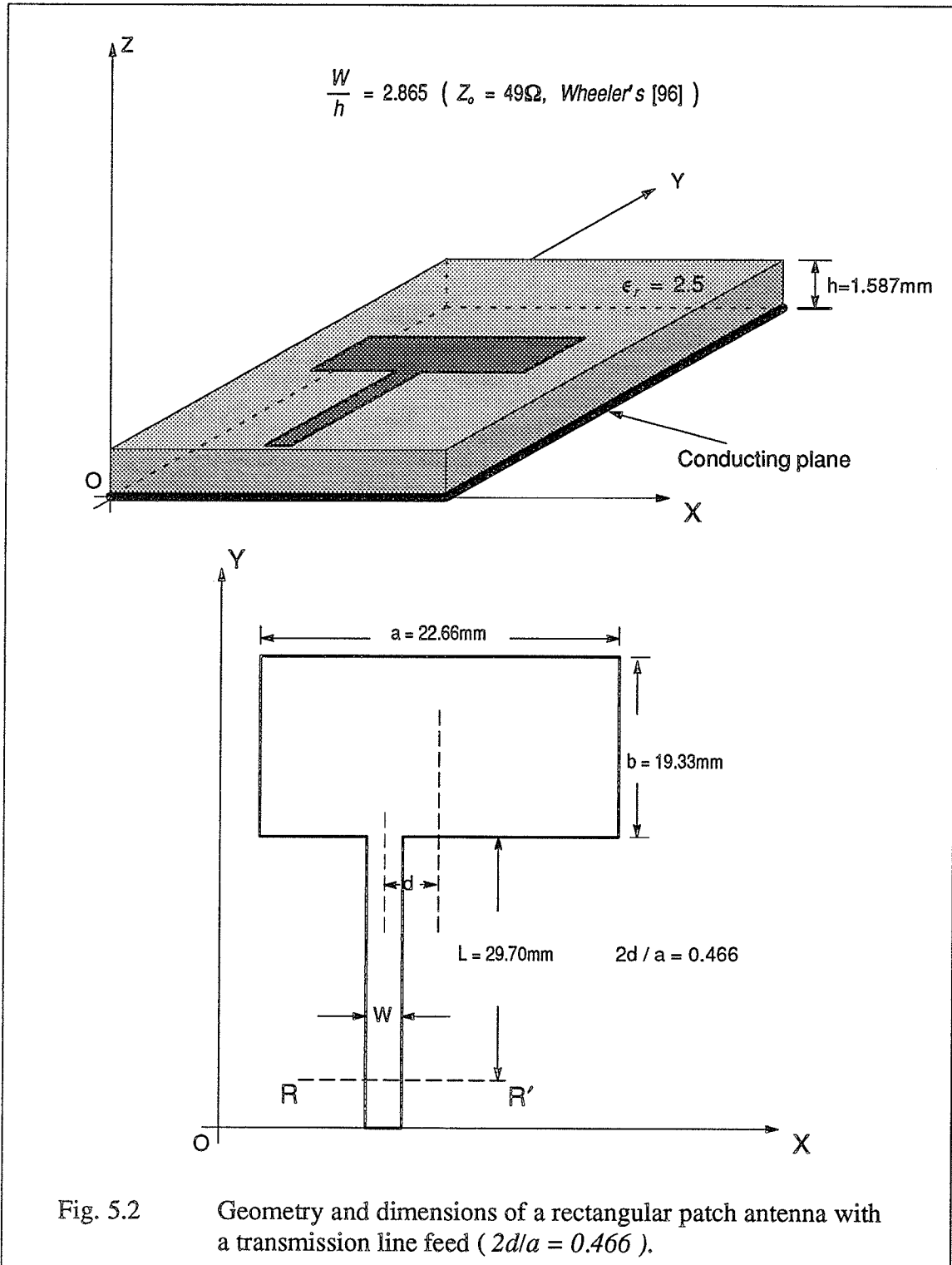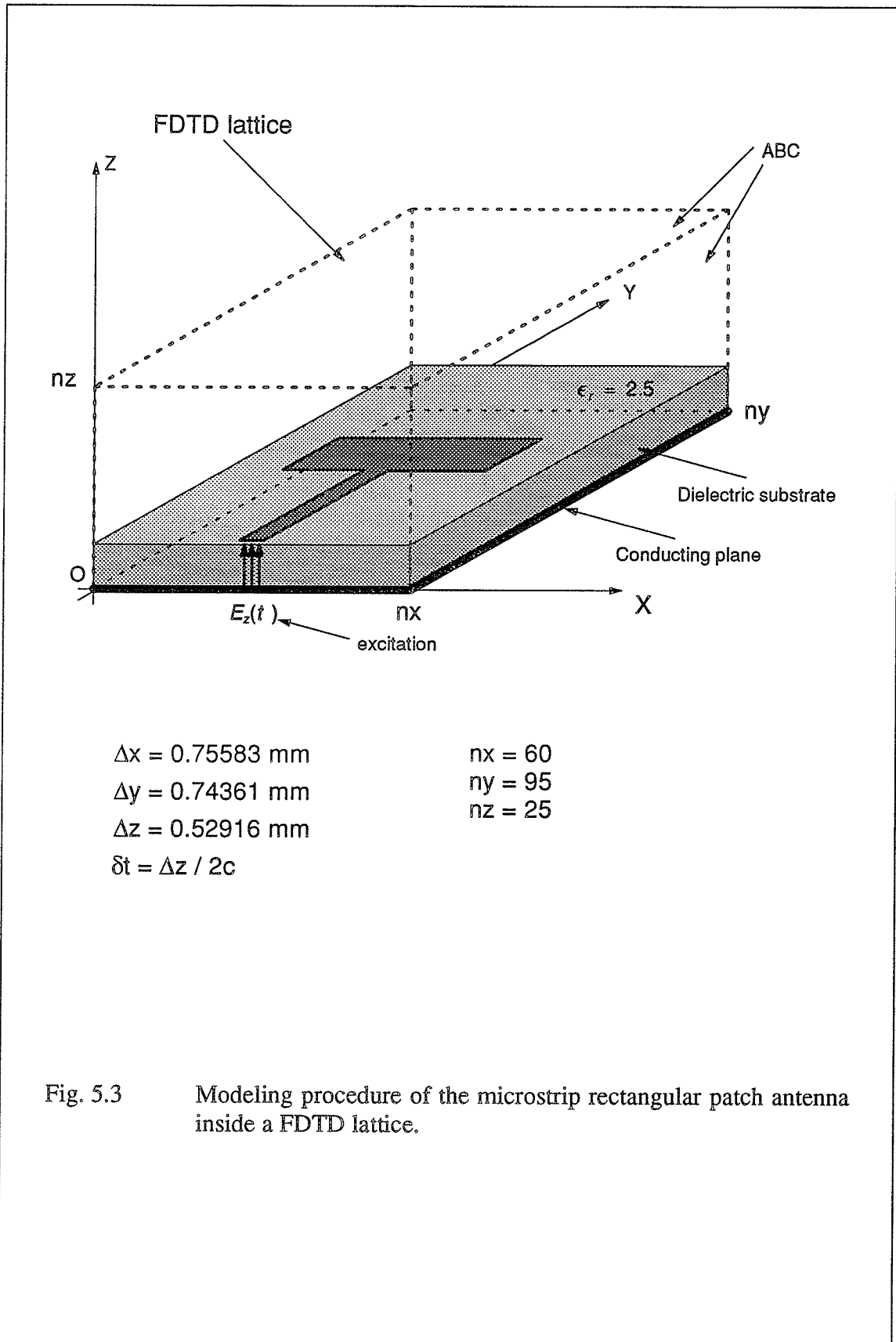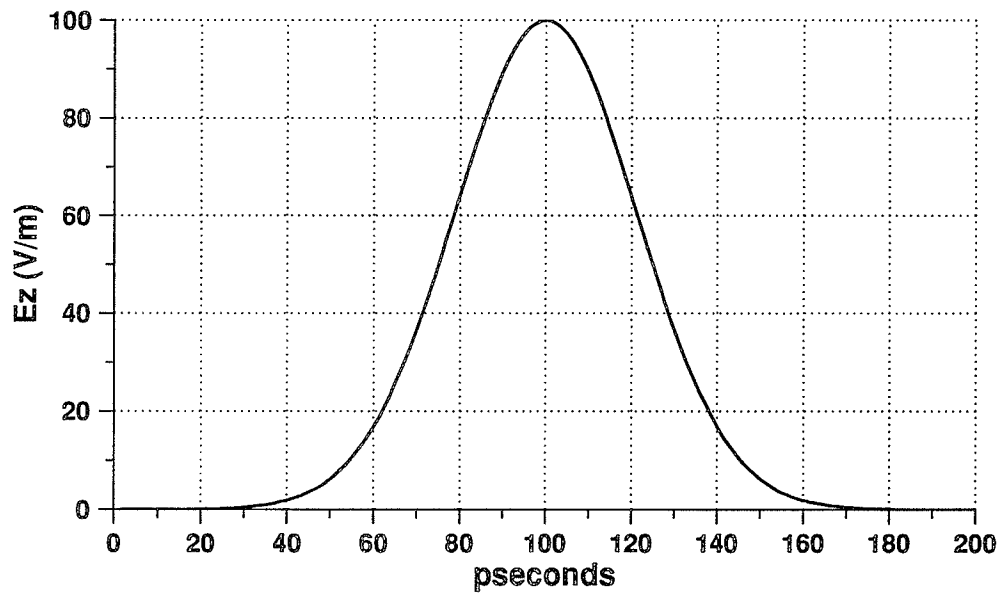
$$E_z(t) = 100 \; Exp \; -\left[\left(t - 100 \times 10^{-12}\right) \Big/ \left(30 \times 10^{-12}\right)\right]^2 \; (V/m)$$

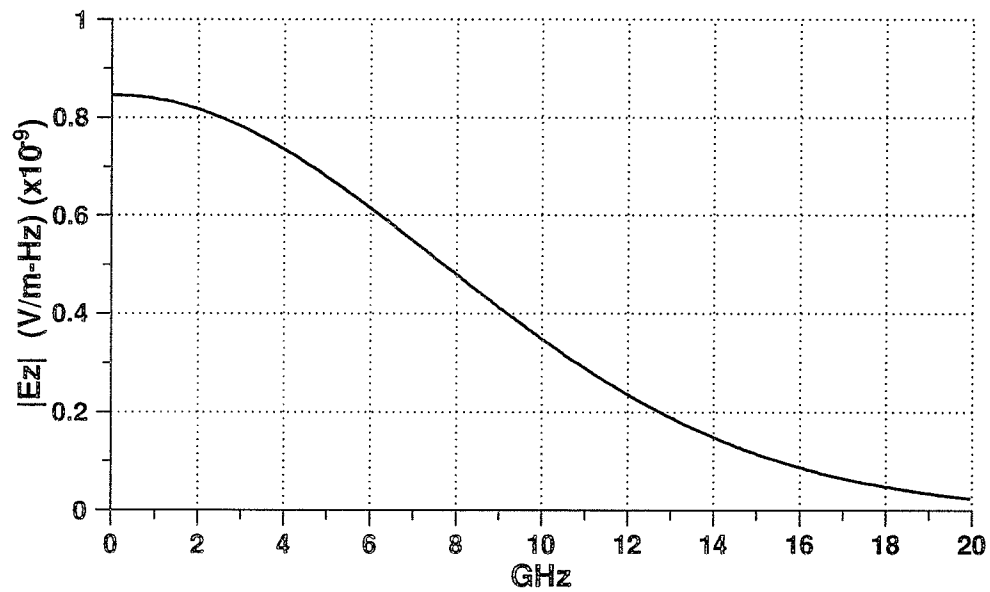Fig. 5.4   The Gaussian pulse time distribution and its corresponding frequency spectrum used in the FDTD modeling.

Initially, all fields in the FDTD lattice are set to zero, the electric field E_z is switched on, with a Gaussian shape variation, below the transmission line in the oxz plane as illustrated in Fig. 5.3. The excitation pulse will propagate along the transmission line until it reaches the transmission line rectangular patch junction where due to the mismatch at this junction part of the incident pulse will be reflected back to the excitation plane where it will be absorbed. It should be noted that after the launching of the excitation pulse into the microstrip structure, the excitation plane is switched into an absorbing plane. The record of the incident and reflected response is done at the reference plane indicated in Fig. 5.2 at $L=0.0297m$ (40ΔY) from the patch. The transmission line is chosen long enough such that a separation in time between the incident and the reflected responses is obtained.

Figure 5.5 shows the time variation of E_z electric field component at different positions along the propagation direction just below the transmission line structure. The dispersive properties of the microstrip are observed clearly from the distortion of the pulse as it travels away from the feeding plane. A useful information that can be obtained from the field response of a transmission line, is the variation of the characteristic impedance Z_o with frequency. Wheeler expression of $Z_o = 50\Omega$ presented in [96] is used initially to compute the corresponding dimensions, w / h, of the transmission line. In our FDTD computations, the variation of Z_o with frequency is obtained via the ratio of $V(\omega) / I(\omega)$. $V(\omega)$ is the Fourier transform of the voltage response computed from the line integral of the vertical electric field under the center of the strip. $I(\omega)$ is the Fourier transform of the current response defined as the loop integral of the magnetic field around the metallic strip of the transmission line. Figure 5.6 shows the spectrum of $Z_o(\omega)$ of the transmission line used in this study agreeing favorably with the pre designed value of Z_o.

Figure 5.7 shows three–dimensional plots of the space distribution of the E_z field component in a plane just below the microstrip structure of Fig. 5.3. These plots are for different FDTD time steps showing the propagation of the excitation pulse and its interaction with the rectangular patch geometry.
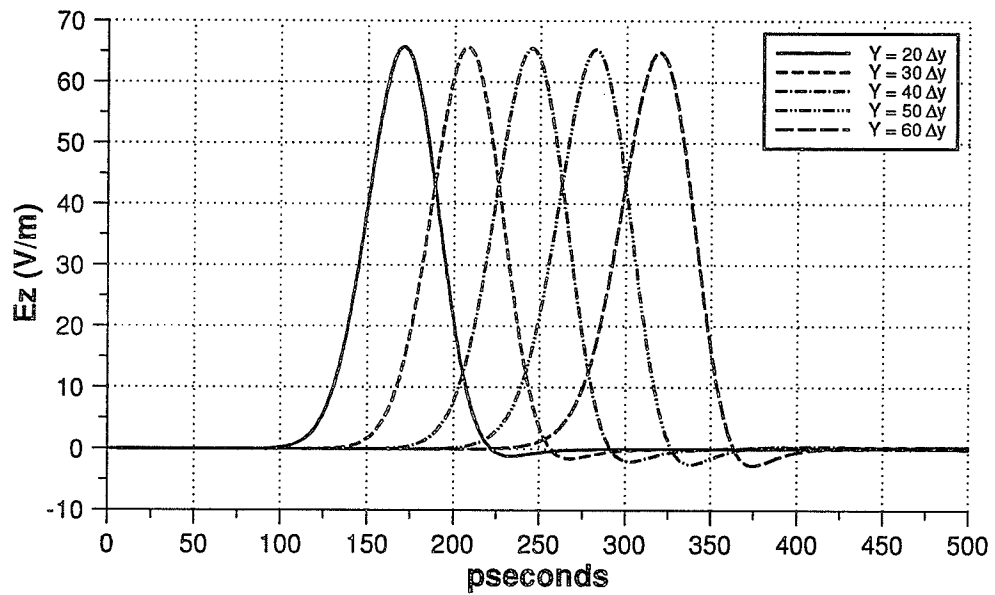
Fig. 5.5   Time variation of E_z at different positions along the direction of propagation.
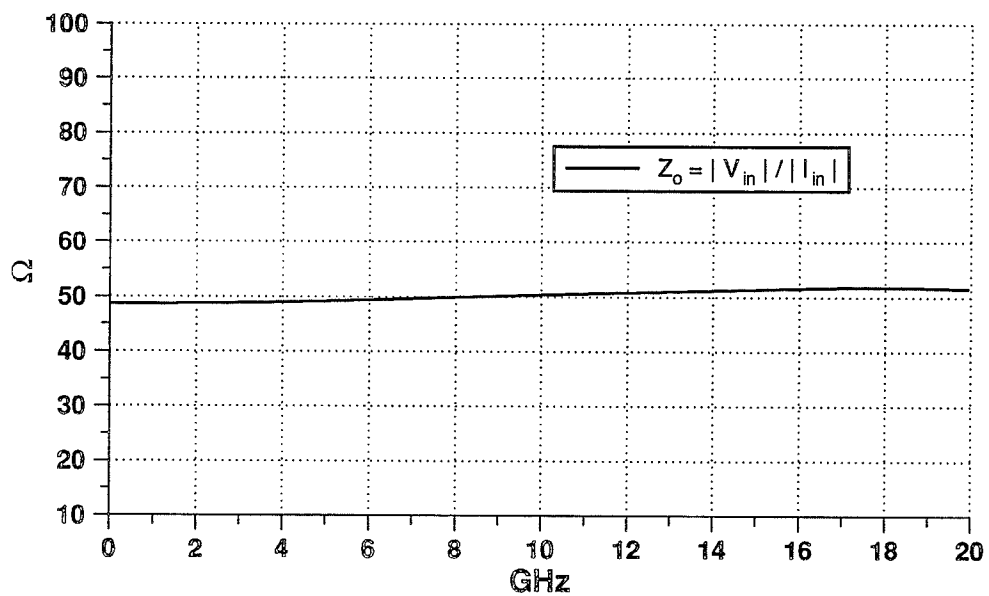

Fig. 5.6   Characteristic impedance Z_o of the feeding transmission line. ($\epsilon_r = 2.5$, $w/h = 2.865$)
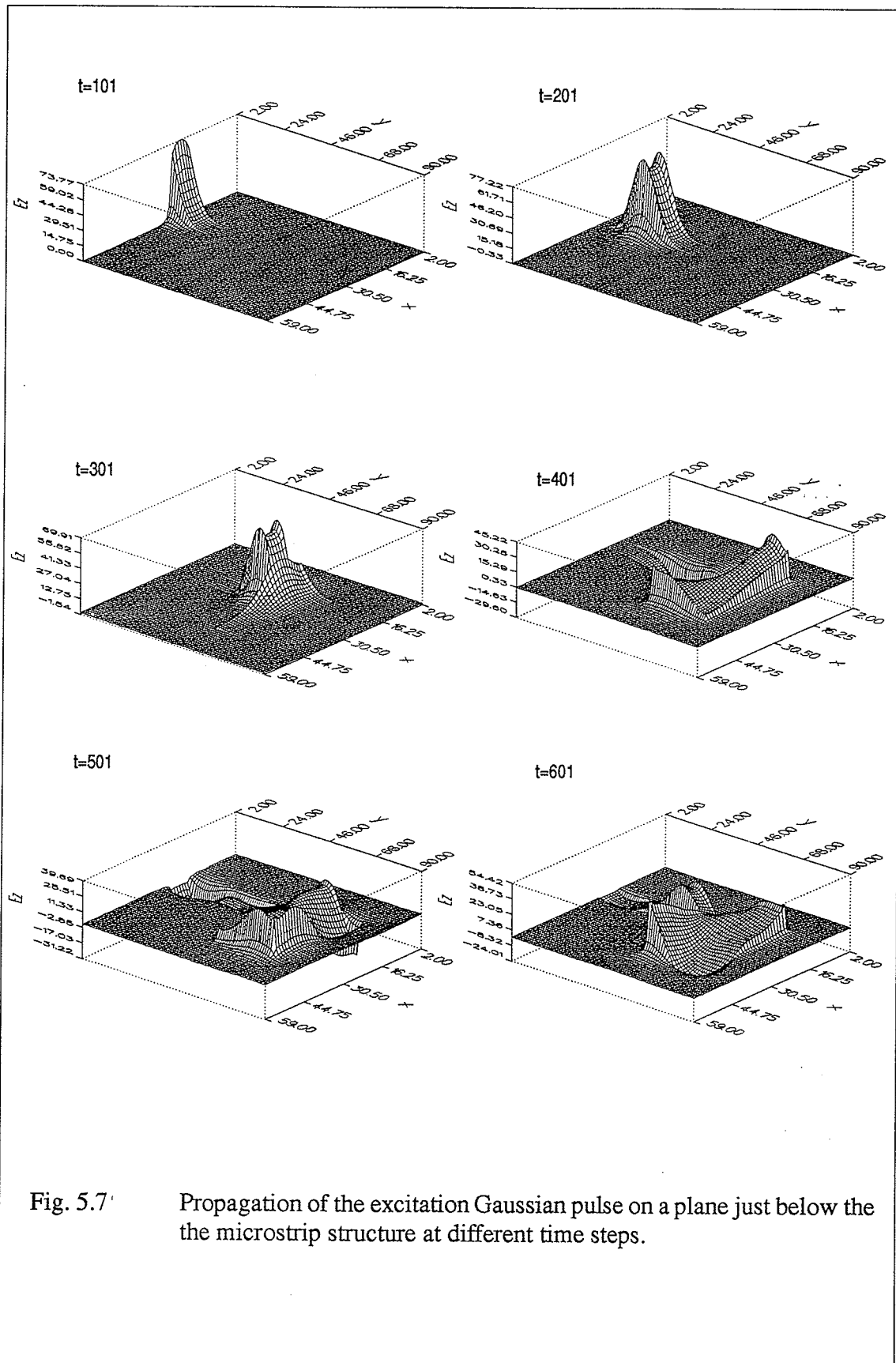
Fig. 5.7   Propagation of the excitation Gaussian pulse on a plane just below the the microstrip structure at different time steps.

ii) Input Parameters.

An important information can be also obtained from the FDTD computation of the microstrip structure considered in this work is the return loss (S_{11}) and the input impedance (Z_{in}) over a range of frequencies. This information is obtained from the field response data at the reference plane RR', Fig. 5.2, at the feeding transmission line. Figure 5.8 shows the voltage time response at RR' showing clearly the incident and reflected responses. In this case the return loss $S_{11}(\omega)$ can be obtained from the following expression via Fourier transformation,

$$S_{11}(\omega) = \frac{FT\left\{V_{ref}(t)\right\}}{FT\left\{V_{inc}(t)\right\}} \tag{5.2}$$

where $V_{inc}(t)$ and $V_{ref}(t)$ are the incident and reflected voltage responses at the feeding line, respectively. *FT* correspond to the Fourier transform operator. These voltage responses can be obtained by 'windowing' (selecting) the desired response from the response data of Fig. 5.8.

Fig. 5.8   The voltage response at the feeding transmission line at the reference plane RR' (Fig. 5.2).
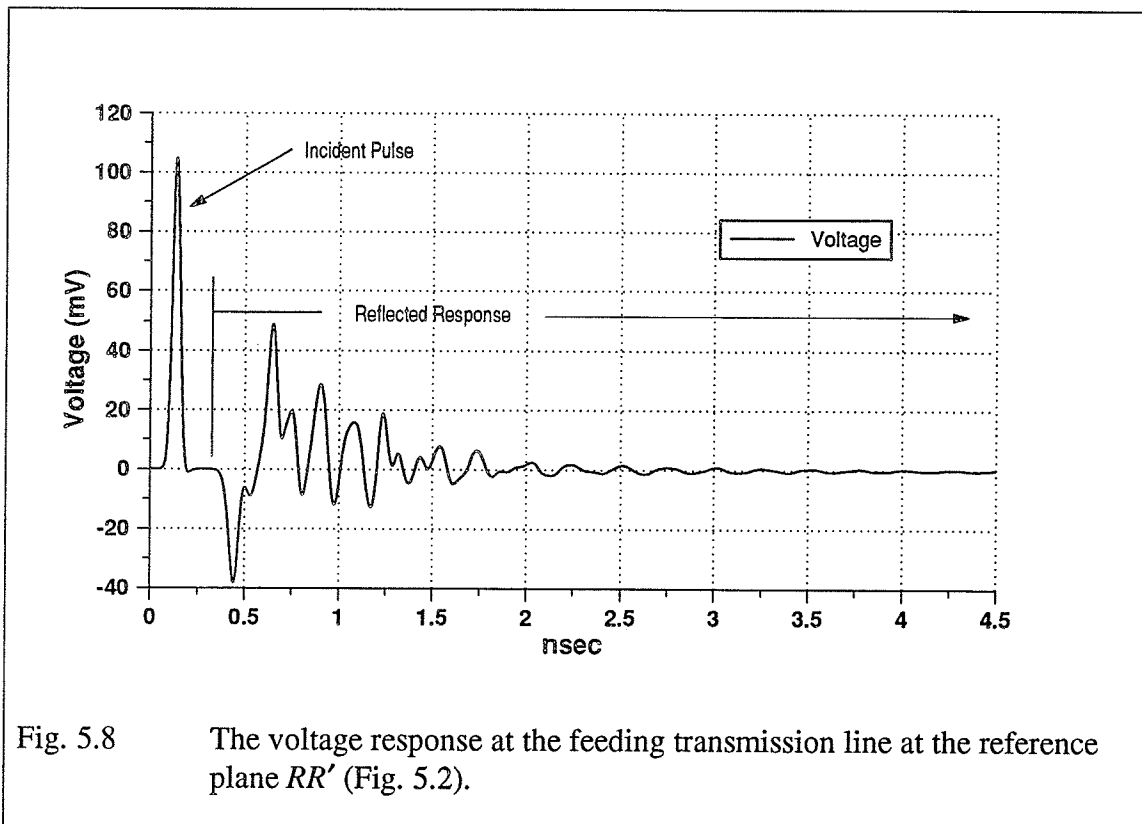
The input impedance Z_{in} of the patch antenna can be calculated from $S_{11}(\omega)$ calculation by transforming the reference plane to the edge of the rectangular patch antenna,

$$Z_{in} = Z_o \frac{1 + S_{11}e^{j2kL}}{1 - S_{11}e^{j2kL}} \qquad (5.3)$$

k being the wavenumber on the microstrip, L is the length from the patch to the reference plane RR'. A value of $Z_o = 49\Omega$ and an effective permitivity of 2.15 are assumed to calculate Z_{in}. Figure 5.9 shows the plot of $|S_{11}|$ and Z_{in} at the patch antenna of Fig. 5.2 for a range of frequencies. A good match is observed at $f = 4GHz$, with $Re[Z_{in}] \approx 50\Omega$, and $Im[Z_{in}] \approx 0$, respectively.

Fig. 5.9   Return loss ($|S_{11}|$) and input impedance (Z_{in}) of the rectangular patch. ($2d/a = 0.466$)
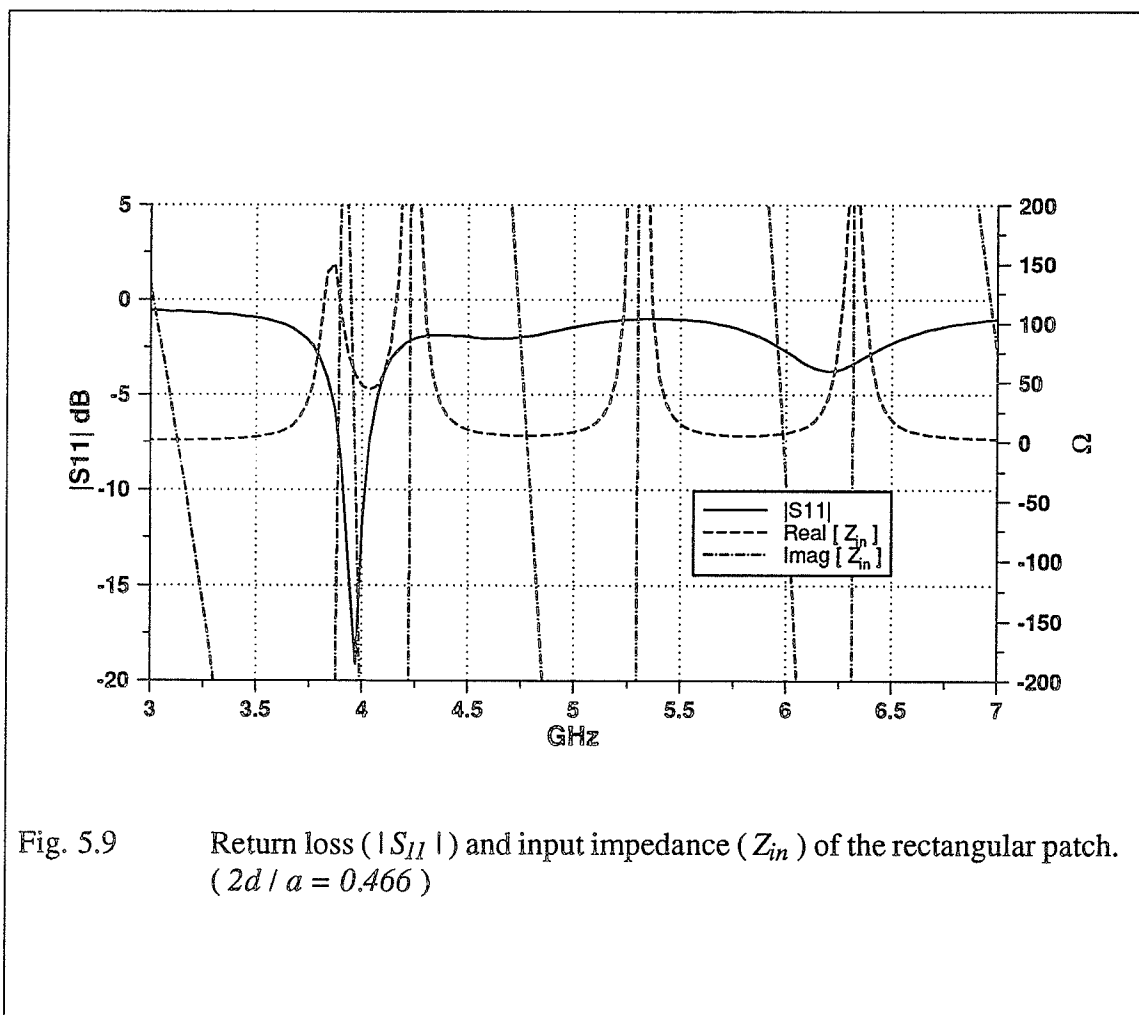
iii) Far–Field Calculations.

The far–field radiation pattern of a microstrip antenna can be obtained with the FDTD method by applying a flexible and straight forward near–field to far–field transformation [43]. The near–field information required for such transformation is a natural product of FDTD computations. The electric (E) and the magnetic (H) field components inside the FDTD lattice and lying on a surface S_p enclosing a modeled target, Fig. 5.10, will represent the equivalent magnetic ($J_{p\ eq}$) and electric ($M_{p\ eq}$) sources on S_p, respectively . According to [97] these quantities are obtained by

$$J_{p\ eq}\ (r\ ) = \hat{n} \times H\ (r\ ) \tag{5.4a}$$

$$M_{p\ eq}\ (r\ ) = -\hat{n} \times E\ (r\ ) \tag{5.4b}$$

where $\hat{n}$ is the outward unit normal vector at the surface S_p. The E and H field components represent the scattered or the total field values depending on the FDTD lattice region on which S_p lies in. The far–field will be given by transforming of the equivalent sources of (5.4) over the free space Green's function as illustrated in [79].

Fig. 5.10   Electromagnetic equivalence to transform near–field to far–field.
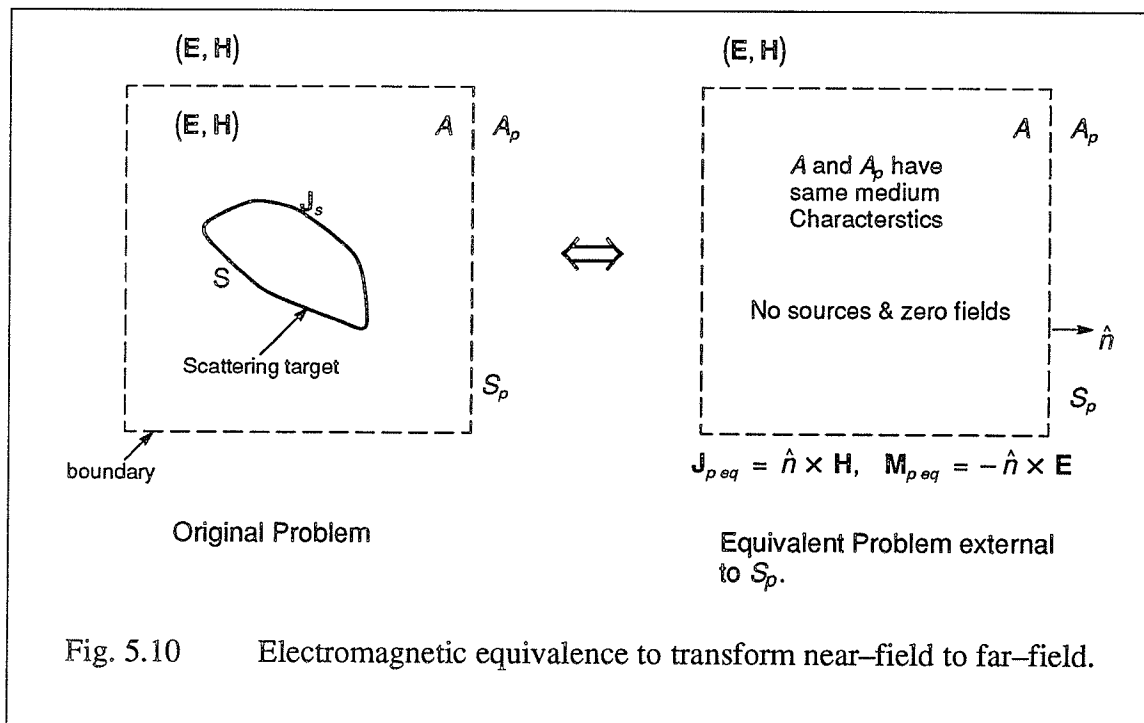
For regions A and A_p of Fig. 5.10 having μ_o and ϵ_o as the medium characteristics with wavenumber $k_o = \dfrac{2\pi}{\lambda_o}$, and intrinsic impedance $\eta_o = 120\pi$ the far–field expressions for θ and ϕ polarization will be given as,

$$E_\theta = \left(-jk_o\eta_o\right)\left[A_\theta + \frac{F_\phi}{\eta_o}\right] \qquad (5.5a)$$

$$E_\phi = \left(-jk_o\eta_o\right)\left[A_\phi + \frac{F_\theta}{\eta_o}\right] \qquad (5.5b)$$

where

$$A_\theta = A_x \cos\theta \ \cos\phi + A_y \cos\theta \ \sin\phi - A_z \sin\theta \qquad (5.6a)$$

$$F_\theta = F_x \cos\theta \ \cos\phi + F_y \cos\theta \ \sin\phi - F_z \sin\theta \qquad (5.6b)$$

$$A_\phi = -A_x \sin\phi + A_y \cos\phi \qquad (5.6c)$$

$$F_\phi = -F_x \sin\phi + F_y \cos\phi \qquad (5.6d)$$

and $\mathbf{A}$ and $\mathbf{F}$ are the magnetic and electric vector potential introduced in [79], respectively. In the far–field region the vector potentials are given by

$$\begin{bmatrix} \mathbf{A} \\ \mathbf{F} \end{bmatrix} = \left(\frac{e^{-jk_o r}}{4\pi \ r}\right) \int\int_{S_p} \begin{bmatrix} \mathbf{J}_{p\,eq} \\ \mathbf{M}_{p\,eq} \end{bmatrix} e^{jk_o r' \cos\zeta}.ds'_p \qquad (5.7a)$$

$$r' \cos\zeta = \left(x' \cos\phi + y' \sin\phi\right) \sin\theta + z' \cos\theta \qquad (5.7b)$$

where $\left(x', \ y', \ z'\right)$ is the location of the equivalent sources in cartesian coordinates.

In our case, the far–field pattern of the microstrip patch antenna considered is obtained in a straight forward manner using the procedure described above. In most of the research envolving microstrip patch antennas the sources contributing significantly to the radiation pattern are considered to be located on the aperture plane of the patch antenna. Hence,

only a planer surface located above the patch containing the equivalent sources is considered in the far–field computations. In this case, surface waves on the substrate along with the fields diffracted at the finite ground plane edges are neglected. Using the FDTD method three procedures can be used to compute the far–field radiation pattern of a rectangular patch antenna. Using the modeling procedure of the patch antenna followed in this chapter and described earlier the radiation pattern is obtained by considering the equivalent sources located on a surface that is slightly larger than the patch and is located at three cells above the patch as illustrated in Fig. 5.11a. A second procedure for calculating the radiation pattern of the patch, shown in Fig. 5.11b, is to enclose the patch and a portion of the substrate in a rectangular box whose surfaces will contain the corresponding equivalent sources for the radiation pattern calculation. In this case, the effect of the surface waves on the radiation pattern are accounted for. For this procedure, only the fields diffracted at the edges of a finite ground plane are not accounted for. It should be noted that the ground plane is assumed infinite in this FDTD modeling of the patch antenna, which is not the case in practice. Figure 5.12 shows the radiation patterns of the patch antenna using the two mentioned procedures. This Figure shows the effect of neglecting the surface waves on the co–polar pattern at large angle values ($\theta < -30°$, $\theta > 30°$), but more significantly in the cross–polar field patterns. These patterns are computed at the first and second resonating modes of the patch. The equivalent sources on the near–field surfaces in frequency–domain were obtained by using DFT (Appendix B) from the time–domain data of selected frequencies.
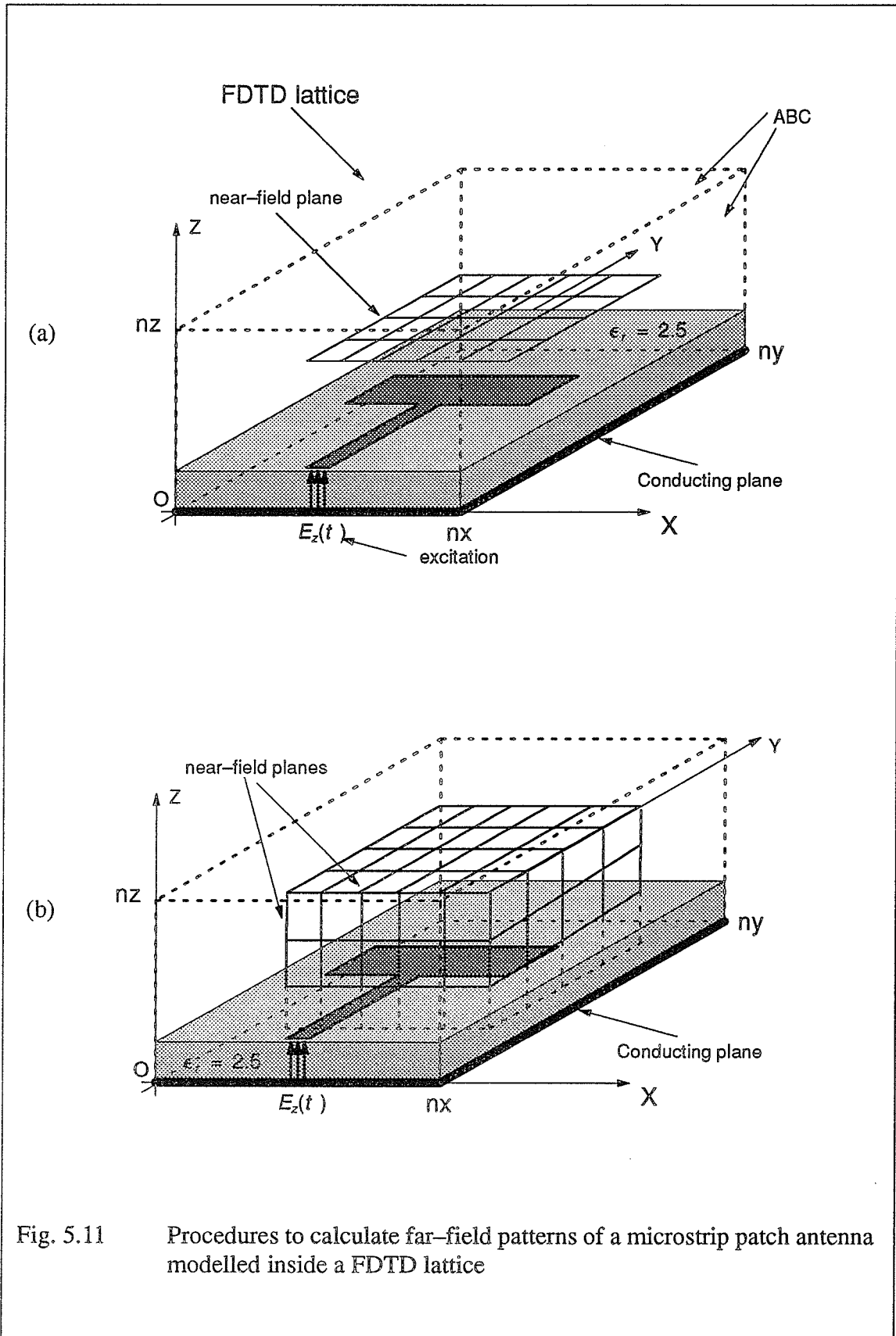
Fig. 5.11   Procedures to calculate far–field patterns of a microstrip patch antenna modelled inside a FDTD lattice
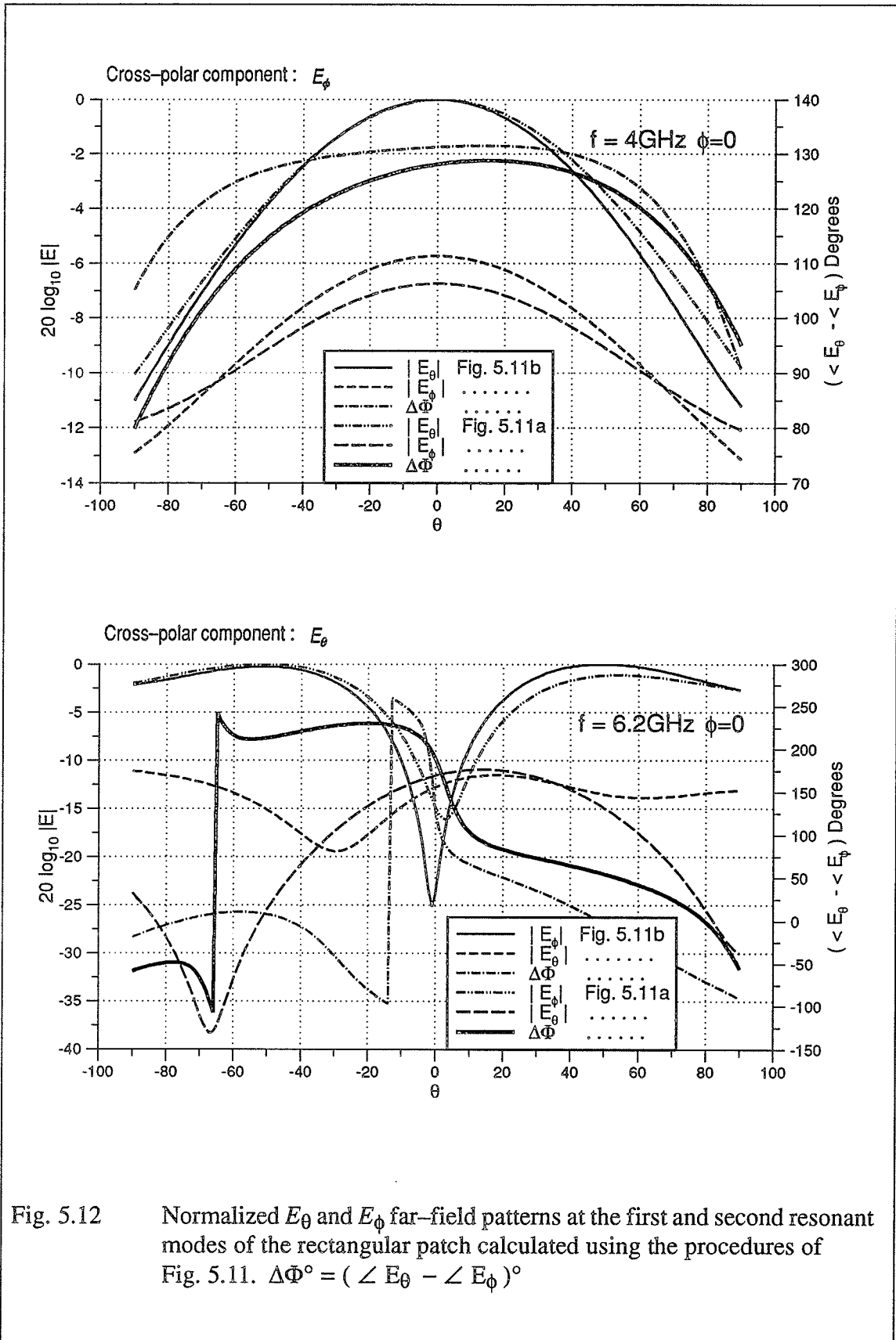
Fig. 5.12   Normalized E_θ and E_ϕ far–field patterns at the first and second resonant modes of the rectangular patch calculated using the procedures of Fig. 5.11. $\Delta\Phi^\circ = (\angle E_\theta - \angle E_\phi)^\circ$

Cross–polar component : E_θ

f = 4GHz ϕ=45

Cross–polar component : E_ϕ

f = 6.2GHz ϕ=45

Fig. 5.12   contd.

Cross-polar component : E_θ

f = 4GHz ϕ=90

Cross-polar component : E_θ

f = 6.2GHz ϕ=90
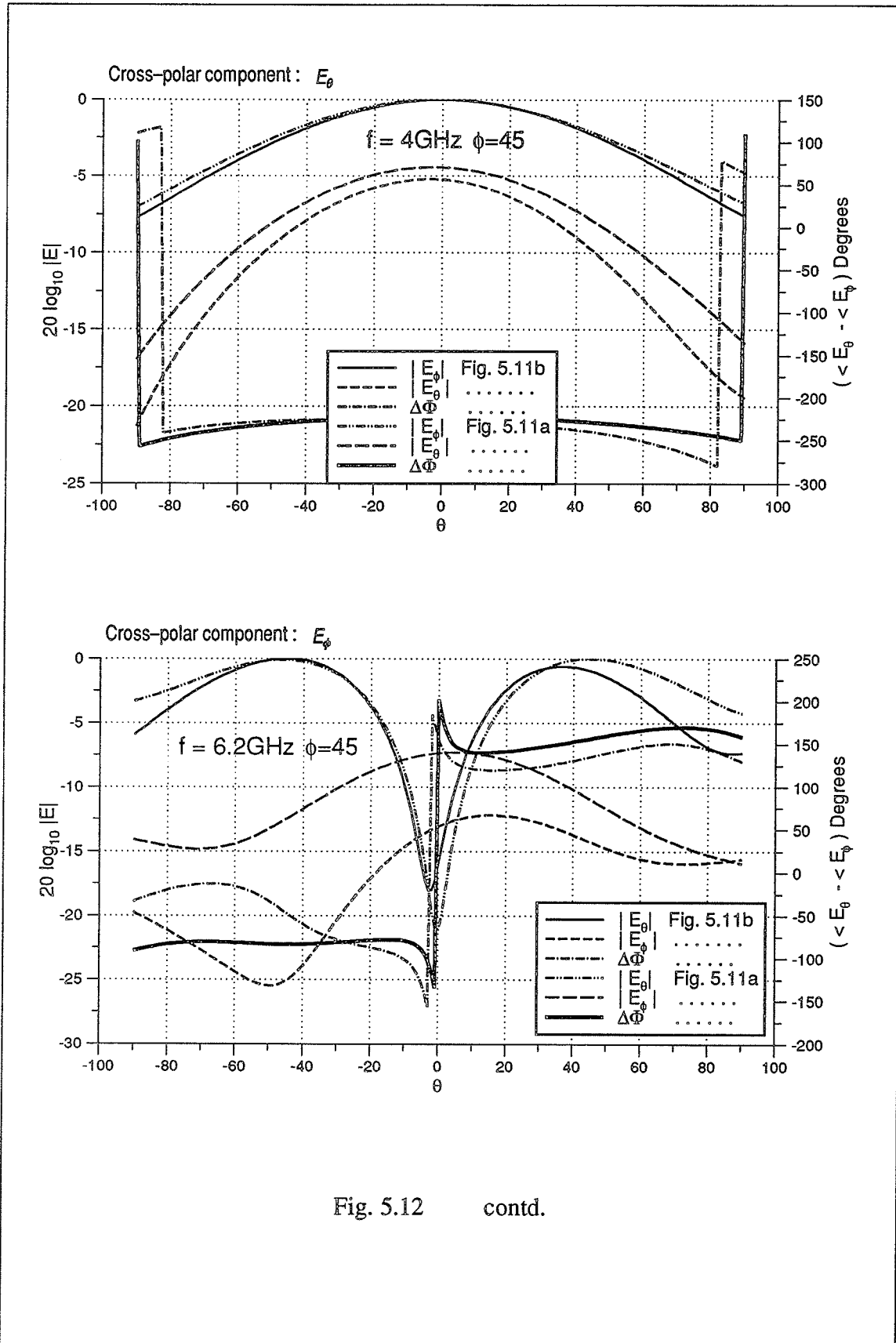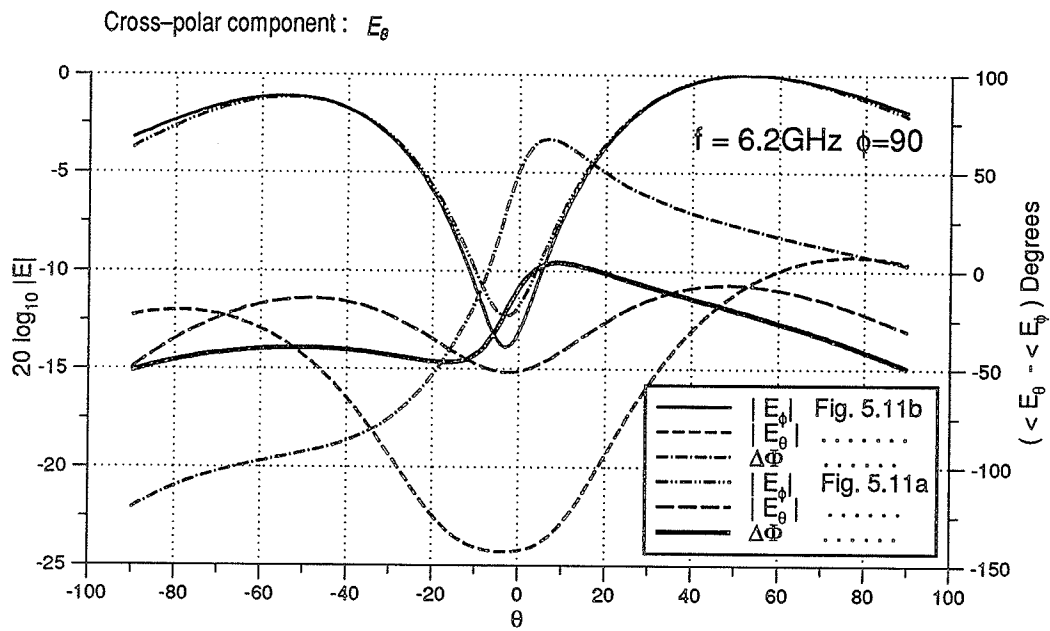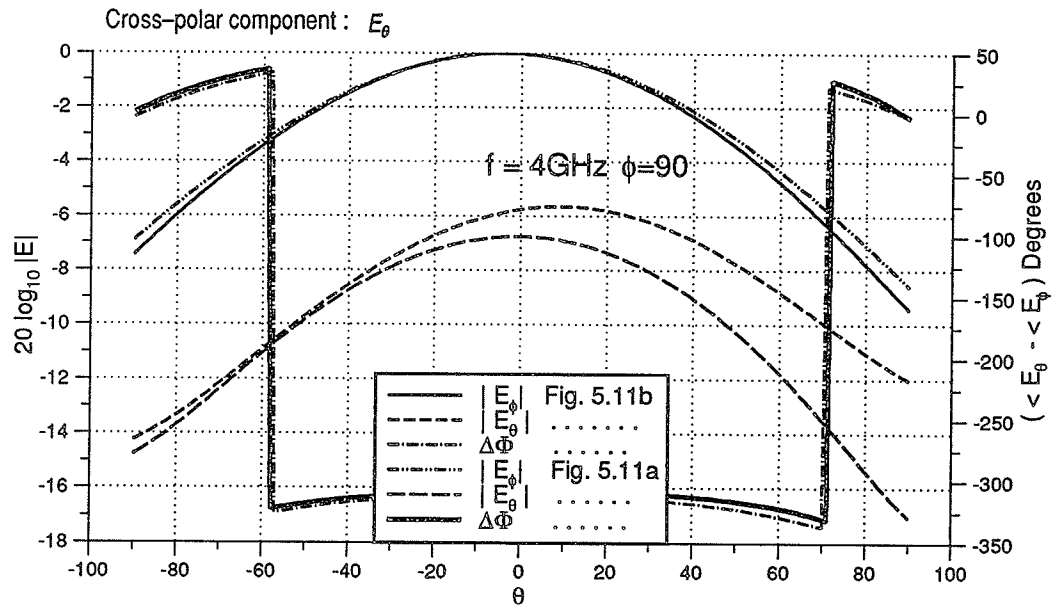
Fig. 5.12   contd.

The third procedure to compute the radiation pattern of a rectangular patch antenna using the FDTD method, is a more realistic procedure but expensive in terms of computer resources. This procedure envolves considering the real geometry of the patch antenna with finite substrate and ground plane, Fig. 5.13. In this case, the antenna geometry will be enclosed in a closed box that contains on its surfaces the equivalent sources for the near–field to far–field transformation. Such procedure will account for all the physical phenomena contributing to the radiation from the antenna geometry. Such a procedure is considered for future work to be done on the analysis of patch antennas.

Fig. 5.13   A realistic procedure to calculate the far–field patterns of a microstrip patch antenna modelled inside a FDTD lattice.

5.2. Results and Discussion.

In this section, the circuit and radiation parameters of the patch antenna of Fig. 5.2 are investigated, and the effect of moving the feeding transmission line along the patch length a (varying d) on the co–polar and cross–polar radiation field patterns will be studied using the procedure of Fig. 5.11b.

i) *Input parameters*

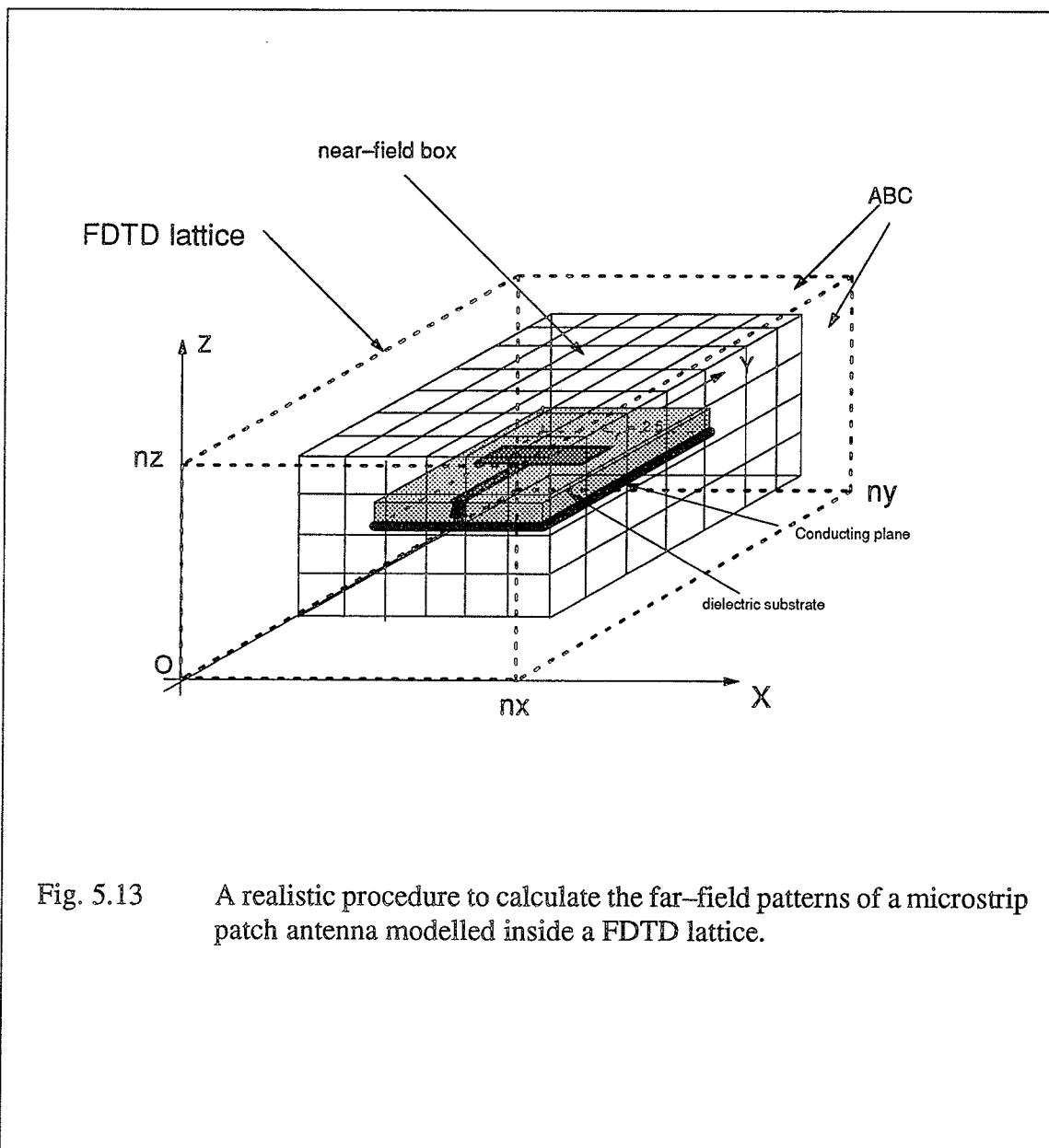The patch geometry considered is that of Fig. 5.2 where the distance d between the center of the transmission line and that of the patch will be the varying parameter. Initially, d is set to zero accounting to a center fed patch, d is then increased till the edge of the transmission line coincided with the patch edge. Figure 5.14 shows plots of return loss ($|S_{11}|$) and the input impedance Z_{in} over a frequency range of *4GHz* for incremental values of *2d/a*. In other words, these plots show the amount of energy absorbed by the patch structure relative to the supplied energy over a range of frequencies. Also, they show the input impedance Z_{in} magnitudes along the side a of the rectangular patch. $d = 0$ feed location, corresponding to a center fed patch, resulted in a *TM_{o1}* mode matched resonance of $\approx 4.6GHz$ due to length b of the patch $\left(f_{01} \approx 1 / (2b \sqrt{\mu_o\ \epsilon}) = 4.9GHz \right)$. For values of *2d/a > 0*, a matched *TM_{10}* mode of $\approx 3.9GHz$ due to length a started to appear $\left(f_{10} \approx 1 / (2a \sqrt{\mu_o\ \epsilon}) = 4.1GHz \right)$, in addition to a *$TM_{11}$* mode $\left[f_{11} \approx \left(1 / \sqrt{\mu_o\ \epsilon} \right) \left(\left[\frac{1}{2a} \right]^2 + \left[\frac{1}{2b} \right]^2 \right)^{\frac{1}{2}} = 6.44GHz \right]$, as well. Larger values of *2d / a* will result in tuning the feed line to a desirable patch input impedance Z_{in} to match the *f_{10}* or *f_{11}* resonant modes. With the feed transmission line characteristic impedance $Z_o \approx$ *50Ω*, Fig. 5.14 shows an improvement in the transmission line–patch matching where a $Re[Z_{in}] \approx 50\Omega$, and $Im[Z_{in}] \approx 0$ is observed for *2d/a = 0.466→0.8* at $f = 4GHz$.
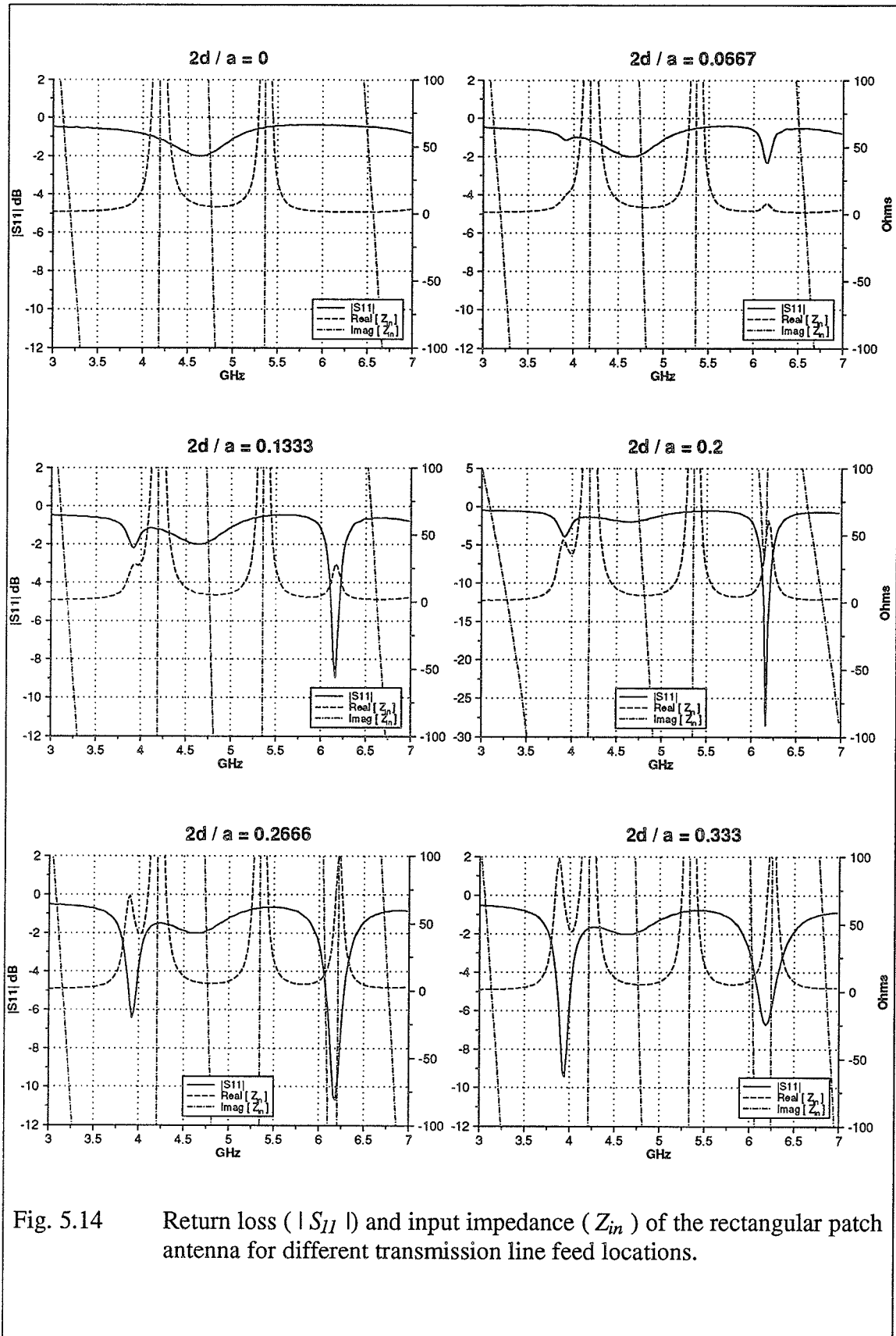
Fig. 5.14   Return loss (| S_{11} |) and input impedance (Z_{in}) of the rectangular patch antenna for different transmission line feed locations.
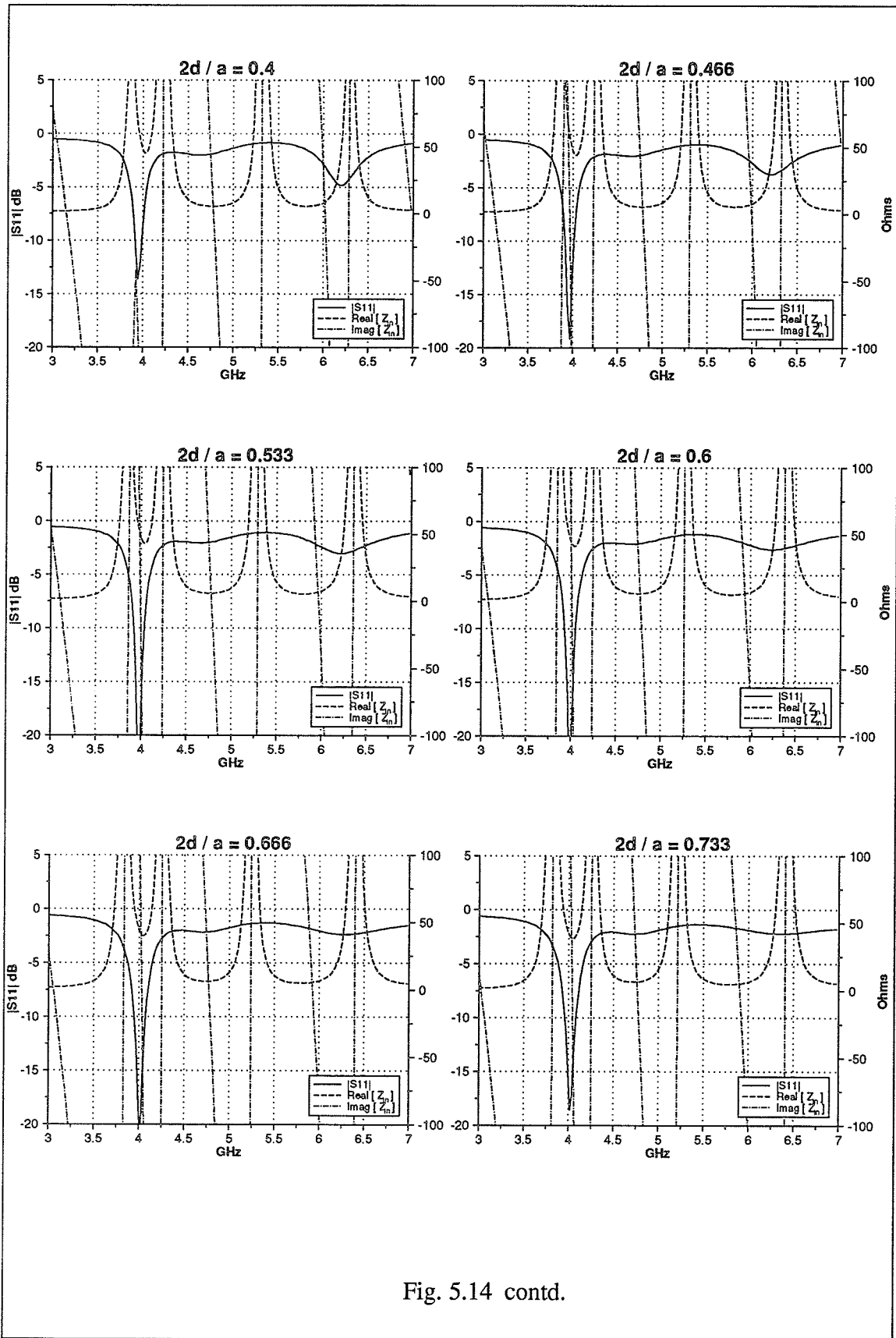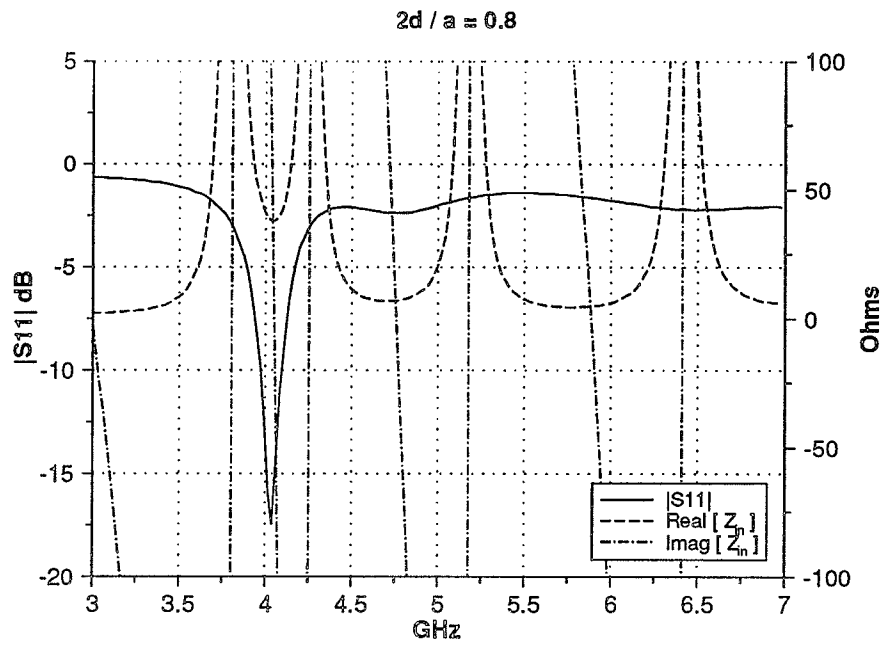
Fig. 5.14 contd.

2d / a = 0.8

Fig. 5.4 contd.

ii) *Near–Field Calculations*

Figure 5.15 shows the near field information on a plane three FDTD cells above the patch and whose sides are five FDTD cells larger. These plots are generated for $f = 4GHz$ which is the matched resonance frequency observed from Fig. 5.14. Figure 5.15 shows both the magnitude and phase of E_x and E_y field components tangential to the ground plane and comprising the aperture field for some values of $2d/a$ corresponding to the feed location along side a of the rectangular patch.

Initially, for the feed location $2d/a = 0$ (center fed) it is observed that E_x field components along side b of the patch are $180°$ out of phase due to the even symmetry of the patch in the x–direction. Hence, the far–field produced by these fields will cancel in the broadside direction of the patch. On the other hand, the E_y field components along side a of the patch are in phase and will add up to give a maximum radiated field in the broad side direction normal to the patch structure. The corresponding far–field pattern is shown in Fig. 5.16. Moving the feed along side a of the patch from its center position $(d = 0)$ will distort the symmetry of the geometry causing the E_x aperture fields along side b not to cancel in the broad side direction, hence, both aperture field components E_x and E_y will contribute to both co–polar and cross–polar radiation field levels of the rectangular patch. Cross–polarization level will vary correspondingly as the feed location is varied. Figure 5.15 shows clearly the change in the aperture field magnitude and phase distribution as the distance d is varied. The corresponding far–field patterns are presented in the next sub–section.

Chapter V

2d / a = 0

2d / a = 0.0667

Fig. 5.15   Magnitude and phase distribution of the aperture fields of the rectangular patch computed for different feed locations at $f = 4GHz$. ($a / b = 1.17$)

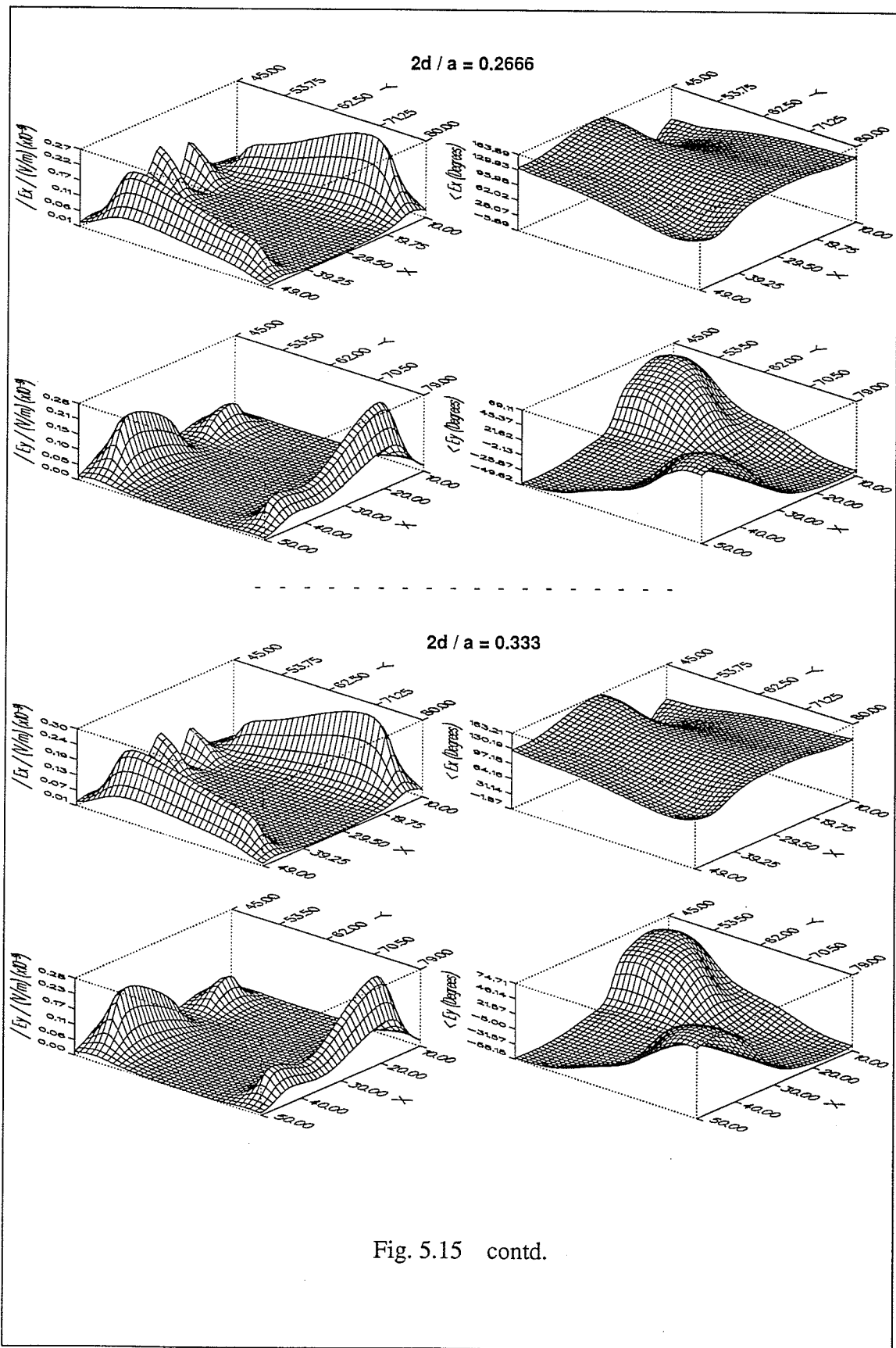**2d / a = 0.2666**

2d / a = 0.333
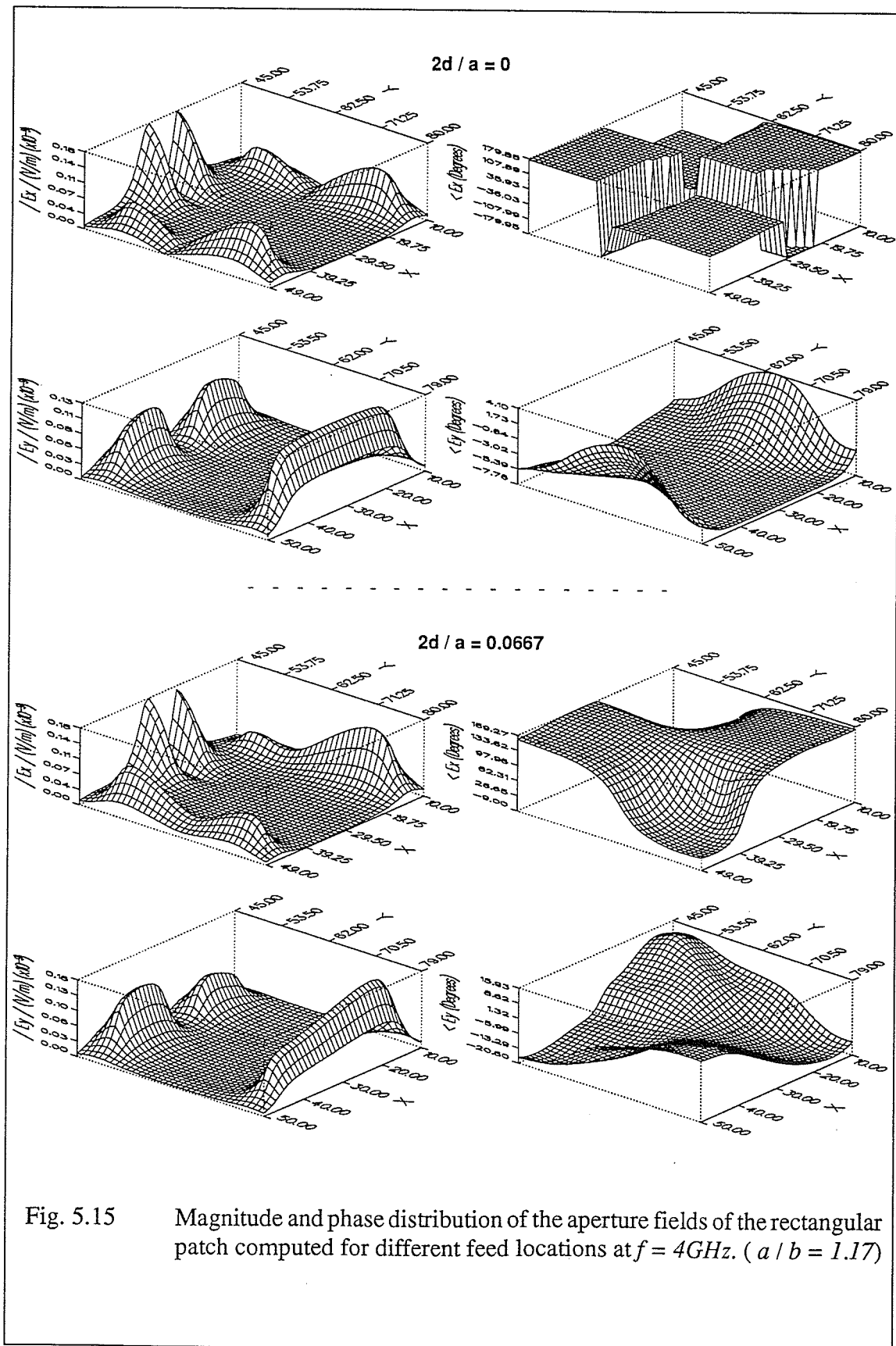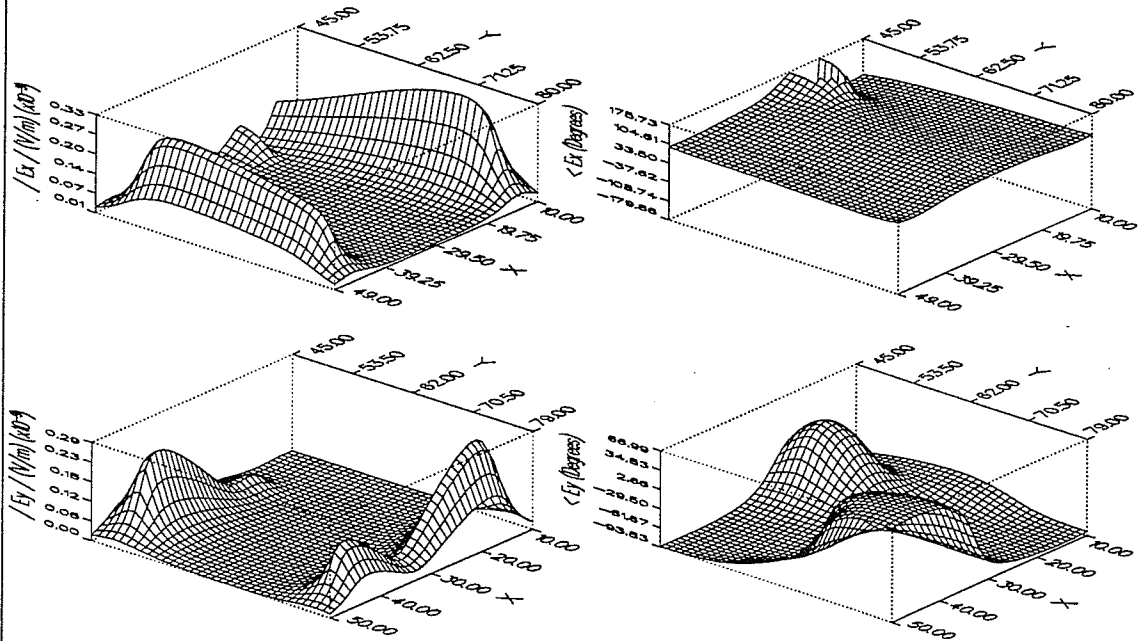
Fig. 5.15   contd.

2d / a = 0.8

Fig. 5.15   contd.

iii) Far–Field Calculations.

Figure 5.16 shows plots of the radiation gain patterns of the patch antenna computed for different values of d in the $\phi = 0°$ and $90°$ planes at $f = 4GHz$. These patterns were obtained using the procedure of Fig. 5.11b and the following gain expressions,

$$Gain\left[E_\theta\ (\theta\ ,\phi\ )\right] = \frac{\frac{4\pi}{2\eta}\ |E_\theta\ (\theta\ ,\phi\ )|^2}{P_{rad}} \tag{5.8a}$$

$$Gain\left[E_\phi\ (\theta\ ,\phi\ )\right] = \frac{\frac{4\pi}{2\eta}\ |E_\phi\ (\theta\ ,\phi\ )|^2}{P_{rad}} \tag{5.8b}$$

where

$$P_{rad} = \int_0^{2\pi}\int_0^{\pi}\ U(\theta\ ,\phi\ )\sin\theta\ d\theta\ d\phi \tag{5.9a}$$

and

$$U(\theta\ ,\phi\ ) \approx \frac{1}{2\eta}\left[\ |E_\theta(\theta\ ,\phi\ )|^2 + |E_\phi(\theta\ ,\phi\ )|^2\ \right] \tag{5,9b}$$

As described earlier, for the case of a center fed patch ($d = 0$) the far–field due to the E_x aperture field component along side b of the patch will cancel in the broadside region, hence the low field levels in Fig. 5.16 for $2d/a = 0$ are attributed to numerical errors, since theoretically such a microstrip geometry will have a *zero* cross–polarization field level in the broadside region of the patch. Fig. 5.16 shows both E_θ and E_ϕ gain patterns in addition to their phase difference, $\Delta\Phi = (\angle E_\theta - \angle E_\phi)°$, between these field components in the $\phi = 0°$ and $90°$ planes of a standard spherical coordinate system.

It is observed that as the value of $2d/a$ is increased the gain values of E_θ and E_ϕ field components change in direct correspondence to the near–field variation observed in Fig. 5.15. For values of $2d/a > 0$ the E_θ gain values in the $\phi = 0°$ plane increased while the E_ϕ gain values decreased. However, for $0.4 < 2d/a \leq 0.8$ both field components maintained a

slightly constant gain values. The variation in the gain level of the E_θ and E_ϕ field components versus the feed location along side a in the $\phi = 0°$ and $45°$ planes is summarized in Fig. 5.17. Figure 5.18(a,b) summarizes the variation of the cross–polar level versus the feed location in the $\phi = 0°$ and $45°$ planes, as well.

The above analysis on rectangular microstrip patch antenna was conducted on a patch geometry having sides dimensions that are almost equal ($a = 22.66$ m.m., $b = 19.33$ m.m.) and having a sides size ratio of $1 < \frac{a}{b} = 1.17 < 1.5$. In the following analysis, rectangular patches whose sides size ratio are $\frac{a}{b} = 1$ (square patch), and $\frac{a}{b} = 1.5$ are considered and the variation of the cross–polar level versus the feed location in the $\phi = 0°$ and $45°$ planes will be computed. The transmission line feeding these patches is identical to the one used earlier. The patches dimensions are chosen such that a matched resonant frequency of $f = 4GHz$ is obtained.

First, the square rectangular patch, $\frac{a}{b} = 1$, is considered and having sides dimensions of $a = b = 22.66$m.m. Fig 5.19 shows sample plots of the magnitude and phase of the E_x and E_y field components tangential to the ground plane and comprising the patch aperture for values of $\frac{2d}{a} = 0$ and 0.4 corresponding to the feed location along side a of the rectangular patch. For $d = 0$ a similar situation to the $\frac{a}{b} = 1.17$ patch occurred, where only the fields along side a of the patch will contribute to the radiated fields in the broadside direction of the patch. For $\frac{2d}{a} = 0.4$, corresponding to an asymmetric feed location, side a tangential electric fields components still dominate over the tangential electric field along side b in contributing to the radiated fields in the broadside direction of the patch. This conclusion can be made by observing Fig. 5.20a showing the cross–polar level versus feed location of the patch in the $\phi = 0°$ where the E_ϕ gain level increases over the E_θ gain values as $\frac{2d}{a}$ is made larger. This is unlike the aperture field behavior of the $\frac{a}{b} = 1.17$ patch where the E_θ gain level increased over the E_ϕ gain level as the feed is moved along side a of the patch as illus-

trated in Fig. 5.18a. Figure 5.20 shows the cross–polar level versus feed location in the $\phi = 45°$ of the square patch, as well.

The last rectangular microstrip patch considered in this analysis is that whose sides ratio is chosen as $\frac{a}{b} = 1.5$, where $a = 22.66m.m$, and $b = 15.108m.m$. Figure 5.21 shows again sample computations of the magnitude and phase distribution of the E_x and E_y field components comprising the patch aperture fields for values of $\frac{2d}{a} = 0$ and 0.333. Again, due to symmetry for feed location $d = 0$, only the fields on side a of the patch contributed to the radiated fields in the broadside direction of the patch, while the radiated fields due to side b canceled out at the broadside direction. Moving the feed line along side a disturbs the antenna symmetry causing the tangential the tangential electric fields along side b of the patch to dominated over those along side a as observed in Fig. 5.22a showing the cross–polar level versus feed location of the considered patch in the $\phi = 0°$ plane where the E_θ gain values increases over the E_ϕ gain values as $\frac{2d}{a}$ ratio is increased. This behavior is similar to that of $\frac{a}{b} = 1.17$ patch but in this case the E_θ gain magnitude relative to the E_ϕ gain magnitude is larger. Fig. 5.22 shows also the cross–polar level versus feed location of the $\frac{a}{b} = 1.5$ patch in the $\phi = 45°$, as well.
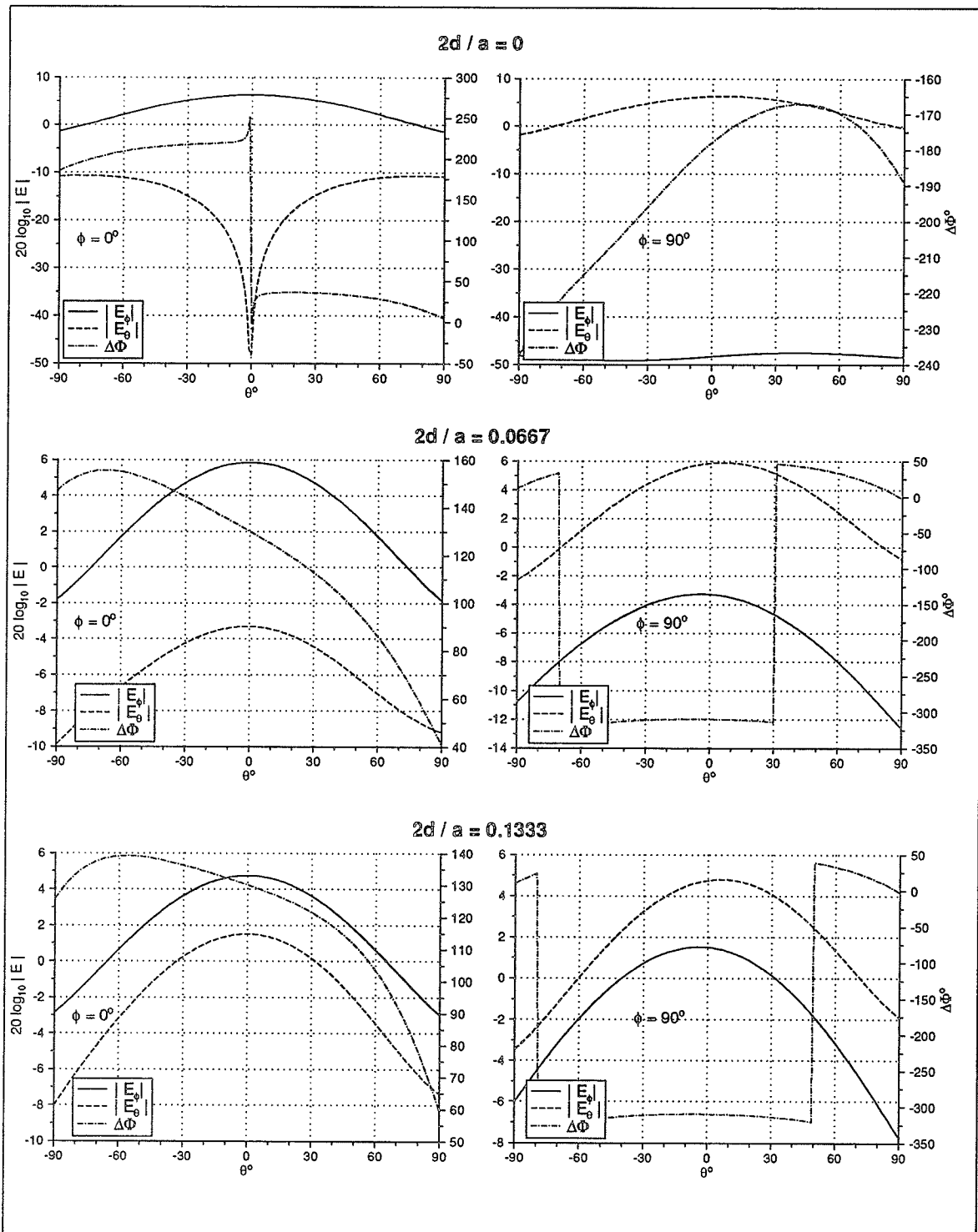
Fig. 5.16   Gain patterns of the rectangular patch computed using procedure of Fig. 5.11b for different transmission line feed location at $f = 4GHz$.

2d / a = 0.4

2d / a = 0.466

2d / a = 0.533
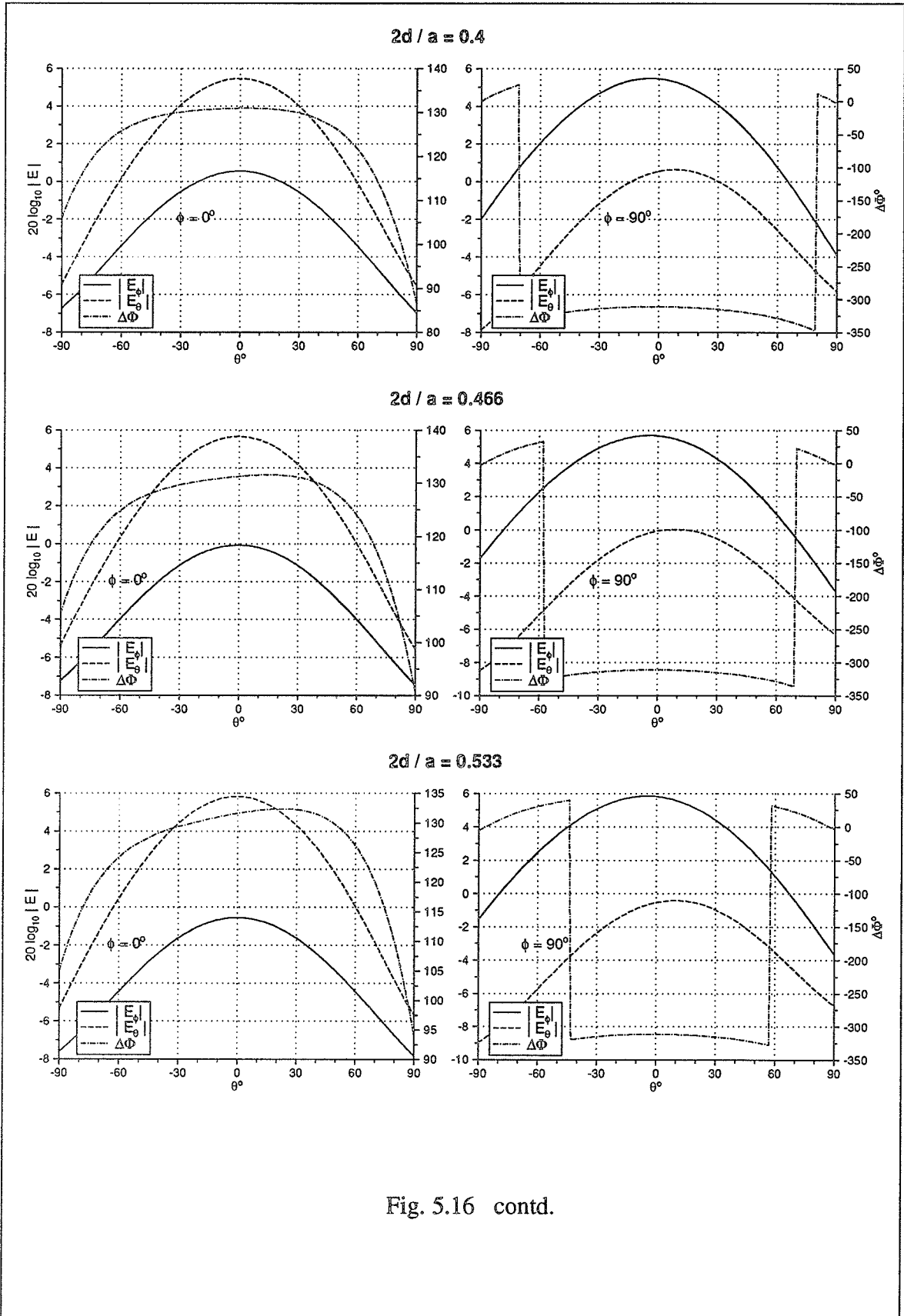
Fig. 5.16   contd.

Fig. 5.16 contd.
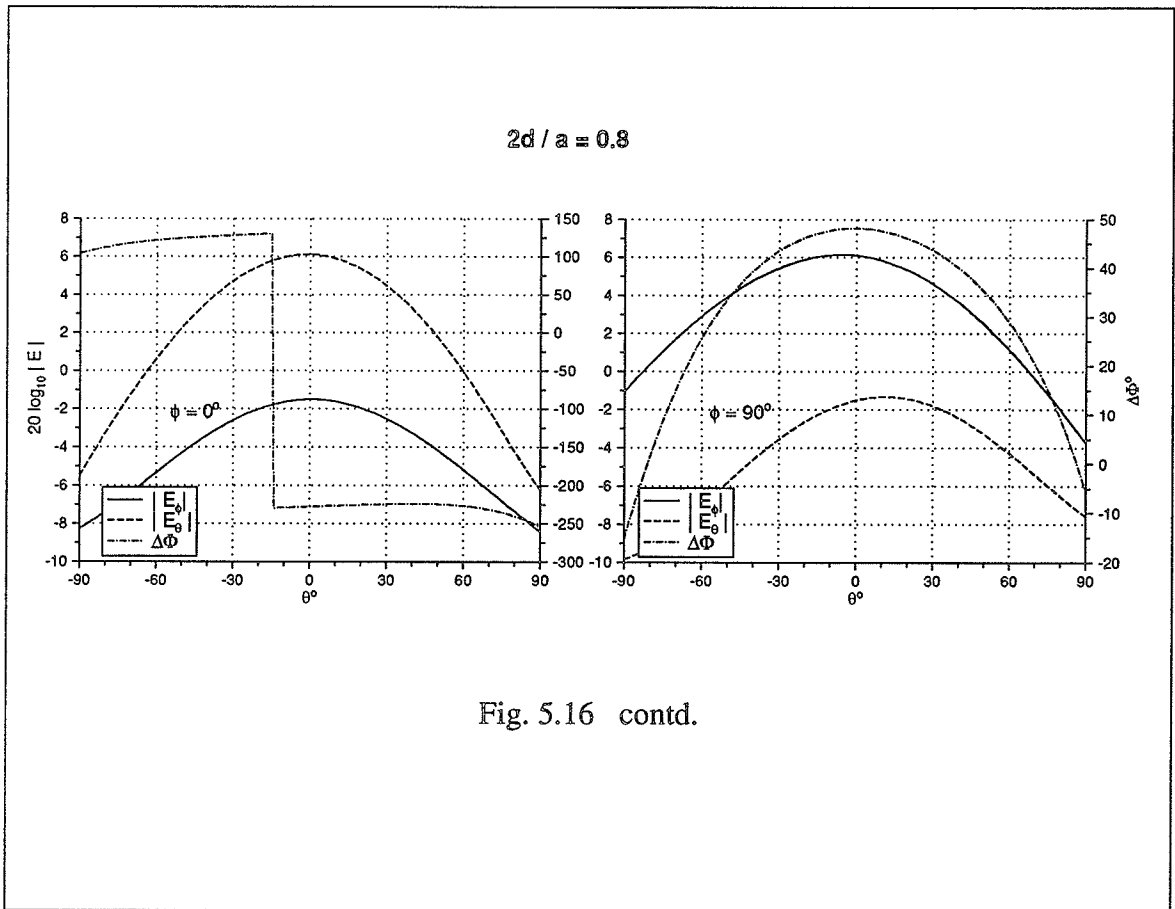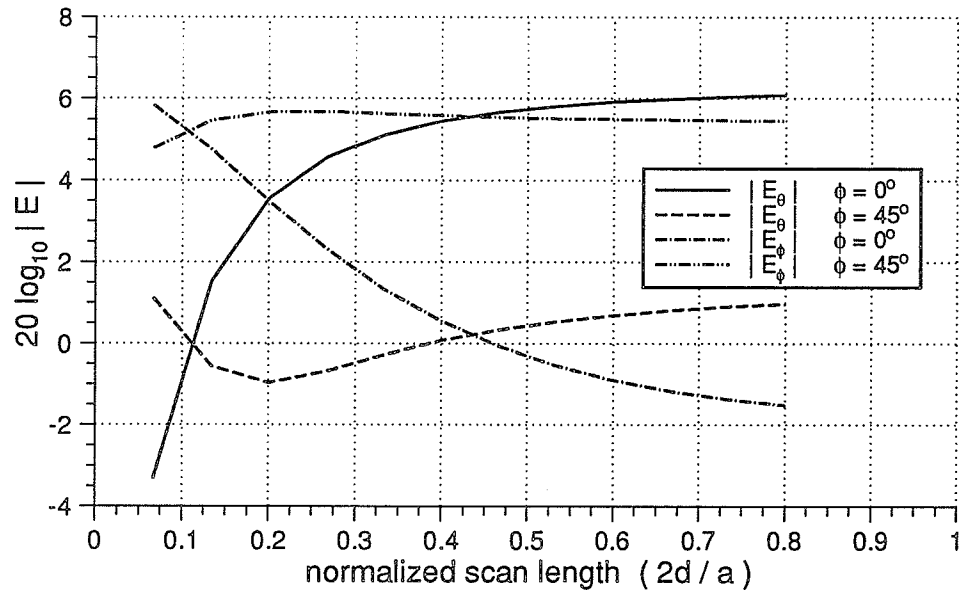
Fig. 5.17 E_θ and E_ϕ gain levels at broadside ($\theta = 0°$) of the rectangular patch versus feed location d. ($a / b = 1.17$)

(a)

(b)
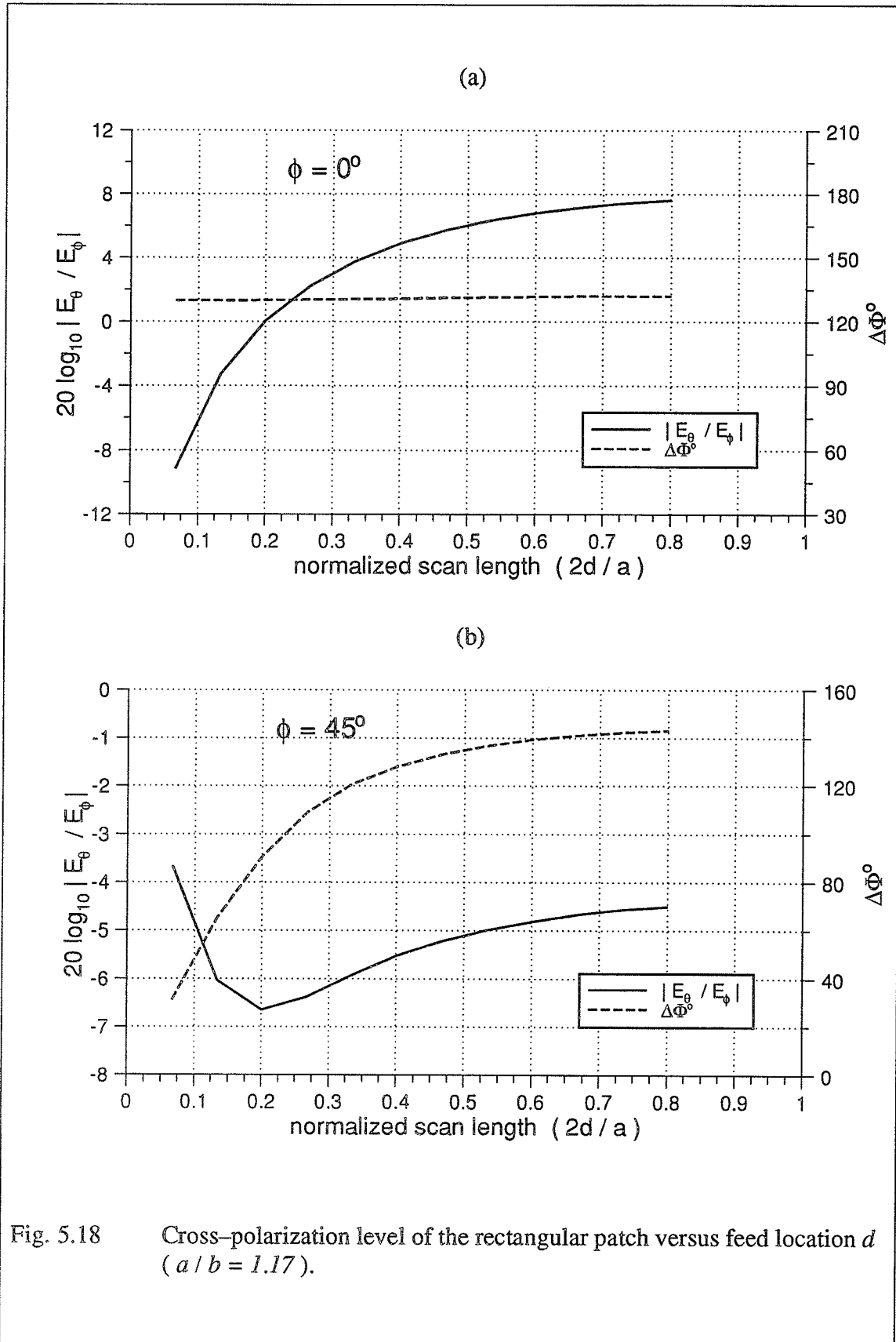
Fig. 5.18   Cross–polarization level of the rectangular patch versus feed location d
($a/b = 1.17$).

Fig. 5.19   Magnitude and phase distribution of the aperture fields of the rectangular
patch computed for different feed locations at $f = 4GHz$. ($a / b = 1$)

(a)

(b)

Fig. 5.20   Cross–polarization level of the rectangular patch versus feed location d
($a / b = 1$).

2d / a = 0

2d / a = 0.333
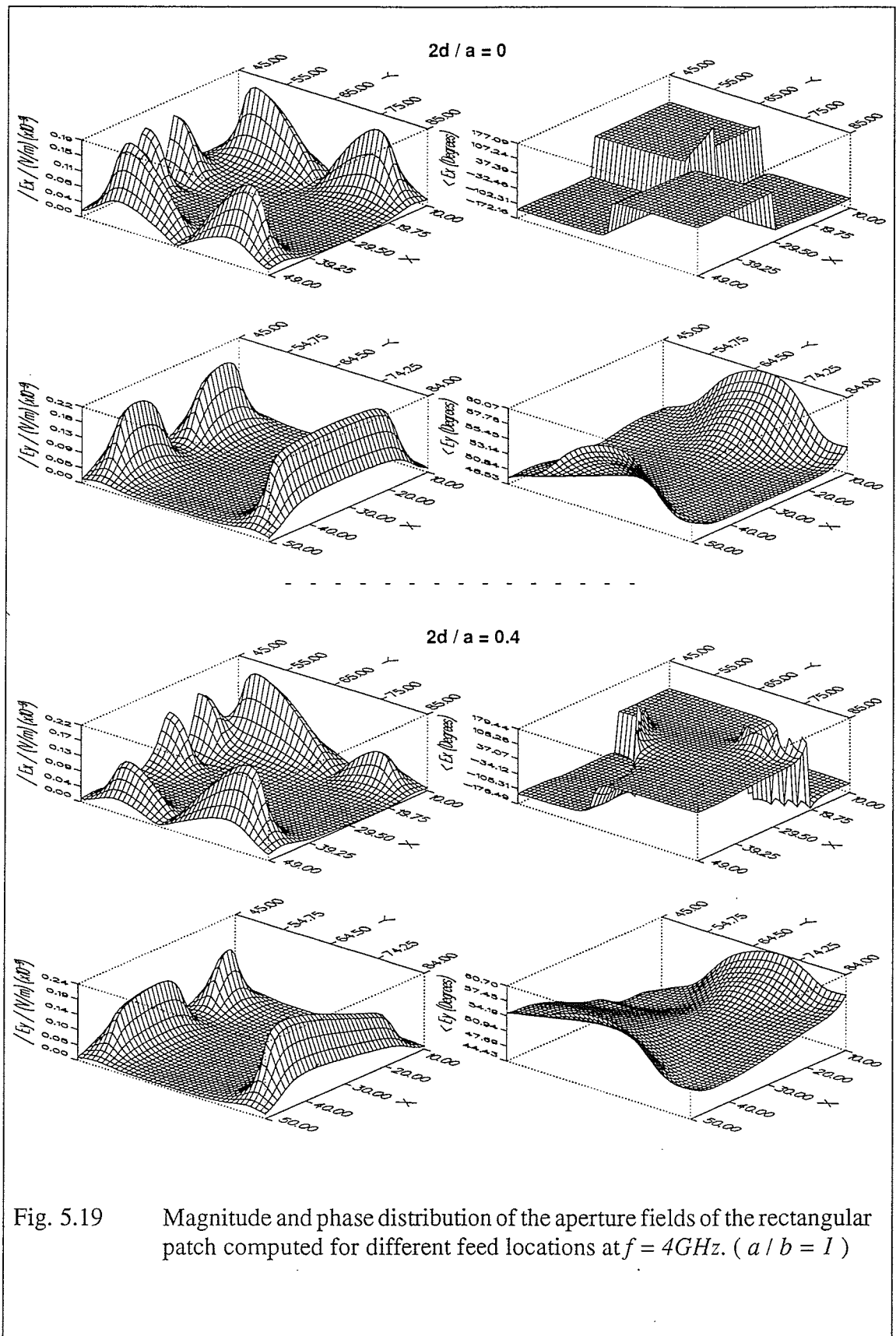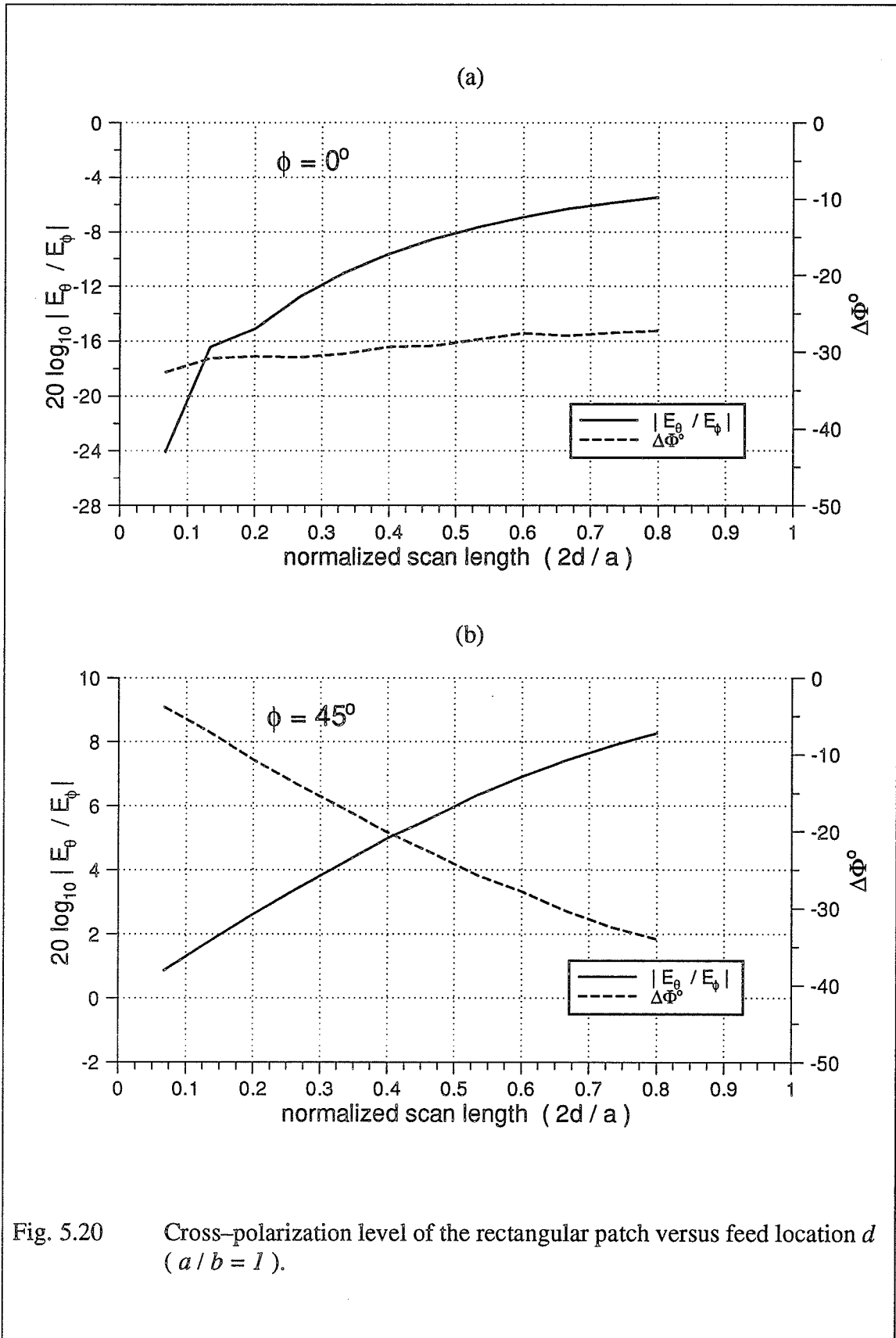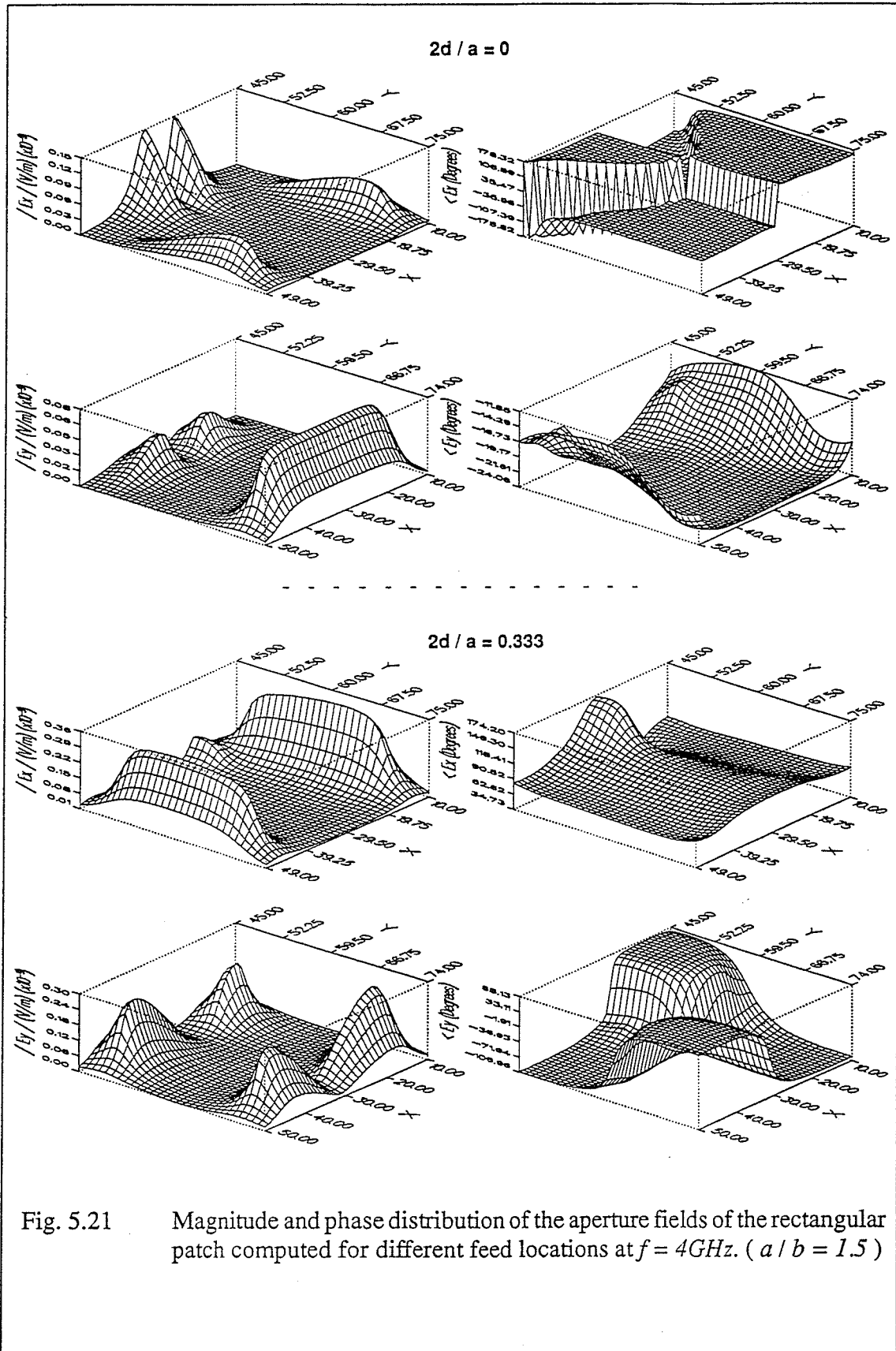
Fig. 5.21   Magnitude and phase distribution of the aperture fields of the rectangular patch computed for different feed locations at $f = 4GHz$. ($a / b = 1.5$)

(a)

(b)

Fig. 5.22   Cross–polarization level of the rectangular patch versus feed location d
($a / b = 1.5$).
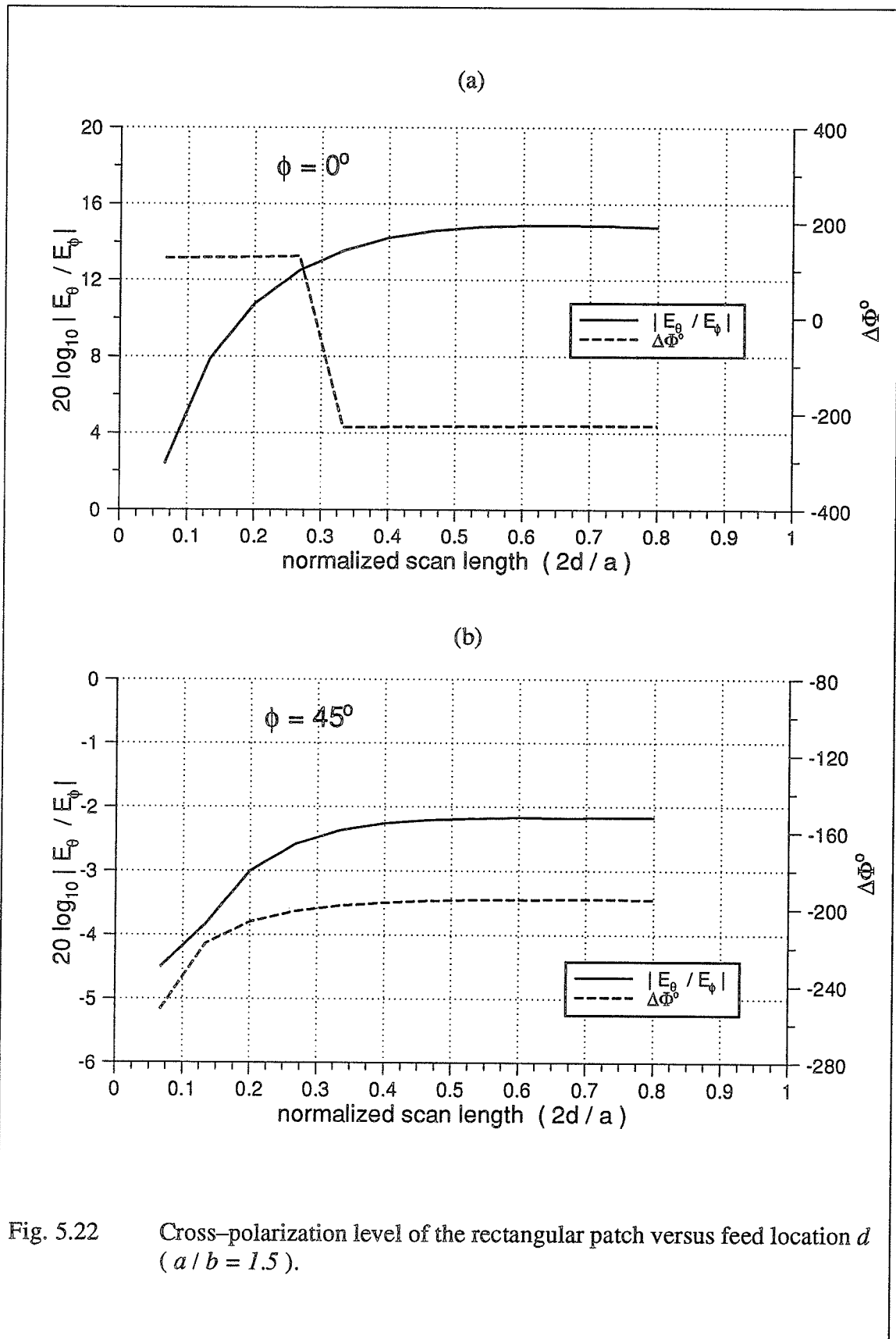
iv) Conclusions

In this chapter, the FDTD technique is used to model and analyze the input and radiation characteries of a rectangular microstrip patch antenna. The return loss ($| S_{11} |$) and the input impedance (Z_{in}) of the rectangular patch were obtained from the input voltage information recorded at the transmission line feeding the rectangular patch. The radiation characteristics were obtained by transforming the equivalent sources obtained from the near–field data, computed by FDTD, on a surface enclosing the rectangular patch over the free space Green's function. Also, the effect of the transmission line location feeding a rectangular patch antenna along the patch length on the co–polar and cross–polar radiation field pattern levels has been studied. Curves relating the gain and cross–polarization field levels to the feed location were obtained for three patch dimensions, of sides rations $\frac{a}{b} = 1$, $\frac{a}{b} = 1.17$, and

$\frac{a}{b} = 1.5$. Such curves will provide a useful design guiding information for a predefined gain and cross–polarization level of rectangular patch antennas of dimensions that are comparable to those considered in this analysis.

CHAPTER VI

CONCLUSIONS AND RECOMMENDATIONS

6.1. Conclusions

The Finite Difference–Time Domain, (FDTD), method approximates the Maxwell's equations by finite–differences and relates the time–dependent quantities to the spatial components of the field vectors. As such, the components of the field vectors are computed directly and progressively from their adjacent values in the past. Thus, the method does not require a dense matrix generation and the objects' local physical constants are used directly during the computational process. Hence, the FDTD technique is an efficient method of computing the field vectors in the vicinity of an object at increasing time steps. In this work, a study of the FDTD numerical technique and its application to scattering and antenna problems is done together with a development of a general purpose code.

In Chapter III, a stability study has been conducted that involved,

– the effect of the spatial step size Δ of the lattice on the FDTD solution, showing a $\Delta \leq \dfrac{\lambda_{min}}{10}$ condition for sufficiently accurate solutions, where λ_{min} is the wavelength of the highest frequency existing in the FDTD solution.

– the distance between the modelled target and the lattice truncation planes, where adequate distance has to be maintained between the target and the lattice walls allowing the ABC to perform accurately.

– the use of second–order ABC (One–Way wave equation eq. 3.9) and the first–order ABC (Averaged Extrapolation eq. 3.1), where a more accurate but less stable performance was observed for the second–order ABC.

The use of a non–uniform gridding in a FDTD lattice is also investigated by examining the propagation of a Gaussian pulse plane wave for different non–uniform gridding

schemes. To insure stability in the FDTD algorithm, the time step increment δt has to be chosen to satisfy the Courant stability criteria taking into account the smallest spatial step size inside the FDTD lattice. This choice might effect the magnitude values of the pulse depending on how small is the smallest Δ relative to the largest Δ, noting also that although there was a change in the peak magnitude of the pulse, in a non–uniform grid, the shape of the pulse is maintained with no distortion as it propagates inside the FDTD lattice.

In Chapter IV, the FDTD method is applied to scattering and field penetration problems. The transient response of a conducting and dielectric circular cylinders illuminated by a step like plane wave is computed. In the conducting cylinder case, the effect of using different rise time values of the excitation plane wave is observed only in the illuminated region of the cylinder. The use of a step like plane wave, having infinite energy, as the excitation function resulted in a steady increase in the magnetic field values on the cylinder's surface due to charge accumulation. A completely different response behavior is observed for the case of the dielectric cylinder. In this case the field values converged to the steady state value of the incident plane wave. The transient response of conducting and dielectric spheres illuminated by a Gaussian pulse plane wave is also computed using the FDTD method. The computed responses agreed favorably with the corresponding analytic solution. The curved surfaces of the cylinder and sphere are modelled by a stepped edge surface inside the rectangular FDTD lattice.

Also in this chapter, the FDTD technique is used to study the field penetration into a conducting box with an open top illuminated normally by a doubly–exponential pulse plane wave. Using the symmetry of the problem only one–quarter of the conducting box geometry was modelled. The effect of modifying the conducting box aperture geometry on the magnitude and frequency content of the transient field penetrating inside the conducting box is studied. It is observed that the aperture edges geometry having the smaller edge size normal to the polarization of the incident wave resulted in a significant reduction of the transient field magnitude at the early time in addition to a resonance phenomena. Adding absorbing material on the aperture wall reduced the transient field magnitude penetrating inside the box cavity, while adding the absorber at the inner walls caused the field resonance to attenuate at a faster rate.

Three different thin wire modeling procedures in the FDTD method were also investigated, where the current magnitude and phase along thin dipoles of different lengths is computed. The three procedures examined are the equal cell area–wire cross–section, $E_{tan} = 0$ on wire, and the contour integral methods.The computed results were compared with those computed from the MoM solution.The equal cell area–wire cross–section procedure gave accurate results but was expensive in computer memory requirements, while the contour integral method provided an efficient and accurate wire modelling technique.

In Chapter V, the use of the FDTD method to antenna analysis is introduced and was applied specifically to rectangular microstrip patch antennas where the corresponding input and radiation characteristics are computed and analyzed. The return loss ($| S_{11} |$) and the input impedance (Z_{in}) of the rectangular patch are obtained from the data recorded at a defined reference plane at the transmission line feeding the patch antenna. The radiation characteristics of the patch antenna are obtained from the near–field data, computed by FDTD, on a surface enclosing the rectangular patch. The effect of the transmission feed line location along the patch length on the cross–polarization field level is investigated for three rectangular patch dimensions of sides ratios, $\frac{a}{b} = 1.0$, $\frac{a}{b} = 1.17$, and $\frac{a}{b} = 1.5$, and curves relating the cross–polarization field level to the feed location are obtained. Keeping the length of side b of the patch constant and increasing the length of side a switched the polarization direction of the patch antenna from a y–polarized ($\frac{a}{b} = 1.0$) to x–polarized ($\frac{a}{b} = 1.5$) radiator.

6.2. Recommendations

It is recommended that further development of the present FDTD code and applying the FDTD method to other scattering and antenna applications to be done. An improvement in the present developed FDTD code can involve the following items

- the capability to model curved surfaces accurately without 'staircase' approximation. One way to implement this capability is by using Maxwell's curl equations in integral form where the curved surfaces are accounted by incorporating field behavior into contour and surface integrals implementing Ampere's law and Faraday's law at selected meshes, and by deforming contour paths as required to conform with the surface curvature.

- investigating the use of more accurate ABC that will model efficiently the free space environment.

- additional study on the use of non–uniform FDTD lattice to model efficiently complex geometries.

- the inclusion of Radar Cross Section (RCS) option into the FDTD code.

the work on the last two items is already in progress.

It is also recommended to apply the FDTD method to inverse scattering and object detection applications using incident plane waves at different angles of incidence and polarization[4]. The FDTD method is also considered to further investigate microstrip patch antennas and to use the modeling procedure of Fig. 5.13 to study the effect of the ground plane size on the main and backlobes of the corresponding radiation patterns. Analysis of circular polarized radiators is also recommended to be studied using the FDTD method. Such types of applications will be studied in the near future.

---

4. This option is already included in the developed FDTD code.

APPENDIX A

TRANSIENT RESPONSE OF A SPHERE

To obtain the transient response of a sphere, the impulse response is first obtained from the frequency–domain data using the inverse Fourier transform. The frequency–domain data is obtained from the Rayleigh–Mei analytical solution of the scattering by a sphere.

Figure A.1 represents a sphere of radius a illuminated by an x–polarized plane wave travelling in the z–direction, that is

$$E_x^i = E_o \, e^{-jkr\cos\theta}$$

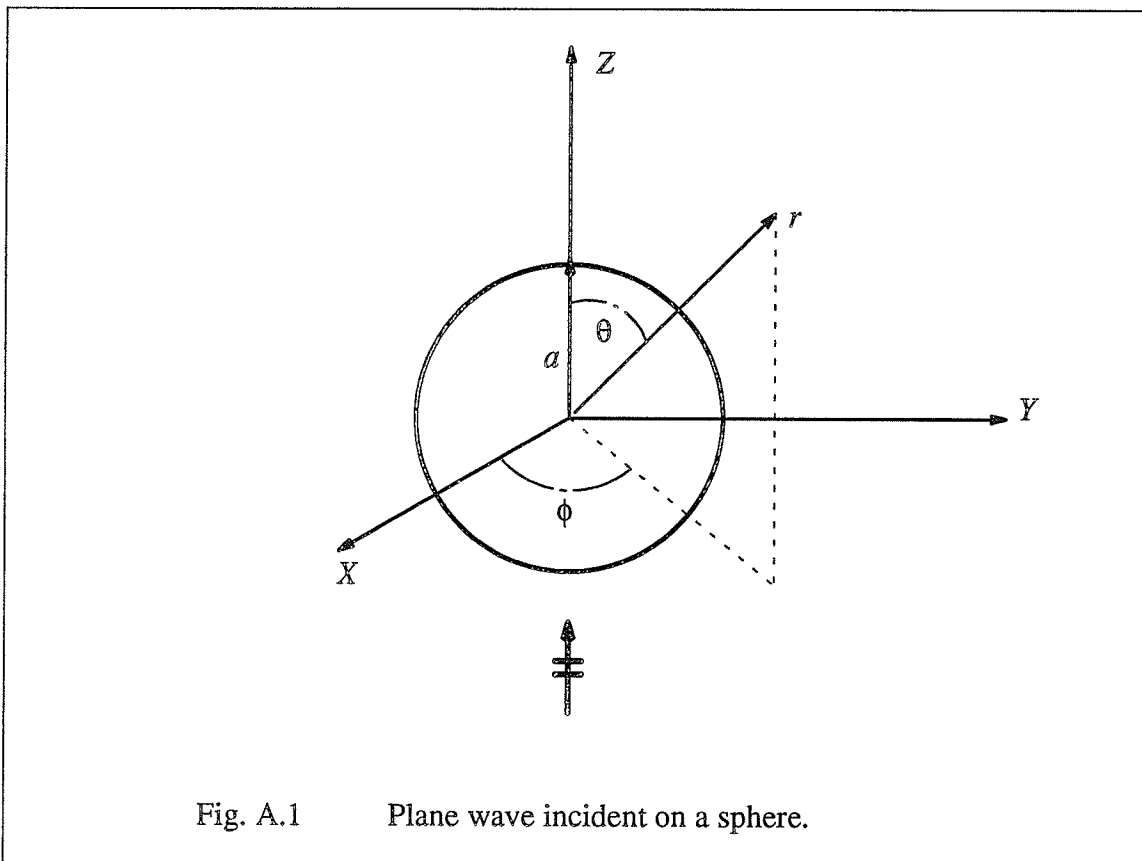$$H_y^i = \frac{E_o}{\eta} \, e^{-jkr\cos\theta} \tag{A–1}$$

Fig. A.1   Plane wave incident on a sphere.

Following the discussion done by Harrington [79, pp. 292], the radial component of the total electric and magnetic vector potentials for the case of a perfectly conducting sphere can be written as,

$$A_r = \frac{E_o}{\omega\mu} \cos\phi \sum_{n=1}^{\infty} \left[a_n \hat{j}_n(kr) + b_n \hat{H}_n^{(2)}(kr) \right] P_n^1(\cos\theta)$$

$$F_r = \frac{E_o}{k} \sin\phi \sum_{n=1}^{\infty} \left[a_n \hat{j}_n(kr) + c_n \hat{H}_n^{(2)}(kr) \right] P_n^1(\cos\theta) \qquad (A-2)$$

where,

$$a_n = \frac{j^{-n}(2n+1)}{n(n+1)}, \quad b_n = \frac{-a_n \hat{j}_n{}'(ka)}{\hat{H}_n^{(2)}{}'(ka)}, \quad c_n = \frac{-a_n \hat{j}_n(ka)}{\hat{H}_n^{(2)}(ka)} \qquad (A-3)$$

$\hat{j}_n$ is the spherical Riccati Bessel function of order n, $\hat{H}_n^{(2)}$ is the spherical Riccati Hankel function of the second kind and order n, k is the wave number, and η is the intrinsic impedance of the media. The field components are found using Eq. 6–26 of [79]. The sphere surface currents can be found according to $\mathbf{J}_s = \hat{u}_r \times \mathbf{H}$ at $r = a$. The result is

$$J_\theta = \frac{j}{\eta} E_o \frac{\cos\phi}{ka} \sum_{n=1}^{\infty} a_n \left[\frac{\sin\theta\, P_n^{1'}(\cos\theta)}{\hat{H}_n^{(2)'}(ka)} + \frac{j\, P_n^1(\cos\theta)}{\sin\theta\, \hat{H}_n^{(2)}(ka)} \right]$$

$$J_\phi = \frac{j}{\eta} E_o \frac{\sin\phi}{ka} \sum_{n=1}^{\infty} a_n \left[\frac{P_n^{1'}(\cos\theta)}{\sin\theta\, \hat{H}_n^{(2)'}(ka)} - \frac{\sin\theta\, P_n^1(\cos\theta)}{j\, \hat{H}_n^{(2)}(ka)} \right] \qquad (A-4)$$

$P_n^1(\cos\theta)$ being the associated Legendre function of argument $\cos\theta$.

For the case of a dielectric sphere the radial vector potentials inside the sphere $(r < a)$, denoted by $-$, can be written as,

$$A_r^- = \frac{E_o}{\omega\mu_o} \cos\phi \sum_{n=1}^{\infty} d_n \, \hat{j}_n(k_d r) P_n^1(\cos\theta)$$

$$F_r^- = \frac{E_o}{k_o} \sin\phi \sum_{n=1}^{\infty} e_n \, \hat{j}_n(k_d r) P_n^1(\cos\theta) \tag{A-5}$$

where

$$d_n = \frac{-j\sqrt{\epsilon_d \, \mu_o}}{\sqrt{\epsilon_d \, \mu_o}\hat{H}_n^{(2)\prime}(k_o a)\hat{j}_n(k_d a) - \sqrt{\epsilon_o \, \mu_d}\hat{H}_n^{(2)}(k_o a)\hat{j}_n{}'(k_d a)} \, a_n$$

$$e_n = \frac{j\sqrt{\epsilon_o \, \mu_d}}{\sqrt{\epsilon_d \, \mu_o}\hat{H}_n^{(2)}(k_o a)\hat{j}_n{}'(k_d a) - \sqrt{\epsilon_o \, \mu_d}\hat{H}_n^{(2)\prime}(k_o a)\hat{j}_n(k_d a)} \, a_n \tag{A-6}$$

where ϵ_d and μ_d are the dielectric constant and permeability of the sphere.

The field components are again obtained from (A-5) using Eq. 6–26 of [79] *i.e.*

$$H_\theta = \frac{1}{r\sin\theta} \cdot \frac{\partial A_r^-}{\partial\phi} + \frac{1}{\hat{z}r} \cdot \frac{\partial^2 F_r^-}{\partial r \, \partial\theta} \tag{A-7}$$

and

$$H_\phi = -\frac{1}{r} \cdot \frac{\partial A_r^-}{\partial\theta} + \frac{1}{\hat{z}} \frac{1}{r\sin\theta} \cdot \frac{\partial^2 F_r^-}{\partial r \, \partial\phi} \tag{A-8}$$

where $\hat{z} = jk\eta = jk_d \, \eta_d$. Substituting (A-5) in (A-7) and (A-8) we obtain for $(r < a)$

$$H_\theta = -\frac{E_o \sin\phi}{k_o r \, \eta_o} \sum_{n=1}^{\infty} \left[d_n \frac{\hat{j}_n(k_d r) \, P_n^1(\cos\theta)}{\sin\theta} - j\frac{e_n}{\eta_r} \, \hat{j}_n{}'(k_d r) \, P_n^1(\cos\theta) \right] \tag{A-9}$$

and

$$H_\phi = \frac{E_o \cos\phi}{k_d r \, \eta_o} \sum_{n=1}^{\infty} \left[d_n \, \hat{j}_n(k_d r) \sin\theta \, P_n^{1\prime}(\cos\theta) - j\frac{e_n}{\eta_r} \, \hat{j}_n{}'(k_d r) \frac{P_n^1(\cos\theta)}{\sin\theta} \right] \tag{A-10}$$

Evaluating (A-9) and (A-10) at $r = a$ the currents are obtained. Computing the current am-

plitude at locations specified by $(a,\ \theta,\ \phi\ )$ on the sphere for a number of frequencies, the impulse response can be obtained by the inverse Fourier transform.

The inverse Fourier transform of $J(\omega\ )$, the current amplitude at frequency ω $rad/$ sec, is written as

$$j\ (t\ )\ =\frac{1}{2\pi}\int\limits_{-\infty}^{\infty}J\ (\omega\ )\ e^{-j\omega t}\ d\omega \qquad (A{-}11)$$

For the case of a plane wave of a non zero pulse width, in our case its the Gaussian pulse $f\ (t\ )\ =\ e^{-\pi\left(\frac{t}{T}\right)^{2}}$, the current response becomes

$$r\ (t\ )\ =\frac{1}{2\pi}\int\limits_{-\infty}^{\infty}R\ (\omega\ )\ e^{-j\omega t}\ d\omega \qquad (A{-}12)$$

where $R\ (\omega\ )\ =\ F\ (\omega\ )J\ (\omega\ )$, $F\ (\omega\ )$ being the Fourier transform of $f\ (t\ )$. Using the discrete Fourier transform concept (Appendix B), the current transient response at location $(a,\ \theta,\ \phi\ )$ on the sphere surface will be given by

$$r(l\ \Delta t\ )\ =\ \left[\ \mathrm{Re}\sum_{n=0}^{N}R\ (n\ \Delta\omega\ ).\exp\ (-j\ n\Delta\omega\ l\ \Delta t)\ \right]\frac{\Delta\omega}{2\pi} \qquad (A{-}13)$$

where $N\ \Delta\omega$ is the highest frequency at which $R\ (\omega\ )$ contains significant energy. If $L\ \Delta t$ is the greatest value of t at which $r(t\ )$ is desired $\Delta\omega$ must be chosen as

$$\Delta\omega\ <\frac{\pi}{L\ \Delta t} \qquad (A{-}14)$$

to prevent aliasing when numerical taking the inverse Fourier transform. In the sphere data presented in this thesis the Rayleigh–Mei expansion is evaluated up to $ka\ =\dfrac{\omega a}{c}\ =\ 30$ where significant energy is present. The total time duration $L\ \Delta t$ is chosen as 2 ns , and $L\ =\ 600$ which provides enough points to plot a smooth curve. $\Delta\omega$ is then chosen to satisfy (A–14).

APPENDIX B

DISCRETE FOURIER TRANSFORM

The Fourier transform of a complex and single–valued function $f(t)$ is defined as

$$F(\omega) = \int_{-\infty}^{\infty} f(t) \cdot e^{-j\omega t}\, dt \qquad (B-1)$$

where t and ω are real variables and j is the imaginary unit. If t designates time in seconds, then ω designates the angular frequency is radians per second (rad/sec). The Discrete Fourier Transform (DFT) corresponding to eq. (B–1) is obtained by evaluating the integral in (B–1) at N discrete points $\{f_o, f_{11}, \ldots, f_{N-1}\}$ resulting in a sequence of complex values $\{F_o, F_{11}, \ldots, f_{NF}\}$ where

$$F_k(k\,\Delta\omega) \approx \Delta t \sum_{n=0}^{N-1} f_n(n\,\Delta t) \cdot \exp(-j\,k\,\Delta\omega\,n\,\Delta t) \qquad (B-2)$$

$k = 0, 1, \ldots, NF$ \qquad\qquad *NF; number of desired frequencies.*

where $f_n(n\,\Delta t)$ is the discrete time–domain field values (from FDTD computations), n is the time step index, N is the total number of discrete time–domain points (total FDTD time steps), $\Delta\omega$ and Δt are the frequency and time resolutions, respectively, k is the frequency index, and $F_k(k\,\Delta\omega)$ is the complex quantity providing the magnitude and phase information at frequency $(k\,\Delta\omega)$.

$\Delta\omega$ is chosen to be consistent with the known sampling theorem. If $N\Delta t$ is the total time duration then a frequency resolution of $\Delta\omega \leq \dfrac{\pi}{N\,\Delta t}$ is to be used to obtain an alising free spectrum.

In our application of the DFT on the time–domain data obtained by the FDTD method, the Fourier transformation was applied separately after the FDTD running has terminated. However, in obtaining the near–field data of the rectangular patch antenna of Chapter V, the DFT summation of (B–2) was updated at every FDTD time step and the fields of selected frequencies are stored.

CONTOUR INTEGRATION TECHNIQUE IN FDTD

C.1 Equivalence to the Yee Algorithm in Free Space.

Following the demonstration done in [20], FDTD expressions will be developed for only one field component in Fig. C.1a using the Ampere's law, and in Fig. C.1b using the Faraday's law. The other field components can be obtained in a similar manner.

Applying Ampere's law along contour C_1 in Fig. C.1a, and assuming that the field value at a midpoint of one side of the contour equals the average value of that field component along that side, we obtain

$$\frac{\partial}{\partial t} \int_{S_1} \mathbf{D} \cdot d\mathbf{S}_1 = \oint_{C_1} \mathbf{H} \cdot d\mathbf{l}_1 \tag{C.1a}$$

$$\frac{\partial}{\partial t} \int_{S_1} \epsilon_0 E_z(i,j,k) \, dS_1 = H_x(i,j-1/2,k)\Delta x + H_y(i+1/2,j,k)\Delta y$$
$$- H_x(i,j+1/2,k)\Delta x - H_y(i-1/2,j,k)\Delta y \tag{C.1b}$$

Now, further assuming that $E_z(i,j,k)$ equals the average value of E_z over the surface S_1; that $\Delta x = \Delta y = \Delta$; and that the time derivative can be numerically realized using a central–difference expression, (C.1b) reduces to

$$\epsilon_0 \Delta^2 \cdot \left[\frac{E_z^{n+1}(i,j,k) - E_z^n(i,j,k)}{\delta t} \right] = \left[H_x^{n+1/2}(i,j-1/2,k) - H_x^{n+1/2}(i,j+1/2,k) \right.$$
$$\left. + H_y^{n+1/2}(i+1/2,j,k) - H_y^{n+1/2}(i-1/2,j,k) \right] \cdot \Delta \tag{C.1c}$$

where the superscripts indicate field values at time steps n, $n+1/2$, and $n+1$. Isolation of $E_z^{n+1}(i,j,k)$ on the left side then yields exactly the Yee time–stepping expression for E_z for the free–space case that was obtained directly from implementing the curl H equation with finite differences.

In an analogous manner, we can apply Faraday's law along contour C_2 in Fig. C.1b, obtaining

$$\frac{\partial}{\partial t} \int_{S_2} \mathbf{B} \cdot d\mathbf{S}_2 = - \oint_{C_2} \mathbf{E} \cdot d\mathbf{l}_2 \qquad (C.2a)$$

$$\frac{\partial}{\partial t} \int_{S_2} \mu_0 H_z(i,j,k) \; dS_2 = - \; E_x(i,j-1/2,k)\Delta x \; - \; E_y(i+1/2,j,k)\Delta y$$

$$+ \; E_x(i,j+1/2,k)\Delta x \; + \; E_y(i-1/2,j,k)\Delta y \qquad (C.2b)$$

$$\mu_0\Delta^2 \cdot \left[\frac{H_z^{n+1/2}(i,j,k) - H_z^{n-1/2}(i,j,k)}{\delta t} \right] = \Big[E_x^n(i,j+1/2,k) - E_x^n(i,j-1/2,k)$$

$$+ \; E_y^n(i-1/2,j,k) - E_y^n(i+1/2,j,k) \Big] \cdot \Delta \qquad (C.2c)$$

Isolation of $H_z^{n+1/2}(i,j,k)$ on the left side yields exactly the Yee time–stepping for H_z for the free–space case that was obtained directly from implementing the curl E equation with finite differences.

C.2 Application to the Thin Wire

To illustrate how the contour integral interpretation permits incorporation of near–field physics the case of a transverse magnetic (*TM*) coupling to a thin wire is considered. Fig. C.2 illustrates the Faraday's law contour path used to derive the special FDTD algorithm for the circumferential magnetic fields immediately adjacent to the wire. Although only H_y is shown, the analysis is easily generalized for the other looping magnetic field components.
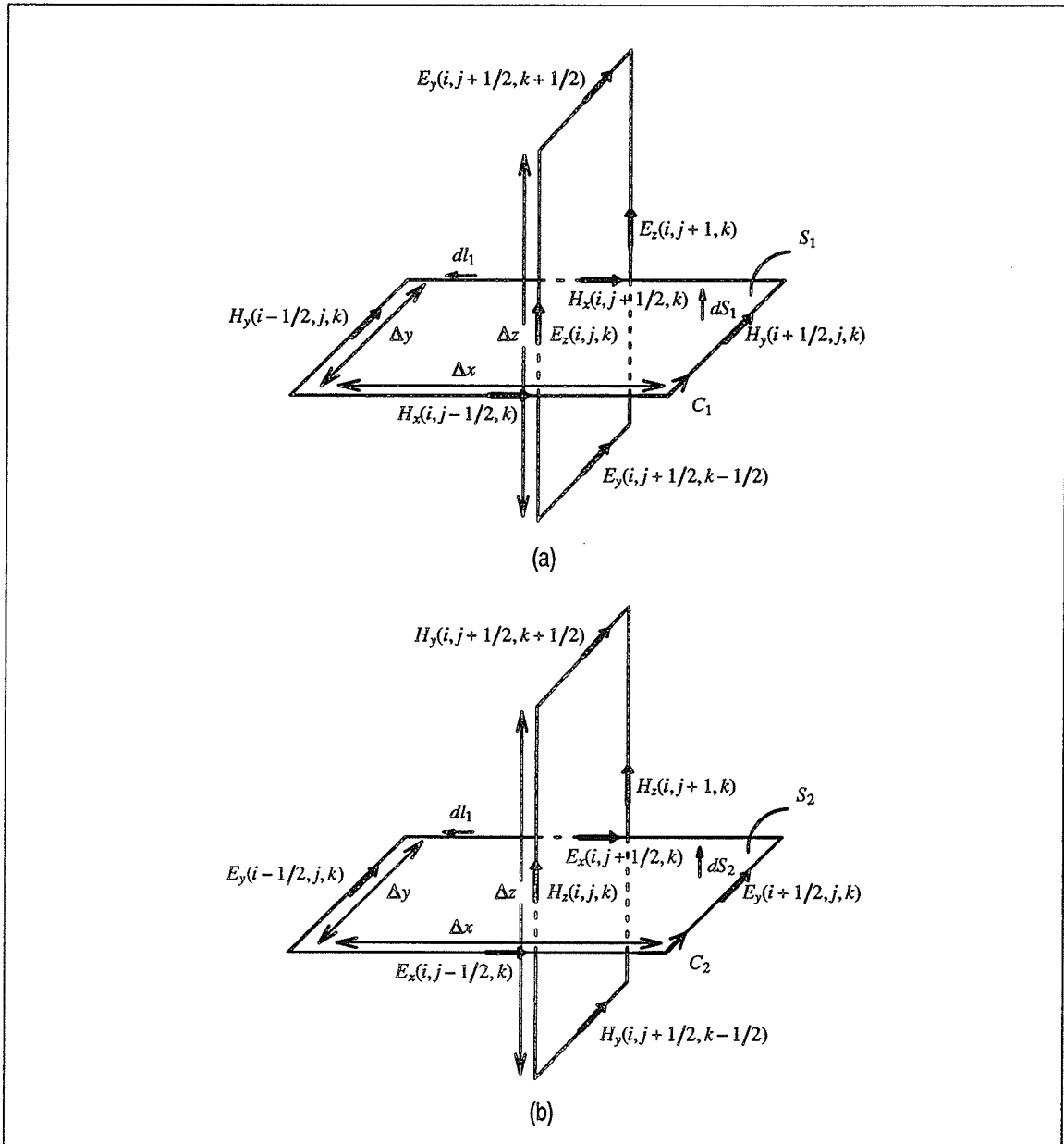
Fig. C.1   Examples of spatially orthogonal contours in free space. (a) Ampere's law for E_z.

(b) Faraday's law for H_z.

The following briefly summarizes the assumptions concerning the near–field physics that are incorporated into the Faraday's law model. First, the near scattered circumferential magnetic field components and the near scattered radial electric field components are assumed to vary as $1/r$ near the wire, where r is the distance from the wire center. With r

constrained to be less than 0.1 wavelength at any point in C (by FDTD spatial resolution requirements), the $1/r$ singularity behavior of the scattered H_y and E_x fields is assumed to dominate the respective incident fields so that the total H_y and E_x fields also take on the $1/r$ singularity. Finally, the near total H_y and the near total E_z fields, evaluated at the z midpoint of the contour, are assumed to represent the average values of their respective fields over the full z interval. These assumptions can be concisely summarized by the following expressions, assumed to apply on and within contour C of Fig. C.2,

$$H_y(x, z) \approx H_y\left(\frac{\Delta}{2}, z_0\right) \cdot \frac{\left(\frac{\Delta}{2}\right)}{x} \cdot \left[1 + c_1 \cdot (z - z_0)\right] \tag{C.3a}$$

$$E_x\left(x, z_0 \pm \frac{\Delta}{2}\right) \approx E_x\left(\frac{\Delta}{2}, z_0 \pm \frac{\Delta}{2}\right) \cdot \frac{\left(\frac{\Delta}{2}\right)}{x} \tag{C.3b}$$

$$E_z(0, z) = 0 \tag{C.3c}$$

$$E_z(\Delta, z) \approx E_z(\Delta, z_0) \cdot \left[1 + c_2 \cdot (z - z_0)\right] \tag{C.3d}$$

where c_1 and c_2 are arbitrary constants that need not be known.

Using the field expressions of (C.3a)–(C.3d), the Fraday's law of (C.2a) can be applied along contour C. In this case the $1/x$ variation in H_y and E_x yield natural logarithms. Also, the linear odd symmetry variation in z assumed for H_y and E_z integrates out. This yields the following expression:

$$\frac{H_y^{n+1/2}\left(\frac{\Delta}{2}, z_0\right) - H_y^{n-1/2}\left(\frac{\Delta}{2}, z_0\right)}{\delta t} \approx$$

$$\frac{\left[E_x^n\left(\frac{\Delta}{2}, z_0 - \frac{\Delta}{2}\right) - E_x^n\left(\frac{\Delta}{2}, z_0 + \frac{\Delta}{2}\right)\right] \cdot \frac{1}{2}\ln\left(\frac{\Delta}{r_0}\right) + E_z^n(\Delta, z_0)}{\mu_0 \frac{\Delta}{2}\ln\left(\frac{\Delta}{r_0}\right)} \qquad (C.4)$$
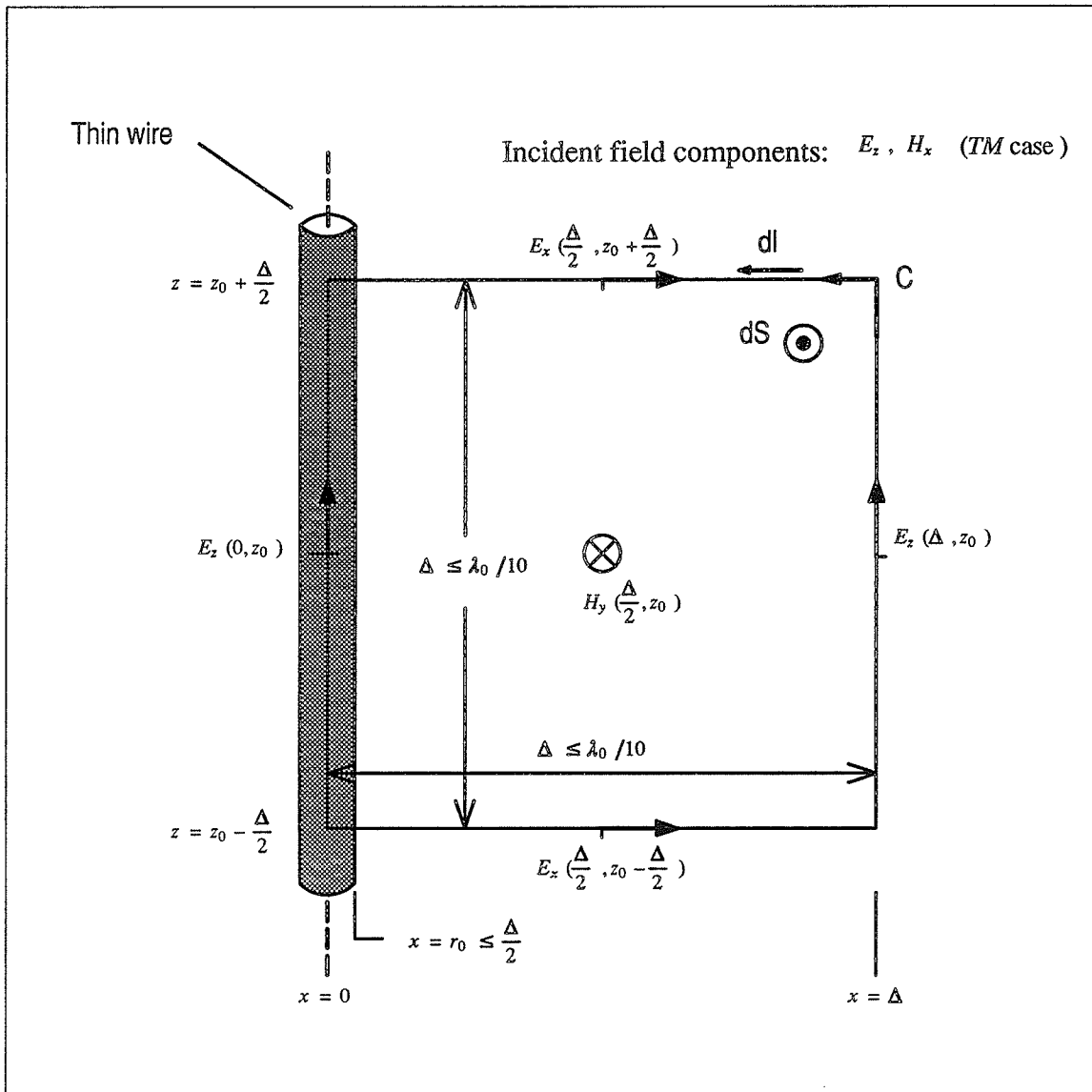
Fig. C.2   Faraday's law contour path for thin–wire model.

where r_0 (assumed to be less than 0.5Δ) is the wire radius. Isolation of $H_y^{n+1/2}(\Delta/2, z_0)$ on the left side of (C.4) yields the required modified time–stepping relation. This analysis can be easily generalized to obtain similar time–stepping relations for the other circumferential magnetic field components immediately adjacent to the wire. It should be noted that no other magnetic or electric field components in the FDTD space lattice require modified time–stepping relations. All other field components are time–stepped using the ordinary free–space Yee algorithm [10].

REFERENCES

[1] C. Bennett and G. Ross, " Time–domain electromagnetics and its applications, " *Proc. IEEE*, 66, pp. 299–318, 1978.

[2] F. M. Tesche, " On analysis of scattering and antenna problems using the singularity expansion technique, " *IEEE Trans. on Antennas Prop.*, vol. AP–21, pp. 53–62, Jan. 1973.

[3] L. B. Felsen, **Transient electromagnetic fields**, New York: Springer–verlag, 1976.

[4] V. Shankar, W. Hall, and A. Mohammadian, " A time–domain differential solver for electromagnetic scattering problems, " *Proc. IEEE*, 77, pp. 709–721, 1989.

[5] A. Sommerfeld, **Partial differential equations in physics** (English translation), New York; Academic Press, 1949.

[6] A. Mohammadian, V. Shankar, and W. Hall, " Computation of electromagnetic scattering and radiation using a time–domain finite–volume discritization procedure, " submitted to publication in the thematic issue of the *Computational Electromagnetics Journal*, 1990.

[7] A. Cangellaris, C. Lin, and K. Mei, " Point–matched time–domain finite–element methods for electromagnetic radiation and scattering, " *IEEE Trans. on Antennas Prop.*, vol. AP–35, pp. 1160–1173, 1987.

[8] P. B. Jhons, " The solution of inhomogeneous waveguide problems using a transmission–line matrix, " *IEEE Trans. on Microwave Theory Tech.*, vol. MTT–22, pp. 209–215, March 1979.

[9] W. Hoefer, " The transmission–line matrix method– theory and applications, " *IEEE Trans. on Microwave Theory Tech.*, vol. MTT–33, pp. 882–893, Oct. 1985.

[10] K. S. Yee, " Numerical solution of initial boundary value problems involving Maxwell's equations in isotropic media, " *IEEE Trans. on Antennas Prop.*, vol. AP–14, pp. 302–307, May 1966.

[11] A. Taflove, and K. Umashankar, " Review of FD–TD numerical modeling of electromagnetic wave scattering and radar cross–section, " *Proc. IEEE*, 77, pp. 682–699, May 1989.

[12] A. Taflove, " Review of the formulation and application of the finite–difference time–domain method for numerical modeling of electromagnetic wave interaction with arbitrary structures," *Wave motion* 10, pp. 547–582, 1988.

[13] G. Mur, " Numerical boundary conditions for the finite–difference approximation of the time–domain electromagnetic field equations, " *IEEE Trans. on Electromag. Compat.*, vol. EMC–23, pp. 377–382, Nov. 1981.

[14] C. Taylor, D. Lam, and T. Shumpert, " Electromagnetic pulse scattering in time varying inhomogeneous media, " *IEEE Trans. on Antennas Prop.*, vol. AP–17, pp. 586–589, Sept. 1969.

[15] A. Taflove and M. Brodwin, " Numerical solution of steady–state electromagnetic scattering problem using the time–dependent Maxwell's equations, " *IEEE Trans. on Microwave Theory Tech.*, vol. MTT–23, pp. 623–630, Aug. 1975.

[16] D. Merewether, " Transient current induced on a metallic body of revolution by an electromagnetic pulse, " *IEEE trans. on Electromag. Compat.*, vol. EMC–13, pp. 41–44, 1971.

[17] K. Kunz, and K. Lee, " A three dimensional finite–difference solution of the external response of an aircraft to a complex transient EM environment : Part 1, the method and its implementation, " *IEEE Trans. on Electromag. Comapt.*, vol. EMC–20, pp. 328–333, May 1978.

[18] B. Enyquist, and A. Majda, " Absorbing Boundary conditions for the numerical simulation of waves, " *Math. Comp.*, vol. 31, pp. 629–651, July 1977.

[19] J. Fang, and K. Mei, " A super–absorbing boundary algorithm for solving electromagnetic problems by time–domain finite–difference method, " *AP–S Symposium*, syracuse, June 1988, pp. 472–475.

[20] K. Umashankar, A. Taflove, and B. Beker, " Calculation and experimental validation of induced currents on coupled wires in an arbitrary shaped cavity, " *IEEE Trans. on Antennas Prop.*, vol. AP–35, pp. 1248–1257, Nov. 1987

[21] R. Holland, " Finite difference solutions of Maxwell's equations in generalized non-orthogonal coordinates, " *IEEE Trans. Nuclear Sci.*, vol. NS–30, pp. 4689–4591, Dec. 1983.

[22] M. Fusco, " FDTD Algorithm in curvilinear coordinates, " *IEEE Trans. on Antennas Prop.*, vol. AP–38, pp. 76–89, Jan. 1990.

[23] N. Madsen, and R. Ziolkowski, " Numerical solution of Maxwell's equations in the time–domain using irregular nonorthogonal grids, " *Wave Motion* 10, pp. 583–596, 1988.

[24] T. Jurgens, A. Taflove *et. al.*, " Finite–Difference Time–Domain Modeling of curved surfaces, " *IEEE Trans. on Antennas Prop.*, vol. AP–40, pp. 357–366, April 1992.

[25] D. Choi, and W. Hoefer, " The finite–difference time–domain method and its application to eigenvalue problems, " *IEEE Trans. on Microwave Theory Tech.*, MTT–34, pp. 1464–1470, Dec. 1986.

[26] J. Hese, and D. Zutter, " Modeling of Discontinuities in General Coaxial waveguide Structures by FDTD–Method, " *IEEE Trans. on Microwave Theory Tech.*, vol. MTT–40 , pp. 547–556, March 1992.

[27] J. Jarem, " A method of moments analysis and a Finite–Difference Time–Domain analysis of a probe–sleeve fed rectangular waveguide cavity, " *IEEE Trans. on Microwave Theory Tech.*, vol. MTT–39, pp. 444–451, March 1991.

[28] L. Wu, and Y. Chang, " Characterization of the shielding effects on the frequency–dependent effective dielectric constant of a waveguide–shielded Microstrip using the Finite–Difference Time–Domain Method, " *IEEE Trans. on Microwave Theory Tech.*, vol. MTT–39, pp. 1688–1693, Oct. 1991.

[29] A. Navarvo, M. Nunea, and E. Martin, " Study of TE_o and TM_o modes in dielectric resonators by a finite difference–time domain method coupled with the discrete Fourier transform, " *IEEE Trans. on Microwave Theory Tech.*, vol. MTT–39, pp. 14–17, Jan. 1991.

[30] R. Holland, " THREDE: A free–field EMP coupling and scattering code, " *IEEE Trans. on Nuclear Sci.*, vol. NS–24, pp. 2416–2421, Dec. 1977.

[31] R. Holland, L. Simpson, and K. Kunz, " Finite–difference analysis of EMP coupling to lossy dielectric structures, " *IEEE Trans. on Electromag. Compat.*, vol. EMC–22, pp. 203–209, Aug. 1980.

[32] J. Prewitt, " Missile EMP interaction: Dielectric and Plume–connection effects, " *IEEE Trans. on Nuclear Sci.*, vol. NS–25, pp. 1412–1416, Dec. 1978.

[33] R. Holland, L. Simpson, and R. Jhon, " Code optimization for solving large 3D EMP problems, " *IEEE Trans. on Nuclear Sci.*, vol. NS–26, pp. 4964–4969, Dec. 1979.

[34] C. Britt, " Solution of electromagnetic scattering problems using time–domain techniques, " *IEEE Trans. on Antennas Prop.*, vol. AP–37, pp. 1181–1192, Sept. 1989.

[35] R. Luebbers *et. al.*, " A Finite–Difference Time–Domain near zone to far zone transformation, " *IEEE Trans. on Antennas Prop.*, vol. AP–39, pp. 429–433, April 1991.

[36] K. S. Yee *et. al.*, " Time–Domain extrapolation to the far field based on FDTD calculations, " *IEEE Trans. on Antennas Prop.*, vol. AP–39, pp. 410–413, March 1991.

[37] X. Zhang, J. Fang, K. Mei, and Y. Liu, " Calculation of the dispersive characteristics of Microstrips by the time–domain finite–difference method, " *IEEE Trans. on Microwave Theory and Tech.*, vol. MTT–36, pp. 263–267, Feb. 1988.

[38] X. Zhang, and K. Mei, " Time–domain finite–difference approach to the calculation of the frequency–dependent characteristics of Microstrip discontinuities, " *IEEE Trans. on Microwave Theory Tech.*, vol. MTT–36, pp. 1775–1787, 1988

[39] D. Sheen, M. Ali, M. Abouzahra, and J. Kong, " Application of the three–dimensional finite–difference time–domain method to the analysis of planer Microstrip circuits, " *IEEE Trans. on Microwave Theory tech.*, vol. MTT–38, pp. 849–857, July 1990.

[40] A. Reineix , and B. Jecko, " Analysis of microstrip patch antennas using finite–difference time–domain method, " *IEEE Trans. on Antennas Prop.*, vol. AP–37, pp. 1361–1369, Nov. 1989.

[41] W. Ko, and R. Mittra, " A combination of FDTD and Prony's method for analyzing Microwave integrated circuits, " *IEEE Trans. on Microwave Theory Tech.*, vol. MTT–39, pp. 2176–2181, Dec. 1991.

[42] A. Taflove, " Application of finite–difference time–domain method to sinusoidal stea-dy–state electromagnetic penetration problems, " *IEEE Trans. on Electromag. Comapt.*, vol. EMC–22, pp. 191–202, Aug. 1980.

[43] A. Taflove, and K. Umashankar, " A hybrid Moment method/Finite–difference Time–domain Approach to electromagnetic coupling and aperture penetration into complex geometries, " *IEEE Trans. on Antennas Prop.*, vol. AP–30, pp. 617–627, July 1982.

[44] K. Umashankar, and A. Taflove, " A novel method to analyze electromagnetic scatter-ing of complex objects, " *IEEE Trans. on Electromag. Compat.*, vol. EMC–24, pp. 397–405, Nov. 1982.

[45] A. Taflove and K. Umashankar, " Radar cross section of general three dimensional scatterers," *IEEE Trans. on Electromag. Comapt.*, vol. EMC–25, pp. 433–440, Nov. 1983.

[46] A. Taflove, K. Umashankar, and T. Jurgens, " Validation of FD–TD modeling of the radar cross section of three–dimensional structures spanning up to nine wavelengths, " *IEEE Trans. on Antennas Prop.*, vol. AP–33, pp. 662–666, June 1985.

[47] C. Furse *et. al.* , " Improvements to the Finite–Difference Time–Domain method for calculating the radar cross section of a perfectly conducting target, " *IEEE Trans. on Microwave Theory Tech.*, vol. MTT–38, pp. 919–927, July 1990.

[48] D. Sullivan, D. Borup, and O. Gandhi, " Use of the finite–difference time–domain method in calculating EM absorption in human tissues, " *IEEE Trans. on Biomed. Eng'g.*, vol. BME–34, pp. 148–157, Feb. 1987.

[49] J. Chen, and O. Gandhi, " Currents induced in an analytically based model of a human for exposure to vertically polarized electromagnetic pulse, " *IEEE Trans. on Micro-wave Theory Tech.*, vol. MTT–39, pp. 31–39, jan. 1991.

[50] D. Sullivan, " Mathematical method for treatment planning in deep Hyperthermia, " *IEEE Trans. on Microwave Theory Tech.*, vol. MTT–39, pp. 864–872, May 1991.

[51] D. Sullivan, " A Frequency–Dependent FDTD method for Biological Applications," *IEEE Trans. on Microwave Theory Tech.*, vol. MTT–40, pp. 532–539, March 1992.

[52] D. Katz *et. al.*, " FDTD analysis of electromagnetic wave radiation from systems containing horn antennas, " *IEEE Trans. on Antennas Prop.*, vol. AP–39, pp. 1203–1212, Augest 1991.

[53] P. Tirkas, and C. Balanis, " Finite–Difference Time–Domain method for Antenna radiation, " *IEEE Trans. on Antennas Prop.*, vol. AP–40, pp. 334–340, March 1992.

[54] R. Chen, and K. Mei, " Analysis of small Broadband flare Antennas by an improved FDTD method, " *in Proc. of IEEE–Ap Symp.*, London, Ontario, pp. 645–648, June 1991.

[55] R. Holland, and L. Simpson, " Finite–difference analysis of EMP coupling to thin struts and wires, " *IEEE trans. on Electromag. Comapt.*, vol. EMC–23, pp. 88–97, May 1981.

[56] C Turner, and L. Bacon, " Evaluation of a thin–slot formalism for finite–difference time–domain electromagnetic codes, " *IEEE Trans. on Electromag. Comapt.*, vol. EMC–30, pp. 523–528, Nov. 1988.

[57] K. Demarest, " A finite difference–Time domain technique for modeling narrow apertures in conducting scatterers, " *IEEE Trans. on Antennas Prop.*, vol. AP–35, pp. 826–831, July 1987

[58] D. Riley, and D. Turner, " Hybrid thin–slot algorithm for the analysis of narrow apertures in finite–difference time–domain calculations, " *IEEE Trans. on Antennas Prop.*, vol. AP–38, pp. 1943–1950, Dec. 1990.

[59] D. Riley, and D. Turner, " The inclusion of wall loss in Finite–Difference Time–Domain thin slot algorithms, " *IEEE Trans. on Electromag. Comapt.*, vol. EMC–33, pp. 304–311, Nov. 1991.

[60] K. Umashankar, A. Taflove, and B. Beker, " Calculation and experimental validation of induced currents on coupled wires in an arbitrary shaped cavity, " *IEEE Trans. on Antennas Prop.*, vol. AP–35, pp. 1248–1257, Nov. 1987

[61] A. Taflove, K. Umashankar, B. Beker, F. Harfoush, and K. Yee, " Detailed FD–TD analysis of electromagnetic fields penetrating narrow slots and lapped joints in thick conducting screen, " *IEEE Trans. on Antennas Prop.*, vol. AP–36, pp. 247–257, Feb. 1988.

[62] M. Bui *et. al.*, " Propagation of Transients in Dispersive dielectric media, " *IEEE Trans. on Microwave Theory Tech.*, vol. MTT–39, pp. 1165–1172, July 1991.

[63] N. E. Hill, *et. al.* , **Dielectric Properties and Molecular Behavior**, NewYork, 1969.

[64] R. Lubbers, F. Hunsberger, and K. Kunz, " A Frequency–dependent Finite–difference Time–domain formulation for transient propagation in plasma, " *IEEE Trans. on Antennas Prop.*, vol. AP–39, pp. 29–34, Jan. 1991.

[65] R. Luebbers *et. al.*, " A Frequency–Dependent Finite–Difference Time–Domain formulation for dispersive materials, " *IEEE Trans. on Electromag. Comapt.*, vol. EMC–32, pp. 222–227, Augest 1990.

[66] T. Moore, J. Blaschak, A. Taflove, and G. Kriegsmann, " Theory and application of radiation boundary operators, " *IEEE Trans. on Antennas Prop.*, vol. AP–36, pp. 1797–1811, Dec. 1988.

[67] J. Blaschak, and G. Kriegsmann, " A comparative study of absorbing boundary conditions, " *J. Comp. Phys.*, vol. 77, pp. 109–139, July 1988.

[68] P. Tirkas, and K . Demarest, " Modeling of thin dielectric structures using Finite–Difference Time–Domain technique, " *IEEE Trans. on Antennas Prop.*, vol. AP–39, pp. 1338–1344, Sept. 1991.

[69] J. Maloney, and G. Smith, " The use of Surface Impedance concepts in the Finite–Difference Time–Domain Method, " *IEEE Trans. on Antennas Prop.*, vol. AP–40, pp. 38–48, Jan. 1992.

[70] J. Beggs *et. al.*, " Finite–Difference Time–Domain Implementation of Surface Impedance Boundary Conditions, " *IEEE Trans. on Antennas Prop.*, vol. AP–40, pp. 49–56, Jan. 1992.

[71] J. Maloney, and G. Smith, " The efficient modeling of thin material sheets in the Finite–Difference Time–Domain Method, " *IEEE Trans. on Antennas Prop.*, vol. AP–40, pp. 323–330, March 1992.

[72] R. Luebbers, and K. Kunz, " FDTD modeling of thin impedance sheets, " *IEEE Trans. on Antennas Prop.*, vol. AP–40, pp. 349–351, March 1992.

[73] L. Wu, and L. Han, " Implementation and application of resistive sheet boundary condition in the Finite–Difference Time–Domain Method, " *IEEE Trans. on Antennas Prop.*, vol. AP–40, pp. 628–633, June 1992.

[74] K. Kunz, and L. Simpson, " A technique for increasing the resolution of Finite–Difference solution of the Maxwell equation, " *IEEE Trans. on Electromag. Comapt.*, vol. EMC–23, pp. 88–97, May 1981.

[75] S. Zivanovic *et. al.*, " A subgridding method for the Time–Domain Finite–Difference method to solve Maxwell's equations, " *IEEE Trans. on Microwave Theory Tech.*, vol. MTT–39, pp. 471–479, March 1991.

[76] S. Xiao *et. al.*, " A fast two–dimensional FDTD full–wave analyzer with adaptive mesh size, " *in Proc. of IEEE–MTT Symp.*, Albuquerque, New Mexico, pp. 783–786, June 1992.

[77] W. A. Chamma, and L. Shafai, " EM Response of Complex Objects, " Scientific Authority, Department of National Defence Ottawa, Canada, Final Report, DSS contract W7714–1–9539/01–ST, March 1992.

[78] W. A. Chamma, and L. Shafai, " Transient response of a Circular Cylinder, a numerical approach, " *Symp. on Antenna Tech. and applied Electromag.*, "ANTEM", Winnipeg, CANADA, pp. 539–543, Aug. 1990.

[79] R. F. Harrington, **Time–Harmonic Electromagnetic Fields**, McGRAW–HILL COMAPNY, New York, 1961.

[80] W. Chamma, and L. Shafai, " Transient field computation within or proximity of complex structures, " *in proc. of Canadian Conference on Elect. and Comp. Engineering*, Ottawa, Sept. 3–6, 1990, pp. 38.3.1–38.3.4.

[81] W. A. Chamma, and L. Shafai, " EMP Response of Arbitrary Conducting and Complex Objects, " Scientific Authority, Department of National Defence Ottawa, Canada, Final Report, DSS contract W7714–8–5648/01–SS, Dec. 1989.

[82] C. J. Bouwkamp, "Theoretical and numerical treatment of diffraction through a circular aperture," *IEEE Trans. on Antennas Prop.*, AP–18, no. 2, pp. 152–176, March 1970.

[83] C. M. Butler and K. Umashankar, " Electromagnetic excitation of a wire through an aperture–perforated conducting screen, " *IEEE Trans. on Antennas Prop.*, AP–24, p. 456, 1976.

[84] H. k. Schumann and D. E. Warren, " Aperture coupling in bodies of revolution, " *IEEE Trans. on Antennas Prop.* , AP–26, no. 6, pp. 778–783, Nov. 1987.

[85] R. F. Harrington, **Field Computation by Moment Methods**, New York: MacMillan, 1968.

[86] W. Chamma, and L. Shafai, " Computation of field penetration into a cavity using FD–TD, " *in proc. of joint URSI IEEE–AP symp.*, Dallas, TX, 1990, pp. 32.

[87] W. A. Chamma, and L. Shafai, " Study EMP Response of Arbitrary Conducting and Complex Objects, " Scientific Authority, Department of National Defence Ottawa, Canada, Final Report, DSS contract W7714–0–9392/01–SS, March 1991.

[88] K. Kunz, *et al.*, " Surface current injection technique: A theoretical investigation, " *IEEE Trans. Nuclear Sci.*, NS–25, 1422–1427, 1978.

[89] K. Kunz, R. Luebbers, and F. Hunsbeger, " A thin dipole antenna demonstration of the antenna modeling capabilities of the FD–TD technique, " *ACES Journal*, 1990.

[90] G. Burke, and A. Poggio, " Numerical Electromagnetic Code (NEC) – Method of Moments, " *Naval Ocean Systems Center*, San Diego, CA, 1980.

[91] W. Chamma, L. Shafai, and S. Kashyap, " Thin wire modeling in FD–TD, " *in Proc. of joint URSI IEEE–AP symp.*, London, Ontario, June 24–28, 1991, pp. 422–425.

[92] J. Maloney, *et. al.*, " Accurate computation of the radiation from simple antennas using the FDTD method, " *IEEE Trans. on Antennas Prop.* , AP–38, pp. 1059–1068, July 1990.

[93] S. Safavi–Naini, and M. Shahabadi, " Time–domain analysis of an array of tapered slot antennas, " *IEEE AP–Symp.*, London Ontario, pp. 434–437, June 1991.

[94] J. Litva, *et. al.*, "Full–wave analysis of an assortment of printed antenna structures using the FDTD method, " *IEEE AP–Symp.*, London Ontario, pp. 410–413, June 1991.

[95] E. Daniel, and C. Railton, " Fast Finite–Difference Time–Domain analysis of microstrip patch antennas, " *IEEE AP–Symp.*, London Ontario, pp. 414–417, June 1991.

[96] J. James, P. Hall, and C. Wood, *Microstrip Antenna, Theory and Design*, 1981, Peter Perqrinus Ltd., IEE, London and New York.

[97] S. A. Schelkunoff, " Field equivalence theorems, " *Commun. Pure Appl. Math.*, vol. 4, pp. 43–59, June 1951.

[98] W. A. Chamma, L. shafai, and S. Kashyap, " Study of transient field penetration inside a conducting box using FDTD method, " conditionally accepted for publication in the *IEEE Trans. on Electromag. Compat. Journal*, Oct. 1992.